

**OBSERVATIONS OF STRESS CORROSION CRACKING  
BEHAVIOUR IN SUPER DUPLEX STAINLESS STEEL**

A thesis submitted to The University of Manchester for the degree of  
Doctor of Philosophy in the Faculty of engineering and physical science

**2011**

**Mohammed Al-Rabie**

**School of Materials**

## Table of Contents

Table of Contents .....	2
List of Figures .....	6
List of Tables.....	17
Abstract.....	18
Declaration.....	19
Copyright Statement.....	20
Acknowledgements .....	21
<b>1 INTRODUCTION.....</b>	<b>22</b>
<b>2 LITERATURE REVIEW .....</b>	<b>25</b>
2.1 STAINLESS STEELS.....	25
2.1.1 <i>Stainless Steel Classes</i> .....	27
2.1.1.1 Ferritic Stainless Steel .....	27
2.1.1.2 Martensitic Stainless Steel .....	28
2.1.1.3 Austenitic Stainless Steels.....	28
2.1.1.4 Precipitation Hardening Steels.....	29
2.1.1.5 Duplex Stainless Steels (Ferritic/Austenitic) .....	30
2.1.2 <i>Summary</i> .....	43
2.2 CORROSION OF STAINLESS STEELS.....	43
2.2.1 <i>Electrochemistry of corrosion</i> .....	43
2.2.2 <i>Forms of Corrosion</i> .....	47
2.2.2.1 Pitting corrosion.....	47
2.2.2.2 Stress Corrosion Cracking.....	53
2.2.3 <i>Summary</i> .....	69
2.3 DIGITAL IMAGE CORRELATION.....	70
2.3.1 <i>Basic Concepts of Digital Image Correlation</i> .....	70
2.3.2 <i>Digital Image Correlation Requirements</i> .....	76

2.3.3	<i>Applications of Digital Image Correlation</i> .....	78
2.3.3.1	Measurement of Crack Opening Displacement and crack developments .....	78
2.3.3.2	<i>Applications of Digital Image Correlation for SCC Study</i> .....	79
2.3.4	<i>Digital Volume Correlation (DVC)</i> .....	85
2.3.5	<i>Summary</i> .....	86
<b>3</b>	<b>EXPERIMENTAL TECHNIQUES AND METHODS</b> .....	<b>87</b>
3.1	MATERIALS AND SPECIMEN PREPARATION.....	87
3.2	METALLOGRAPHIC SPECIMEN PREPARATION .....	88
3.3	ELECTROCHEMICAL MEASUREMENTS.....	88
3.4	ELECTROPOLISHING .....	90
3.5	U-BEND TEST .....	91
3.6	COLD ROLLING.....	92
3.7	MECHANICAL TESTING.....	93
3.7.1	<i>Hardness Testing</i> .....	93
3.7.2	<i>Tensile Testing</i> .....	93
3.8	DIGITAL IMAGE CORRELATION.....	94
3.9	CONSTANT LOAD TEST.....	95
3.10	SALT LOADING ON THE TENSILE SAMPLE.....	97
3.11	MICROSCOPY.....	98
3.11.1	<i>Optical Microscope (OM)</i> .....	98
3.11.2	<i>Scanning Electron Microscope SEM</i> .....	99
3.11.3	<i>Electron Back Scattered Diffraction on SEM</i> .....	99
3.12	IN-SITU MICRO-TENSILE TESTING .....	100
3.13	TOMOGRAPHY .....	103
<b>4</b>	<b>RESULTS</b> .....	<b>105</b>
4.1	MICROSTRUCTURE OF MATERIALS AS RECEIVED.....	105
4.2	ELECTROCHEMICAL MEASUREMENTS.....	106
4.3	OBSERVATIONS OF PITTING AFTER ELECTROCHEMICAL TESTING .....	108

4.4	CHARACTERISATION OF U-BEND TEST WITH SALT DEPOSITS.....	110
4.5	MECHANICAL TESTING.....	112
4.6	SURFACE PREPARATION FOR THE DIGITAL IMAGE CORRELATION ANALYSIS.....	114
4.7	DIGITAL IMAGE CORRELATION ACCURACY WITHIN THE SALT DROPLETS.....	117
4.8	ATMOSPHERIC STRESS CORROSION CRACKING TESTS.....	124
4.8.1	<i>DIC Analysis</i> .....	124
4.8.1.1	Rolled Sample: (Transverse to Tensile)/(wet salt droplet).....	124
4.8.1.2	Rolled Sample: (Transverse to Tensile)/(evaporated salt droplet).....	130
4.8.1.3	Rolled Sample: (Longitudinal to Tensile).....	136
4.8.1.4	As Received: (Transverse to Tensile).....	138
4.8.1.5	As Received: (Longitudinal to Tensile).....	143
4.8.2	<i>Surface Characterization and Fractography</i> .....	143
4.8.2.1	Rolled Sample: (Transverse to Tensile).....	143
4.8.2.2	Rolled Sample: (Longitudinal to Tensile).....	157
4.8.2.3	As Received: (Transverse to Tensile).....	159
4.8.2.4	As Received: (Longitudinal to Tensile).....	163
4.8.2.5	Rolled sample tested without load.....	165
4.8.2.6	Solution annealed sample tested without load.....	167
4.9	IN-SITU TENSILE TESTING.....	169
4.9.1	<i>DIC Analysis</i> .....	170
4.9.2	<i>EBSD Analysis</i> .....	172
4.9.3	<i>Pitting initiation test</i> .....	173
4.9.4	<i>Strain distribution in both phases</i> .....	173
4.9.5	<i>Pitting Density vs. Strain</i> .....	176
4.9.6	<i>Summary</i> .....	180
<b>5</b>	<b>DISCUSSION</b> .....	<b>182</b>
5.1	MATERIAL AND ELECTROCHEMICAL CHARACTERIZATION.....	182
5.2	CRACK NUCLEATION FROM CONCENTRATED SALT DEPOSITS.....	183
5.3	ANALYSIS OF CRACK PATH AND ARRESTED CRACK.....	187
5.4	SUITABILITY OF DIGITAL IMAGE CORRELATION.....	196

5.5 STRAIN PARTITIONING AND PITTING.....201

5.6 SUMMARY .....203

**6 CONCLUSION AND FUTURE WORKS ..... 205**

**7 REFERENCES ..... 208**

**8 APPENDIX.....219**

Final word count: 40,459

## List of Figures

<b>Figure 2-1:</b> Schaeffler diagram, effect of alloying elements on the basic structure of Cr- Ni stainless steels .	27
<b>Figure 2-2:</b> BCC and FCC Crystal structures in stainless steels	28
<b>Figure 2-3:</b> Family Relationships in Stainless Steels	29
<b>Figure 2-4:</b> Possible Precipitates in Duplex Stainless Steels	33
<b>Figure 2-5:</b> Stress-strain curves for some stainless steels	34
<b>Figure 2-6:</b> Impact toughness for different types of stainless steels	35
<b>Figure 2-7:</b> N, Cr and Mo effects on the Yield strength and microhardness of the austenitic and the ferritic phases	38
<b>Figure 2-8:</b> Types of slip bands in deformed duplex stainless steel	39
<b>Figure 2-9:</b> a) Local strain map obtained by using the EBSD (thick black lines are high angle grain boundaries, thin black lines are low angle boundaries and red lines are phase boundaries. B) Phase map of the same observed area ( $\alpha$ -Blue/ $\gamma$ -Red)	40
<b>Figure 2-10:</b> AFM micrographs: (a) before the tensile test; (b, c and d) after an elongation of 0.5 mm, 0.6mm and 0.9 mm, respectively	40
<b>Figure 2-11:</b> AFM micrographs showing a slip transmission through phase boundary in a DSS. (a) Austenite/ferrite boundary at lower magnification. (b) Higher magnification for the black square	41
<b>Figure 2-12:</b> Basic corrosion cell showing reactions and transfer of electrons	44
<b>Figure 2-13:</b> Effect of chromium content on passivity (Corrosion Rate in air)	45
<b>Figure 2-14:</b> Schematic active-passive polarisation behaviour.	46
<b>Figure 2-15:</b> Pitting corrosion form	48
<b>Figure 2-16:</b> ASTM-G46 standard visual chart for pitting corrosion shapes .	48
<b>Figure 2-17:</b> Temperature dependence of pitting potential of Zeron 100, standard duplex 2205 and Ferralium alloy 225 duplex stainless steels on temperature	49
<b>Figure 2-18:</b> Polarisation curve of Zeron100 at 130°C in 15, 100 and 1000 ppm chloride solution showing the critical pitting current density	50
<b>Figure 2-19:</b> CPT for various Stainless Steels in the Solution Annealed condition as measured by the ASTM G 48 procedures (10% ferric chloride)	50
<b>Figure 2-20:</b> Stress corrosion cracking conditions	54

<b>Figure 2-21:</b> SCC fracture surface of 25%Cr duplex stainless steel (50% ferrite) in NaCl-H <sub>2</sub> S solution at 80°C, showing flat, cleavage-like cracking of ferrite and mainly ductile fracture of austenite .....	55
<b>Figure 2-22:</b> A schematic diagram show the intergranular and transgranular cracking methodology.....	56
<b>Figure 2-23:</b> SCC resistance in various steels .....	57
<b>Figure 2-24:</b> Schematic diagram illustrating the effect of applied potential on the environmentally assisted cracking for 2205 duplex stainless steel .....	58
<b>Figure 2-25:</b> The relative influences of electrochemical and mechanical factors in the corrosion and SCC damage of a susceptible material .....	59
<b>Figure 2-26:</b> A schematic diagram describing the stress distribution at a point near to the crack tip for a crack of length $2a$ .....	60
<b>Figure 2-27:</b> Schematic relationship between $K_I$ and $da/dt$ .....	62
<b>Figure 2-28:</b> Schematic representation of crack velocity with time .....	62
<b>Figure 2-29:</b> Schematic curve showing the threshold between propagating and non-propagating cracks .....	64
<b>Figure 2-30:</b> Schematic of crack initiation and growth by slip-dissolution.....	65
<b>Figure 2-31:</b> Schematic drawing of crack growth by film-induced cleavage .....	66
<b>Figure 2-32:</b> Schematic description of hydrogen assisted stress corrosion cracking in adsorption mechanism.....	67
<b>Figure 2-33:</b> Specimens used for stress corrosion cracking tests .....	69
<b>Figure 2-34:</b> Subsets before and after deformation in x-y plane .....	71
<b>Figure 2-35:</b> Evaluation of recorded patterns image subset using auto correlation.....	71
<b>Figure 2-36:</b> DIC Basics: (a) two images obtained at different strains are divided into subsets. (b) Corresponding pairs of subsets are compared using correlation or FFT algorithms. The displacement vector joins the centre of the subset and the point of highest correlation .....	73
<b>Figure 2-37:</b> Schematic Figure of field deformation showing subsets with rotation and deformation due to straining .....	74
<b>Figure 2-38:</b> Typical 10x10 pixel subset shows intensity pattern values .....	75
<b>Figure 2-39:</b> Three interpolation levels for the same raw image to represent the intensity values of the 10x10 pixel subset shown in Figure 2-37 .....	75

<b>Figure 2-40:</b> Images of the same observed surface before and after painting .....	77
<b>Figure 2-41:</b> Patterns obtained using the focused ion beam technique of a smooth surface (a) Random patterns bitmap, (b) Scanning Electron Microscope photograph of the surface and (c) Atomic Force Microscopy line profiles of the surface before and after patterns creation .....	78
<b>Figure 2-42:</b> Left: Digital Image Correlation strain maps, obtained by differentiation of the displacements maps measured between selected images in three time intervals ( $t_3 > t_2 > t_1$ ). Right: Displacements profiles measured along the horizontal dashed line shown on the strain maps .....	80
<b>Figure 2-43:</b> Crack length and Crack Opening Displacement versus time obtained from the Digital Image Correlation Results .....	81
<b>Figure 2-44:</b> DIC analysis: (a) Optical images at 1500 hours, 1668 hours, 1836 hours, 2004 hours, 2388 hours, 2676 hours, 3036 hours and 3232 hours (left to right). (b) Strain maps relative to first image at 1668 hours, 1836 hours, 2004 hours, 2388 hours, 2676 hours, 3036 hours and 3232 hours (left to right).....	82
<b>Figure 2-45:</b> Evaluation of crack length as measured by DIC analysis, optical microscope and calculated nominal stress on sample A shown in Figure 2-43. Uncertainty in DIC crack length is 30 $\mu\text{m}$ .....	83
<b>Figure 2-46:</b> Surface finishes prepared a) Scratching by abrasive paper, b) Thermal etching and c) Chemical/electroetching .....	84
<b>Figure 2-47:</b> Crack growth rate ( $dc/dt$ ) and crack driving force as functions of time for two intergranular steel corrosion cracks initiated in sensitised 304 stainless steel .....	85
<b>Figure 2-48:</b> Principle of Digital Volumetric Correlation – evaluation of sub-volume template displacement vector between reference image data and deformed image data.....	86
<b>Figure 3-1:</b> Orientations of specimens taken from the plate, specimen orientation (first letter) to the loading direction identification (second letter). L and T are longitudinal and transverse principal direction of metal working (rolling) respectively .....	87
<b>Figure 3-2:</b> Potentiostats from ACM Instruments and EG&G. ....	88
<b>Figure 3-3:</b> General view of the experiment setup.....	89
<b>Figure 3-4:</b> A schematic diagram shows the main setup of the cell. ....	89
<b>Figure 3-5:</b> Schematic image of the electro-polishing cell. ....	91
<b>Figure 3-6:</b> U-Bend Sample preparation .....	91

<b>Figure 3-7:</b> Typical U-Bend Specimen Dimensions .....	92
<b>Figure 3-8:</b> Mechanical tensile testing machine INSTRON 5569. ....	93
<b>Figure: 3-9:</b> Setup of the rig under the DIC optical microscope. ....	94
<b>Figure 3-10:</b> The constant load cell and the dimensions of the sample. ....	96
<b>Figure 3-11:</b> A schematic Figure shows the position of the strain gauge on the flat tensile sample. ....	97
<b>Figure 3-12:</b> NI 9237 C Series and NI CompactDAQ 8-Slot Data Logger. ....	97
<b>Figure 3-13:</b> Image shows the salty droplets on the observed area. ....	98
<b>Figure 3-14:</b> Image shows the main setup of the experiment. ....	98
<b>Figure 3-15:</b> Optical Microscope (OM), Olympus-BH2. ....	99
<b>Figure 3-16:</b> Schematic diagram showing the main EBSD mechanism .....	100
<b>Figure 3-17:</b> Mini Flat Tensile Sample with dimensions included. ....	101
<b>Figure 3-18:</b> Micro-tensile-testing device tester with control units, and optical microscopy, interfaced to the ZEISS MRm AxioCam digital camera. ....	102
<b>Figure 3-19:</b> Steps of the tests applied on the mini flat sample. ....	102
<b>Figure 3-20:</b> Schematic diagram showing the main X-ray Tomography mechanisms [160, 167]. ....	103
<b>Figure 3-21:</b> XRADIA MicroXCT Scanner: left is the X-ray source; sample on rotation stage in the middle; right is the detector with different lenses for different optical magnifications .....	104
<b>Figure 4-1:</b> Optical micrographs of (a) the 3-mm plate SDSS as-received and (b) forged SDSS sheet as received microstructures (ferrite is dark and austenite is light). ....	105
<b>Figure 4-2:</b> Cyclic polarisation of sample in 0.5%, 1.5% and 3.5% NaCl solution at room temperature. ....	106
<b>Figure 4-3:</b> Half cycle polarisation curves for SDSS samples at Room Temperature, 55°, 70° and 80°C in 5M NaCl at pH=5.8. ....	107
<b>Figure 4-4:</b> Change in the solution colour after testing samples in 30%NaCl at 80°C, pH=5.8, half cycle polarisation test shown in Figure 4-3. ....	107
<b>Figure 4-5:</b> Optical micrographs for a) the pits with lacy appearance and b) for cross section of sample all created in the sample after polarisation testing in 5M NaCl at 70°C. ....	108

<b>Figure 4-6:</b> Optical micrographs for a) the pits on the surface and b) for cross section of sample all created in the sample after polarisation testing in 5M NaCl at 80°C. ....	109
<b>Figure 4-7:</b> SEM micrographs for sample after polarisation testing in 5M NaCl at 80°C, a) At 30x and b) higher magnification shows the formations of metallic caps cover the pits. ....	110
<b>Figure 4-8:</b> Optical micrograph for the top surface of the U-bend sample after testing under droplets of 0.52M MgCl <sub>2</sub> at 80°C and 42% RH. The white arrows on Figure indicate to the tensile direction. ....	111
<b>Figure 4-9:</b> Optical micrograph for the top surface of the U-bend sample after the test shows the initiation of the stress corrosion cracking normal to the loading direction.....	111
<b>Figure 4-10:</b> Macrohardness test of the U-Bend sample.....	112
<b>Figure 4-11:</b> Stress/Strain behaviours of the rolled and solution annealed sample tested at 80° C, dashed line indicated to the selected strain (3%) and the considered stresses (1.05σ <sub>y</sub> ) for both samples. ....	113
<b>Figure 4-12:</b> Strain gauge data for the first 11 hours at 80°C. ....	114
<b>Figure 4-13:</b> Electroetched surface under three magnifications (5X, 10X and 20X) respectively. ....	115
<b>Figure 4-14:</b> Displacement map of the electroetched surface moved in x-axis direction by around 20 pixels under the optical microscope (10X magnifications). ....	116
<b>Figure 4-15:</b> RMS value vs. window sizes for the electroetched surface tested at three levels of magnifications 5X, 10X and 20X.....	117
<b>Figure 4-16:</b> Optical images of a) a wet droplet and b) an evaporated droplet of MgCl <sub>2</sub> at the beginning of the test. ....	118
<b>Figure 4-17:</b> A series of DIC images show changes inside a wet droplet as a function of time during the first 600 hours. ....	119
<b>Figure 4-18:</b> A series of DIC images show the changes inside an evaporated droplet in function of time during the first 600 hours. ....	120
<b>Figure 4-19:</b> DIC image shows the gray scale profile along the yellow line from right to left in the wet droplet after 500 hours. ....	121
<b>Figure 4-20:</b> DIC image shows the gray scale profile along the yellow line from right to left in the evaporated droplet after 500 hours. ....	122

<b>Figure 4-21:</b> Noise development with time inside the wet and evaporated droplets during the test (at 10X-Magnification).....	123
<b>Figure 4-22:</b> The change in the droplets average diameter in function of time.....	123
<b>Figure 4-23:</b> Montage images showing a) the droplet at the beginning of the test, b) after 706 hours and c) after 942 hours d) after 952 hours. ....	125
<b>Figure 4-24:</b> Image of the crack in the wet droplet after 1050 hours.....	126
<b>Figure 4-25:</b> The first observed (a) vectors and (b) displacement maps after the crack initiated after (942 Hours-wet droplet)-right branch. Dashed line show the x-position for SCOD measurements. ....	127
<b>Figure 4-26:</b> Strain maps of the propagated crack after 942 hours showing a) the $E_{yy}$ strain (perpendicular to the crack) and b) $E_{xx}$ strain (parallel to the crack). Dashed rectangles show the actual locations of two sets of images used to obtain the overlapped strain maps. ....	128
<b>Figure 4-27:</b> Sketch of the right crack after 942 hours shows how the SCOD measured by using the DIC vertical line profiles analysis from y-displacements images ( $V_y$ ).....	129
<b>Figure 4-28:</b> SCOD in ( $\mu\text{m}$ ) vs. distance from the edge of the droplet for the right and left cracks after 942 hours. ....	129
<b>Figure 4-29:</b> Strain gauge reading data and average background strain calculated by the DIC displacement analysis vs. time. ....	130
<b>Figure 4-30:</b> A series of DIC images show different stages of the experiment: a) and b) before the crack initiation, c), d) and e) show the crack propagation out of the salt droplet, f) show the crack view after 665 hours after stopping the test.....	131
<b>Figure 4-31:</b> A series micrographs with strain maps superimposed and vertical displacements maps to show crack opening displacements relative to the first image (T-T sample, crack propagation perpendicular to the loading direction). ....	132
<b>Figure 4-32:</b> A series micrographs with strain maps superimposed and vertical displacements maps to show crack opening displacements relative to the first image (T-T sample, crack propagation perpendicular to the loading direction). ....	133
<b>Figure 4-33:</b> Eyy strain profile vs. y-position measured along a line close to the edges of the droplet (indicated by dotted lines in Figures 4-31 and 4-32) with uncertainty $\approx 0.01 \mu\text{m}$ . ....	134

<b>Figure 4-34:</b> Crack length and crack opening displacement with time for the left crack shown in Figure 4-31. ....	134
<b>Figure 4-35:</b> Crack length and crack opening displacement with time for the right crack shown in Figure 4-32. ....	135
<b>Figure 4-36:</b> Strain gauge reading data and average background strain calculated by the DIC vs. time. ....	135
<b>Figure 4-37:</b> Evaluation of crack length as measured by optical measurements and DIC (strain analysis) for left and right cracks shown in Figures 4-31 and 4-32.....	136
<b>Figure 4-38:</b> A series micrographs with strain maps superimposed and vertical displacements maps to show crack opening displacements relative to the first image (L-T sample, crack propagation perpendicular to the loading direction). ....	137
<b>Figure 4-39:</b> Crack length and crack opening displacement with time for the crack shown in Figure 4-38.....	138
<b>Figure 4-40:</b> Strain gauge reading data and average background strain (contains the crack) calculated by the DIC vector displacement analysis vs. time. ....	138
<b>Figure 4-41:</b> Series micrographs with strain maps superimposed relative to the first image, a) after 1116 hours-no cracks out of the droplet , b) after 1263 hours-crack propagated out of the droplet and normal to the loading direction, c) strain map at 1263 hours- shows the strain profile along the crack.....	140
<b>Figure 4-42:</b> Series micrographs with strain and vectors displacement maps superimposed relative to the first image a) after 1116 hours, b) after 1263 hours and c) vectors displacement map after 1263 hours (crack propagation perpendicular to the loading direction). ....	141
<b>Figure 4-43:</b> SCOD along the left crack ( $\mu\text{m}$ ) vs. distance from the crack tip. ....	142
<b>Figure 4-44:</b> SCOD along the right crack ( $\mu\text{m}$ ) vs. distance from the crack tip.....	142
<b>Figure 4-45:</b> Strain gauge reading data and average background strain (contains the crack) calculated by the DIC vector displacement analysis vs. time (uncertainty $\approx 0.00027$ ). ....	143
<b>Figure 4-46:</b> SEM micrograph shows the salt droplets and the crack locations. ....	144
<b>Figure 4-47:</b> Selective dissolution and pitting resulted in initiation of short cracks perpendicular to the load direction under the salt droplets. ....	144
<b>Figure 4-48:</b> SEM micrograph shows interphase corrosion intergranularly ( $\alpha/\gamma$ ). ....	145
<b>Figure 4-49:</b> EBSD analysis for the crack shown in Figure 4-48 ( $\alpha$ -Blue/ $\gamma$ -Red).....	145

<b>Figure 4-50:</b> SEM micrographs show pitting in ferrite phase and short cracks initiated from the pit in ferrite phase under the salt droplets shown in Figure 4-44, the austenite and ferrite were identified by using the EBSD technique.....	146
<b>Figure 4-51:</b> EBSD analysis for the microcracks initiated under the salt droplets shown in Figure 4-50 ( $\alpha$ -Red/ $\gamma$ -Blue).....	147
<b>Figure 4-52:</b> Trace of the short crack shown in the phase map (Figure 4-51) on {110} planes in $\alpha$ -Phase, Euler1=19°, Euler2=4.8°, Euler3=51°, RD[1-30], TD[62-1] and normal [001]......	148
<b>Figure 4-53:</b> Intergranular corrosion, selective dissolution and pitting observed under the salt droplets. ....	148
<b>Figure 4-54:</b> Cracks at the backside of the gauge length, arrows are representing to the tensile direction. ....	149
<b>Figure 4-55:</b> EBSD analysis for the backside cracks shown in Figure 4-52 ( $\alpha$ -Blue/ $\gamma$ -Red). ....	150
<b>Figure 4-56:</b> Trace of the crack shown in Figure 4-55 on {110} planes in $\alpha$ -Phase, Euler1=22.6°, Euler2=9.7°, Euler3=23.5°, RD[6-61], TD[55-1] and normal [016]. ....	150
<b>Figure 4-57:</b> Mechanical fracture of the rolled Sample to compare it with the SCC fracture surface. ....	151
<b>Figure 4-58:</b> The fracture surface shows a typical stress corrosion cracking fracture.....	151
<b>Figure 4-59:</b> SEM micrograph of the fracture surface shows a microcrack along the facets in ferrite ( $\alpha$ -Phase indicated by EDX analysis).....	152
<b>Figure 4-60:</b> Austenite and ferrite grains Cr/Ni ratio measured by EDX analysis in as polished sample. ....	152
<b>Figure 4-61:</b> Austenite and ferrite grains Cr/Ni ratio measured by EDX analysis in the fracture surface.....	153
<b>Figure 4-62:</b> Fracture surface observed for specimen shows secondary cracking in $\alpha/\gamma$ ..	153
<b>Figure 4-63:</b> SEM image shows the secondary cracks in the cross section of the fracture surface propagated vertical to the main cracking direction along $\alpha/\gamma$ interphase. ....	154
<b>Figure 4-64:</b> Reconstructed 3-D tomography images for the crack created in the rolled sample, the arrows show the loading direction. ....	155
<b>Figure 4-65:</b> 2D Tomography sections through the data collected from the crack in the rolled sample. ....	156

<b>Figure 4-66:</b> SEM micrograph shows the localized corrosion under the salt droplet and the crack propagated out of the droplet and normal to the loading direction. ....	157
<b>Figure 4-67:</b> SEM micrograph shows the slip bands corrosion in the austenite phase under the salt droplets shown in Figure 4-66, the austenite and ferrite grains were identified by using the EDX technique. ....	158
<b>Figure 4-68:</b> EBSD analysis of the crack tip shown in Figure 4-66 ( $\alpha$ -Blue/ $\gamma$ -Red).....	158
<b>Figure 4-69:</b> SEM Micrograph shows the crack tip position and the un-cracked portion in the same crack shown in Figure 4-68.....	159
<b>Figure 4-70:</b> SEM micrograph shows the localized corrosion under the salt droplet and the crack propagated out of the droplet and normal to the loading direction. ....	160
<b>Figure 4-71:</b> SEM micrographs show a) the localized corrosion under the salt droplet and the crack propagated out of the droplet, b) the grain deformation at the crack tip and c) the deflection of the crack at the austenite grain, the grains were identified by using the EBSD analysis.....	160
<b>Figure 4-72:</b> Forms of the localized corrosion and cracks created under the salt droplet.	161
<b>Figure 4-73:</b> EBSD analysis for the crack in Figure 4-71 shows the band contrast and phase maps ( $\alpha$ -Blue/ $\gamma$ -Red).....	162
<b>Figure 4-74:</b> Traces of the cracks shown in Figure 4-73 on $\{110\}$ and $\{112\}$ planes in $\alpha$ -Phase, Euler1=344°, Euler2=35.4°, Euler3=22.2°, X[6-1-1], Y[03-2] and normal [123]..	162
<b>Figure 4-75:</b> Localized corrosion morphology found under the salt droplet after 1500 hours in the solution annealed sample with rolling direction longitudinal to the tensile...	164
<b>Figure 4-76:</b> SEM micrograph shows the wavy slip bands corrosion in the ferrite phase under the salt droplet after 1500 hours, the austenite and ferrite grains were identified by using the EDX technique. ....	165
<b>Figure 4-77:</b> Localized corrosion morphology found under the salt droplet after 1500 hours. Localized corrosion occurred at the interphase boundaries $\alpha/\gamma$ and in the ferrite phase.....	166
<b>Figure 4-78:</b> A close-up view of the localized corrosion behaviour in the ferrite phase reflected the fine-scale crystallographic (faceted) corrosion. ....	167
<b>Figure 4-79:</b> Localized corrosion morphology found under the salt droplet after 1500 hours. Localized corrosion occurred mostly at the interphase boundaries $\alpha/\gamma$ . Ferrite is dark gray and austenite is light gray.....	168

- Figure 4-80:** Nominal stress vs. strain curve of the Mini-Flat tensile test in the Microtester. The markers indicate to the points at which images were acquired.....169
- Figure 4-81:** Optical micrographs captured at four different strain levels of a) No Stress, b) at 511 MPa -1% Strain, c) at 574 MPa – 2% Strain and d) at 590 MPa -3% Strain (ferrite is dark and austenite is light). .....170
- Figure 4-82:** Strain map from last image taken at 3% bulk strain (window size is 64x64 and smoothing = 2) and external squares show examples of strain localization regions...171
- Figure 4-83:** Maximum strain maps from images taken at 1%, 2% and 3% (bulk strain) respectively without smoothing. The scale bar ranges from 0.0% to 5.0 % maximum strain (window size is 64x64, 1 pixel is = 0.46  $\mu\text{m}$ ). .....171
- Figure 4-84:** EBSD phase map ( $\alpha$ -Blue/ $\gamma$ -Red), local misorientation map and misorientation's frequency of both phases of the same deformed area (3% strain), black pixels are unindexed points. ....172
- Figure 4-85:** Potentiodynamic polarisation curve of the strained mini flat sample in 5M NaCl at 70°C, potential was measured versus a saturated calomel electrode (SCE) with a scan rate of 10 mV/min. ....173
- Figure 4-86:** SEM micrographs of deformed area showing the slip bands formation, ferrite is dark and austenite is light. ....174
- Figure 4-87:** Optical images of the strained area showing the selected (a) austenite grains and (b) ferrite grains, ( $\alpha$ -light/ $\gamma$ -dark). ....175
- Figure 4-88:** Grain number vs. the average maximum strain (from DIC analysis) for the grains shown in Figure 4-87. ....175
- Figure 4-89:** Strain map of the observed area shows the maximum strain level, 1 pixel is = 0.46  $\mu\text{m}$ . ....176
- Figure 4-90:** SEM Micrographs of area (B) shown in Figure 4-89 as examples of areas with strain > 3% after potentiodynamic polarisation showing attack of phase boundaries within corroded area and micropitting corrosion. ....177
- Figure 4-91:** SEM Micrograph of area (D) shown in Figure 4-89 as an example of areas with strain < 3% after potentiodynamic polarisation showing attack of phase boundaries within corroded area and micropitting corrosion. ....178
- Figure 4-92:** SEM micrographs show the localized corrosion attack on the interphase boundaries  $\alpha/\gamma$  and the pitting occurred in the austenite grains. ....179

<b>Figure 4-93:</b> SEM micrographs show the pitting corrosion attack occurred preferentially on the slip bands within the austenite grains ( $\gamma$ ). .....	179
<b>Figure 4-94:</b> SEM micrographs show close-up views of pits reflected the fine-scale crystallographic (faceted) pit in ferrite phase.....	180
<b>Figure 5-1:</b> Temperature versus Relative Humidity of $MgCl_2$ and $NaCl$ to show the deliquescence regions for those salts .....	184
<b>Figure 5-2:</b> A schematic Figure shows the deposited $MgCl_2$ salt which transferred to saturated $Cl$ solution at R.H. (30-35%) resulted in atmospherically induced SCC. ....	184
<b>Figure 5-3:</b> SEM micrograph for the arrested crack with the deformation bands at the crack tip and the traces of the crack on $\{110\}$ for $\alpha$ -Phase and on $\{111\}$ for $\gamma$ -Phase. ....	189
<b>Figure 5-4:</b> Relationship between the specimen coordinate system RD, TD, ND and the crystal coordinate systems $[100]$ , $[010]$ , $[001]$ .....	190
<b>Figure 5-5:</b> a) stereographic projection $\{111\}$ pole Figure for grain G1 with the plane system of the highest Schmid factor trace, b) determination of cracked plane, twist and tilt angles components; $\{111\}$ pole Figure for grains G1 and G2. ....	193
<b>Figure 5-6:</b> Schematic describing the crack plane misorientation across a grain boundary in terms of the tilt angle (a), and the twist angle (b). ....	194
<b>Figure 5-7:</b> Schematic of tunnel model showing the formation of corrosion tunnels at slip steps and ductile deformation and fracture of the remaining ligaments .....	196
<b>Figure 5-8:</b> Displacement across the crack derived from the DIC analysis presented in Figures 4-31 (left) and 4-32 (right), the crack tip plastic zone is also shown (RMS = $\pm 0.3 \mu m$ ). ....	199
<b>Figure 5-9:</b> Comparison of cracks measurements done by DIC and optical means showing the potential of the DIC to give better inspection. ....	201

## List of Tables

<b>Table 2-1:</b> Summary of the main advantages of various stainless steels . . . . .	26
<b>Table 2-2:</b> Compositions of various duplex stainless steels . . . . .	31
<b>Table 2-3:</b> Typical mechanical properties of duplex stainless steels . . . . .	34
<b>Table 2-4:</b> The most important elements and their effects on the stainless steels . . . . .	37
<b>Table 2-5:</b> Pitting Resistant Equivalent number (PRE#) for various types of stainless steel .....	51
<b>Table 2-6:</b> Stress Corrosion Cracking test standards- Smooth Specimens . . . . .	68
<b>Table 2-7:</b> Stress Corrosion Cracking test standards- Precracked specimens.....	68
<b>Table 2-8:</b> DIC's calculated strain for all tested surface finishes. . . . .	83
<b>Table 3-1:</b> Chemical compositions of materials used (wt %), Fe. BAL., Supplier's certificates. ....	87
<b>Table 4-1:</b> Strain and hardness values achieved from three levels of reduction. ....	112
<b>Table 4-2:</b> Mechanical properties of samples tested at 80°C. ....	113
<b>Table 5-1:</b> Orientation data for the grains G1 and G2 from the EBSD analysis.....	191
<b>Table 5-2:</b> The Schmid factors (absolute values) of slip systems in G1 and G2 (highlighted rows show highest Schmid factor). The angles $\emptyset$ and $\lambda$ are relative to the load direction. .....	192

## **Abstract**

The new generation of highly alloyed super duplex stainless steels such as Zeron 100 are preferable materials for industrial applications demanding high strength, toughness and superior corrosion resistance, especially against stress corrosion cracking (SCC). SCC is an environmentally assisted failure mechanism that occurs due to exposure to an aggressive environment while under a tensile stress. The mechanism by which SCC of duplex stainless steel is expected to suffer depends on the combination of electrochemical and the mechanical interaction between austenite and ferrite in the duplex alloys. The main aims of this work are to study the suitability of digital image correlation (DIC) to monitor the initiation and propagation of SCC and to understand how the microstructure of duplex stainless steel influences the kinetics of crack initiation and growth. The combined analysis of DIC, SEM and EBSD was used to study the relative crack propagation and the effect of interphase boundaries on crack growth as well.

Cracking was initiated beneath saturated  $\text{MgCl}_2$  droplets in an atmospheric environment at  $80^\circ\text{C}$  and relative humidity of 30-33%. As-received and 10% cold rolled samples (with two orientations transverse and longitudinal to the loading direction) were subjected to an applied strain of 0.03 under displacement controlled tests. Regular optical observations were recorded of the droplets and their surrounding area. DIC analyses used the differentiation of the displacement fields to obtain the apparent surface strains used to detect crack initiation and propagation, and to measure crack opening displacements.

It was found that DIC efficiently observed the strain developments and the displacements in observed surfaces outside of the droplets but it could not identify or quantify the initiation of the cracks inside the droplets because of the mobility of the salt film and the high amount of the corrosion products formed which obscure the vision under the droplets. In addition, results showed that early stage microcracks were initiated in  $\alpha$  phase and  $\alpha/\gamma$  interfaces and propagated preferentially in the ferrite phase. Also, SCC initiation and propagation was accelerated by cold rolling and the grains orientations were of major effects on the retardation of crack propagation which was more severe in the transverse rolling direction. Also, there was no relation established between the strain level and the density of pitting in either phase.

## **Declaration**

No portion of the work referred to in the thesis has been submitted in support of an application for another degree or qualification of this or any other university or other institute of learning.

## **Copyright Statement**

- (i) The author of this thesis (including any appendices and/or schedules to this thesis) owns certain copyright or related rights in it (the “Copyright”) and he has given The University of Manchester certain rights to use such Copyright, including for administrative purposes.
- (ii) Copies of thesis, either in full or in extracts and whether in hard or electronic copy, may be made only in accordance with the Copyright, Designs and Patents Act 1988 (as amended) and regulations issued under it or, where appropriate, in accordance with licensing agreements which the University has from time to time. This page must form part of any such copies made.
- (iii) The ownership of certain Copyright, patents, designs, trade marks and other intellectual property (the “Intellectual Property”) and any reproductions of copyright works in the thesis, for example graphs and tables (“Reproductions”), which may be described in this thesis, may not be owned by the author and may be owned by third parties. Such Intellectual Property and Reproductions cannot and must not be made available for use without the prior written permission of the owner(s) of the relevant Intellectual Property and/or Reproductions.
- (iv) Further information on the conditions under which disclosure, publication and commercialisation of this thesis, the Copyright and any Intellectual Property and/or Reproductions described in it may take place is available in the University IP Policy in any relevant Thesis restriction declarations deposited in the University Library, The University Library’s regulations and in The University’s policy on presentation of Theses.

## **Acknowledgements**

First and foremost, I would like to express my sincere gratitude and respect to **Prof. James Marrow**, my academic supervisor, for having been so supportive and for his never-ending enthusiasm and encouragement throughout the period of this work. I am extremely appreciative for his guidance from a technical, professional and personal front. Also, my deep appreciation is due to **Dr. Nicholas Stevens** for his helpful guidance and his invaluable assistance to complete this research under his supervision.

I gratefully acknowledge **Dr. Dirk Engelberg** for his continuous advice, supervision, and crucial contribution in all parts of this thesis. My acknowledgements also go to **Dr. Jonathan Duff** and to **Dr. Catherine Verdu** (France) for their support and cooperation in the Digital Image Correlation. Also, it is my pleasure to acknowledge **Prof. Bob Cottis**, **Prof. Stuart Lyon** and **Dr. Tony Cook** for their great advice in the corrosion parts. Many thanks to all people who taught and helped me through all stages of this project, **Michael Faulkner**, **Ken Gyves** and especially people in workshop **Mark Harris**, **Stuart Morse** and **Christopher Hyde** who have always been helpful in all sample preparations and tensile rig design.

I would like to express my gratitude to my employer, Saudi Basic Industries Corporation (SABIC) for providing me this opportunity to carry out this work. Especially thanks to SABIC Technology Centre General Manager **Dr. Waleed Al-Shalfan** and my section manager **Mr. Mahmoud Al-Manea**, for their advice, encouragement and support.

I am grateful to **Dr. Roger Francis** at Weir Materials for providing super duplex stainless steel samples. Also, I would like to thank all my colleagues in the School of Material Science and the others in the corrosion and protection centre for their help and friendship.

Lastly, I would like to thank my parents, wife (Um Saad), my daughters (Renad and Wedad), my sons (Saad and Sultan) and **all my family** members. I regret spending so much time away from them and many thanks for their unbroken support in my life, which I could not express in words and can not repay them by any means.

## 1 INTRODUCTION

Stainless steels were developed during the first decades of the twentieth century in the United Kingdom and Germany. Stainless steel is the term for iron based alloys that contain at least 10.5% of chromium. The earliest grades of stainless steels were martensitic and ferritic (Fe-Cr) steels. Later austenitic stainless steel (Fe-Cr-Ni) became the largest group and was used extensively due to its ease of production and fabrication. Despite it was sensitive to grain boundary carbide precipitation during heat treatment and welding, and also to inter-granular corrosion attack. Addition of Ni to ferritic stainless steels changes the structure to a duplex microstructure which, as its name implies, contains two-phases in significant quantities (both ferrite and austenite). It has typical contents of 18 - 28% Cr and 4 - 7% Ni, but both the phases should be in equal proportion of (50% - 50%) to exhibit the best performance. The first two-phase microstructures (duplex stainless steels) appeared in 1927 when Bain and Griffith published data on ferritic-austenitic structures [1].

Shortage of nickel during the Korean War (1950-1951) accelerated research into low nickel-content duplex alloys which has better resistance to chloride stress corrosion cracking than a fully austenitic microstructure [1]. In the late 1960s and early 1970s [2], there were two main reasons for the development of duplex alloys. First, there was a nickel shortage that pushed up the price of austenitic steels. This was concurrent with increased activity in the offshore oil industry, which required large quantities of stainless steel that could be used in aggressive environments. Second, steel production procedures using enhanced vacuum and argon oxygen decarburization (VOD and AOD) techniques made it possible to produce much cleaner steels with a very low carbon level and well-controlled nitrogen content. In the mid-1970s the German steel producer Krupp developed the first commercial grade in this way, mainly known today as 2205. This achievement encouraged other steel producers to continue to research and produce improved duplex grades, both lower alloyed duplex grades and higher alloyed super-duplex grades [3].

Duplex steels have much in common with austenitic and ferritic stainless steels, but they have several unique advantages. They have better stress corrosion crack (SCC) resistance than most austenitic grades, are tougher than most ferritic grades and have a higher strength than most grades of either type. They also have the advantage of lower nickel content than comparable austenitic alloys while providing similar corrosion resistance in

many environments. Higher strength stainless steels with lower nickel content makes duplex steels an attractive alternative to austenitic grades, especially when the cost of nickel is high [1].

Life assessment of structures, equipment, machinery, etc., in all industrial and commercial fields is an essential element for the continuous improvement of a safer environment. An important and dangerous problem that causes service failure in engineering materials is environmentally induced crack propagation. A substantial part of the lifetime of a component which finally fails due to stress corrosion cracking, will be while the crack is short (i.e. of the order of a few grains in size). Under these conditions, its growth may be very sensitive to the local microstructure. There is a lack of information on the degree of sensitivity of crack growth to local conditions during this stage. Such data may be obtained by in-situ observation of short crack growth. This PhD project used Digital Image Correlation (DIC) for the observation of short stress corrosion cracks because of its capability to measure the surface displacements caused by the strain field around a crack. This two dimensional technique could be utilized with other techniques (e.g. SEM and EBSD) to provide better vision and understanding of stress corrosion cracking behaviour in duplex stainless steel. Its main objective is to test the ability of digital image correlation to observe the initiation and propagation of short stress corrosion cracking and to provide more knowledge about stress corrosion cracking behavior of super duplex stainless steel (Zeron 100) in chloride environment.

This thesis is divided into several chapters. It starts by presenting a survey of the literature in chapter two which is essential for the understanding of the ideas being investigated in this study. It begins by giving an introduction of the stainless steels classes, microstructure and mechanical and physical properties with more emphasis on the DSS grades. The effects of alloying elements, deformation and strain partitioning in duplex were also briefly outlined as well as some major applications of DSS and super DSS in different industrial fields. This part also describes the concept of corrosion in stainless steels (with a focus on duplex), then pitting corrosion and SCC failure have been briefly presented, together with a summary of the most widely accepted mechanisms for crack initiation and propagation in chloride environments. The effects of environment and duplex microstructure on SCC phenomenon as well as fracture mechanics analysis were also described. Furthermore, the

basics of digital image correlation (DIC) and its related techniques and applications are described. These include the detection of crack initiation, crack propagation and measuring the crack development by using the strain maps. Also, the digital volume correlation (DVC) was introduced briefly at the end of this section.

The third chapter give details about the materials examined (Zeron 100) during this study and the experimental techniques used to investigate the microstructures and its corrosion behavior in function of percentage of chloride contents and environments. It also explains the techniques used for data analysis with more attention to the DIC technique.

The fourth chapter illustrates the observations made and key findings achieved from the presented experiments through this study. Atmospheric-induced chloride stress corrosion cracks have been initiated and grown in the tested samples loaded to  $1.05\sigma_y$  beneath magnesium chloride droplets at a temperature of  $80^\circ\text{C}$  and relative humidity 30-33% with the assistance of localized corrosion as pitting and selective dissolution preferentially in the ferrite phase. It shows the details of preparation and investigations for DIC as well as the potential of this technique to monitor the SCC occurrence. In addition, SEM and EBSD were tools used to characterise cracks and pits morphologies in all samples. The in-situ tensile testing was also performed and shows no correlation between the locations of strain gradients during deformation and the pitting density. The crystallographic morphology of the pitting in the ferrite phase could describe the effects of crystallographic orientations on the pitting experience in ferrite phase.

The fifth chapter is a discussion of all the implications of those experiments and results presented in this work related to the recent studies and published literature. This chapter discusses the behavior of stress corrosion cracking established in the tested environment of this study and the importance nature of the DIC technique when compared to traditional crack opening displacements and strain gauge techniques.

Finally, conclusions generated from this study have been summarised in the last chapter.

## **2 LITERATURE REVIEW**

This literature review begins with a brief introduction to stainless steels, particularly duplex grades (Section 2.1). Next, Section 2.2 outlines the corrosion of stainless steel with special attention to duplex stainless steels (DSSs). Finally, Section 2.3 summarises the basics of DIC and its applications to the observation of SCC initiation and propagation.

### **2.1 Stainless Steels**

Stainless steel is a category of steel, especially used for its corrosion resistance due to the material's chromium content which, when exposed to the atmosphere, forms a thin surface-layer of chromium oxide that insulates the metal surface from the external environment [4]. Many kinds of stainless steels exist, classified according to the percentage of chromium, nickel and molybdenum they contain [5-7].

Stainless steels are more expensive than typical steels but in many cases they offer the most cost-efficient long-solution in the many applications where good corrosion resistance is required. Many kinds of stainless steels with different properties have been developed for a wide variety of applications. The main characteristic of stainless steels is corrosion resistance, and their mechanical properties are still being documented. They are classified as Ferritic, Austenitic, Duplex (ferrite/austenite), Martensitic and Precipitation Hardening. Each has its special characteristics as summarized in Table 2-1 [5].

Type	Examples	Advantages	Disadvantages
<b>Ferritic</b>	410S, 430, 446	Low cost, moderate corrosion resistance & good formability	Limited corrosion resistance, formability & elevated temperature strength compared to austenitic
<b>Austenitic</b>	304, 316	Widely available, good general corrosion resistance, good toughness. Excellent formability & weldability	Work hardening can limit formability & machinability. Limited resistance to stress corrosion cracking
<b>Duplex</b>	1.4462	Good stress corrosion cracking resistance, good mechanical strength in annealed condition	Application temperature range more restricted than austenitic. More expensive, and less widely available than austenitic.
<b>Martensitic</b>	420, 431	Low cost, hardenable by heat treatment with high hardness	Corrosion resistance compared to austenitic & formability compared to ferritics limited. Weldability is limited.
<b>Precipitation Hardening</b>	17/4PH	Hardenable by heat treatment, but with better toughness and corrosion resistance than martensitic	Limited availability, corrosion resistance, formability & weldability restricted compared to austenitic

**Table 2-1: Summary of the main advantages of various stainless steels [5].**

The Schaeffler diagram, often used in welding, is a convenient way of representing how the addition of various elements affects the basic structure of chromium–nickel stainless steels, see Figure 2-1. The compositional limits at room temperature of austenite, ferrite and martensite are plotted in terms of their nickel and chromium equivalents. The diagram shows the regions where the three phases for iron–chromium–nickel alloys exist. However, the diagram has a much wider application when the equivalents of chromium and of nickel are used for the alloying of other elements [8-10].

The chromium equivalent can be determined using the most common ferrite-forming elements:

$$\begin{aligned} \text{Cr equivalent} = & (\text{Cr}) + 2(\text{Si}) + 1.5(\text{Mo}) + 5(\text{V}) + 5.5(\text{Al}) + 1.75(\text{Nb}) \\ & + 1.5(\text{Ti}) + 0.75(\text{W}) \end{aligned} \quad (\text{eq. 2-1})$$

The nickel equivalent can be determined by using the austenite-forming elements:

$$\text{Ni equivalent} = (\text{Ni}) + (\text{Co}) + 0.5(\text{Mn}) + 0.3(\text{Cu}) + 25(\text{N}) + 30(\text{C}) \quad (\text{eq. 2-2})$$

All concentrations expressed by weight percentages.

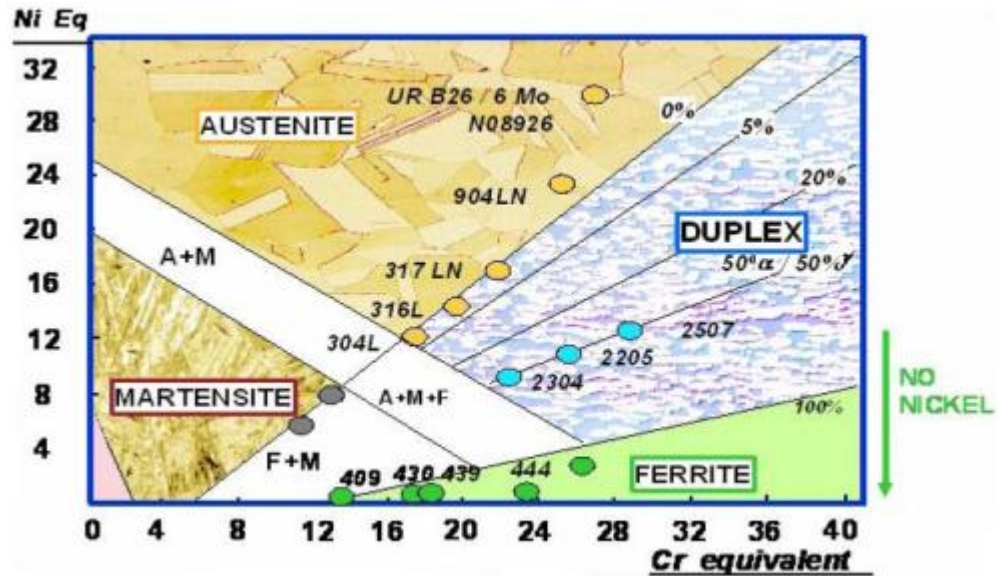
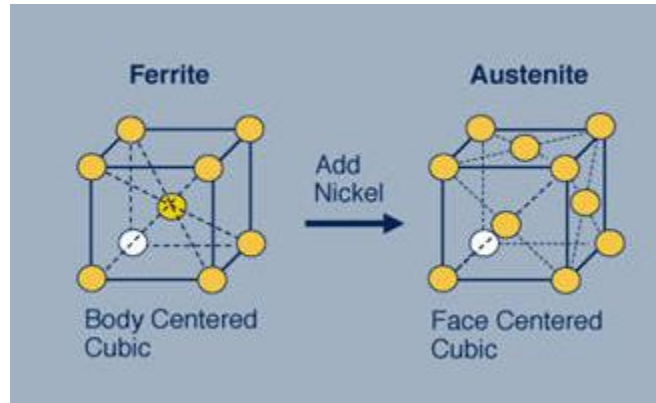


Figure 2-1: Schaeffler diagram, effect of alloying elements on the basic structure of Cr- Ni stainless steels [10].

## 2.1.1 Stainless Steel Classes

### 2.1.1.1 Ferritic Stainless Steel

The Ferritic group of stainless steels (400 series) consist of 10.50 – 28.00% chromium only, no nickel, but often with a small amount of other alloying elements. Chromium is a ferrite stabilizer that retains the alloy in the Body-Centred Cubic (bcc) crystal structure as shown in Figure 2-2. These steels keep their ferritic structure after being rapidly cooled from a high temperature and so they are not hardenable. Ferritic stainless steels are relatively low cost and have limited corrosion resistance compared to the more popular austenitic steels. Also they have limited toughness, formability and weldability in comparison to the austenitics, and are magnetic [5-10].



**Figure 2-2: BCC and FCC Crystal structures in stainless steels [9].**

### 2.1.1.2 Martensitic Stainless Steel

Martensitic stainless steels have a structure similar to the ferritic with a body-centred tetragonal (bct) crystal lattice. With the addition of carbon they can be hardened and strengthened by heat treatment. The Martensitic class of stainless steels has a chromium content of 11- 20% and with a carbon content more than 0.15%. This makes them hardenable which means when they are rapidly cooled off from the fully austenitic high temperature phase, hard and brittle martensite is formed. The hardness can then be reduced and toughness improved to the required level by tempering. Martensitic stainless steels are mainly used in cutlery, aerospace and some general engineering applications such as the main structures of plants [5-11].

### 2.1.1.3 Austenitic Stainless Steels

The austenitic class of stainless steels (300 series) has a Cr content of 18-28%. The addition of nickel to iron-chromium alloys stabilizes the Face-Centred Cubic (fcc) as austenitic phase and improves corrosion resistance in combination with chromium, Figure 2-2. The corrosion resistance comes from a thin chromium-rich, passive surface layer. These grades of stainless steels have good formability, good weldability and excellent mechanical properties over a wide range of temperatures. They are non-magnetic and cold working can increase their hardness and strength. They appear to have significantly greater corrosion resistance than the ferritic grades because the addition of nickel, manganese and nitrogen all contribute to the passivity. The austenitics and particularly the 304 grades [10] are most popular among the stainless steel grades (Figure 2-3). They account for more than 80% of the total stainless steel market.

Austenitic stainless steels are commonly used in several important industrial applications such as food processing and the pharmaceutical industry where contamination is critical and where dissolved corrosion products may catalyse unwanted biochemical reactions. Also, they have been used for architectural trim in industrial and marine environments.

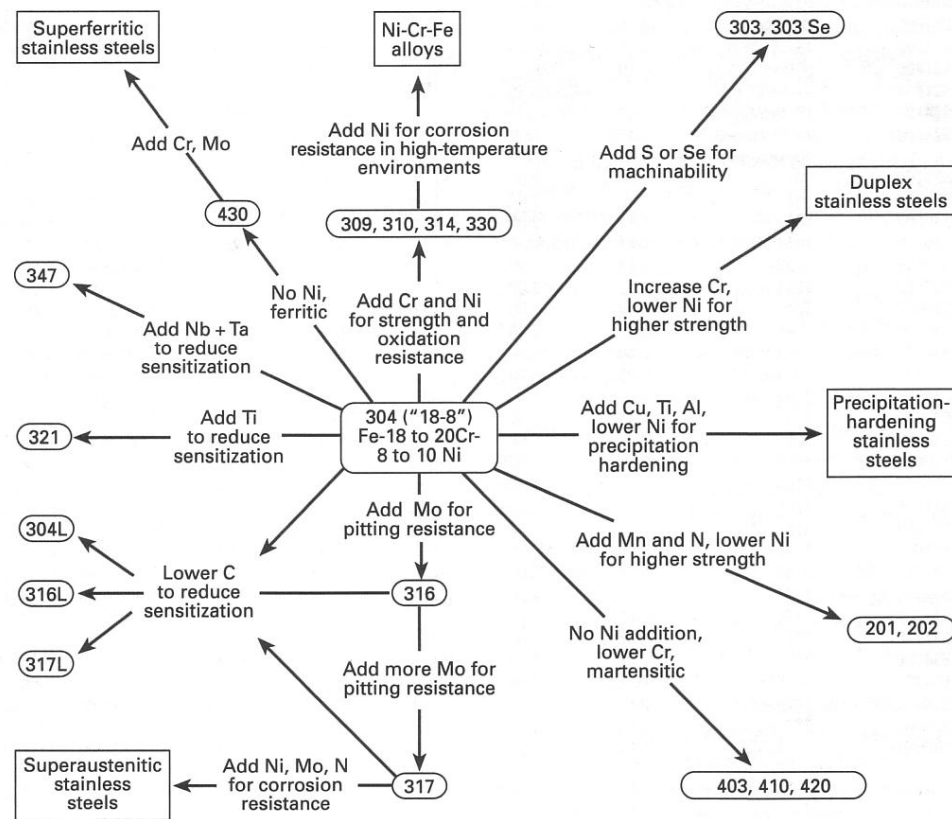


**Figure 2-3: Family Relationships in Stainless Steels [12].**

#### 2.1.1.4 Precipitation Hardening Steels

This type of stainless steel has a higher Cr content, above 16%, Ni above 7% and approximately 1% of Al. The Al is added to form precipitated nickel-aluminium particles. In the annealed condition the structure is austenitic but during cold deformation the austenitic structure is transformed to the harder phase of martensite. These are age hardened through a precipitation reaction which occurs in a temperature range of 450°C to 600°C. Precipitation-hardened (PH) stainless steels have the greatest useful strength and the highest useful operating temperature. Their corrosion resistance is almost comparable to the (304) austenitic. They can be welded more readily than martensitic grades and have been developed and used more widely in the US than in the UK, for example in aerospace applications [5-9, 11].

### **2.1.1.5 Duplex Stainless Steels (Ferritic/Austenitic)**

DSSs are an intermediate grade located between ferritic and austenitic stainless steels, see Figure 2.1. DSSs are more resistant to stress corrosion than austenitic grades but less than the ferritic grades. They have better toughness than ferritic steels but not as good as the austenitic, Figure 2-5. On the other hand, the strength of DSSs is greater than that of austenitics. As a result of recent extensive research and development, a host of new wrought alloys have been developed and adequate technical data generated to validate the treatment of the duplex steels as a separate grade of steel [1-3, 5-12].

DSSs have a structure of austenite and ferrite phases. Chromium and nickel are the principle alloying elements, the chromium is between 18-28% and the nickel is between 4.5-8%. Copper, molybdenum, tungsten, nitrogen, manganese, and silicon may be added to control structural balance and to provide certain corrosion resistance. Molybdenum is typically added to also enhance crevice corrosion and pitting corrosion resistance [1-3, 5-12]. The amount of the two phases is controlled by the composition of the alloy and its heat treatment. The ratio of the phases plays a significant role in defining their properties. The proportion of ferrite- $\alpha$  and austenite- $\gamma$  varies with temperature and at high temperatures the structure becomes more ferritic, less Ni and more Cr equivalents. The relationship between both phases is usually about 50% (by volume) although it can vary between 40% and 60%, and even between 30% and 70%. The duplex grades are not hardenable by heat treatment but are stronger than either the ferritic or austenitic grades in the annealed condition and have approximately double the yield strength of the common austenitic grades. Like the ferritic, they are ferro-magnetic, but have the good formability and weldability of the austenitics (although larger forces are required in forming due to their higher strength), and have lower thermal expansion and higher heat conductivity than austenitic grades. The duplex grades are known to be resistant to chloride SCC, pitting and crevice corrosion.

DSSs are often identified by four digits, the first two digits stand for the weight percent of chromium and the second two digits show the weight percent of nickel; e.g. 2205 means there is 22% Cr and 5% Ni present. However, some types of DSSs have registered trade names such as Uranus 50, Ferralium 255, and Zeron 100. Table 2-2 lists some common duplex alloys and their trade names.

UNS N	Common Name	Cr	Ni	Mo	Cu	Mn	Si	C	N
S32205	2205	22-23	4.5-6.5	3.0-3.50	-	2.0 Max	1.0 Max	0.03 Max	0.1-0.2
S32404	Uranus 50	20.5-22.5	5.5-8.5	2-3	1-2	2.0 Max	1.0 Max	0.04 Max	0.2 Max
S32520	Uranus 50N+	24-26	5.5-8.0	3-4	0.5-2.0	1.5 Max	0.8 Max	0.03 Max	0.2-0.35
S32550	Ferrallium 255	24-27	4.5-6.5	2.9-3.9	1.5-2.5	1.5 Max	1.0 Max	0.04 Max	0.1-0.25
S32750	SAF 2507	24-26	6-8	3-5	-	1.2 Max	0.8 Max	0.03 Max	0.24-0.32
S32760	Zeron 100	24-26	6-8	3-4	0.5-1.0	1.0 Max	1.0 Max	0.03 Max	0.2-0.3

**Table 2-2: Compositions of various duplex stainless steels [1, 5, 7].**

DSSs are generally classified into four categories [1, 5-7, 10]:

*a. Lean Alloy*

The low cost molybdenum free DSSs of the type 23Cr-4Ni-0.1N, provide alternatives to AISI 304 and 316.

*b. Standard 22%Cr*

DSSs of the type 22Cr-5Ni-3Mo-0.17N: these steels, which include SAF Alloy 2205, are the most popular and the least expensive in the duplex family. It has a corrosion resistance that lies between AISI 316 and 6 Mo super-austenitic stainless steels.

*c. High Alloy*

DSSs of the 25 Cr varieties have varying contents of Mo and N and also contain Cu or W as alloy elements. Wrought Ferralium 255 fits into this category.

*d. Super Duplex*

Super DSSs of the type 25 Cr-7Ni-3.5Mo-0.27N has superior corrosion resistance. Zeron 100 fits into this category.

Recently, a new category of DSSs was developed to provide high chloride corrosion resistance combined with improvements in mechanical properties, and have been designated 'hyper-duplex'. These include, for example, UNSS 32707 (also designated Sandvik SAF 2707 HD), which has a chromium content of 27% and almost same Ni contents as super DSSs (6.5%) [13].

### ***2.1.1.5.1 Metallurgy of Duplex Stainless Steels***

In cast duplex, a structure of austenite islands in a ferrite matrix can be observed. For wrought alloys, the morphology of the microstructure has laths of austenite in a ferrite matrix. The presence of ferrite with austenite not only provides better inter-granular corrosion resistance but also improves SCC resistance compared to fully austenitic stainless steels. Also, the presence of austenite in the structure could enhance the mechanical properties and improve the localized corrosion resistance due to the availability of austenite stabilizing elements (N and Ni). Moreover, DSSs become increasingly ferritic as they are heated to high temperatures [1, 8, 14].

However, the presence of ferrite in austenite may cause complex metallurgical reactions that include the formation of a variety of secondary phases, which have unpleasant effects on both corrosion resistance and mechanical properties. The precipitation is usually caused by decomposition of the ferrite phase, which contains large amounts of Cr and Mo, and has low solubility of N and C. Since toughness and corrosion resistance are the criteria of interest, the composition of DSS and their processing, including fabrication practice, must ensure sufficient formation of austenite and prevention of inter-metallic compounds. Figure 2-4 shows the precipitates in DSS and it is evident that most of these precipitates concern ferrite and ferrite promoting elements such as Cr, Mo and W. The Figure also illustrates that almost all these reactions take place over the temperature range of 300° - 1000°C [1, 6].

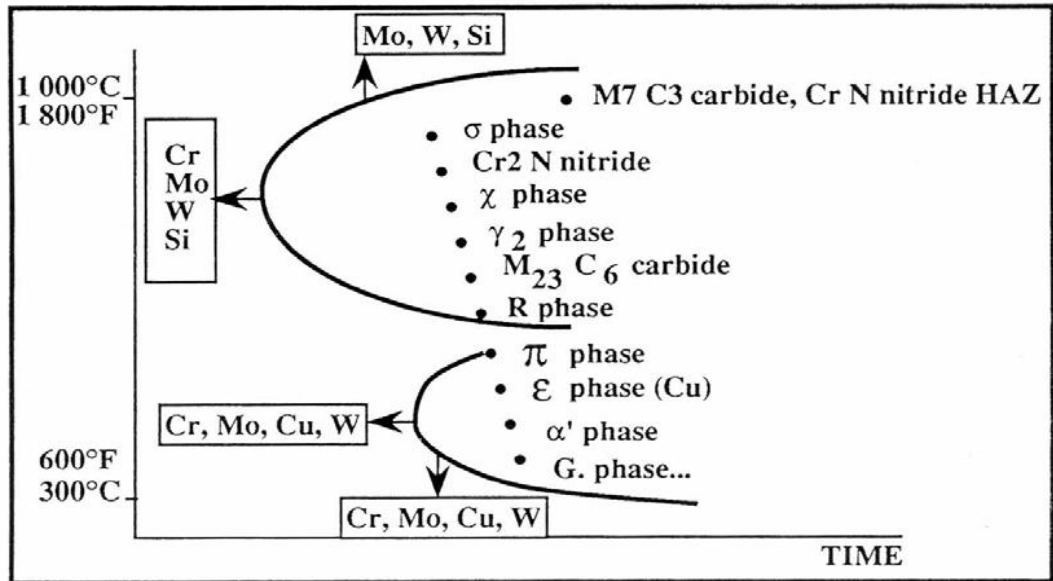


**Figure 2-4: Possible Precipitates in Duplex Stainless Steels [1].**

The high alloy content of duplex grades makes them susceptible to formation of inter-metallic phases after extended service at high temperatures or due to incorrect heat treatment. In addition, these inter-metallic phases could be formed in DSS during isothermal ageing or quenching. The unwanted creation of secondary phases decreases the overall corrosion resistance and makes the alloy more susceptible to localized corrosion attack. Moreover, such precipitations may also affect the mechanical properties, mainly the toughness. Due to this, service temperatures are usually restricted to be less than about 300°C [15-17].

#### **2.1.1.5.2 Mechanical and physical Properties of Duplex Stainless Steels**

DSSs have excellent mechanical properties. In the solution annealed condition, they have a yield strength almost double the yield strength of the austenitic stainless steels at the room temperature. Table 2-3 presents some typical mechanical properties of various DSSs. These superior mechanical properties give the designer and the manufacturer an opportunity to reduce the wall thickness in some application, with good savings in costs. The ductility is about half that of austenitic stainless steel, but still high enough to give good formability, Figure 2-5. DSSs have better toughness than ferritic but less than the austenitic stainless steels as shown in Figure 2-6 [1, 5, 7-9].

Name	Tensile Strength (MPa)	Yield Strength (0.2% offset) (MPa)	Elongation	Hardness (Rockwell B or C)
SAF 2304	600	400	25	B97
2205	760	520	27	----
Uranus 50	600	386	25	C8
Ferralium 255	869	676	30	B100
SAF 2507	800	550	25	C28
Zeron 100	750	550	25	C28

Table 2-3: Typical mechanical properties of duplex stainless steels [12].

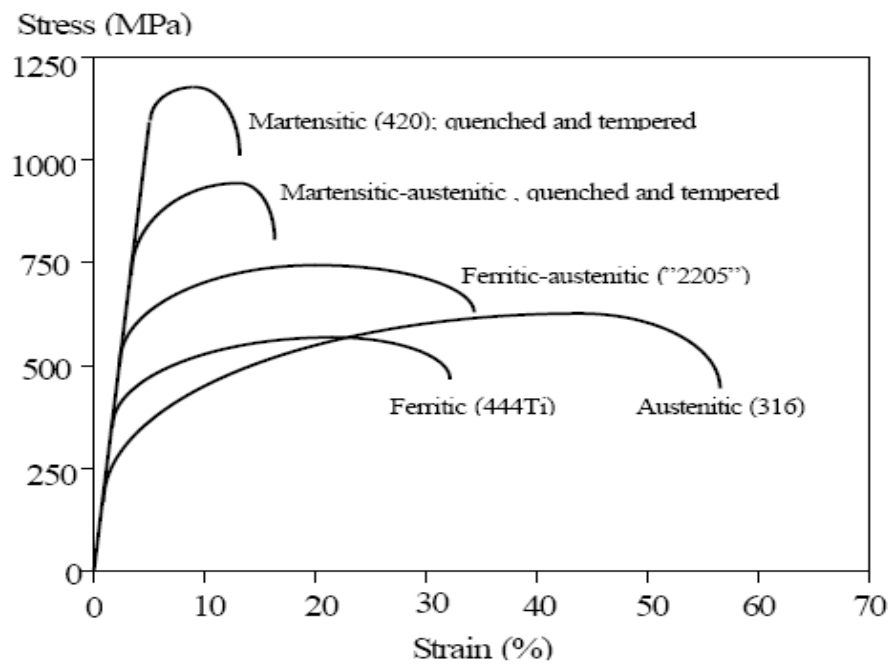
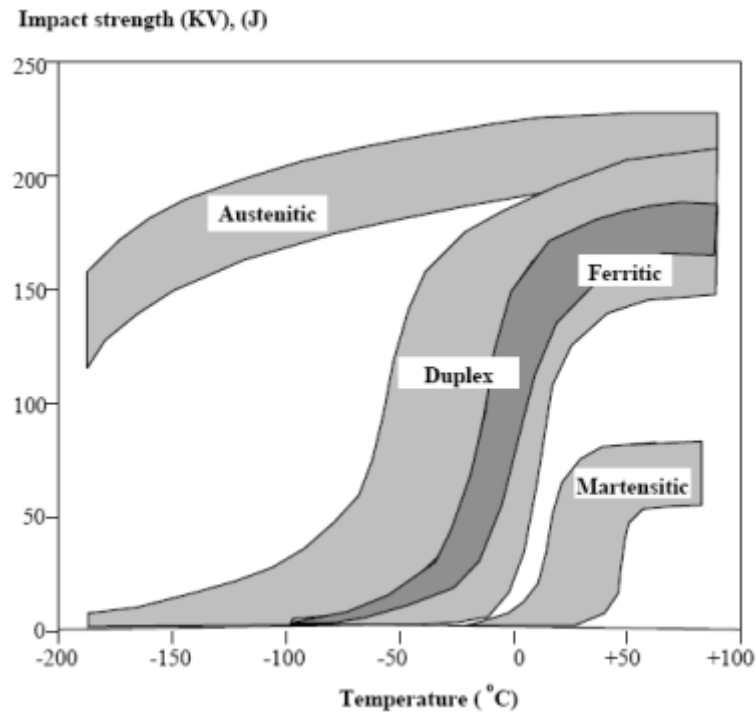


Figure 2-5: Stress-strain curves for some stainless steels [7].



**Figure 2-6: Impact toughness for different types of stainless steels [7].**

In terms of physical properties, duplex grades are ferromagnetic, and have lower thermal expansion and higher heat conductivity than austenitic grades. Austenitic steels have higher thermal expansion than the other stainless steel types which cause thermal stresses in applications that have temperature variation. Carbon steels have higher thermal conductivity than stainless steels which generally decreases with increase in alloy level in the stainless steels grades [1, 5, 7].

#### **2.1.1.5.3 Alloying Effects**

Some elements are added to the composition of stainless steels to improve certain properties or are necessary to balance the main structure, so it is important to know the role that each of these elements plays. The most important elements are Chromium, Nickel and Molybdenum beside the Iron that balances the main structure. Preventing secondary phases from forming is not the only concern when duplex is subjected to solution heat treatment or welding. General information of the alloying effects of these elements are introduced below and summarized in Table 2-4.

**Chromium**

Cr is the most important element for improving the corrosion resistance of the alloy; it does this by forming a passive oxide film on the surface. It is considered as a ferrite stabiliser and has a bcc structure [18]. Chromium improves the corrosion resistance in oxidizing environments and also provides resistance to pitting and crevice attack.

**Molybdenum**

Mo has a beneficial influence on the pitting and crevice corrosion resistance of an alloy in chloride solutions which enriches significantly in the ferrite phase [18]. It is very effective with chromium in stabilizing the passive film in the existence of chlorides. For example, in high temperature sea water, the addition of at least 3% Mo is recommended to prevent crevice corrosion.

**Nickel**

Ni is added to stabilize the austenitic structure of the stainless steel and enhance the mechanical properties and fabrication characteristics. Nickel has a structure of (fcc) and enriches in the austenite phase. Also, it supports the re-passivation in the case where the protective film is broken.

Element	The most important effects
Aluminium	Deoxidizes and restricts grain growth.
Boron	Increases hardenability.
Carbon	Increases hardenability and strength
Nitrogen	A strong austenite former; it improves localized corrosion, its addition to duplex encourages austenite reformation in the HAZ.
Lead	Increases machinability
Manganese	Increases hardenability and stabilizes the austenite.
Phosphorus	Increases strength, machinability, and corrosion resistance.
Silicon	Deoxidizes, helps electrical and magnetic properties, improves hardness and oxidation resistance.
Titanium	Strong former for ferrite and carbides to prevent formation of chromium carbide, increases the mechanical properties at high temperatures.
Tungsten	Increases wear resistance and raises hot strength and hot-hardness.
Vanadium	Increases hardenability.

**Table 2-4: The most important elements and their effects on the stainless steels [1, 6, 9, 12].**

By adding alloying elements to ferrite and austenite structures [19], the atomic diameter of the solute changes the lattice parameter of that structure. Depending on the atomic diameter of the added elements, the strain introduced causes changes in the lattice parameters which increase the yield stress of the ferrite or the austenite. The solute atoms in the base microstructure are placed either interstitially or substitutionally. Nitrogen located as an interstitial solution in austenite and has a great solid solution strengthening effect [20]. Ferrite stabilizer solutes such as Mo located are as a substitutional solution in

ferrite and affect the mechanical properties. Dakhlaoui et al. [21] evaluated the effect of the increasing content of N, Cr and Mo on the phase's yield strength and hardness in three grades of Uranus DSS that has different amount of N, Cr and Mo increasing respectively in UR35, UR45 and UR52+. It was shown that increasing the proportion of these elements will increase the yield strength and the hardness of both phases, Figure 2-7. The hardness of the austenite phase increases because of the nitrogen content whereas chromium and molybdenum enhance the hardness of both phases (mostly ferrite).

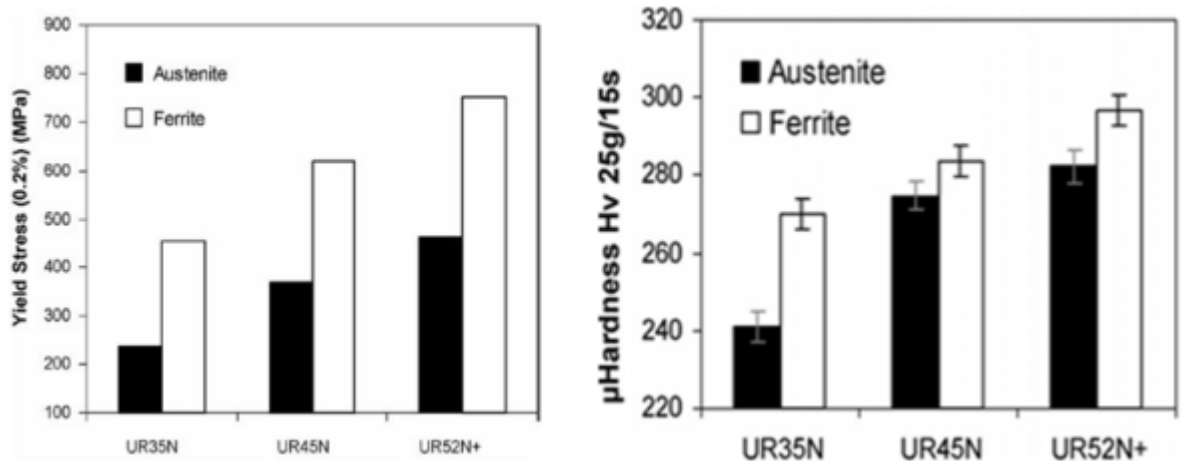


**Figure 2-7: N, Cr and Mo effects on the Yield strength and microhardness of the austenitic and the ferritic phases [21].**

#### **2.1.1.5.4 Deformation and strain partitioning in duplex stainless steels**

The deformation behaviours of materials are related to the ease of dislocation movement in those materials because the dislocations are able to move more easily in some crystallographic slip planes and slip directions than others [22]. Early metallurgists showed that the active slip system in the fcc- $\gamma$  occurs along the close-packed slip plane  $\{111\}$  and the direction  $\langle 110 \rangle$  which means it has 12 possible slip systems. On the other hand, the active slip planes in the bcc- $\alpha$  could occur on  $\{110\}$ ,  $\{112\}$  and  $\{123\}$  but always in the direction of  $\langle 111 \rangle$  [23, 24].

The two phases of ferrite and austenite have different deformation characteristics [25]. Slip in the austenite is planar, representing a low stacking fault energy which slows down the recombination of dissociated dislocations and their subsequent cross-slip. In comparison, cross-slip is easy in ferrite and the slip character is described as wavy [23]. This is clearly illustrated in the work of Serre et al. who used Atomic Force Microscopy (AFM) to

investigate the slip bands that could be created through plastic deformation in a DSS [26]. They showed that the austenite developed straight slip bands while the ferrite could have two kinds of slip bands, see Figure 2-8.

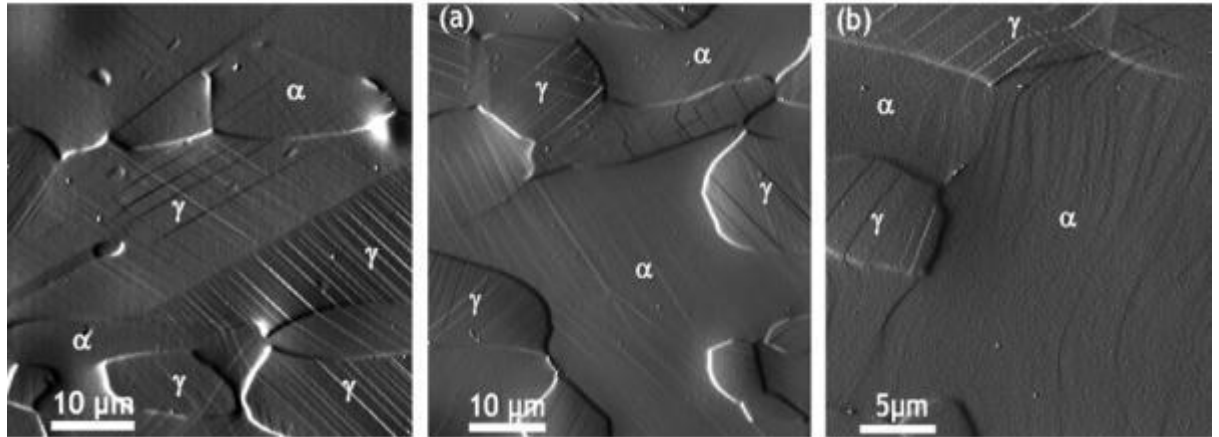


**Figure 2-8: Types of slip bands in deformed duplex stainless steel [26].**

Jia et al.[27] performed an in situ test on a sample of super DSS (SAF 2507) by using the electron back-scattering diffraction (EBSD) technique to characterize the heterogeneity of deformation at microscopic level. They observed that with development of the deformation, there was a continuous increase in the fraction of low-angle boundaries. Also local strain gradients developed at grain and twin boundaries and in the interior of some grains, Figure 2-9. Moreover, the large grain orientation dependent stresses that formed in the austenite led the authors to believe that phase boundaries in austenite operated as significant boundaries to dislocation motion. On the other hand, the boundaries between ferrite and austenite ( $\alpha/\gamma$ ) did not appear to generate very large local strains (i.e. small phase stresses which is the case when the Kurdjumov-Sachs (K-S) relation exists ( $\{111\}\gamma//\{110\}\alpha$  and  $\langle 110 \rangle\gamma//\langle 111 \rangle\alpha$  [26]). Where phase boundaries acted as barriers (i.e. where the K-S relationship did not exist between phases) the dislocations accumulating at the austenite/ferrite ( $\alpha/\gamma$ ) phase boundary caused the formation of dislocation sources in neighboring ferrite.

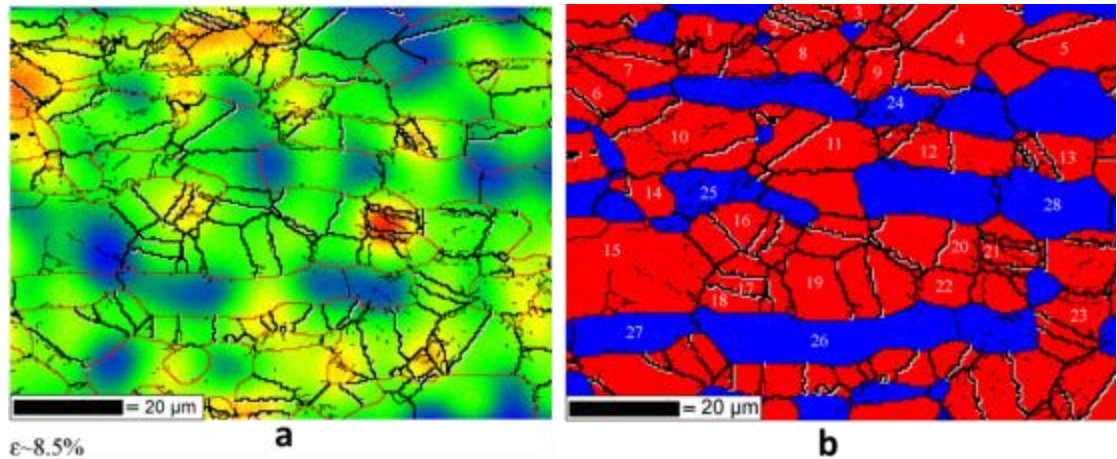


**Figure 2-9: a) Local strain map obtained by using the EBSD (thick black lines are high angle grain boundaries, thin black lines are low angle boundaries and red lines are phase boundaries. B) Phase map of the same observed area ( $\alpha$ -Blue/ $\gamma$ -Red) [27].**

A similar study was done by using AFM to observe the details of the slip systems developed in Uranus 50 during a tensile test [28]. It was established that the density of slip traces is high in all the austenite grains which has mostly one slip system comparing to the ferrite grains that have at least two slip systems found in this study, Figure 2-10, it was also suggested that the plastic deformation in ferritic grains is generated by dislocations building up in the neighbouring austenitic grains, Figure 2-11.

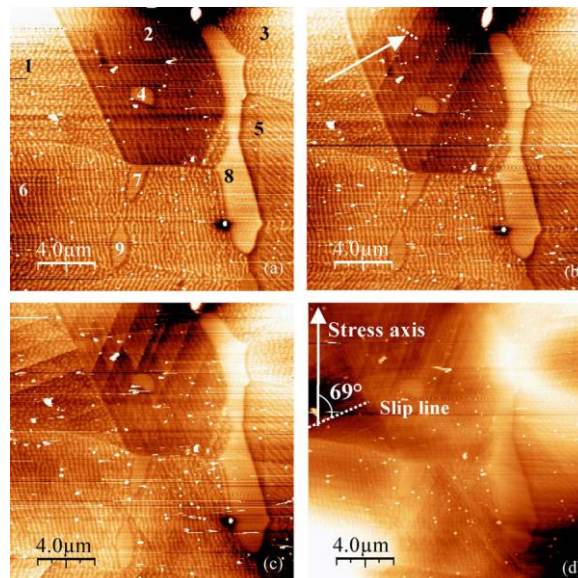


**Figure 2-10: AFM micrographs: (a) before the tensile test; (b, c and d) after an elongation of 0.5 mm, 0.6mm and 0.9 mm, respectively [28].**

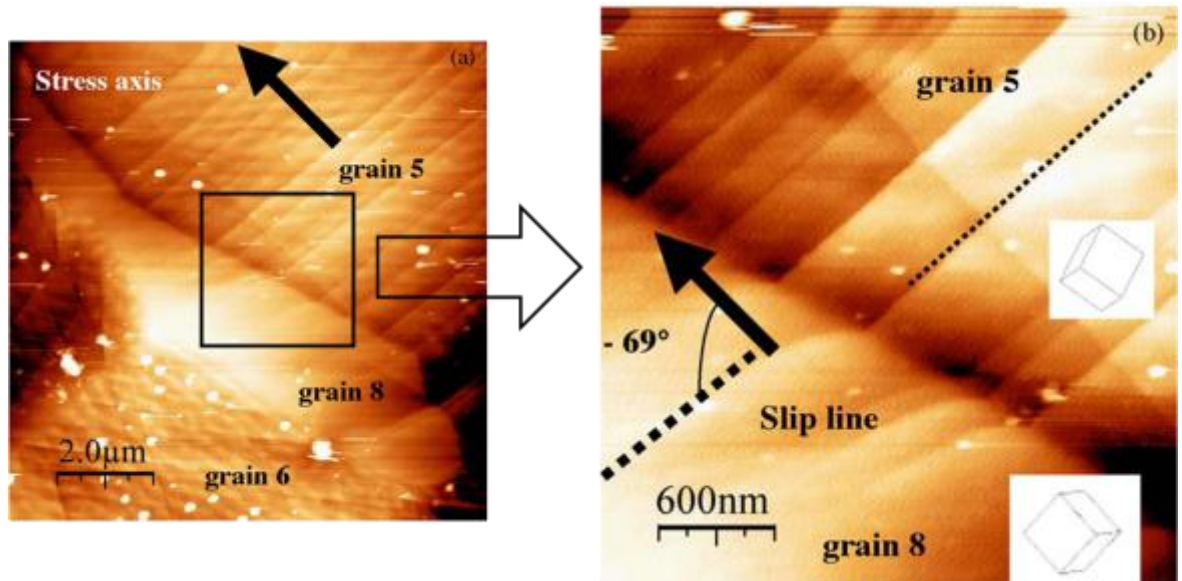


**Figure 2-11: AFM micrographs showing a slip transmission through phase boundary in a DSS. (a) Austenite/ferrite boundary at lower magnification. (b) Higher magnification for the black square [28].**

A study of the strain distribution in DSS was performed by D. Kempf et al. [29] to map strain gradients within grains and between. They used a lithography fabricated grid points at a microscale allowed to measure the displacements between those points under applied strain of 4.6%. At straining conditions, it was found that the austenite experience a higher strain level of 6% in average. Also, a highly heterogeneous strain distribution controlled the morphology and density of the slip bands established in this phase. In contrast, the ferrite phase was less in tension which shows an average strain value of 3.7% and the strain gradients were found only close to the interfaces with other austenite grains.

#### **2.1.1.5.5 Applications of Duplex Stainless Steels**

As a result of their mechanical properties, corrosion resistance and economic advantages compared with austenitic stainless steels, DSSs have increased their applications. Due to its very fine-grained structure, nitrogen alloying, and ferrite and austenite mixture, the mechanical strength of DSS is very high. Also, it can be used in many corrosive environments within the temperature range of approximately -50°C up to 300°C [2, 8]. For example, there has been wide use of DSS grades in oil and gas production equipment due to its excellent combination of strength and resistance to the corrosive brines that occur naturally in that environment [30-32].

Chloride containing process media or cooling water is common in the refining and petrochemical industry. Even at very low concentrations, aggressive chloride ions may cause rapid failure if an improper material is selected. In the petrochemicals industry [33], there are some major corrosion problems in the production of acids. In such conditions, duplex and super-duplex have great advantages and could be the best materials to select. For example, formic acid is the most aggressive of the organic acids, but at temperatures up to 40°C, AISI 304 may be used, while at higher temperature 316L can be employed if the concentration is low. At higher concentrations, and temperatures above 80°C, higher alloyed stainless steels such as S32803 / S32205 and S32750 DSS that have good resistance within certain limits must be used to keep the corrosion rate low [2].

Down-hole piping as well as gathering line-pipe, oil-gas separators, heat exchangers, and process piping have been constructed of several DSSs. Alloy 2205 was used extensively in the Endicott and Lisburne Fields on the North Slope of Alaska. In the chemical process industries there has been a growing use of the DSSs. Initially attractive because of their resistance to SCC, these grades are finding a broader application in a variety of process environments [15].

Wilhelmsson from Sandvik Steel in Sweden has outlined many practical experiences and use of DSS (SAF 2205) to replace austenitic grades like 304L, 316L, 321, when these have failed because of pitting and/or SCC [33]. Also described are cases where carbon steel, ferritic steel and austenitic steel has been replaced by duplex grades due to the latter's high strength and low thermal expansion [34]. Equipment fabricated from DSSs includes heat exchangers, pressure vessels, tanks, columns, pumps, valves and shafting. The strength of the DSS allowed the wall thickness to be reduced which means lower cost and maintenance with extra safety in the fields.

In the power utility industry, the new DSSs have been used for feed water heaters and flue gas scrubbers. They are also used in mining, desalination plants, food industry storage tanks and particularly in structures such as bridges where corrosion is difficult to avoid [15, 32].

### 2.1.2 Summary

A brief introduction of the stainless steels classes has been given, and the microstructure, mechanical and physical properties were presented with more emphasis on the DSS grades. The effects of alloying elements, deformation and strain partitioning in duplex were also briefly outlined as well as some major applications of DSS and super DSS in different industrial fields.

## 2.2 Corrosion of Stainless Steels

While the most important property of stainless steels is their corrosion resistance they could still suffer from corrosion if used incorrectly. The corrosion of metals is, in contrast to mechanical wear, the degradation of the metallic structure at its surface through a chemical reaction of the metal with the environment. The surface damage is not the result of abrasion of metal particles, but rather the transition of metal atoms from the metallic to the non-metallic state of a chemical compound [35-38]. For corrosion the most important process in the corrosion of metals is electrochemical which, under controlled conditions, can be measured, repeated and predicted. Corrosion processes can cause uniform surfaces damage, act on isolated regions or result in subsurface microscopic damage.

### 2.2.1 Electrochemistry of corrosion

It is necessary to understand the electrochemical nature of corrosion before continuing with the various forms of corrosion and three terms need to be understood [39-41]: **anode** is that part of the metal surface that is corroded and from which current leaves the metal and goes into solution; **cathode** is the area of the metal surface from which current leaves the solution and enters metal; **electrolyte** is a solution capable of conducting electricity because of the presence of positively or negatively charged ions. The electrolyte forms a corrosive environment, and for liquids can be anything from fresh or salt water through to the strongest acids or alkalis. The corrosion cell shown in Figure 2-12 has a flow of electricity from one part of a metal surface through a solution able to conducting electricity. The current in the metal will be the flow of electrons but in the electrolyte will be the flow of ions. Figure 2-12. Shows two types of chemical reactions involved in

oxidation or reduction. Assuming the metal is iron, the following can help clarify the oxidation process, which is an anodic reaction, and the cathodic (reduction) reaction [39]: -

Oxidation (anodic reaction)



Reduction (cathodic reaction)

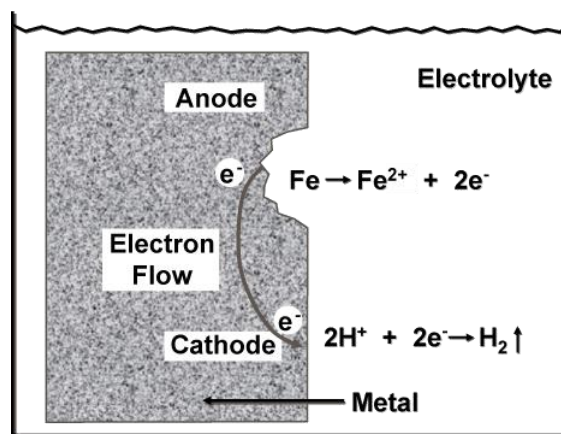


**Figure 2-12: Basic corrosion cell showing reactions and transfer of electrons [42].**

The resistance of stainless steels to corrosion comes, in an aggressive and oxidizing environment, from the formation a very thin oxide surface film that acts as a barrier to the anodic dissolution reaction and shields the surface of the steel from attack. Because of this film there is a marked reduction in the rate of corrosion of the metal surface, the phenomenon is known as passivity. More generally passivity can be defined as the reason a metal does not corrode when it would be expected to. The strength of the passive film (decrease in corrosion rate) increases fairly rapidly with increasing chromium content of the stainless steel, up to about 17%, Figure 2-13. Other alloying elements such as molybdenum, nickel and nitrogen also contribute to the corrosion resistance of stainless steels as mentioned above concerning the effects of alloying elements. Chemical or mechanical breaks in the passive film can heal themselves (repassivate) in oxidizing environments [12, 39].

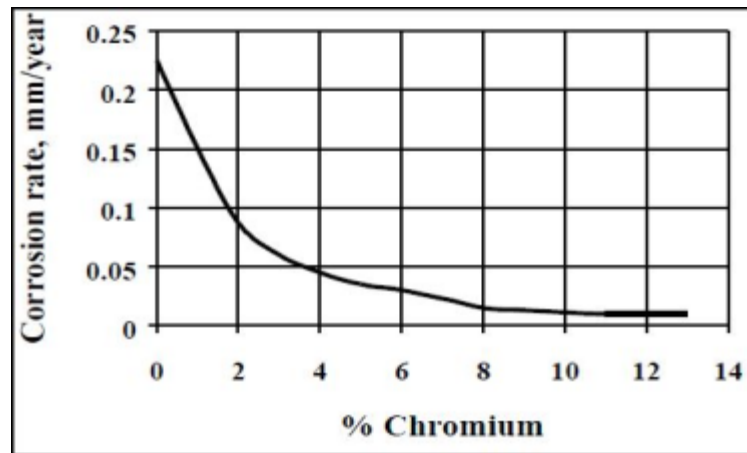


**Figure 2-13: Effect of chromium content on passivity (Corrosion Rate in air) [9].**

Metals and alloys satisfying the above definition of passivity display distinctive behavior as potential and anodic polarisation increases will have the shape shown in Figure 2-14. At relatively low potential values, within the "active" corrosion region the behavior is linear (on Log current density axes) for normal metals. With increasing potential, the current density decreases to a very low value which then remains essentially independent of potential; this is termed the passive region. Finally, at even higher potential values, the current density again increases suddenly with potential in the transpassive region. Depending on the potential, or oxidizing power of the solution, a metal may exist in the passive or the active state [39, 41, 43].

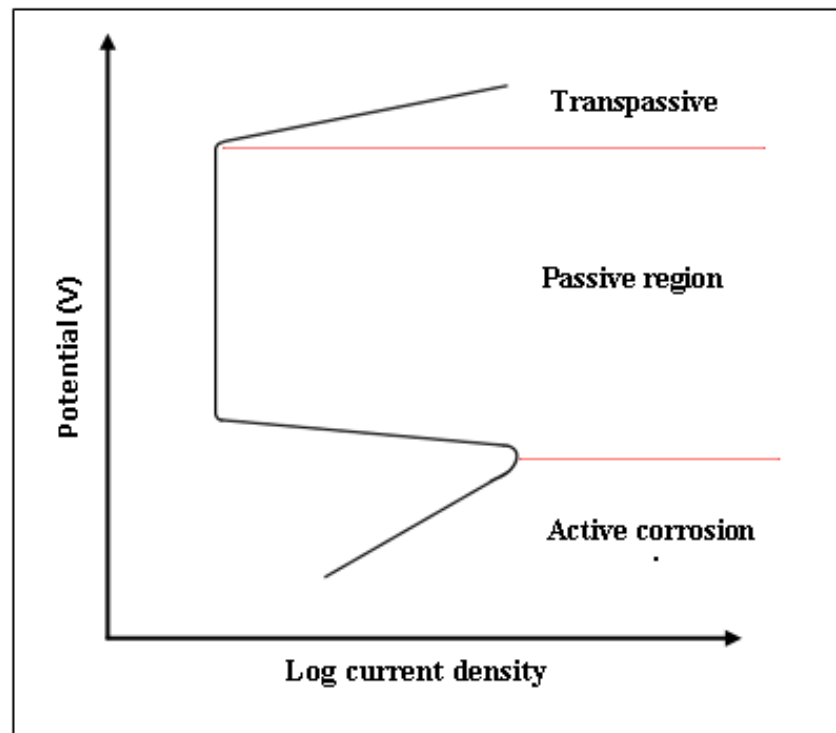


**Figure 2-14: Schematic active-passive polarisation behaviour.**

Breaks in the passive film can be unpredictable but will result in localized corrosion including SCC or pitting. In this study the performance of DSSs with these forms of corrosions will be described briefly below.

## **2.2.2 Forms of Corrosion**

The uniform or localized breakdown of the passive film can be caused by different mechanisms depending on the conditions of use. The most common types of corrosion are [44]:

- General Corrosion
- Pitting Corrosion
- Crevice Corrosion
- Stress Corrosion Cracking
- Sulphide Stress Corrosion Cracking
- Inter-granular Corrosion
- Galvanic Corrosion

DSSs have a high level of corrosion resistance in most environments where it is practical to use standard austenitic grades. However, there are some notable environments in which duplex steel is immune to several types of corrosion. This property can be attributed to the high Cr and sufficient Mo and Ni alloying which provides better corrosion resistance in acid environments. Due to availability of ferrite in the main structure by at least 30%, DSS can provide better resistance to chloride SCC than the austenitic stainless steels such as the 304 or 316 grades, as will be seen later in this literature review.

Pitting corrosion and SCC in chloride containing environments are the forms of corrosion of most interest to this study. Thus DSSs and these two types corrosion, particularly in DSS, are discussed below.

### **2.2.2.1 Pitting corrosion**

Like all metals and alloys that rely on a passive film for corrosion resistance, stainless steels are susceptible to localized corrosion which can be considered as corrosion taking place at one part of a metal surface at a much higher rate than over the rest of the surface. Pitting, as the name suggests, is a form of localized corrosive attack that produces pits in the surface of the metal as shown in Figure 2-15. This form of corrosion could occur in neutral environments but the risk of attack increases in the presence of chloride ions which

increase the severity of attack, both the breakdown of the passive film and the initiation of pits [12, 41, 45].

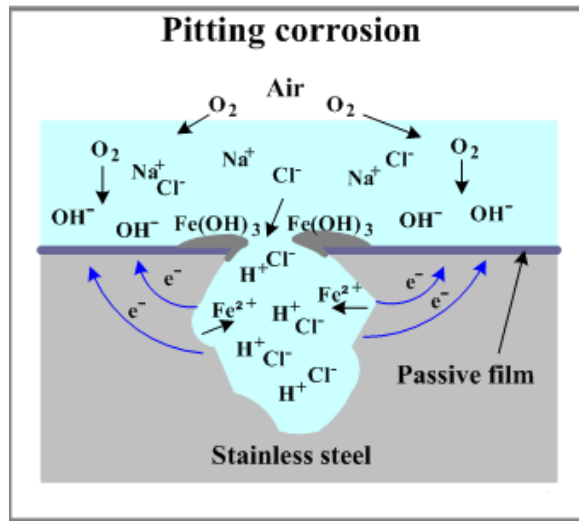


Figure 2-15: Pitting corrosion form [46].

Often pitting starts, stops, starts again, stops again, and so on. Thus pits are formed in a number of irregular geometries, see Figure 2.16. In some cases the pits will undercut the surface so that the apparent pit cross-section observed at the surface will be far less than the real cross-section of the pit [45].

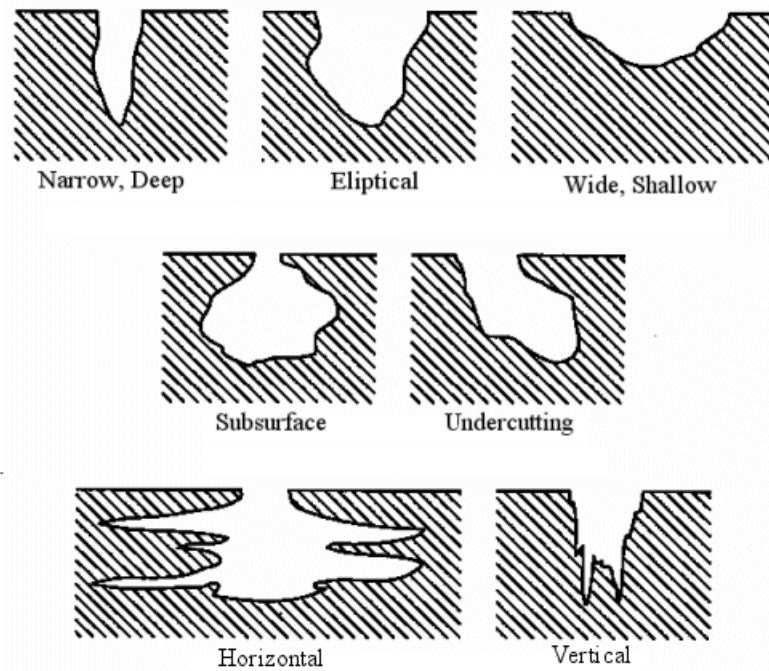
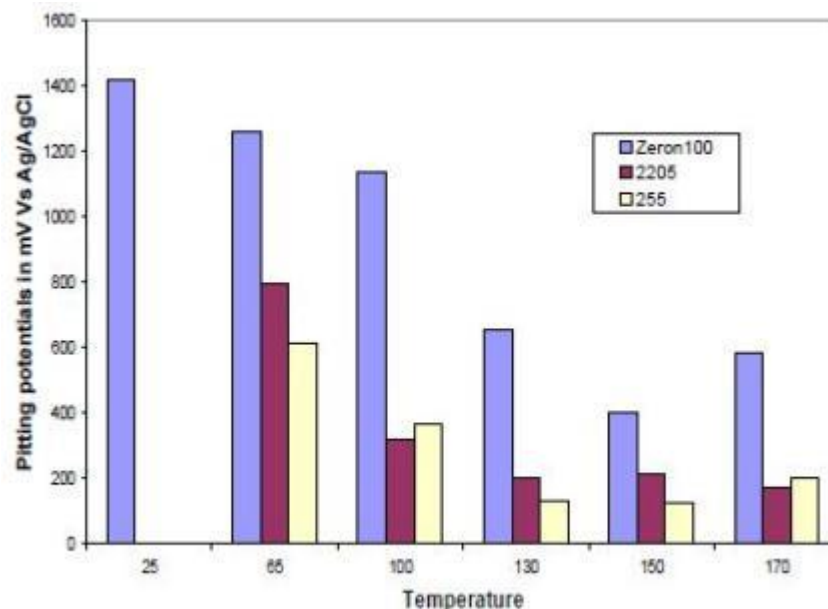


Figure 2-16: ASTM-G46 standard visual chart for pitting corrosion shapes [44].

Temperature is a critical factor affecting localized corrosion processes. It is well known that resistance to localized corrosion decreases as temperature increases since corrosion is activation controlled by chemical reaction rates, which are highly sensitive to temperature. It is useful to define the concept of a critical pitting temperature (CPT) as the temperature at which pitting corrosion starts. For a particular chloride environment, each stainless steel has a CPT above which pitting corrosion will initiate and propagate to a visibly detectable level. Below this CPT pitting initiation will tend not occur unless already initiated [12, 41].

Manning and Duquette [47] conducted studies on pit initiation on single phase and duplex phase stainless steels in 100ppm  $\text{Cl}^-$  solution over the temperature range 25°-289°C. They confirmed the linear dependence of pitting potential ( $E_p$ ) with temperature. Janardhan and Atkinson [48] investigated on the pitting behavior of Zeron 100, standard duplex 2205 and Ferralium alloy 225 DSSs various in chloride concentrations in the range 15 – 1000 ppm, for temperatures between 25°C and 170°C, using the cyclic polarisation technique, see Figures 2-17 and 2-18. They showed that the pitting potential ( $E_p$ ) decreased with increase in the temperature tested. Zeron 100 consistently showed the highest pitting potential of the three materials tested. Also, the increase in chloride concentration increases the critical pitting current density and decreases the critical pitting potential for various temperatures [48-50].



**Figure 2-17: Temperature dependence of pitting potential of Zeron 100, standard duplex 2205 and Ferralium alloy 225 duplex stainless steels on temperature [48]**

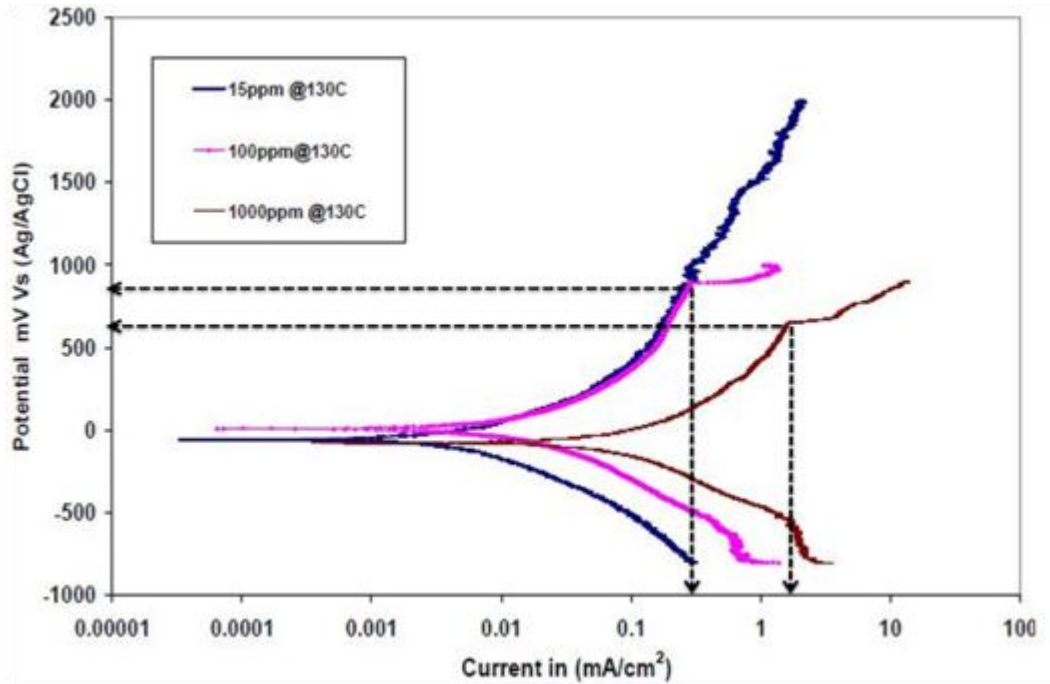


**Figure 2-18: Polarisation curve of Zeron100 at 130°C in 15, 100 and 1000 ppm chloride solution showing the critical pitting current density [48].**

A comparison of pitting corrosion resistance for a number of stainless steels in the solution annealed condition as measured by the ASTM G48 procedure (10% ferric chloride) is shown in Figure 2-19 [51]. Higher CPT means better resistance to the initiation of pitting corrosion. The CPT of DSS is well above the CPT of Type 316 which makes DSS an appropriate material that could be used in applications where chlorides are concentrated by evaporation, as in the vapor spaces of heat exchangers.

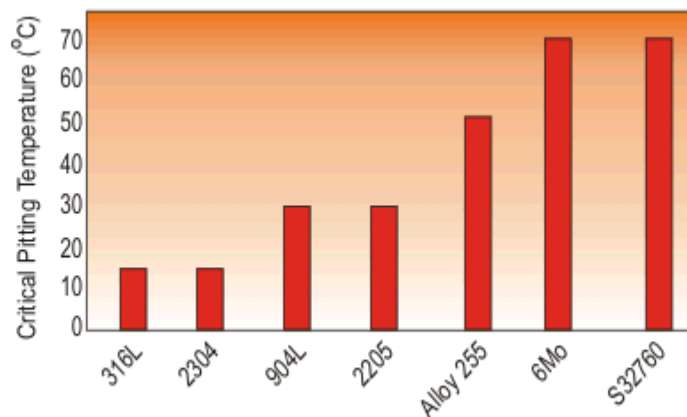


**Figure 2-19: CPT for various Stainless Steels in the Solution Annealed condition as measured by the ASTM G 48 procedures (10% ferric chloride) [51].**

Calculated Pitting Resistance Equivalent (PRE) numbers predict the pitting resistance based on alloying elements nitrogen, molybdenum and chromium [44]. A higher PRE number means higher predicted pitting corrosion resistance. PRE is given by Equation 2-5 which is a formula that allows for the different proportions of chromium, molybdenum and nitrogen contents by weight %:

$$\text{PRE} = \% \text{Cr} + 3.3 \times \% \text{Mo} + 16 \times \% \text{N} \quad (\text{eq.2-5})$$

From Equation 2.5 it would appear that the most important alloying element in determining the PRE number for stainless steels is nitrogen, but, in fact, because by weight there is more than 100 times as much chromium as nitrogen, chromium invariably makes the greatest contribution to the PRE number. Other alloying elements such molybdenum may make an important contribution to corrosion resistance in particular environments, for example copper in sulphuric acid [52].

Alloy	PRE Number	%Cr	%Mo	%N
2507	42.2	25	4.0	0.25
2205	35	22	3.0	0.20
316	24	17	2.1	0.06

**Table 2-5: Pitting Resistant Equivalent number (PRE#) for various types of stainless steel [12].**

The so-called superduplex grades typically have PRE numbers greater than 40. Tungsten has also been shown to raise the pitting potential and decrease the passive current density, and for stainless steels containing tungsten, the factor (1.65 x %W) is added to the PRE equation. Traditionally this term is integrated with that for molybdenum as 3.3(%Mo + 0.5%W). Tungsten is an alloying addition to the Japanese DSS DP-3W at the level of 2%W and to the British super DSS Zeron 100 (S32760) at the level of 0.7%W [12]. Silicon

is also reported to move the pitting potential in the noble direction. High-silicon DSSs such as Uranus S and Uranus SD, containing up to 4% silicon, are manufactured for use in highly oxidizing environments.

Generally, when the passive film or any another protective surface layer breaks-down locally, pitting corrosion takes place. An anode forms where the film has broken, while the unbroken film acts as a cathode. In this case the localized attack will be accelerated and pits will develop at the anodic spots. The electrolyte inside the growing pit becomes more aggressive probably by hydrolysis reactions and leads to further acceleration of the corrosion process [39, 44]. The effect of the chloride concentration, pH, dissolved oxygen and temperature on the pitting behavior of 316L stainless steel in aqueous solutions under dynamic and static conditions has been examined and it was found that the number and depth of pits increase with increasing  $\text{Cl}^-$  concentration. Also it was established that low pH, high  $\text{Cl}^-$  content and stagnancy are the conditions most appropriate for initiation and propagation of pitting in 316L stainless steel [44, 53].

Schmidt-Rieder et al., have reported the pitting behavior of DSSs is structure sensitive and complicated by the fact that manganese sulphide, if present, resides at grain boundaries; chromium diffuses more slowly in the austenite than in the ferrite at elevated temperatures; molybdenum and chromium preferentially partition to ferrite, while nitrogen preferentially partitions to austenite and has an important effect of the stability of the passive film on that phase [54]. Decreasing the manganese content of stainless steels below 0.5%Mn favours the formation of the more corrosion-resistant chromium sulphide. This may be one of several reasons for the high pitting resistance of the British duplex grade Zeron 100, which contains only 0.4%Mn [12]. Jeffrey et al., compared the corrosion behavior of 2205 DSS with 316L stainless steel [55]. Both stainless steels were subjected to electrochemical and immersion corrosion tests in 37°C, 0.9 wt% NaCl solution. Electrochemical testing indicated that the 2205 DSS has a larger passivation range than 316L and the corrosion rate of 2205 DSS was 0.416 mpy (milli-inch per year), whereas the Figure for 316L was 0.647 mpy.

Garfias-Mesias, and many other researchers have investigated localized corrosion attack on DSS in chloride solutions, and it has been shown that pitting corrosion of DSS in chloride

solutions takes place preferentially in the ferrite phase rather than the austenite phase [56-59]. Other studies in chloride environments have shown that the localized corrosion processes occur at the grain boundaries (interfaces) as preferential sites of nucleation, and then grow in the ferrite phase [60, 61]. Tseng et al., have noted that both types of behavior depend on the chemical composition of both phases, but particularly on whether nitrogen is present as an alloying element in the DSS [20]. If nitrogen is present only as an impurity (e.g., 0.02%), the preferential partitioning of chromium and molybdenum to the ferrite renders the ferrite more resistant to pitting with the result that pit propagation, and ultimately selective phase attack, occur in the austenite phase. However, with the presence of nitrogen as an added alloying element (e.g., 0.14%), it is preferentially partitioned to the austenite phase which in combination with the residual chromium and molybdenum provide the austenite phase with greater resistance to pitting than the ferrite phase, with the result that pit propagation occurs into the ferrite [12].

Cold working can generate a number of metallurgical and physical changes in the metal including slippage of dislocations and plastic deformation [62]. The effect of such changes on pitting appears to be slight compared to addition of alloying elements or the changes in the chloride concentration. However, a number of researchers have linked pit sites to the interfaces between ferrite and austenite induced by cold working and/or deformation bands [63-66]. Vignal and Kempf [67] found that the susceptibility of a DSS to pitting increased dramatically as a result of plastic strain and that pits preferentially initiated at slip bands. Peguet et al., and Takatoshi et al., have claimed that pit propagation rate increases with reduction in thickness due to cold rolling (i.e. with total plastic strain), and that then tendency for pit re-passivation decreases resulting in a larger number of stable pits, suggesting that dislocations result in the formation of a defective passive film [68, 69].

#### **2.2.2.2 Stress Corrosion Cracking**

SCC is a complex subject and its mechanisms remain unresolved in some environments, despite the attempts made investigate and characterize its various aspects. SCC is one of the most common and hazardous forms of corrosion. It has three components necessary requirements; a susceptible material, an environment that could cause SCC for that material, and sufficient tensile stress (either residual, applied or a combination of both) that will lead to the initiation of crack nucleation and its subsequent growth, Figure 2-20.

Generally it initiates from surface defects created during fabrication, or produced by other types of corrosion that create a stress concentrator, and leads to a crack failure [12, 70].

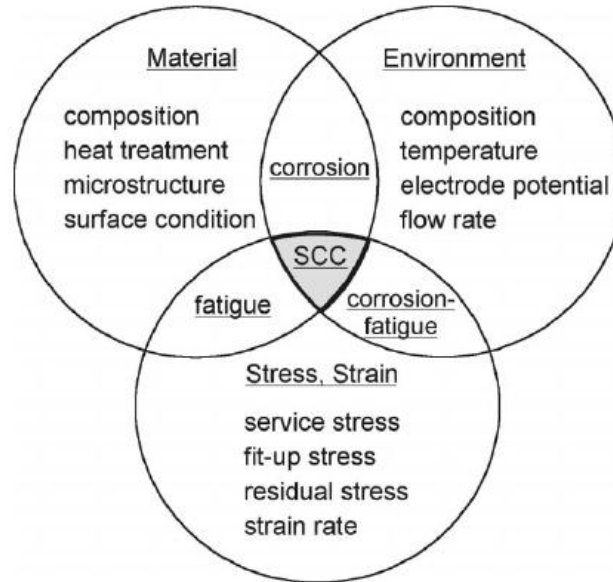


**Figure 2-20: Stress corrosion cracking conditions [71].**

The transition of these pits to SCC is influenced by the local electrochemistry, local stresses, the strain distribution at the bottom and walls of the pit and pit geometry [72, 73]. The pit geometry is of particular importance as it determines stress intensity factors and stress intensity concentrations [74]. Theoretically it is possible to detect the initiation points from which cracks can propagate, in most cases it is virtually impossible to achieve experimentally because there is no agreed or precise definition of when a corrosion pit becomes a crack, or intergranular corrosion becomes intergranular SCC. Nor is there a clear distinction between crack initiation and crack growth, although Sedricks has proposed considering pits as short cracks and the pit bottom as a crack tip [12, 75].

#### ***2.2.2.2.1 Effects of Environmental and Microstructure Variables***

SCC is a problem which must be taken into account when considering the suitability of a material as they can be very expensive modes of failures, of particular relevance to desalination, oil, petrochemicals or power plants. SCC has the appearance of a brittle fracture but can occur in highly ductile materials. In duplex microstructures, one phase often cracks more easily than the other, leading to characteristic patterns, see Figure2-21.

The cracks form and propagate at roughly right angles to the direction of the tensile stress at stress levels much lower than those required to cause material fracture [76, 77]. Susceptibility to SCC is thought to be orientation dependent [78, 79]. It was found that SCC was more severe in transverse direction specimens than longitudinal direction specimens and that this was caused by the configuration of the austenite grains, which have a keying effect.

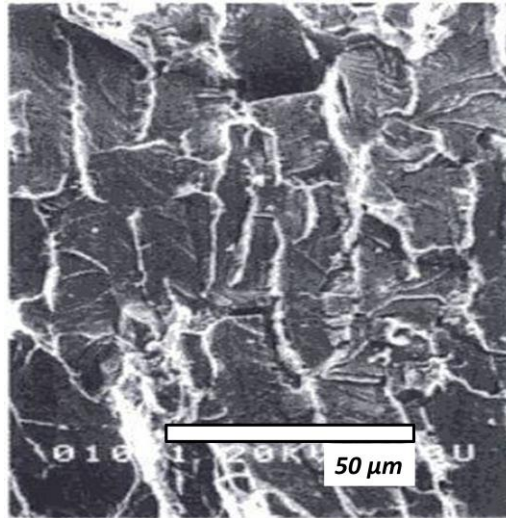


**Figure 2-21: SCC fracture surface of 25%Cr duplex stainless steel (50% ferrite) in NaCl-H<sub>2</sub>S solution at 80°C, showing flat, cleavage-like cracking of ferrite and mainly ductile fracture of austenite [76].**

Most of the published work related to SCC of DSSs was carried out in very aggressive environments like boiling (150°C) MgCl<sub>2</sub>, CaCl<sub>2</sub>, and NaCl solutions [80, 81]. Cottis and Newman [82] have assessed the stress corrosion resistance of DSS, collecting an important sources of such data, and pointed out that insufficient data exists in the temperature range of 60°-130°C. They noted that understanding of SCC mechanisms in this range of temperature was unclear. Of the environmental conditions studied, the temperature appears to have the largest effect on the occurrence of SCC [79].

SCC is an insidious form of corrosion that may produce a marked loss of mechanical strength with mechanical fast fracture and catastrophic failure of components and structures when there has been little metal loss and the damage is not obvious to casual inspection. It is a mechanical-chemical process leading to cracking of a certain alloy at

stresses considerably below their tensile strengths. Cracking may proceed either intergranularly or transgranularly, see Figure 2-22. It was noticed that in case of SCC of DSS, the cracking morphology varies showing transgranularity in the case of ferrite and intergranularity in austenite/austenite grain boundaries [70, 80].

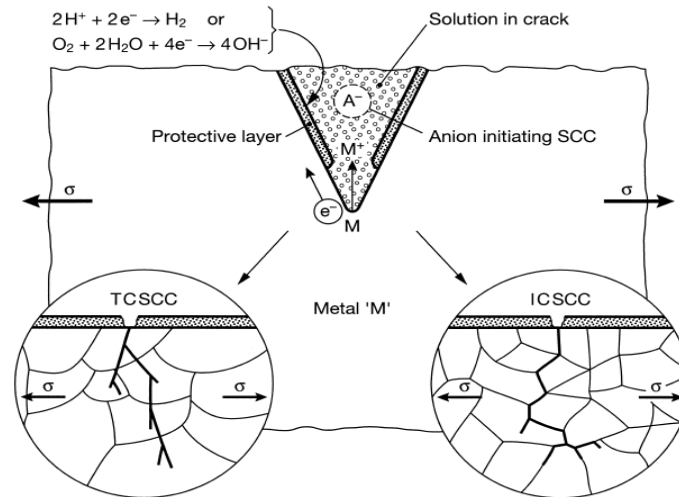


**Figure 2-22: A schematic diagram show the intergranular and transgranular cracking methodology.**

Aqueous solutions containing chlorides are the most frequently environment to produce SCC in stainless steels, but are not the only environments to have this effect. Other solutions such as caustic solutions, for example sodium and potassium hydroxides, can also cause SCC in stainless steels at temperatures above the boiling point [83].

Based on their resistance to chloride SCC, many of the earliest uses of DSSs in the chemical and petrochemicals process industries were as replacements for austenitic grades where there was a significant risk of SCC. Figure 2-23 illustrates the SCC resistance in various steels [82] of DSSs against austenitics in the presence of different percentages of chloride ions and as a function of temperature. However, DSSs may be susceptible to SCC under certain conditions: such as in chloride containing environments at high temperatures. Examples of environments in which DSSs have shown SCC include the boiling 42% magnesium chloride test, drop evaporation with high metal temperature, and a pressurized aqueous chloride system in which the temperature was higher than could be achieved at ambient pressure [81, 84-87].

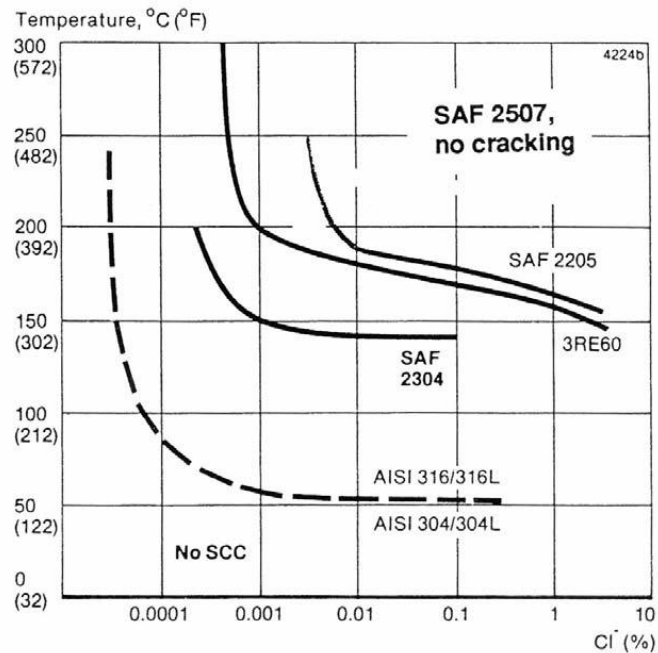


**Figure 2-23: SCC resistance in various steels [82].**

Briefly, chloride level, boiling, elevated temperatures, and variation in loading can all greatly magnify the rate of SCC. The time-to-failure is decreased when local temperature, chloride content or both are raised. If there is a concentration mechanism, such as cyclic evaporation of condensates, the chloride content will be more effective than the nominal content [37, 82-84].

Early works [82, 88] concluded that ferrite protects austenite against SCC, as it has a lower corrosion potential in an acidified crack solution. However in modern DSSs, cracking can occur preferentially in the ferrite phase because ferrite in austenite matrix DSS has at least 3%Ni in comparison to the older ferrite matrix stainless steels, which are nickel free. This makes ferrite phase susceptible to SCC. Cottis and Newman [82] explained the mechanism in terms of electrochemical behavior and mechanics of crack propagation through the two phases. The crack reaches the austenite, but to propagate through it requires the prevailing potential and pH to be favorable to cracking in this phase. However the ferrite would tend to leave the austenite unbroken unless the stress was high enough to cause ductile tearing, which will require high levels of stress [88, 89].

Magnin et al., [90] studied SCC of ferrite phase in DSSs (Uranus 45, 47 and 50). It was reported that damage due to twins in ferrite appears before damage due to slip and due to de-passivation; localized corrosion can start in the twins. According to Magnin et al., the threshold stress for SCC in DSSs is the stress at which ferrite begins to be sufficiently strained to start twinning because that will produce cracking in the material with electrochemical assistance.

Tsai et al., [91] have found that in near neutral 26 wt% NaCl solution at 90°C, 2205 DSS was immune to SCC with the potential held in the passive region. However, when the potential was held above the pitting corrosion potential in the solution, pitting assisted SCC occurred and the dissolution of  $\alpha$ -phase participated in the crack growth process. Under the same test conditions, 316 SS has transgranular fracture, indicating the occurrence of SCC in austenite. Based on these observations [92], a schematic diagram illustrating the effect of applied potential on the environmentally assisted cracking for 2205 DSS is shown in Figure 2-24. As indicated in this diagram, 2205 DSS is susceptible to environmentally assisted cracking which is strongly dependent on the potential applied. At high anodic polarization conditions, pitting corrosion assists the initiation of SCC in chloride solutions. On the other hand, the pick-up of hydrogen promotes hydrogen-assisted cracking (HAC) under deep cathodic polarization conditions [93].

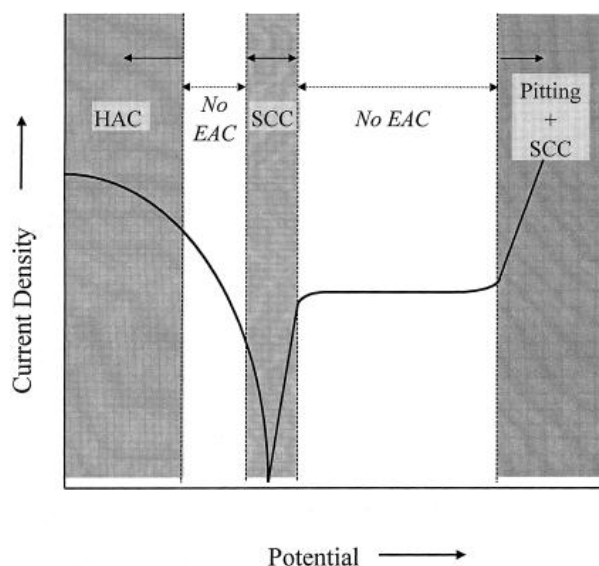


**Figure 2-24: Schematic diagram illustrating the effect of applied potential on the environmentally assisted cracking for 2205 duplex stainless steel [92].**

### 2.2.2.2.2 Fracture mechanics and short cracks

SCC is a time-dependent failure process. That is, cracks initiate and propagate at a slow rate, until the stresses in the remaining ligament of metal become greater than the fracture strength and it totally fails [44]. The sequence of the SCC process is usually divided into three stages:

- Stage 1, crack initiation,
- Stage 2 steady-state crack propagation, and
- Stage 3 crack propagation and final failure

Figure 2-25 summarize the main stages of SCC from initiation. The shaded area shows the transition of driving force from solely electrochemical to mainly mechanical. Cracking by hydrogen may also be involved in this transition region.

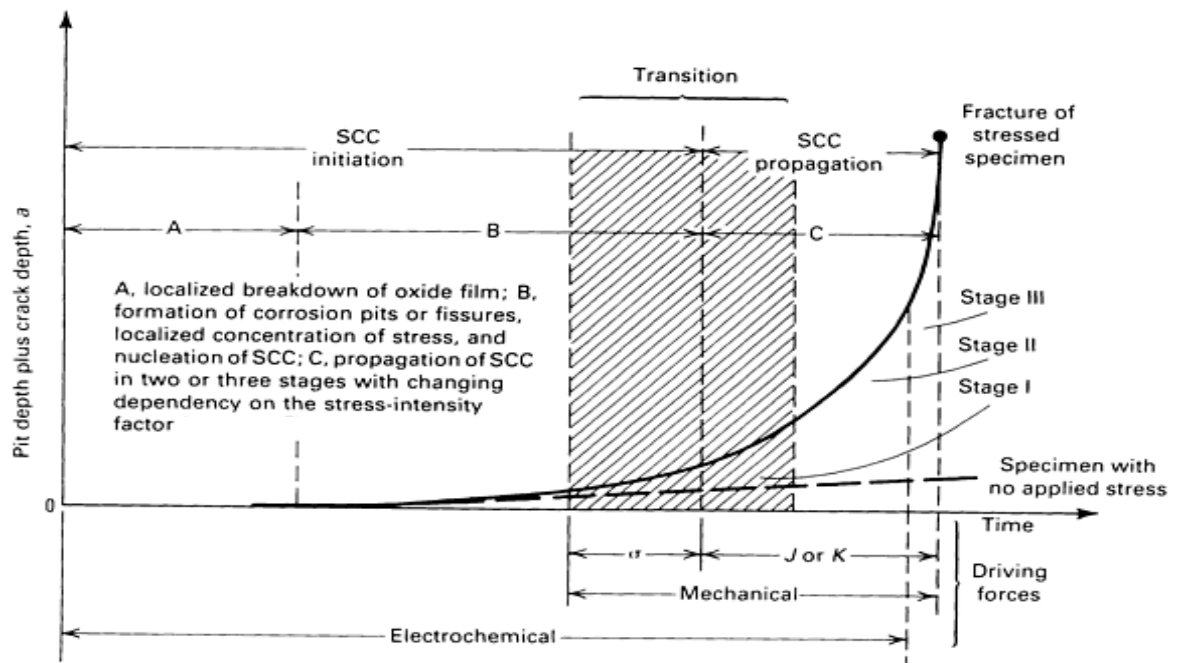


**Figure 2-25: The relative influences of electrochemical and mechanical factors in the corrosion and SCC damage of a susceptible material [44].**

Tensile stress is necessary for crack propagation. Using fracture mechanics of materials, the parameter calculated from load which best describes crack propagation is stress intensity factor  $K$  rather than stress. The stress to which the metal might be subjected without cracking is identified by a threshold stress. The stress distribution around the crack

tip is defined by the stress intensity factor (K) which is related to the elastic strain distribution around the crack tip [12]. Figure 2-26 is a schematic representation of the application of a tensile load to a thin plate containing a crack. The load is perpendicular to the crack length and acts along the entire length of the crack. This results in a stress distribution in the crack tip described by Equations 2-6, 2-7 and 2-8 [23].

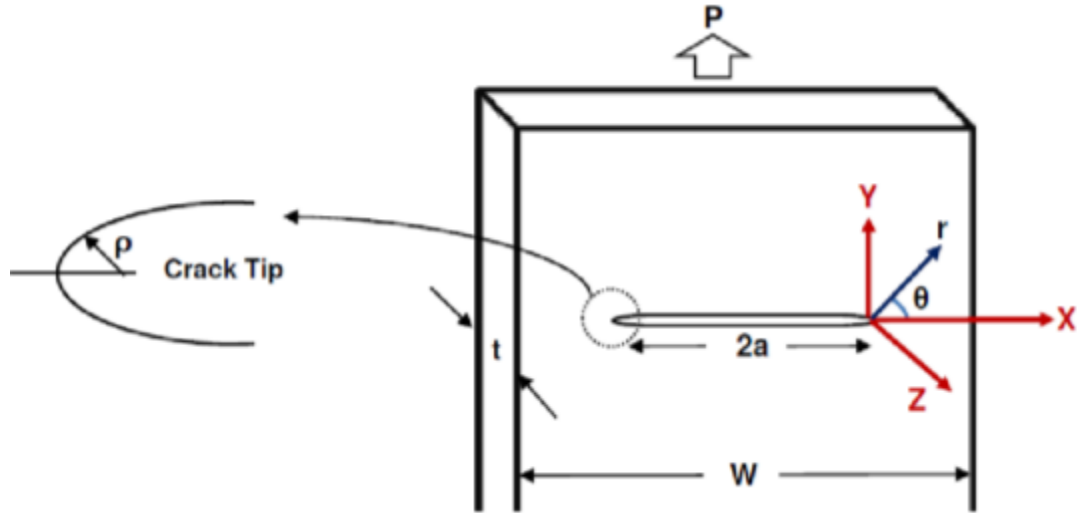


**Figure 2-26: A schematic diagram describing the stress distribution at a point near to the crack tip for a crack of length  $2a$  [23].**

$$\sigma_x = \sigma \left( \frac{a}{2r} \right)^{\frac{1}{2}} \left[ \cos \frac{\theta}{2} \left( 1 - \sin \frac{\theta}{2} \sin \frac{3\theta}{2} \right) \right] \quad (\text{eq.2-6})$$

$$\sigma_y = \sigma \left( \frac{a}{2r} \right)^{\frac{1}{2}} \left[ \cos \frac{\theta}{2} \left( 1 + \sin \frac{\theta}{2} \sin \frac{3\theta}{2} \right) \right] \quad (\text{eq.2-7})$$

$$\tau_{xy} = \sigma \left( \frac{a}{2r} \right)^{\frac{1}{2}} \left[ \sin \frac{\theta}{2} \cos \frac{\theta}{2} \cos \frac{3\theta}{2} \right] \quad (\text{eq.2-8})$$

These equations are valid when  $a > r > \rho$ , where P is the applied load, t is the thickness of the specimen containing the crack and W is the width,  $\sigma$  is the total nominal applied stress equal to  $P/(Wxt)$  with its normal parallel to the direction of applied load,  $\rho$  is the radius of curvature at the crack tip and  $\theta$  is the angle between a line along the crack length (the X-axis in the above Figure) and an arbitrary direction in front of the crack. For a position directly in front of the tip  $\theta = 0$  and Equations 2-6, 2-7 and 2-8 simplify to

$\sigma_x = \sigma_y = \sigma (a/2r)^{1/2}$  and  $\tau_{xy}=0$  [23]. The term  $\sigma(a/2r)^{1/2}$  is known as the stress intensity factor ( $K_I$ ). For a sharp elastic crack in an infinitely wide plate:

$$K = \sigma\sqrt{\pi a} \quad (\text{eq.2-9})$$

For stress intensity factor below a certain threshold intensity level ( $K_{ISCC}$ ) crack growth would not be expected. The parameter  $K_{ISCC}$  is defined as the threshold stress intensity factor for continued crack growth in the sense that above this value any initiated crack will continue to grow, and below growing cracks could be arrested and can be dealt with as short cracks that strongly depend on the microstructure [44].

However for  $K > K_{ISCC}$  an initial SCC growth would accelerate until a constant crack growth rate is reached [44, 70, 82]. Experimental evidence has demonstrated that, for a given material/environment combination, a unique relation exists between  $K_I$  and the growth rate of a stress corrosion crack [44, 94]. The usual way of representing this relationship is to plot crack growth rates ( $da/dt$ ) as a function of  $K_I$ . In the typical schematic diagram shown as Figure 2-27, at a lower value of  $K_I$  that is, just above the stress corrosion threshold the first measurable crack (long crack) extension occurs. Cracking propagates with increasing rate with increasing  $K_I$ . In region II, transport and electrochemical processes are the rate-limiting parameters, controlling the crack growth kinetics. Region III - a second region where crack growth is strongly dependent on  $K_I$  - occurs as the critical stress intensity increases to the stress intensity factor corresponding to fracture. Here, pure mechanical rupture dominates over subcritical crack extension caused by SCC.

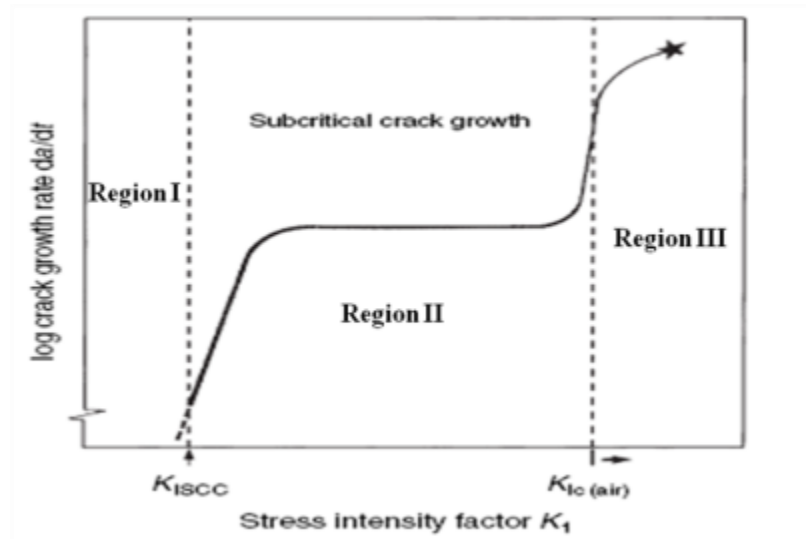


Figure 2-27: Schematic relationship between  $K_I$  and  $da/dt$  [44].

Several micro-structural studies have revealed that short crack initiation (at free surfaces or at defects) is formed due to accumulation of localized plastic strain. It is very important to note that short crack initiation and propagation can occur at stress conditions far below the threshold value  $K_{ISCC}$ , can be initiated by local stress raisers such as inclusions or pits [95], and can grow at higher rates than the rates predicted for long crack growth, Figure 2-28 [96, 97].

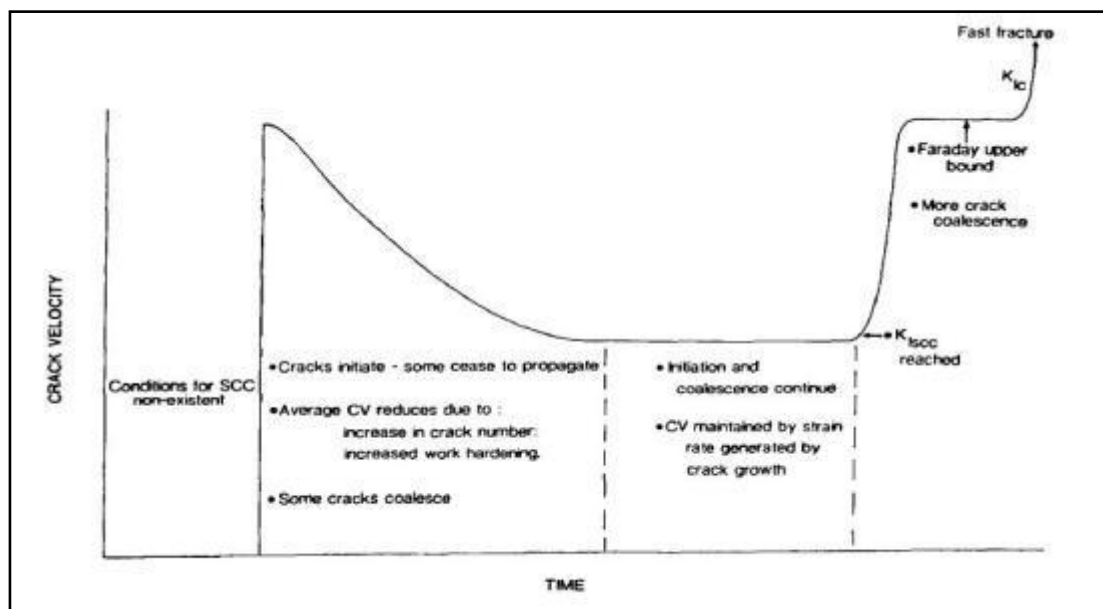
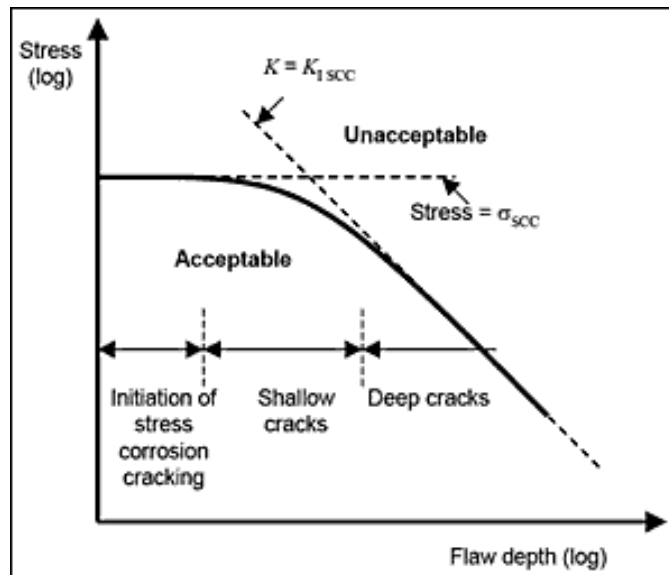


Figure 2-28: Schematic representation of crack velocity with time [97].

In a corrosive environment [98], the dissolution process can support the progress of the corrosion crack by dissolving the barrier with the net effect of an increased crack growth rate. Crack growth still slows at the barrier but the growth rate remains higher than in air. The crack length corresponding to the transition from stage I to stage II cracking, the regime of physically small cracks, is reduced in a corrosive environment and can be as low as one to two grain diameters. Such short cracks have strong interactions with microstructural features and their considerably different growth mechanisms (stage I) compared to long cracks (stage II) which also depend on some macroscopic mechanical properties such as the plasticity of the material, and can be well described depending on the stress intensity factor  $K$ .

The micro-structurally short crack propagation could be identified as a propagation that is affected by grain boundaries and defects that act as stress raisers and as barriers. The propagation behavior can principally be divided into stage I and stage II [99]. Stage I is described by a shear-controlled crack advance which takes place on slip planes. But, the stage II mechanism does not take place on a certain slip plane but perpendicular to the direction of the normal stress. During the crack growth in stage I [100], grain and phase boundaries may act as barriers against slip transmission into adjacent grains (depending on the orientation of the respective slip bands) and then reduce the shear displacement at the crack tip. This causes a fluctuating crack growth rate. During the increase in crack length, additional slip bands get activated and the crack can propagate on different slip bands [100].

In addition to enhancing slip [98], a corrosive environment can influence initiation directly, by preferential dissolution of emerging slip steps and by corrosion pit formation. Figure 2-29 illustrates the link between stage I and stage II as a function of crack length and stress level [101]. It shows that short cracks can grow within the grain at a lower stress amplitude compared to a stage II crack.



**Figure 2-29: Schematic curve showing the threshold between propagating and non-propagating cracks [101].**

#### 2.2.2.2.3 Mechanisms of Stress Corrosion Cracking

SCC is driven by the local environment, mechanics, and material characteristics. As mentioned earlier, cracks tend to initiate at micro-structural and microchemical inhomogeneities at stress concentrators. Certainly, for many systems, crack initiation may occur directly from pitting or crevice attack corrosion. These processes generate stress concentrators and establish the critical local solution chemistry for cracking [102]. Once cracking has initiated, the internal environment in the crack continues to determine the local electrochemical kinetics and the nature and stability of surface oxide films.

The SCC characteristics of DSSs have been explained by the cathodic protection of the austenite phase by the ferrite phase, as well as by a blocking effect of cracks in the ferrite by the austenite. It was demonstrated for DSSs that the ferrite was anodic to the austenite in the unstressed state but that anodic sites could appear in the austenite in the stressed state [103]. Shimodaira et al., reported that the keying action or a mechanical suppression of crack propagation in the austenite by the ferrite occurred at low applied stress but at high applied stress, SCC propagated in a transgranular mode through both the ferrite and the austenite [103, 104].

There have been many mechanisms and models proposed to explain and predict the stress corrosion interaction that occurs at the crack tip [71, 105]. Slip-dissolution, film-induced cleavage, and hydrogen embrittlement are models that may account for most known cases of SCC in metals and will be described briefly [70, 76]:

- ***Slip-Dissolution Model***

According to this model, crack growth occurs by extremely localized anodic dissolution. The sides of the crack are protected by a film, typically an oxide film, which is fractured as a result of plastic strain in the metal at the crack tip. Crack growth proceeds by a cyclic process of film rupture, dissolution, and film repair, see Figure 2-30. Slip is highly localized, microscopic strain leads to a surface offset or step where the slip plane intersects the surface and, thus, can rupture the passive film present at the surface. This cracking mechanism has been successfully applied to model SCC of austenitic stainless steel [70, 76].

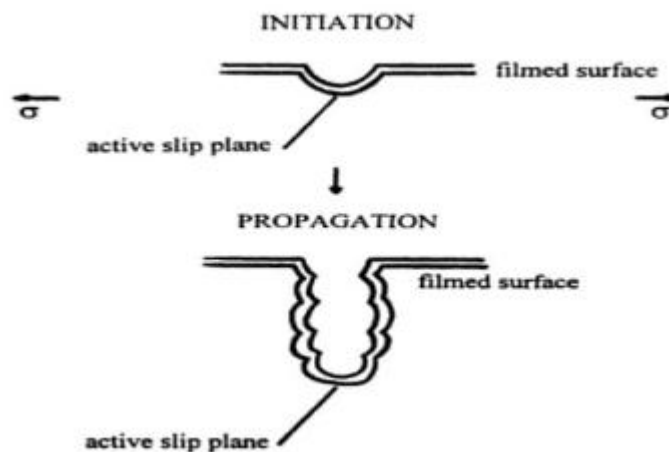


**Figure 2-30: Schematic of crack initiation and growth by slip-dissolution[76].**

- ***Film-Induced Cleavage Model***

In this model, a brittle crack (fracture) initiated in the protection film propagates into the material until it is arrested by ductile blunting. A brittle crack begins in the thin film surface layer, crosses the film-metal interface and propagates into the metal dealloying and inducing brittle fracture. This would be expected to cause a transgranular fracture by

repeating the same process. Figure 2-31 illustrates the film-induced cleavage mechanism [70, 76, 106].

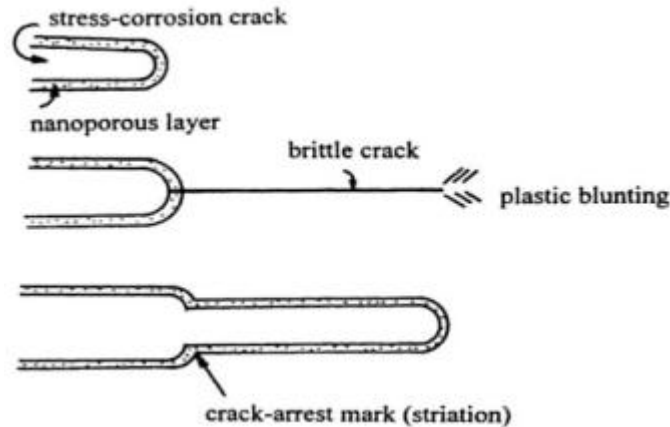


**Figure 2-31: Schematic drawing of crack growth by film-induced cleavage [76].**

- **Hydrogen Embrittlement Model**

Hydrogen absorption is clearly responsible for SCC of high-strength steels in aqueous environments. Hydrogen may enter metals by the absorption of hydrogen atoms produced either by dissociation of hydrogen in hydrogen-containing gases, or by electrochemical reaction in solution. Cathodic polarisation of DSS causes embrittlement because of absorbed hydrogen produced during cathodic reactions. The lower the applied cathodic potential the relatively fewer hydrogen ions there will be in the solution and more absorbed hydrogen atoms will diffuse into the steel. Hydrogen pre-charging was reported to increase the brittle areas on the fracture surface and enhance SCC initiation. The most significant feature of hydrogen in steels is the embrittlement of the bcc crystal structure due to its high diffusivity of the hydrogen atoms in this phase and the bcc lattice is inherently susceptible to embrittlement. Generally, hydrogen embrittlement of DSSs is associated with cleavage in the ferrite phase and ductile failure of austenite [107-110]. Figure 2-32 illustrates the adsorption mechanism module of hydrogen embrittlement [102].

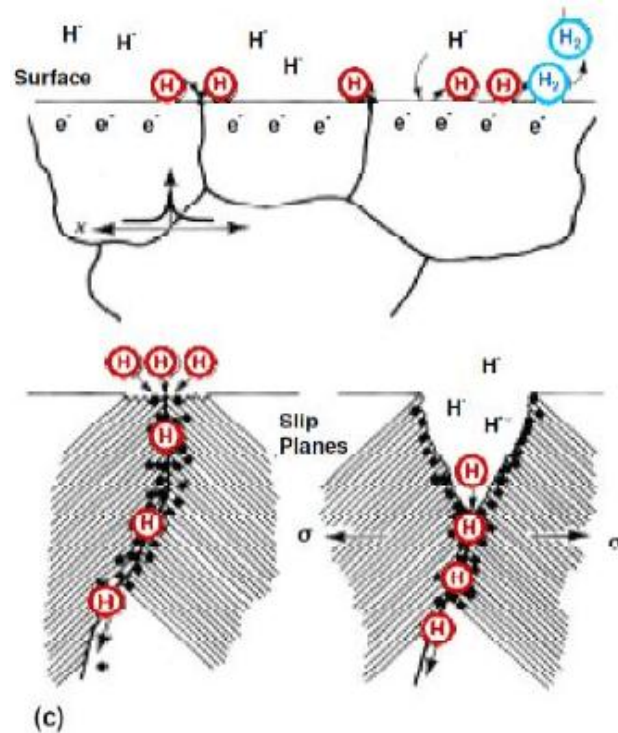


**Figure 2-32: Schematic description of hydrogen assisted stress corrosion cracking in adsorption mechanism [70, 102].**

#### 2.2.2.2.4 Stress corrosion cracking test specimens

Several types of tests are available to determine the susceptibility of alloys to SCC. To predict SCC behavior of any desired alloy for service in a specific environment, it is usually necessary to obtain that information rapidly time which needs accelerated testing by increasing the severity of the environment or the critical test parameters. Parameters that can be changed to accelerate the testing time include the application of higher stresses, continuous straining, and precracking.

Stress corrosion specimens can be categorized into two groups: smooth and precracked or notched, summarized in Tables 2-6 and 2-7 [77, 111].

<i>SCC test standards- Smooth Specimens</i>		
<b>Constant load</b>		<b>ASTM G 49-85 (2000)</b>
		<b>NACE TM 0177-05</b>
<b>Constant displacement</b>	<i>Bend specimens</i>	<b>ASTM G 39-99</b> <b>NACE TM 0177-05</b>
	<i>C-ring specimens</i>	<b>ASTM G 38-01</b> <b>NACE TM 0177-05</b>
	<i>Uniaxially strained tension specimens</i>	<b>ASTM G 49-85 (2000)</b> <b>NACE TM 0177 05</b>
<b>Constant total strain/plastic strain specimens</b>		<b>ASTM G 30-97 (2003)</b>
<b>Dynamic straining/slow strain rate test</b>		<b>ASTM G 129-00</b>
		<b>NACE TM0198-04</b>

**Table 2-6: Stress Corrosion Cracking test standards- Smooth Specimens [111].**

<i>SCC test standards-Precracked specimens</i>	
<b>Constant load</b>	<b>ASTME 1681-99</b>
	<b>British Standard BS 6980</b>
<b>Constant displacement</b>	<b>ASTME 1681-99</b>
	<b>British Standard BS 6980</b>
<b>Rising load/rising displacement</b>	<b>NACE TM 0177-05</b>
	<b>ASTM G 129-00</b>

**Table 2-7: Stress Corrosion Cracking test standards- Precracked specimens [111].**

Different types of constant extension tests are available, depending on the specific arrangement of the test conditions. The most common type used for such tests are bent beam, C-ring, U-bend, and tensile type specimens, see Figure 2-32. Tensile testing specimens with machined notches are appropriate for studying SCC and hydrogen embrittlement. The presence of a notch causes a triaxial stress at the root of the notch, which make the applied stress greater by a factor that depends on the notch geometry.

Localization of cracking to the notch region and acceleration of failure are the advantages of such test specimens [111].

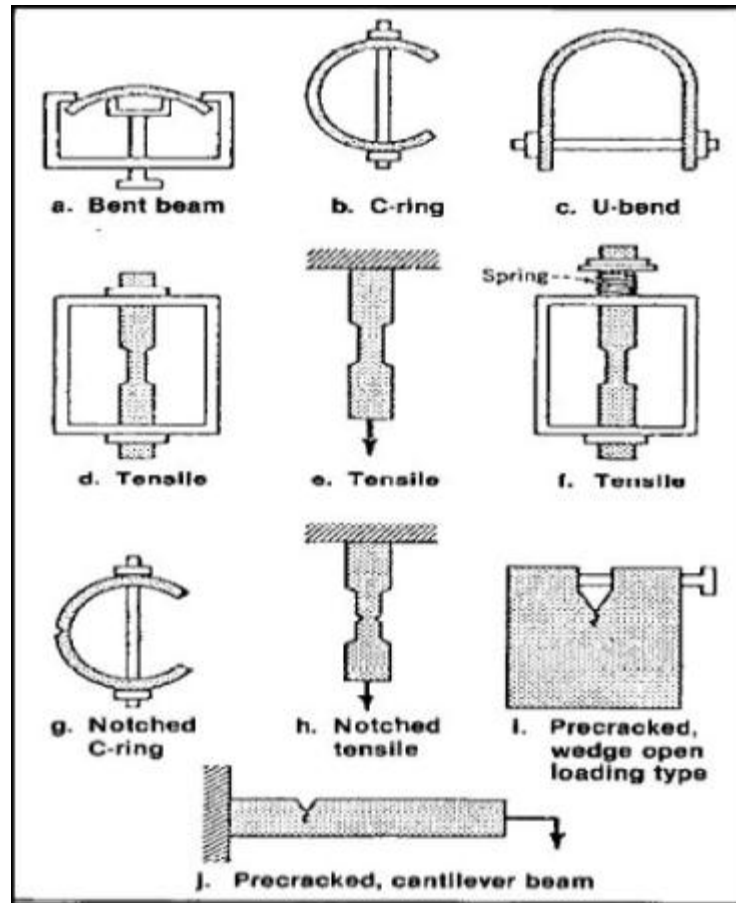


Figure 2-33: Specimens used for stress corrosion cracking tests [44].

### 2.2.3 Summary

The concept of corrosion in stainless steels (more concentration in duplex) has been introduced, then pitting corrosion and SCC failure have been briefly presented, together with a summary of the most widely accepted mechanisms for crack initiation and propagation in chloride environments since chloride has been used for all the corrosion experiments in this PhD thesis. The effects of environment and duplex microstructure on SCC phenomenon as well as fracture mechanics analysis were also described.

## **2.3 Digital Image Correlation**

The microstructure of a material plays a very important role in its strain development particularly in materials which display anisotropic deformation such as DSS, as discussed earlier in this chapter.

In this section, the fundamentals of DIC are discussed as this technique has been employed in this thesis for direct evaluation of crack development of SCC and in-situ observation of strain localisation in the super DSS, Zeron 100.

### **2.3.1 Basic Concepts of Digital Image Correlation**

DIC is an optical numerical technique (non-contact method) that obtains images of an object's surface in digital form and then performs image analysis to get a full field profile, deformation and motion measurements. When a sample is exposed to a light, depending on the surface condition, light with differing intensities will be reflected from its surface. These distributed intensities can be seen as a set of grey levels by a suitable camera to obtain a digitised image.

The DIC technique compares and correlates pixel patterns and distributions from two different images and tries to match them, using the pixel intensities as a guide. It uses a grid of individual subsets of pixels (Figure 2-33) to compare the digital images of the test specimen at different states of deformation [112]. The technique makes the simplifying assumption that there is a one-to-one correspondence between the images recorded by the camera during the deformation of the surface of the object. Thus displacement (and velocity of change) of any point on the surface can be obtained by accurate mapping of the deformed image onto the undeformed image [113]. A cross-correlation algorithm is used to compare subsets of the deformed image to the undeformed image, and to maximize a given comparison function (Figure. 2-34). The displacement result is an average of the displacements of all the pixels in each subset. These displacements can then be transformed into strain measurements by differentiation [114-116].

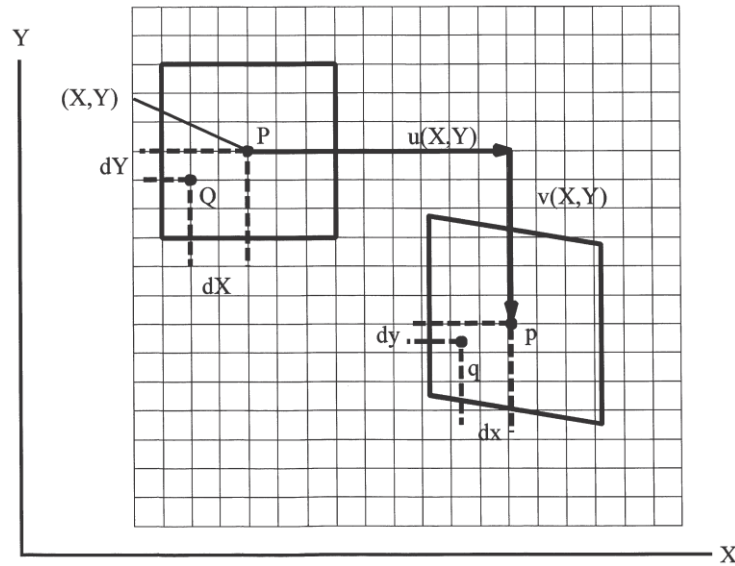


Figure 2-34: Subsets before and after deformation in x-y plane [113].

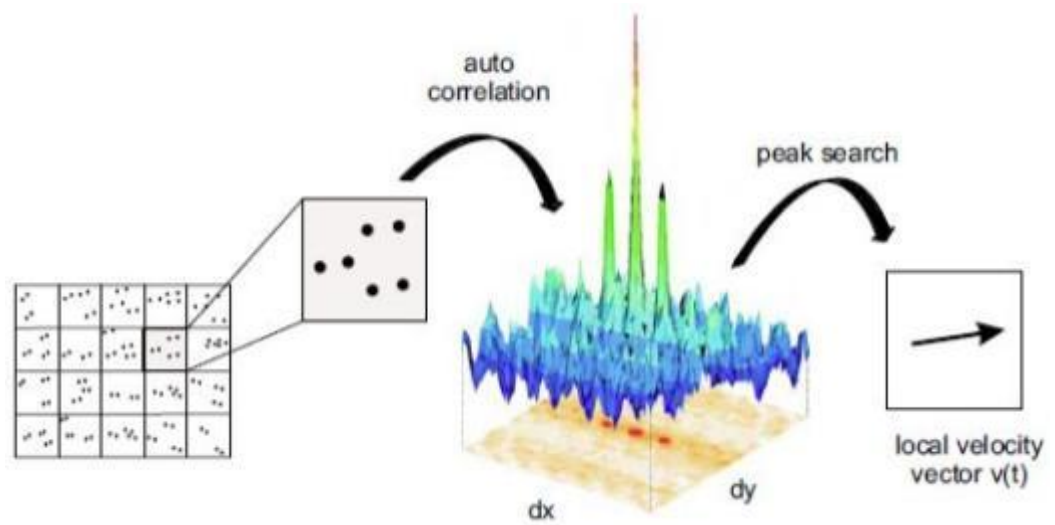


Figure 2-35: Evaluation of recorded patterns image subset using auto correlation [116].

By performing the cross-correlation between recorded subsets of the two images it is possible to quantify displacements of a given region relative to a unique reference [112] which can be derived mathematically by using the correlation relationship between the deformed and undeformed images. If the intensity division of the deformed image that has undergone a passive displacement is given by  $(g)$ , and the intensity division of the

undeformed image is given by  $(f)$ , then  $(g)$  and  $(f)$  are related by the following equation [117].

$$g(\mathbf{x} + \mathbf{u}) = f(\mathbf{x}) + b(\mathbf{x}) \quad (\text{eq.2-10})$$

Where  $b(\mathbf{x})$  is the noise incurred as part of the image acquisition during the test [118], and  $u(\mathbf{u}, \mathbf{v})$  is a displacement field vector which is the most indistinct term of Equation 2-10, because  $f$  and  $g$  functions can be obtained from the images before and after deformation while the determination of displacement field vector needs further assumptions to determine the term  $u$  with a reasonable accuracy [117].

It is important for each corresponding subset contains a sufficient number of distributed features (minimum from 2 to 4 pixels) [119] as to obtain the required accuracy, as shown schematically in Figure 2-35(a) [120]. These features can be added onto the surface of the sample as patterns or can be microstructural features created by a chemical etchant. The images of the surface obtained at two different stages of deformation are divided into interrogation windows (subsets), and then a fast Fourier transform (FFT) performed to evaluate the field displacement of the features inside that interrogation window, Figure 2-35 [120].

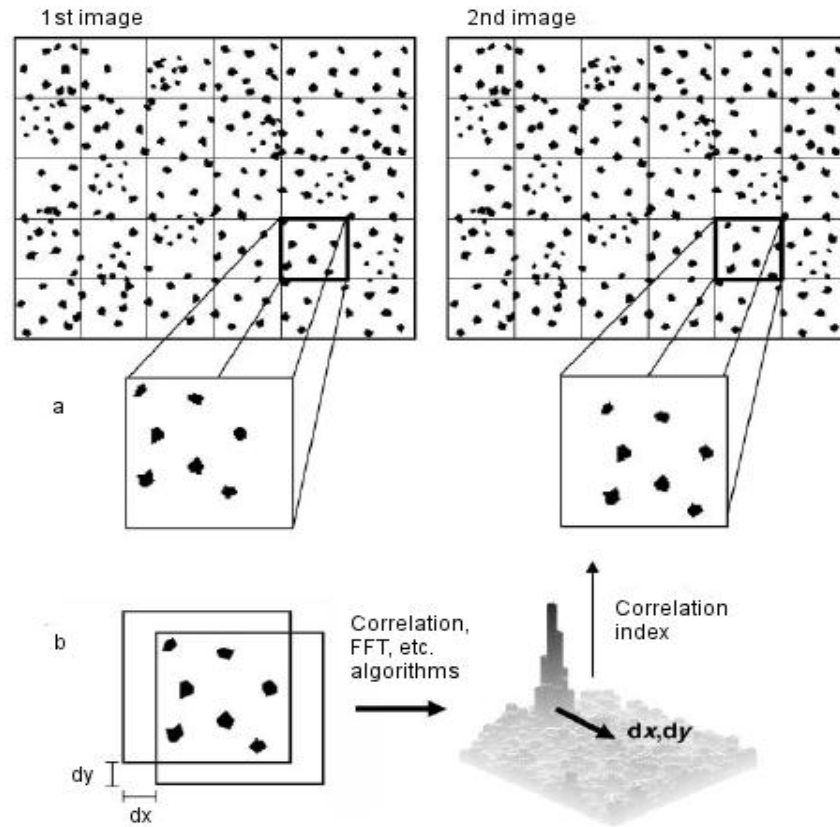


**Figure 2-36: DIC Basics: (a) two images obtained at different strains are divided into subsets. (b) Corresponding pairs of subsets are compared using correlation or FFT algorithms. The displacement vector joins the centre of the subset and the point of highest correlation [120].**

The evaluations of the offset between the interrogation windows of the deformed and undeformed images could be carried out by using various algorithmic methods such as least-squares [121, 122], Bayesian probability methods [123-125] and Fourier transform techniques [126]. The latter is the algorithm used in this study. The FFT transforms the images into a frequency domain which can then be recovered using computational methods [113, 126] to determine the displacements which can then be used to produce the strain maps of the observed surfaces. The FFT has been found to be fast and accurate for even a large number of pixels and interrogation windows [113].

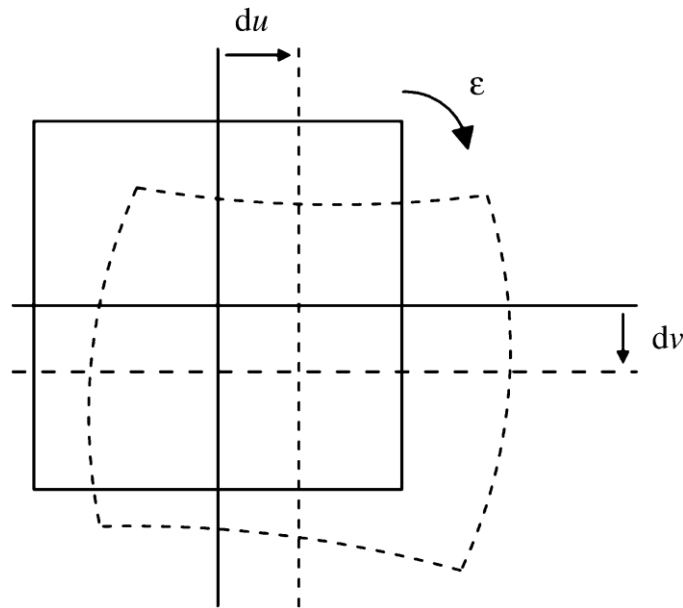


**Figure 2-37: Schematic Figure of field deformation showing subsets with rotation and deformation due to straining [120].**

The displacements of the subsets in x-y plane could also contain some rotation, Figure 2-36, which could lead to significant errors and that could be minimized by stabilising the observed surface and using rotation correction function through the batching process of the images [116, 120].

In order to accurately measure surface displacement and then consistently map strain data in sub-pixel resolution, the initial obtained images undergo a process called ‘interpolation’ prior to the DIC analysis. This process does not modify the data obtained from the digital image; however it extends the image to give sub-pixel resolution by mounting the effective number of pixels in their subsets. For example, Figure 2-37 shows a typical intensity pattern for a 10x10 pixel subset, where white and black stand for high and low intensity respectively. Figure 2-38 shows three levels of interpolation that could be applied to the raw image for the subset shown in Figure 2-37 [113].

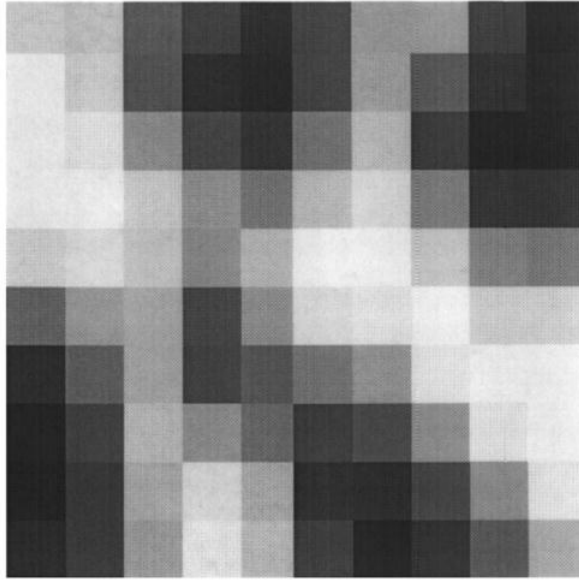


**Figure 2-38: Typical 10x10 pixel subset shows intensity pattern values [113]**

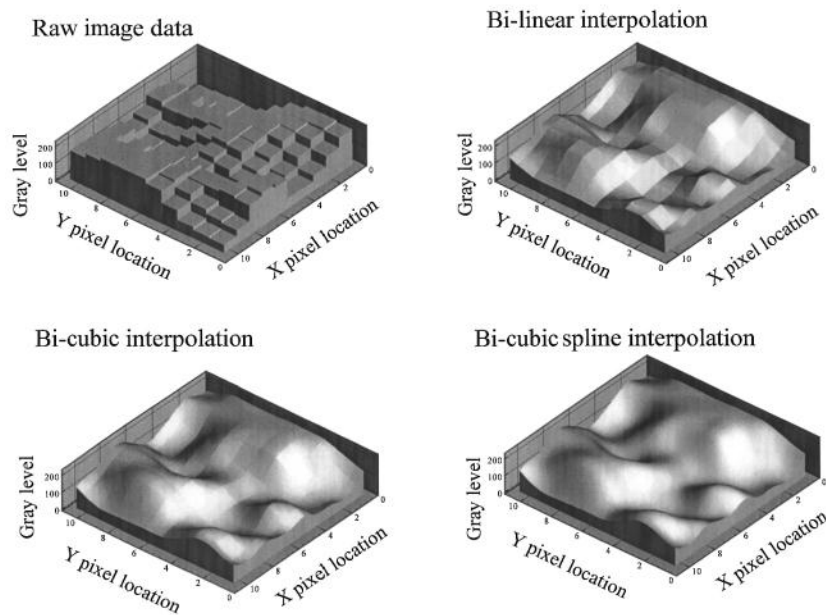


**Figure 2-39: Three interpolation levels for the same raw image to represent the intensity values of the 10x10 pixel subset shown in Figure 2-37 [113].**

It is also important to understand that the accuracy of the displacement vectors measurements depend on the size of the interrogation window, the larger the window the more accurate the results but the spatial resolution of the displacement vector map would decrease [127]. In dividing the images into interrogation windows, it has been assumed

that the displacements of all features in a single subset are the same. On the other hand, each subset must be large enough to include a sufficient number of distributed features to allow the system to recognize that subset in the following images. The accuracy of correlation process then is a balance between maximising the number of features in each subset and maximising the number of windows[120].

DIC analysis resulted in a displacement map which was used to obtain the observational strain map according to the traditional mechanical engineering definition of strain as a derivative of displacements (eq.2-11) [120].

$$\varepsilon_{xx} = \frac{du}{dx} \quad , \quad \varepsilon_{yy} = \frac{dv}{dy} \quad , \quad \varepsilon_{xy} = \frac{du}{dy} \quad , \quad \varepsilon_{yx} = \frac{dv}{dx} \quad \text{(eq.2-11)}$$

From the given (u, v) displacement vector, dx and dy, are the in-plane displacement magnitudes in x and y directions respectively.

### 2.3.2 Digital Image Correlation Requirements

To obtain the best results from the DIC technique two main requirements must be met. First, the surface of the object (specimen) must have patterns (features) that alter the intensities of the light reflected from its surface. These patterns may be added to the object or may be natural. Secondly, the digital images have to be captured under stable conditions to avoid any unwanted external movement or distortion due to straining which may result in errors in the actual surface displacements.

There are several ways to achieve usable random patterns (speckles or features) on the observed surface. The speckles could be applied as a light spray of black or white paint, Figure 2-39, or as a light coating of Xerox toner powder on the surface [113, 128-130]. The technique could be refined through successive trial applications. Previous researchers have used ultra-thin gold films (thicknesses <20 nm) vapour assisted to have discontinuous island structures [131, 132]. The most important aspect of such methods is the adherence to the surface of these added features especially in high strain regions around cracks or stress concentrators [133]. An additional method of producing features on the surface could be by ion milling using focused ion beams to introduce the micro-markers shown in Figure 2-40 [134-137]. In addition, some researchers used conventional electron beam lithography to deposit grid points on the specimen surface that could be used in micro scale strain

distribution [67, 138]. Metallographic etching is another approach of adding features on the surface which allows a direct observation of the surface in contrast with the methods mentioned above[120].

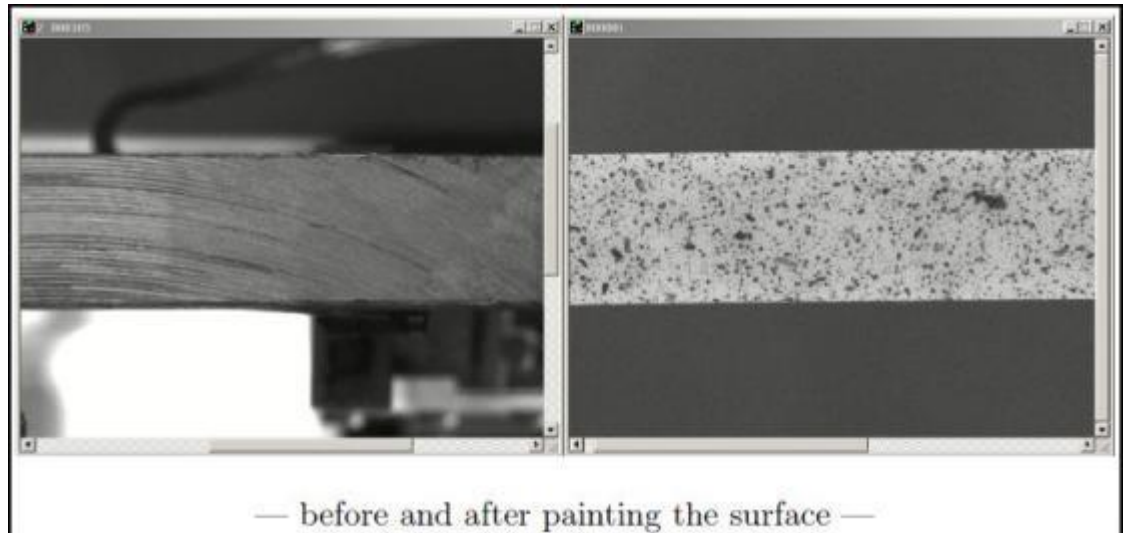


**Figure 2-40: Images of the same observed surface before and after painting [116].**

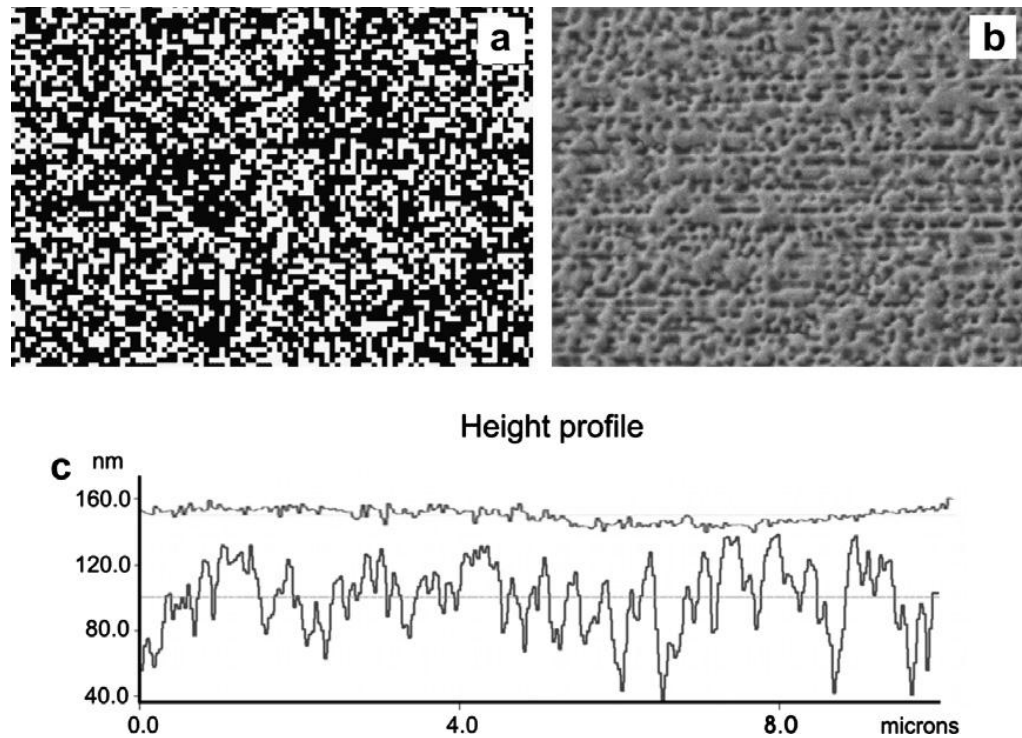


**Figure 2-41: Patterns obtained using the focused ion beam technique of a smooth surface (a) Random patterns bitmap, (b) Scanning Electron Microscope photograph of the surface and (c) Atomic Force Microscopy line profiles of the surface before and after patterns creation [137].**

### 2.3.3 Applications of Digital Image Correlation

DIC is used in a number of applications to quantify displacement and strain distributions in the field of experimental mechanics. Strain field measurements by DIC offer possibilities for analysing the mechanical behaviour of materials in situ during tests to follow specifically the progress of surface strain fields and damage micro-mechanisms on the micro-structural scale, to better understand and obtain quantitative values of the surface damage in a two-phased alloy [139]. DIC also gives the opportunity to observe the initiation of micro-cracks in real time [112, 127, 139]. Forquin et al., [140] used DIC to analyze displacement fields of cracked samples. It allows for an accurate estimation and monitoring of the crack tip location with a sub-pixel correlation algorithm.

#### 2.3.3.1 Measurement of Crack Opening Displacement and crack developments

Several studies have shown that the crack opening displacement (COD) measurement is a practical parameter for predicting the crack initiation and development under static or altered loading conditions [141-146]. Lots of methods have been developed for measuring

COD [113, 147-149] such as strain gauges and clip gauges applied to locations near the crack, including back-face and side-face positions. However, these methods present data at fixed locations on the specimen or far from the crack's location, which means that the acquired data cannot present the optimum data for crack measurements.

Using the full-field strain mapping DIC will provide more accurate measurements and is a technique which has been used successfully to evaluate surface displacements, strain development and estimations of stress intensity factors in fracture mechanics applications [150-153]. For example, it was used effectively in fatigue pre-cracked specimens to test the crack development relative to the rolling direction in 2024-T3 aluminium sheet material [113, 144].

### **2.3.3.2 Applications of Digital Image Correlation for SCC Study**

Most research using DIC techniques were applied in air. Recently DIC has been successfully extended to study the occurrence of stress corrosion cracking and microstructural effects on the crack nucleation and propagation [127, 154-157]. Such studies should be done in-situ through a corrosive environment and this increases the complications in resolving the required surface displacement caused by crack opening because those results are on a scale of micrometers.

The COD would be investigated by using interrogation windows across the surface of a sample and by differentiation of the measurements identify the crack as a region of strain gradient [145, 155]. This is shown in Figure 2-41 which also contains the surface displacement measurements at three intervals for austenitic stainless steel type AISI 304 containing an intergranular SCC [156]. These DIC measurements allowed the researchers to show the crack opening displacement and the crack length as a function of time as shown in Figure 2-42.

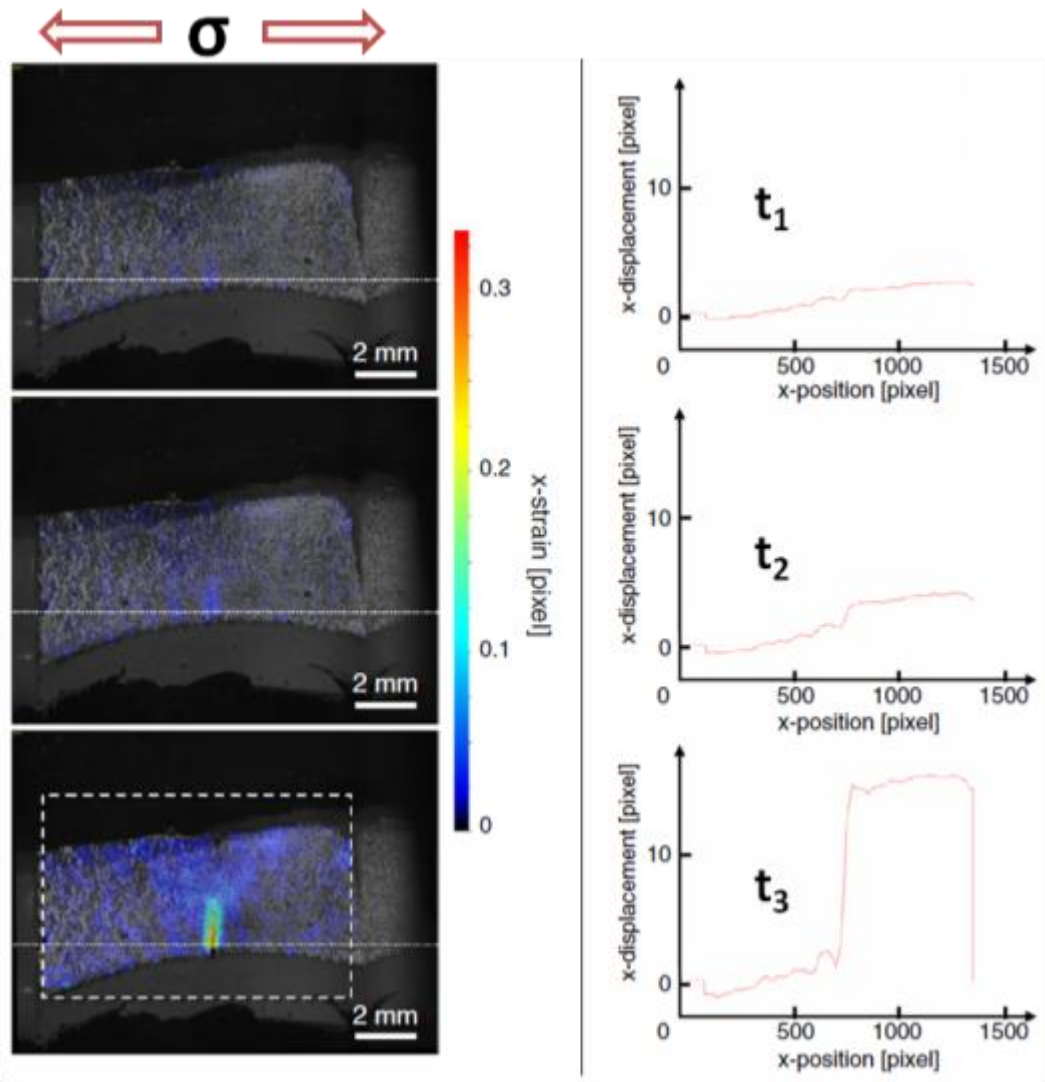
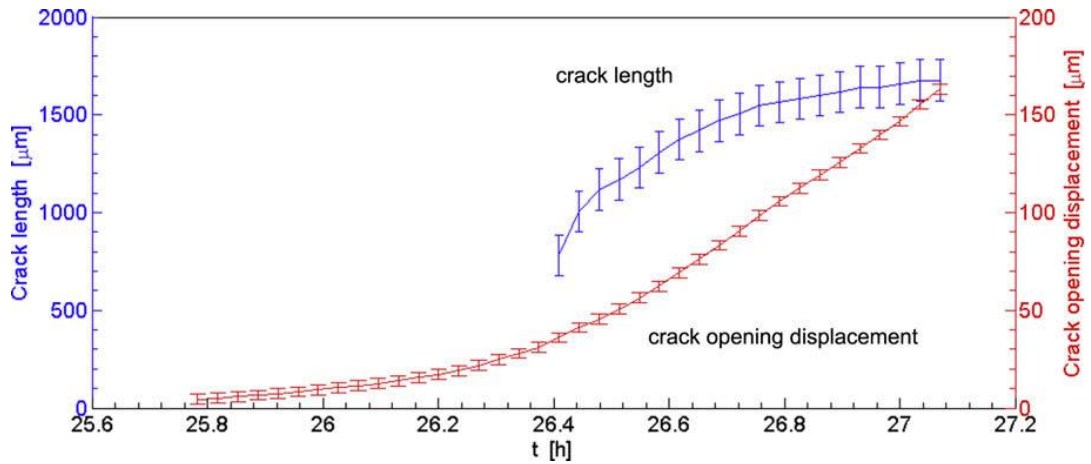
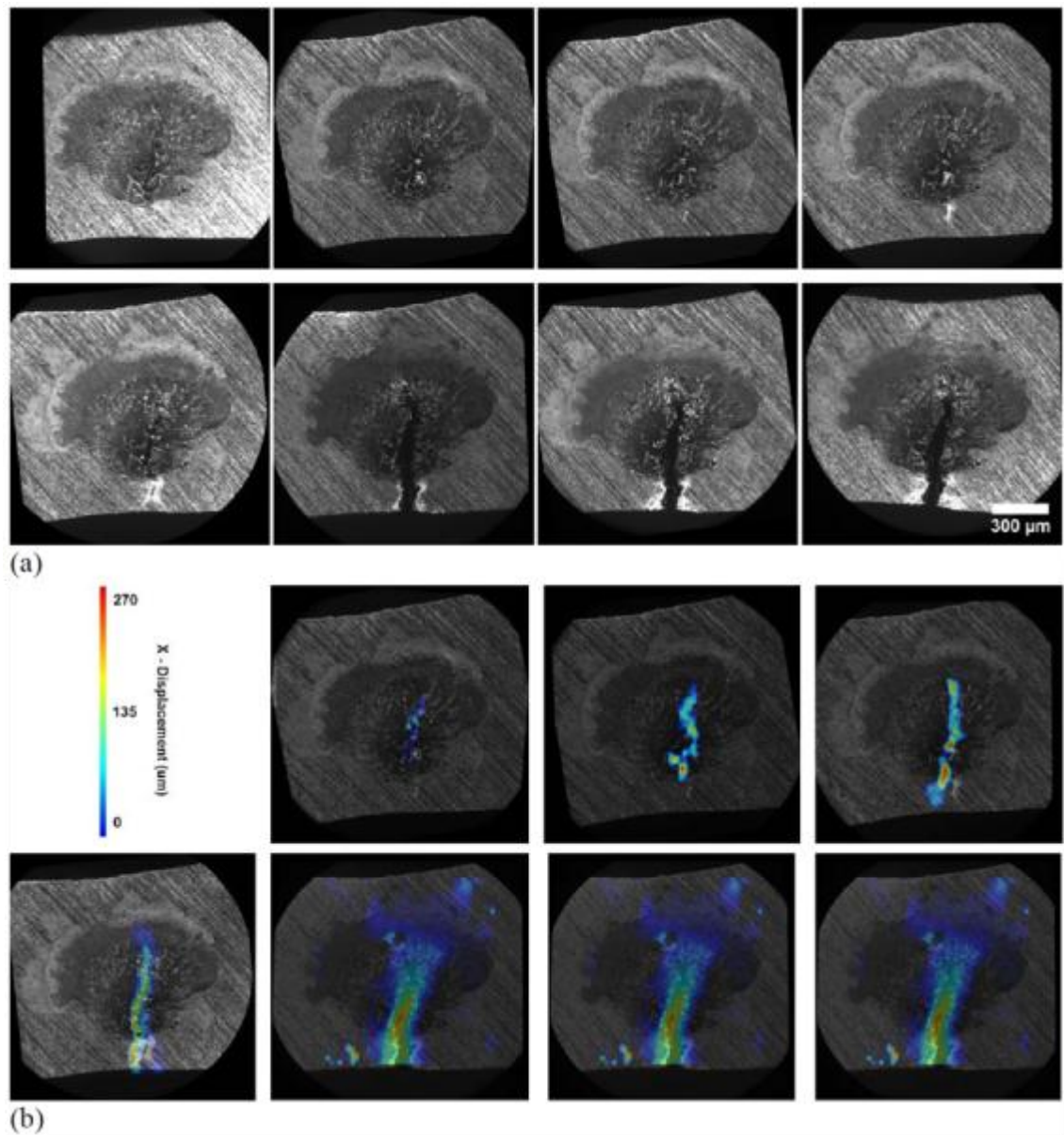


Figure 2-42: Left: Digital Image Correlation strain maps, obtained by differentiation of the displacements maps measured between selected images in three time intervals ( $t_3 > t_2 > t_1$ ). Right: Displacements profiles measured along the horizontal dashed line shown on the strain maps [156].



**Figure 2-43: Crack length and Crack Opening Displacement versus time obtained from the Digital Image Correlation Results [156].**

A. Cook et al. [157] used digital image correlation technique to observe the growth of atmospheric induced chloride stress corrosion cracking in austenitic stainless steel type 304L loaded to  $1.2\sigma_y$  under controlled conditions of temperature ( $40^\circ\text{C}$ ), relative humidity (30%) and deposition of magnesium chloride droplets, Figure 2-43 . This study confirmed the capability of the DIC technique of detecting changes in crack dimensions that are difficult to be identified via conventional optical microscopy, i.e. crack growth beneath salt layers and measurement of crack opening displacements, Figure 2-44.



**Figure 2-44: DIC analysis: (a) Optical images at 1500 hours, 1668 hours, 1836 hours, 2004 hours, 2388 hours, 2676 hours, 3036 hours and 3232 hours (left to right). (b) Strain maps relative to first image at 1668 hours, 1836 hours, 2004 hours, 2388 hours, 2676 hours, 3036 hours and 3232 hours (left to right)[157].**

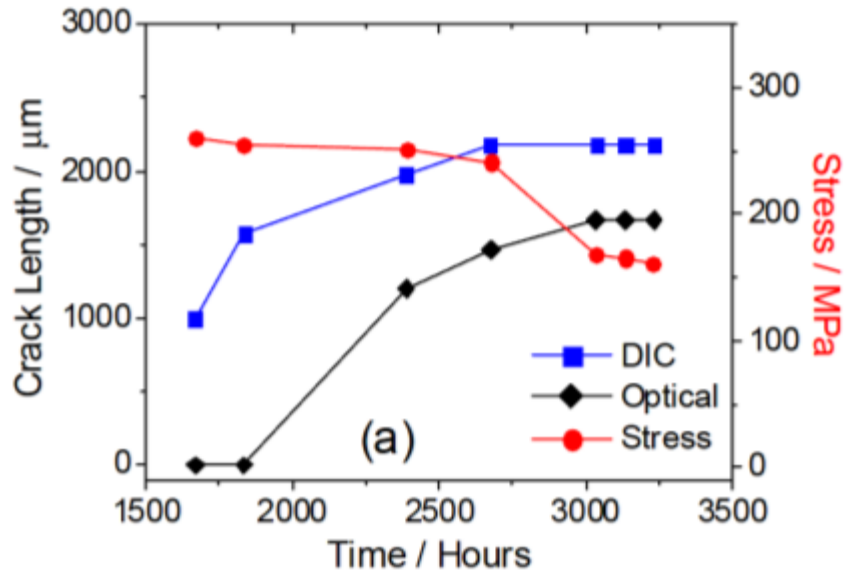


**Figure 2-45: Evaluation of crack length as measured by DIC analysis, optical microscope and calculated nominal stress on sample A shown in Figure 2-43.**

**Uncertainty in DIC crack length is 30 µm [157].**

Such research at the microstructure level needs more trials on the applications of surface features. Duff et al., tried three different procedures including scratching by classic abrasive paper, thermal etching and chemical electroetching on a type 304 H stainless steel specimen as shown in Figure 2-45 [127]. Those three different surface finishes were evaluated for DIC accuracy measurements by moving the sample a distance < 20µm then obtaining the strain maps using the DIC (applied strain was zero) with interrogation window size of 16x16. The results showed the electro-etching method gave the best accuracy of the three methods when applied to the in-situ intergranular stress corrosion test, see Table 2-8 [127].

Surface Finish	Mean Strain	Standard Deviation
Scratches	0.22%	12.68%
Thermal Etching	0.047%	0.64%
Electroetching	0.041%	0.48%

**Table 2-8: DIC’s calculated strain for all tested surface finishes [127].**

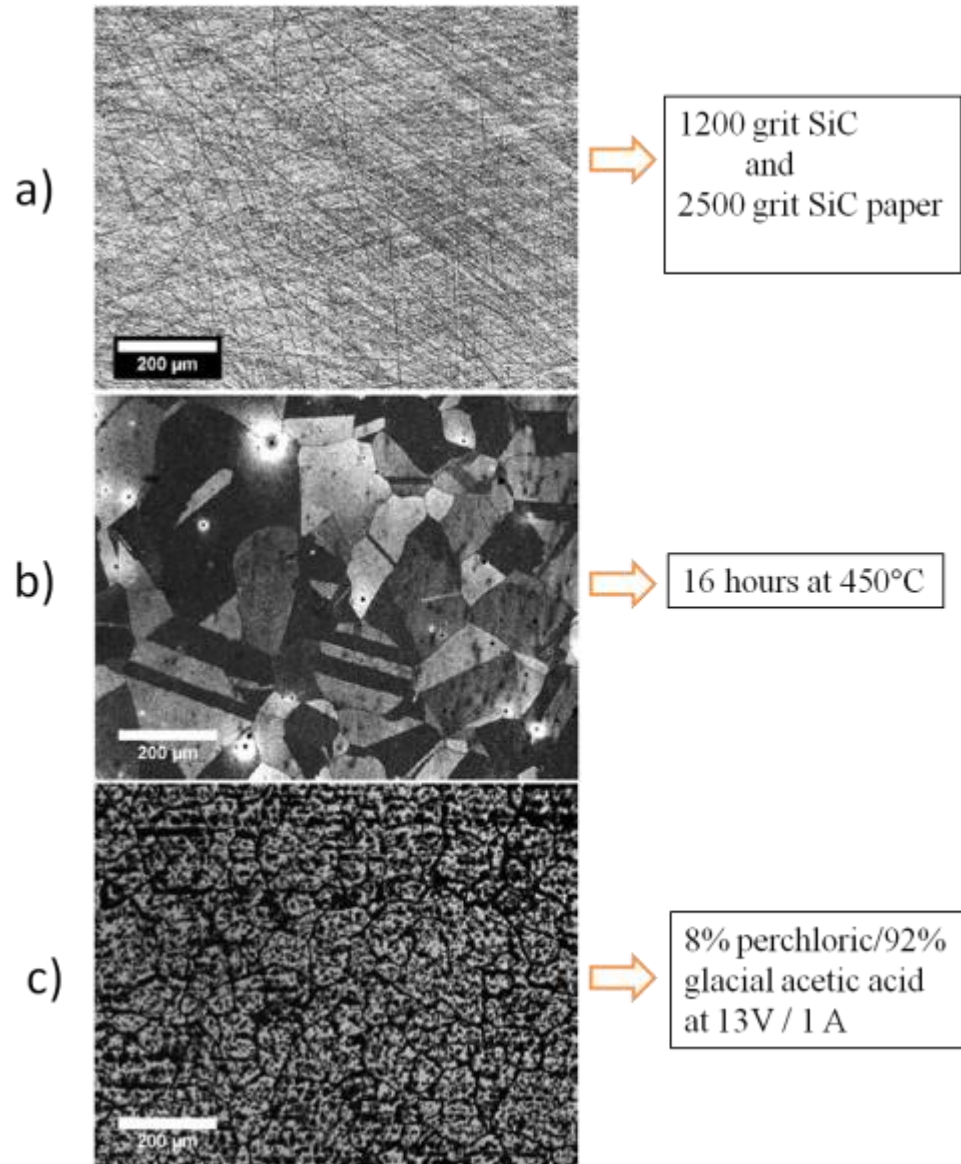


**Figure 2-46: Surface finishes prepared a) Scratching by abrasive paper, b) Thermal etching and c) Chemical/electroetching [127].**

Using the above procedures make it possible to make an in-situ investigations of crack initiation sites, incubation period for crack opening and also surface crack propagation rate. DIC analysis should give the opportunity to measure the surface crack growth rate ( $dc/dt$ ) approximately from the digital images obtained by using the surface crack  $c$  and the time  $t$  at which the image was recorded for the  $(n+1)$  and  $(n-1)$  images as shown in Equation 2-12 and Figure 2-46 [127].

$$\frac{dc_n}{dt} = \frac{c_{(n+1)} - c_{(n-1)}}{t_{(n+1)} - t_{(n-1)}} \quad (\text{eq. 2-12})$$

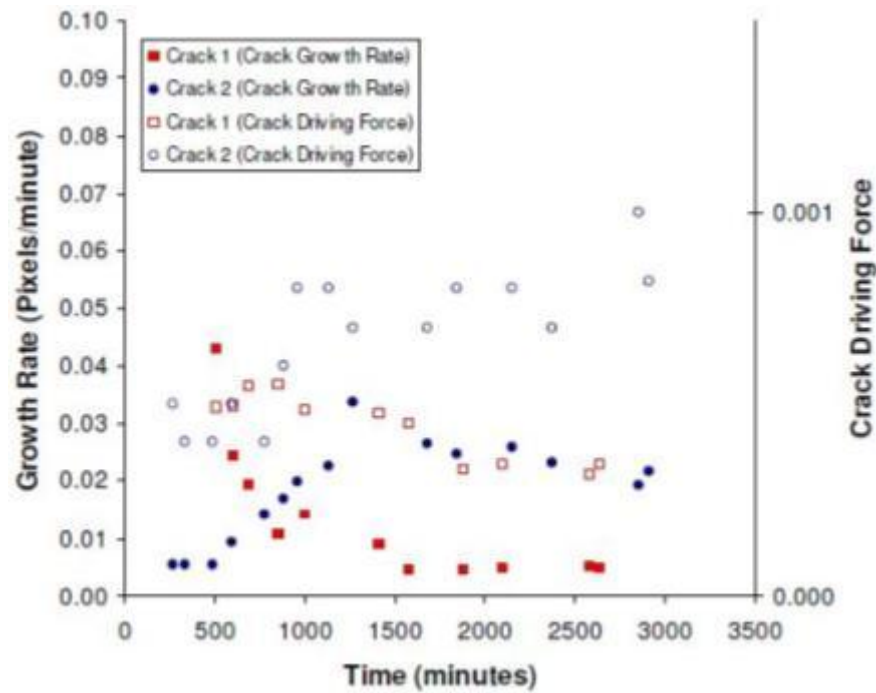


**Figure 2-47: Crack growth rate ( $dc/dt$ ) and crack driving force as functions of time for two intergranular steel corrosion cracks initiated in sensitised 304 stainless steel [127].**

### 2.3.4 Digital Volume Correlation (DVC)

Digital volume correlation (DVC) is a new technique for 3D strain map and deformation measurements across entire material volumes [152, 158]. It is an extension of the two-dimensional digital image correlation (DIC) which is restricted to surface measurements. It computes displacements in a 3D volume and quantifies strains throughout the interior of a specimen. DVC needs volume images contain random patterns; local changes in contrast due to the changes in local density or voids. The technique uses a sequence of sequential 3D images data that represent the development of the object displacements and deformations. In this sequence, DVC observes the movement of each sub-volume templates by using the correlation technique to calculate the deformation and strain between volume images of the specimen in the unloaded reference state, and the volume image of the specimen in the loaded as shown in Figure 2-48.

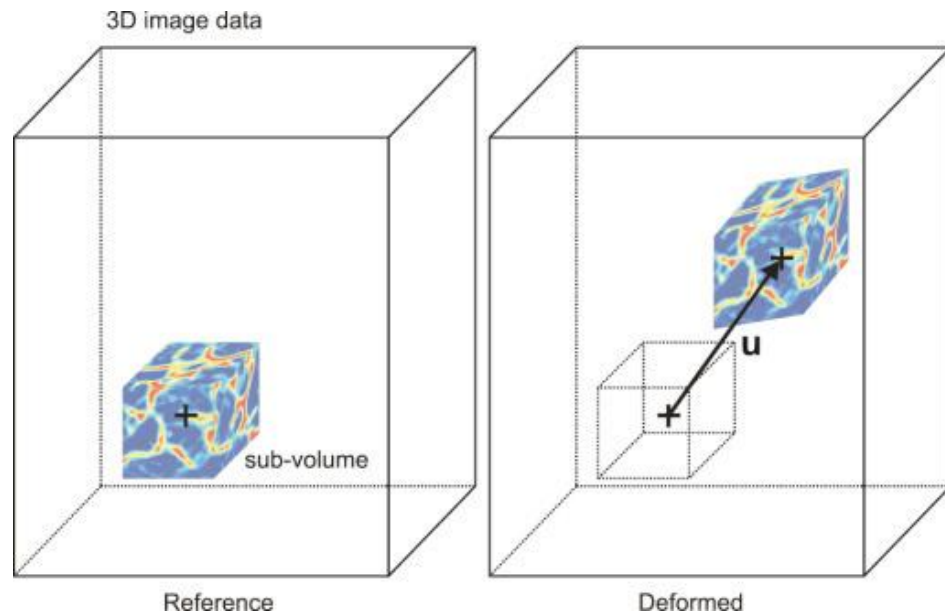


**Figure 2-48: Principle of Digital Volumetric Correlation – evaluation of sub-volume template displacement vector between reference image data and deformed image data [158].**

DVC successfully used to do a micromechanical study on the fracture of nuclear graphite and observe crack propagation mechanisms during gradually specimen loading and volumetric strain measurements [159]. It provides better discrimination of the crack dimensions, and allows measurement of the crack opening displacements. Volume images can be imported from a variety of sources such as X-Ray Computer Tomography and Confocal Microscopy [159, 160].

### 2.3.5 Summary

The basics of digital image correlation (DIC) and its related techniques and applications are described. These are included the detection of crack initiation, crack propagation and measuring the crack development by using the strain maps obtained from recorded surface displacements as a result of crack opening. This two dimension technique could be utilized with other techniques (e.g. SEM and EBSD) to provide better vision and understanding of stress corrosion cracking behaviour in duplex stainless steel. Also, the digital volume correlation (DVC) was introduced briefly at the end of this section.

### 3 EXPERIMENTAL TECHNIQUES AND METHODS

In this chapter, the experimental work details and the different techniques and equipment used in experiments are introduced.

#### 3.1 Materials and Specimen Preparation

The materials used in this study were commercial super duplex stainless steel Zeron 100, supplied by Weir Materials Ltd with chemical compositions as shown in table 3-1. All materials were solution annealed at 1100 °C for 1 hour and water quenched to produce a microstructure of approximately 50% austenite and to homogenize the structures.

Element	Cr	Ni	Mo	N	C	Si	Mn	P	W	Cu	$\gamma$ %
3mm Plate	25.40	7.00	3.7	0.23	0.02	0.40	0.66	0.026	0.62	0.63	50
33mm Plate (Forged)	25.30	7.08	3.72	0.23	0.021	0.28	0.66	0.016	0.62	0.57	40

**Table 3-1: Chemical compositions of materials used (wt %), Fe. BAL., Supplier's certificates.**

The tensile samples used in this research were machined in longitudinal and long transverse directions with respect to loading and rolling directions as shown in Figure 3-1.

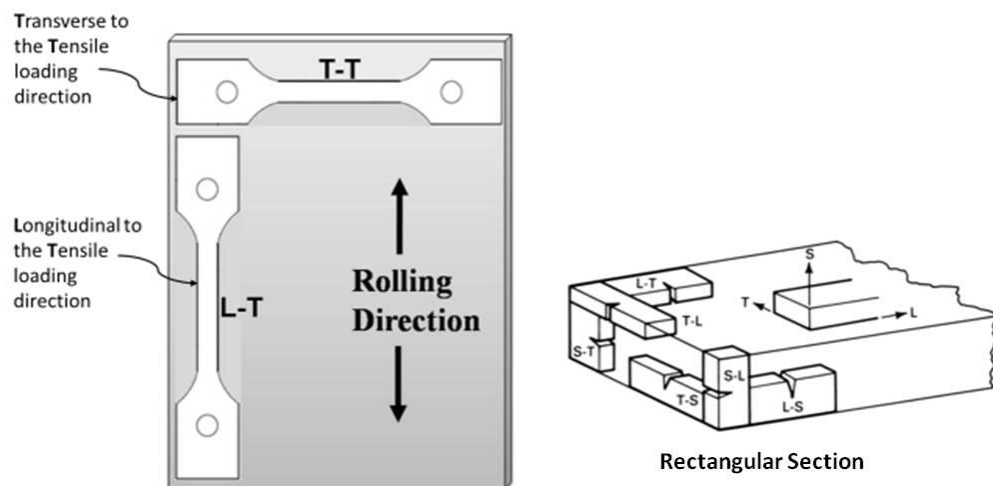


**Figure 3-1: Orientations of specimens taken from the plate, specimen orientation (first letter) to the loading direction identification (second letter). L and T are longitudinal and transverse principal direction of metal working (rolling) respectively [105].**

### 3.2 Metallographic Specimen Preparation

The microstructures of the as-received specimens were characterized using optical microscopy (Olympus BH2-UMA). Standard metallographic preparation techniques were used to reveal the microstructures of materials. The specimens were mounted in Bakelite-type compression mounting resin then mechanically ground by using SiC papers, i.e., 240, 400, 600, 800 and 1200 grit, with water as lubricant. Then, the specimens were fine polished with 6, 1 and 1/4 $\mu\text{m}$  diamond pastes (Buehler) using oil as lubricant. Finally, they polished with a colloidal silica suspension for at least 30 minutes to get a mirror-like surface (free of scratches).

The polished samples were then etched by using electrochemical etching in a solution of 20% KOH at 10.0V for 20 s at room temperature and then observed by using optical microscopes.

### 3.3 Electrochemical Measurements

The electrochemical measurements were performed to study the pitting susceptibility of Zeron 100 SDSS. These tests were carried out by using either a Gill AC three electrode potentiostat from ACM Instruments or an EG&G potentiostat, depending on availability (Figure 3-2).



**Figure 3-2: Potentiostats from ACM Instruments and EG&G.**

The potentiodynamic polarisation curves were determined from the cathodic potential towards the anodic direction at a potential scan rate of 10 mV/min, mostly from -500 mV toward the anodic direction until +800 mV. All potentials were measured versus a saturated calomel electrode (SCE) and the counter electrode was platinum. The specimens,

acting as a working electrode, were connected to copper wire at the rear surface of the specimen by spot welding then mounted in epoxy resin with an exposure area of  $1\text{cm}^2$  as shown in Figure 3-3 and Figure 3-34 [105, 161].

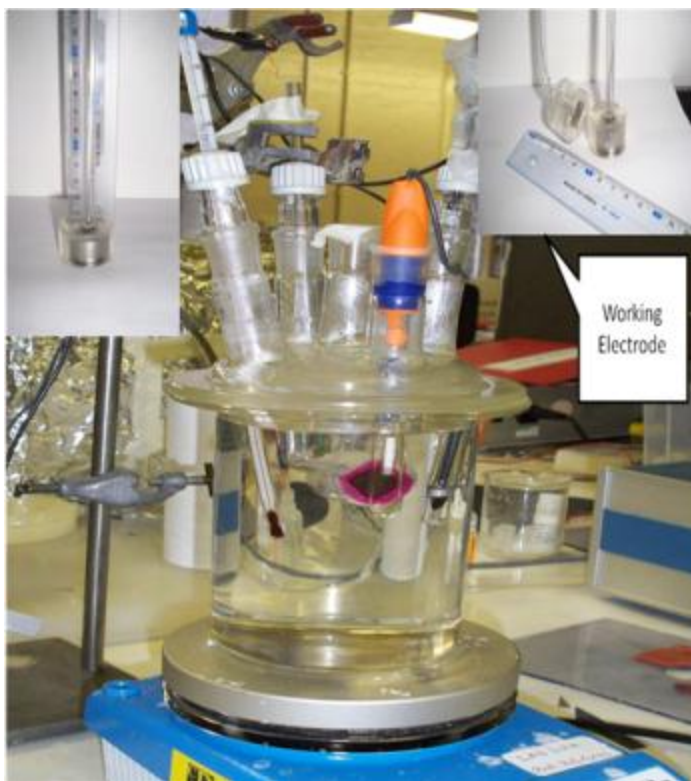


**Figure 3-3: General view of the experiment setup.**

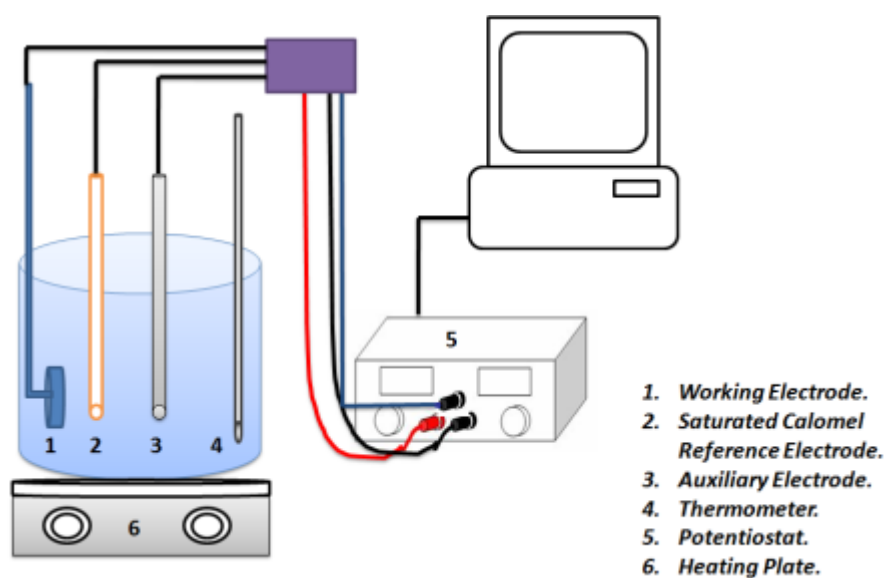


**Figure 3-4: A schematic diagram shows the main setup of the cell.**

Prior to each experiment, the specimens were abraded by silicon carbide papers down to 4000 grit, washed with deionised water and dried in warm air. Each test was repeated at least two times to assure its repeatability. Potentiodynamic cyclic polarisation curve determination was conducted using the Zeron 100 samples in NaCl solutions at room temperature with concentrations of 0.5, 1.5 and 3.5 wt% to test the effects of the chloride concentration. Potentiodynamic half cycle polarisation tests were done as well for samples in 5M NaCl solution (close to the highest limit of NaCl solubility in water at room temperature) and at various temperatures of 55°, 70° and 80°C. Also, potentiodynamic half cycle polarisation test was done for the mini flat tensile sample in 5M NaCl solution and at temperature of 70°. The specimens were allowed to stabilize at open circuit potential for 15 min at room temperature before each test. The edges of the samples were coated by lacquer to reduce the exposed area and to avoid the crevice corrosion creation at the edges of the working electrode (the specimen). After the electrochemical tests the samples were cleaned with deionised water and then analysed by the optical microscopy (OM).

### **3.4 Electropolishing**

Electropolishing is a method by which material is removed from the surface of the metallic work piece by an electric current while the work piece is submerged in an electrolyte. It can be used to remove residual stresses from surface preparation and give a mirror finish to the surface of the work piece which will improve the electron backscattered diffraction analysis for the desired surface. Figure 3-5 is a schematic illustration of the electropolishing cell. The work piece was connected to the positive (anodic) terminal, while the negative (cathodic) terminal was connected to a piece of AISI 304 or AISI 316 sheet. Both positive and negative terminals are submerged in a solution of 8% perchloric acid ( $\text{HClO}_4$ ) and 92% acetic acid ( $\text{CH}_3\text{COOH}$ ) at room temperature under a voltage tension of 45 V for 50-60s (time).

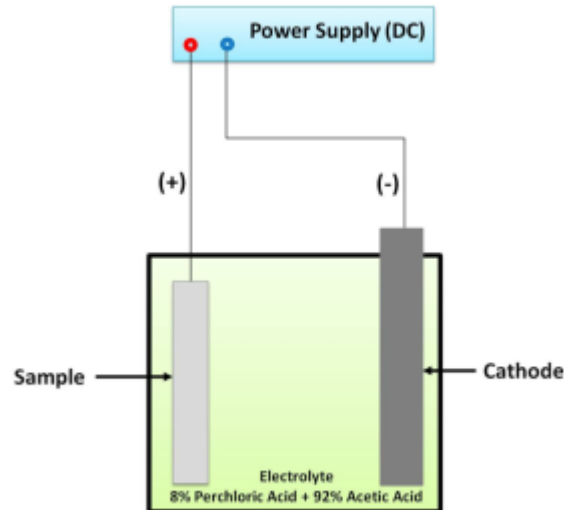


Figure 3-5: Schematic image of the electro-polishing cell.

### 3.5 U-Bend test

The U-bend specimen is a rectangular machined strip, taken from the 3-mm plate as shown in Figure 3-6. It was then pressed into a U shape using jig and cylinder of approximately 38 mm diameter and was maintained in this constant strain condition during the stress corrosion test as per the standard (ASTM G30-97 [162]) for the evaluation of stress corrosion cracking. The strip's dimensions are shown in Figure 3-7.

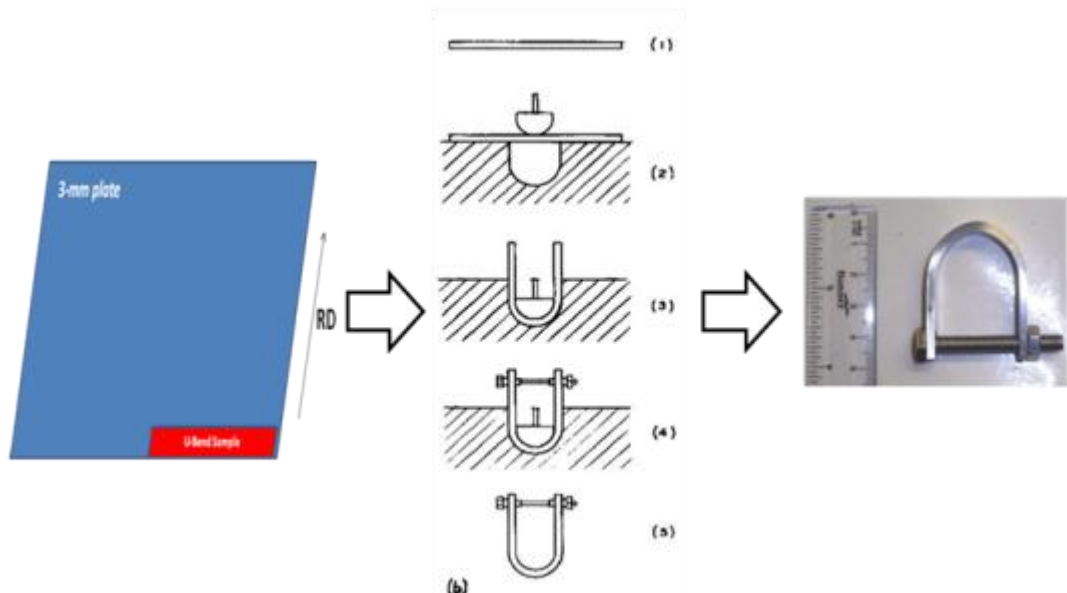
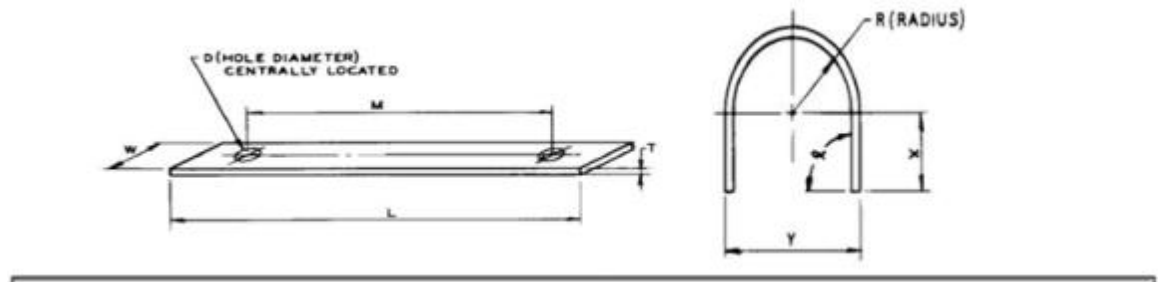


Figure 3-6: U-Bend Sample preparation [162].

L, mm	M, mm	W, mm	T, mm	D, mm	X, mm	Y, mm	R, mm	A, rad
100	90	9	30	7	25	38	16	1.57



**Figure 3-7: Typical U-Bend Specimen Dimensions [162].**

The sample was coated with a lacquer, leaving an exposed area of around to 1 cm<sup>2</sup> at its apex. It was then coated with a film of MgCl<sub>2</sub> solution with 0.52 Molar concentration dissolved in methanol because of its low viscosity and its low boiling temperature around 65°C, which was smeared onto the surface of the sample uniformly to cover the exposed area. The testing was carried out at 80°C for 1800 hour in a closed container within a water bath of 80°C temperature. The humidity and temperature in all experiments were monitored by a Rotronic's HygroClip S probe and a HygroLog D data logger. The data retrieval and displaying were done by the company's HW3 software. The relative humidity was recorded at around 42% RH. Potassium carbonate K<sub>2</sub>CO<sub>3</sub> was placed in the test container during testing to maintain the relative humidity [163].

### 3.6 Cold Rolling

Cold rolling was performed by using a two-high rolling mill with 250mm diameter rolls operating with a roll surface speed of 150 mm/s and with light paraffin lubrication. The purpose was to match the degree of work hardening that was created in the top surface of the U-bend sample in tensile samples. The degree of hardening was verified by using hardness testing (30 Kg) in different strain levels. The total strain ( $\epsilon$ ) on the outside of the bend was estimated from the applied displacement using the following equation [162]:

$$\epsilon = T/2R \quad (\text{eq.3-1})$$

Where:

$T$  = specimen thickness and  $R$  = radius of bend curvature.

The strain achieved from the reduction in thickness was estimated using the following equations:

$$\varepsilon = \ln\left(\frac{t_i}{t_f}\right) \quad (\text{eq.3-2})$$

$$t_f = (\exp(-\varepsilon) \times t_i) \quad (\text{eq.3-3})$$

### 3.7 Mechanical Testing

#### 3.7.1 Hardness Testing

Vickers macrohardness testing with a load of 30 kg used to measure the hardness at room temperature. The surface of the specimen was ground to 1200 grit prior to the test. Ten indentations were performed on each specimen to find out the average hardness of the specimen.

#### 3.7.2 Tensile Testing

The mechanical tensile tests were carried out on flat tensile samples before and after the strain hardening via cold-rolling. The tensile testing was performed at 80°C on an INSTRON 5569 mechanical testing machine at a cross-head speed of 1 mm / minute. An extensometer of 8mm gauge length attached to the specimens to calculate the elongation during the test.



**Figure 3-8: Mechanical tensile testing machine INSTRON 5569.**

### 3.8 Digital Image Correlation

Digital image correlation analysis (DIC) was employed to measure the surface displacements and hence calculate surface strains on deforming or cracking test specimens.

The digital image correlation DIC software (La Vision Davis 7.2) was used to analyse the observations of the surfaces. For this purpose, the surfaces of the samples were prepared by grinding (4000 grit) then electroetching in 50% Nitric Acid at 3V-4Min. The noise level (RMS) was calculated as a function of window size to evaluate the optimum analysis conditions. For the examination of stress corrosion specimens, a rigid stage was fabricated to place the specimen loading rig in position under the optical microscope to prevent any undue lateral movements each time the sample was taken for assessment (Figure 3-9).



**Figure: 3-9: Setup of the rig under the DIC optical microscope.**

Digital Image Correlation DIC was carried out with a 14-bit Image Pro Plus CCD digital camera, and images were recorded with resolution of 2048 by 2048 pixels. A 10x MS-Plan objective lens was used for the observations, which gives a viewed area of approximately 942  $\mu\text{m}$  by 942  $\mu\text{m}$ . A total of 20 images were recorded for each position, and the recorded images averaged to reduce the potential noise from vibration and lighting

variations. The averaged images were then analyzed with the LAVision DaVis Image Correlation Software (ver. 7.2) and surface displacement vectors obtained for each position. The optimum window size used was 64 x 64 pixels (minimum noise level), where 1 pixel is = 0.46  $\mu\text{m}$ . Differentiation of these displacement vectors gives local surface strains. In this analysis, the principle surface strains in X- ( $E_{xx}$ ), Y-direction ( $E_{yy}$ ) and ( $E_{\text{max.normal}}$ ) are reported, where the Y direction is the loading direction.

### **3.9 Constant Load Test**

The main purpose of the constant load cell is to create controlled stress conditions. Its design was derived from the spring-loaded stressing frame described in ASTM G 49-85 [70, 105]. The rig body was built from 316 austenitic stainless steel and the loading screw was fabricated from Zeron 100 SDSS (Figure 3-10).

A strong frame holds the dog-bone shaped sample which is held under a constant mechanical tension by means of spring washers compressed by a nut. It is loaded by tightening the nut manually and the value of the strain on the sample is monitored by a strain gauge attached to the back of the specimen close to the observed region. The strain gauge, with an effective length of 5 mm (Figure 3-11) and Gauge resistance 120 $\Omega$ , was attached by using epoxy resin. The strains were recorded using a NI 9237 C Series Module datalogger through *LabVIEW SignalExpress 3.0 Software* from National Instruments Corporation (U.K.) Ltd. (Figure 3-12). The strain gauges had thermal induced output of  $\pm 2\mu$  strain per  $^{\circ}\text{C}$  ( $20 \rightarrow 160^{\circ}\text{C}$ ), linear expansion factor of  $10.8 \times 10^{-6}/^{\circ}\text{C}$  (steel) and a maximum operating temperature of  $180^{\circ}\text{C}$  making them suitable for the experiment temperature of  $80^{\circ}\text{C}$ .

The dimensions of the rig were set by a certain number of requirements. The construction should be able to stress the duplex specimen of  $1 \times 5 \text{ mm}^2$  section without itself undergoing deformation. Also, the structure has to be short enough to be hold in a sealed box which will fit inside an oven. The frame should also enable the observation of the strained specimen using the digital image correlation microscope.

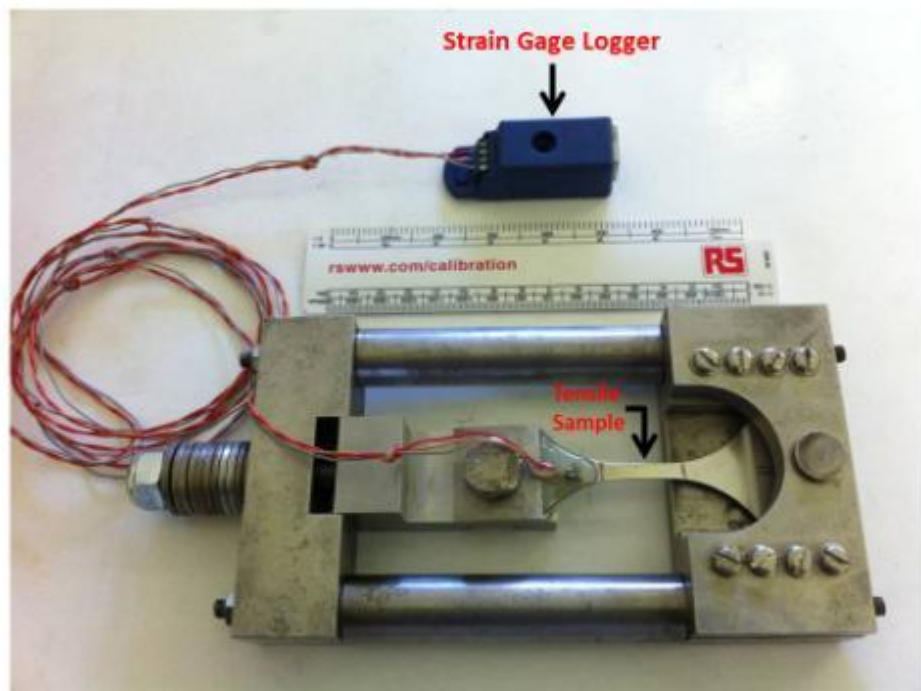
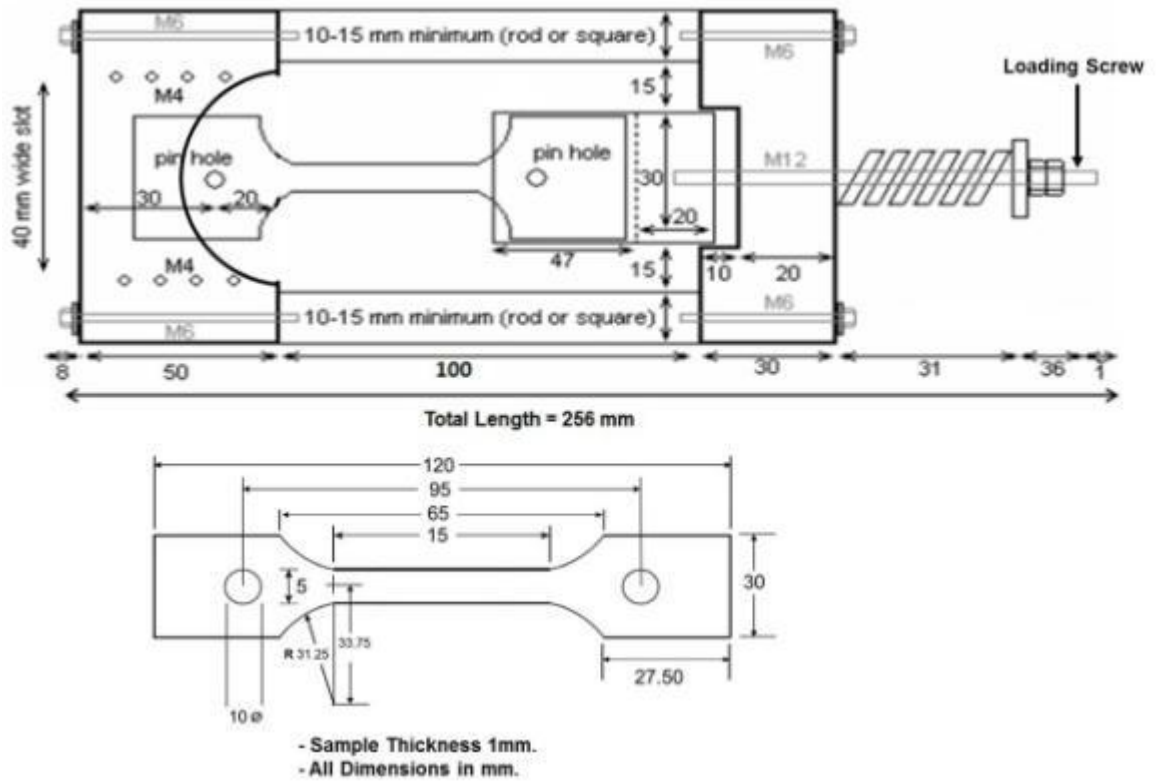
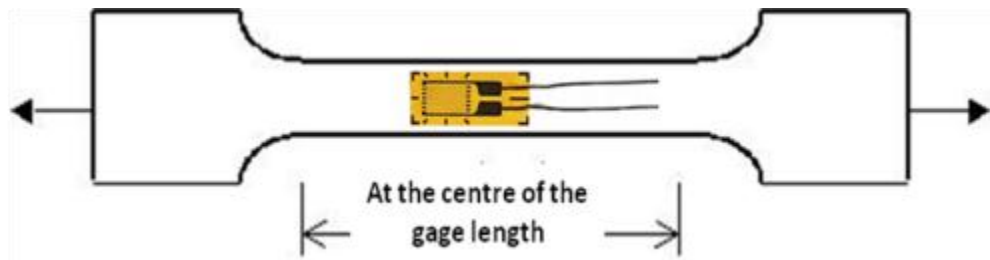


Figure 3-10: The constant load cell and the dimensions of the sample.



**Figure 3-11:** A schematic Figure shows the position of the strain gauge on the flat tensile sample.



**Figure 3-12:** NI 9237 C Series and NI CompactDAQ 8-Slot Data Logger.

### **3.10 Salt loading on the tensile sample**

A 0.52M solution of magnesium chloride dissolved in methanol was prepared to be deposited manually as “wet” or “evaporated” droplets onto the centre position of the surface of the loaded sample using a fine syringe needle that had been immersed in the salt solution. The “wet” droplet was applied by adding the droplet on the tensile loaded sample at the room temperature (Figure 3-13) while the “evaporated” droplet was done by adding the droplet on the sample, preheated at 100°C temperature in a dry oven. The droplets’ initial diameters varied from 0.5 to 1 millimetre. The whole cell was placed in a sealed container whose bottom is filled with a saturated salt (magnesium chloride) to set the relative humidity at 30-33% when placed in the oven at 80°C (Figure 3-14).

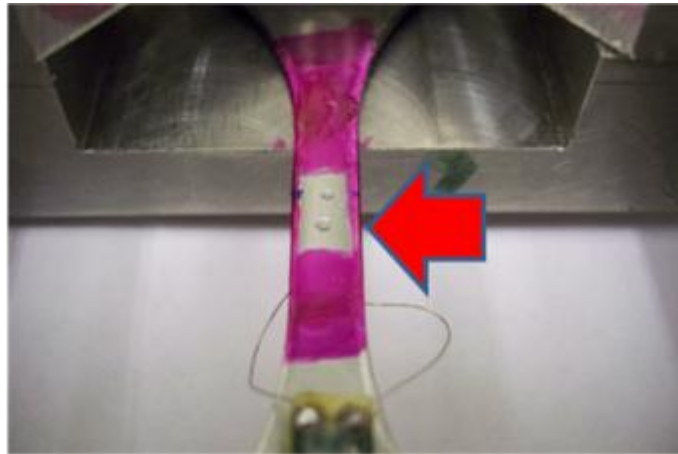


Figure 3-13: Image shows the salty droplets on the observed area.

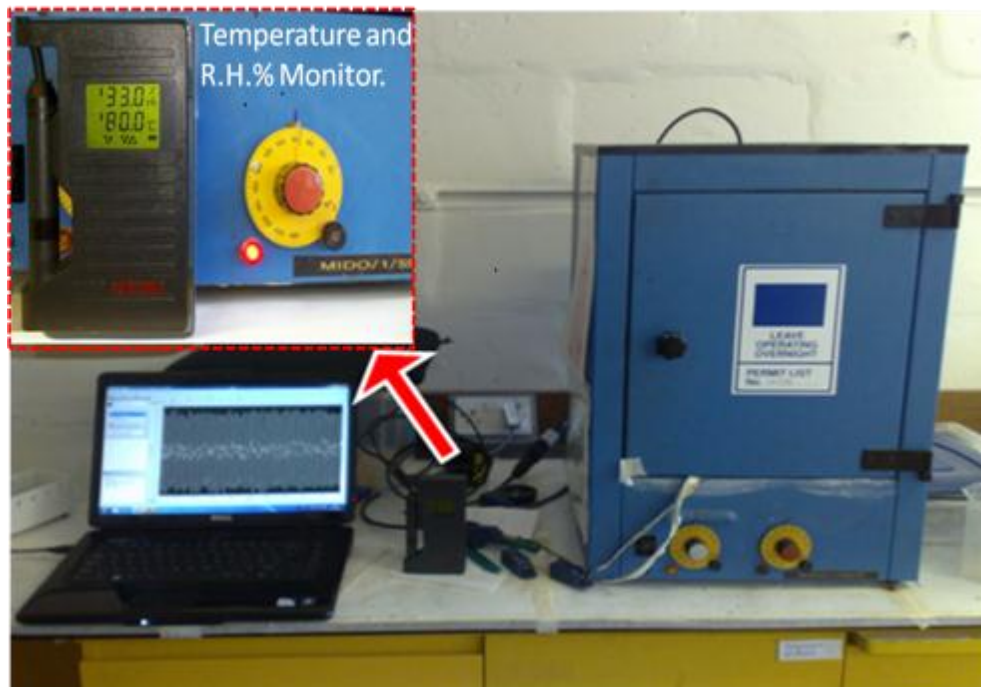


Figure 3-14: Image shows the main setup of the experiment.

### 3.11 Microscopy

#### 3.11.1 Optical Microscope (OM)

The light optical microscope used was the Olympus-BH2 which is interfaced with Axio Cam MRm ZEISS and equipped with an Olympus MSPlane lens (Figure3-15).



**Figure 3-15: Optical Microscope (OM), Olympus-BH2.**

### **3.11.2 Scanning Electron Microscope SEM**

The morphology of pits and cracks formed in the specimens and the fracture surface were observed by using the Scanning Electron Microscope (SEM) (Phillips XL30) which is equipped with field emission gun (FEG-SEM). Secondary electron (SE) and Backscatter (BSE) modes were employed. The machine was operated at an accelerating voltage from 10 to 20 kV and spot size of 3-5 (beam diameter). Also, a Zeiss Scanning Electron Microscope (EVO 50) was employed to do energy-dispersive X-ray (EDX) analysis.

### **3.11.3 Electron Back Scattered Diffraction on SEM**

Electron backscattered diffraction (EBSD) is widely used for many applications including the studying of individual grain orientations correlations, local textures and phase recognition. Figure 3-16 is a schematic diagram of the main configuration of the EBSD system [164]. The electron backscattered diffraction (EBSD) investigations were carried out on the Philips XL30 and CAMSCAN depending on the availability, the working distance ranged from 13 to 27 mm depending on the microscope used while the accelerating voltage and the sample tilt with respect to the electron beam were mostly 20 KV and  $70^\circ$ , respectively. Bands Edge detection with minimum bands of 6 and maximum bands of 8 were used for the phase identification. Channel 5 Tango Maps software (HKL

Instruments) and Vmap V.8 (in-house software developed by J. Humphreys [165, 166]). These softwares produce an orientation maps using the three Euler angle colouring scheme, and enable the quantitative analysis of microstructures including misorientation statistics, boundary statistics and orientation representation by pole Figures. High angle grain boundaries (HAGBs) were defined to have misorientation  $\theta > 15^\circ$  and are represented by thick black lines in the images in this thesis, while low angle grain boundaries (LAGBs) had  $15 > \theta > 2^\circ$ .

Specimen's surface preparation has very important role for optimum EBSD analysis. In this work, the specimens were prepared by the same sequence as the preparation for optical microscopy mentioned in the Metallographic Specimen Preparation section (3.2) but without electrochemical etching. In some cases (especially with the highly corroded specimens to give better surface finish), the specimens were electropolished by using the same procedures mentioned in section 3.4.

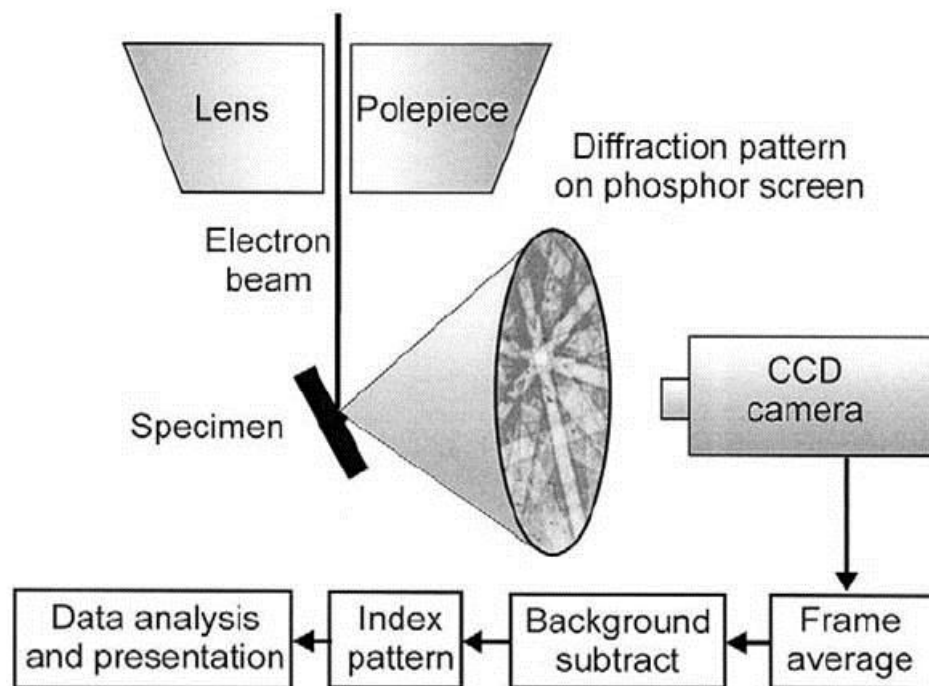


Figure 3-16: Schematic diagram showing the main EBSD mechanism [164].

### 3.12 In-Situ Micro-Tensile Testing

This in-situ test was used to observe the development of the strain in super duplex stainless steel Zeron 100; using Digital Image Correlation to map the strain gradients within grains

of super duplex stainless steels at the microscale under straining conditions (Max. 3% plastic strain). The micro tensile test was carried out with mini flat tensile specimens, with dimensions shown in Figure 3-17. The specimens were cut using spark erosion cutting by RotaData, England, Derby.

A micro-tensile testing device (Kammrath's & Weiss GmbH 5 kN tensile/compression, Germany) was used to carry out the test, with the sample surface observed by optical microscopy. This tensile module has load resolution better than 10mN. The microprocessor provides pre-selected displacement speeds over a range of 0.1 $\mu$ m/s to 20 $\mu$ m/s. The module can be operated from a microprocessor/PC combination, which displays the applied force and the applied displacement. The micro-tensile-testing device with its control units is shown in Figure 3-18. The mini flat tensile specimens were mounted in the micro-tester, and a tensile load was applied with an elongation rate of 2  $\mu$ m/s until a selected load increment was reached. The tests were then stopped and a number of images (20 images) for DIC taken, with short exposures, over a period of 10 seconds. The load was stable within less than 10 N over this period. The tensile test was then continued until the next load increment was accomplished.

The DIC analysis and the surface preparation were done as mentioned before in the Digital Image Correlation section 3.8. The smallest final window size used was 64x64 pixels.

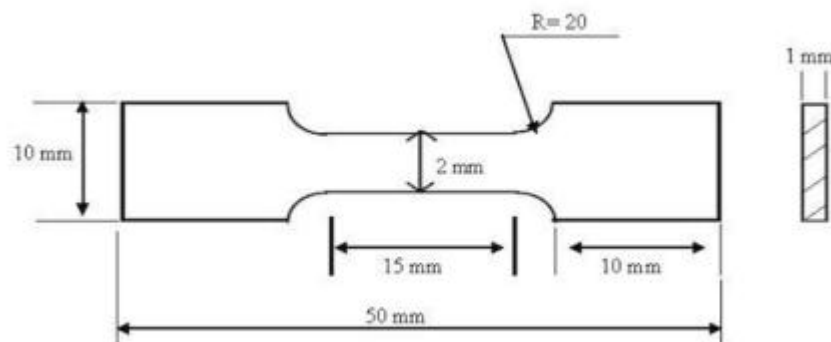


**Figure 3-17: Mini Flat Tensile Sample with dimensions included.**

The deformed sample was then studied by the EBSD (as mentioned in section 3.11.3) to show the phase map and local misorientations within the observed area. Then an immersion electrochemical test in 5M NaCl at 70°C was applied to initiate the pitting

corrosion in the observed area. The sequence of tests applied on the mini flat sample is shown in Figure 3-19.

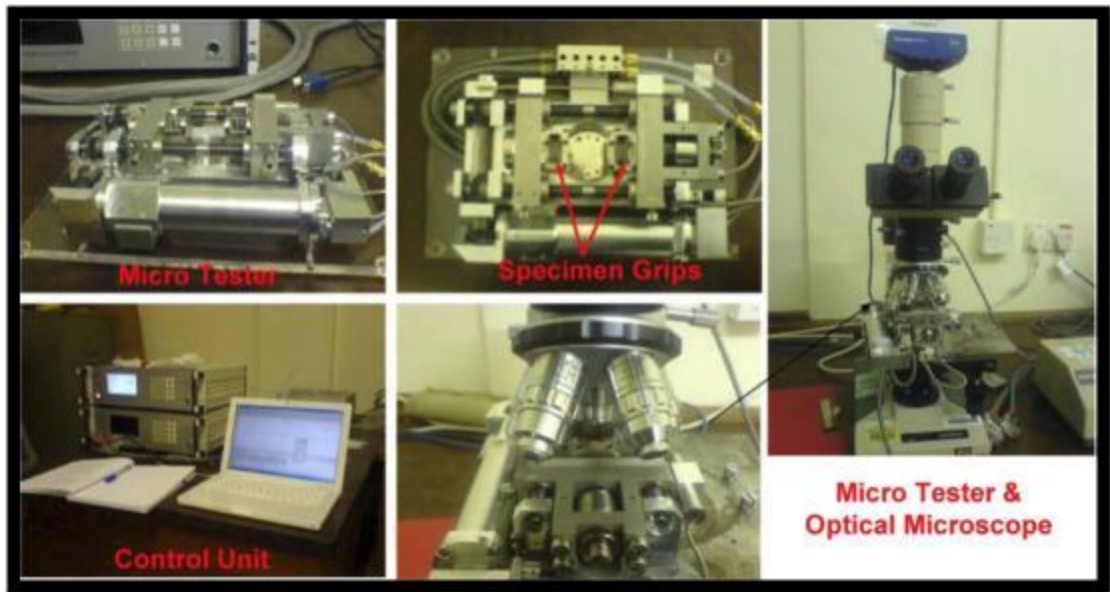


Figure 3-18: Micro-tensile-testing device tester with control units, and optical microscopy, interfaced to the ZEISS MRm AxioCam digital camera.

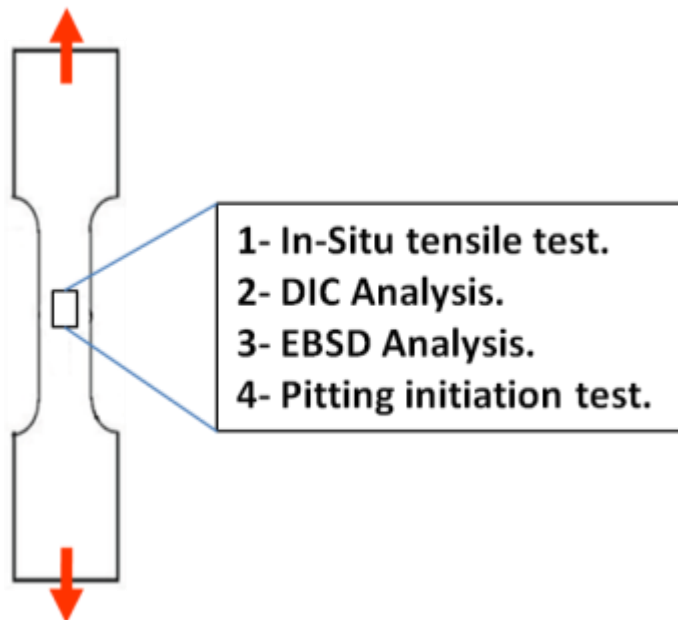
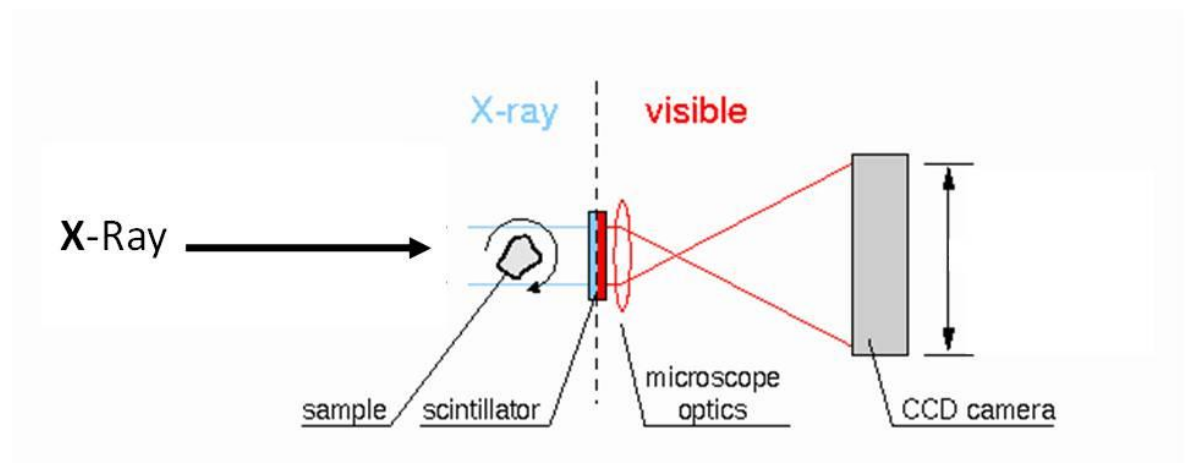


Figure 3-19: Steps of the tests applied on the mini flat sample.

### 3.13 Tomography

X-ray tomography is the construction of a 3-D image from two dimensional projections taken at different orientations of the tested sample (typically with different phase contrasts or absorption contrast imaging). The X-ray produced from the gun to pass through the sample and projected on the scintillator which is converting the X-ray to visible lights. Then, the visible lights are magnified through the lenses and then digitized through the CCD camera as shown in Figure 3-20. Highly coherent radiation allows high spatial resolution with a good signal to noise ratio and providing a tool for non-destructive examination of internal features. This technique has many applications in the engineering fields. It can be used to characterise the internal structure of pitting corrosion to determine the size and shape of cracks and other defects inside components which may give more knowledge on pit to crack transition principles in stress corrosion cracking [72, 167].



**Figure 3-20: Schematic diagram showing the main X-ray Tomography mechanisms [160, 167].**

The X-ray tomography technique was used to obtain 3-D images of the crack, and hence perform virtual sectioning. The instrument used is XRADIA MicroXCT Scanner shown in Figure 3-21. It was set at 100 KV (100W) and 100 $\mu$ A. The total number of projections was 2418, recorded between angles of -93° to +93° angle. The exposure time for each radiograph was 15s using an optical magnification of 4X. The image was recorded on a CCD array of 2000x2000 pixels, where 1 pixel was equal to 2.724  $\mu$ m.

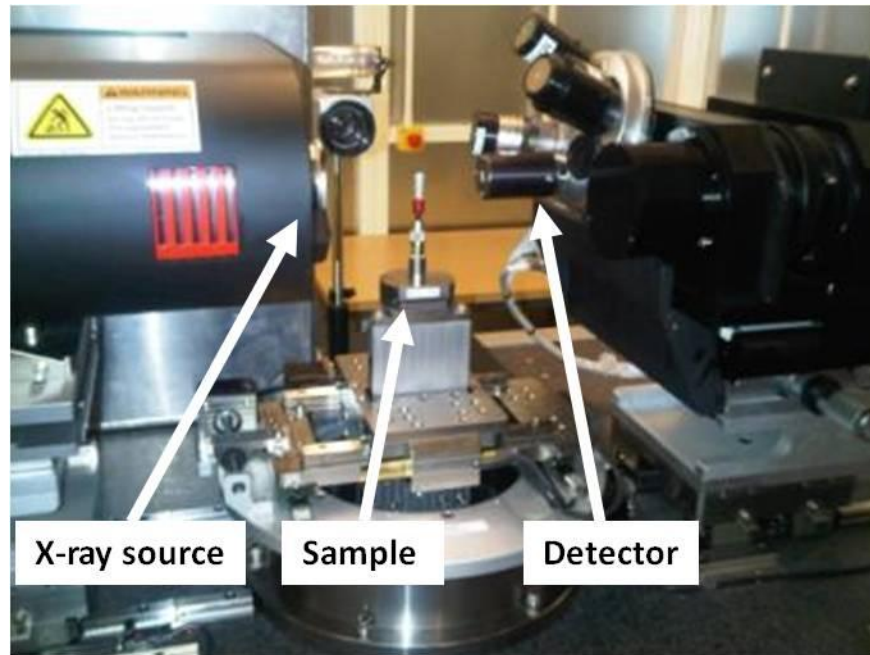


**Figure 3-21: XRADIA MicroXCT Scanner: left is the X-ray source; sample on rotation stage in the middle; right is the detector with different lenses for different optical magnifications [167].**

## 4 RESULTS

### 4.1 Microstructure of materials as received

Figure 4-1 shows the microstructure of the 3 mm sheet plates and the 33 mm forged plate respectively. Mainly, the microstructures consist of austenitic islands ( $\gamma$ -phase) elongated in the heavier rolling direction, embedded in a ferritic matrix ( $\alpha$ -phase). The ferritic phase is dark and the austenitic phase is light. Plate (3 mm sheet plate) samples had been cross rolled, and this created a microstructure with more elongated austenite grains in the heavier rolling direction.

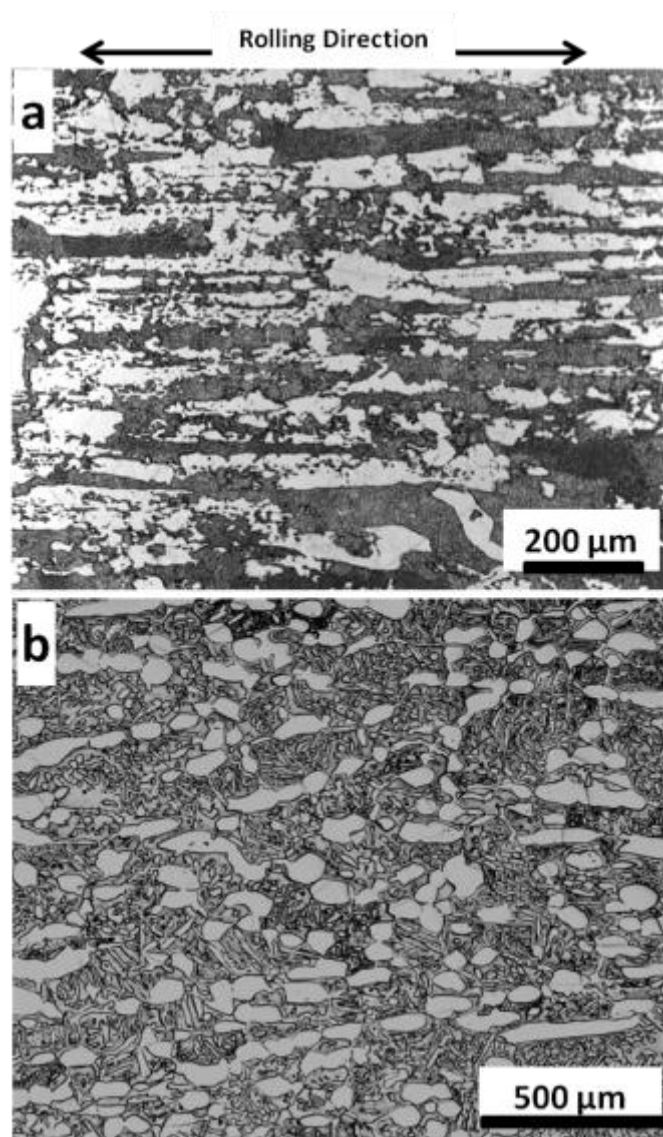


**Figure 4-1: Optical micrographs of (a) the 3-mm plate SDSS as-received and (b) forged SDSS sheet as received microstructures (ferrite is dark and austenite is light).**

## 4.2 Electrochemical Measurements

The polarisation curves (Figure 4-2) shows the effect of three different concentrations of NaCl salt (0.5, 1.5 and 3.5 wt%) on the material at room temperature. Passivation is not clearly observed, as there was no stable region of constant current density. However, the current's reduction in the reverse curve shows there is no pitting in these samples.

The study of effects of temperature shows that pitting was observed only in the samples at 70° and 80°C (Figure4-3). The pitting potential  $E_p$  and the passivation ranges of the tested samples were decreased with increasing solution temperature as shown in the polarisation curve. Figure 4-4 shows the change in the solution colour after testing samples in 5M NaCl at 80°C. This was not observed in the other tests.

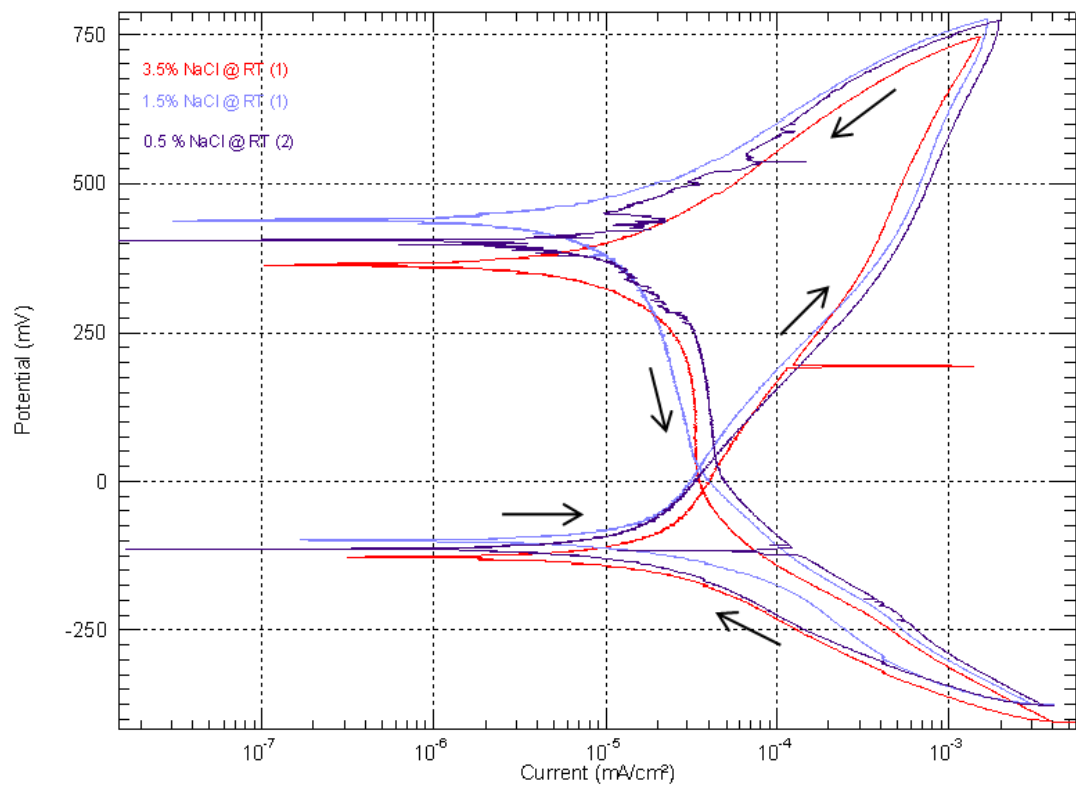


**Figure 4-2: Cyclic polarisation of sample in 0.5%, 1.5% and 3.5% NaCl solution at room temperature.**

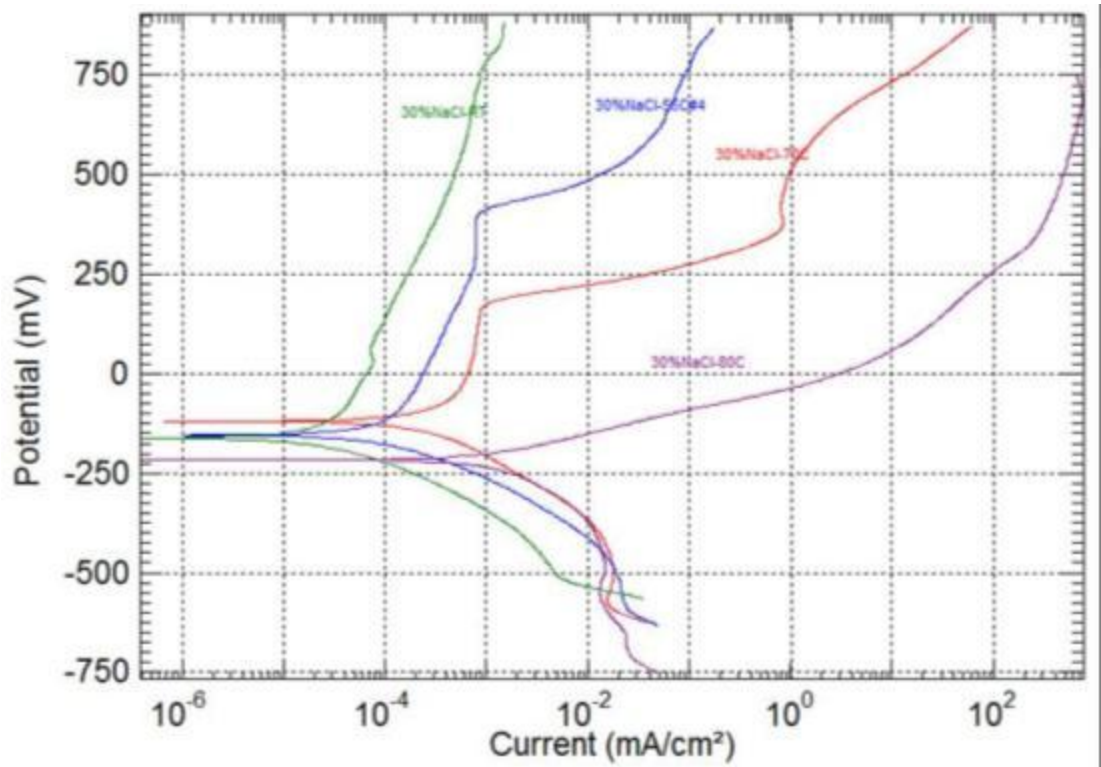


Figure 4-3: Half cycle polarisation curves for SDSS samples at Room Temperature, 55°, 70° and 80°C in 5M NaCl at pH=5.8.

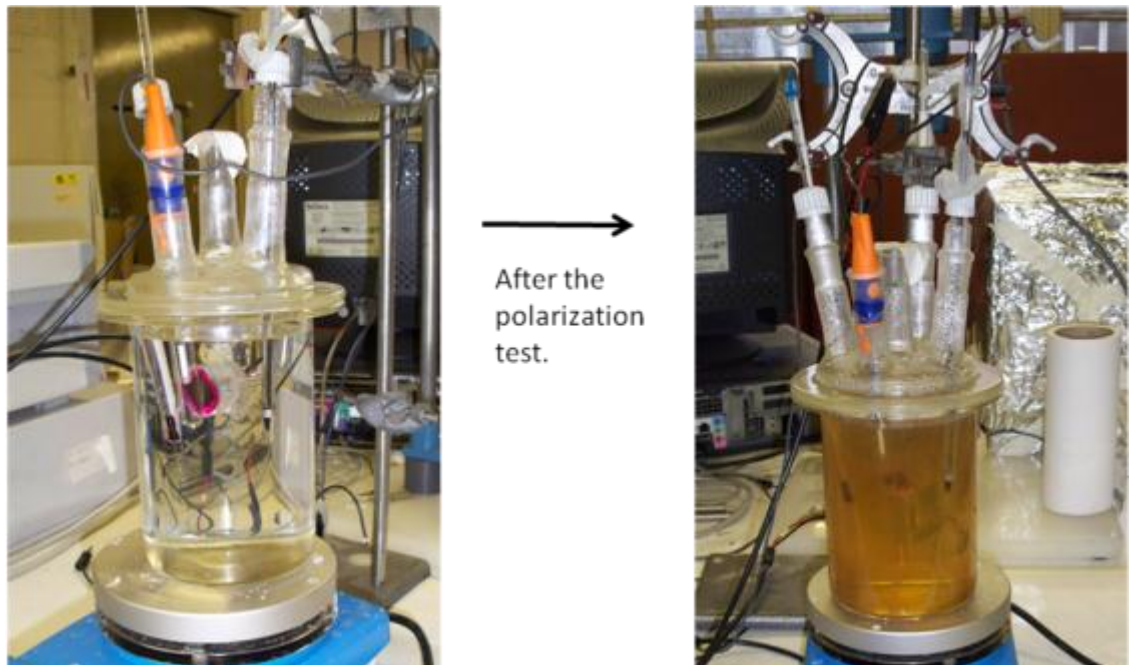
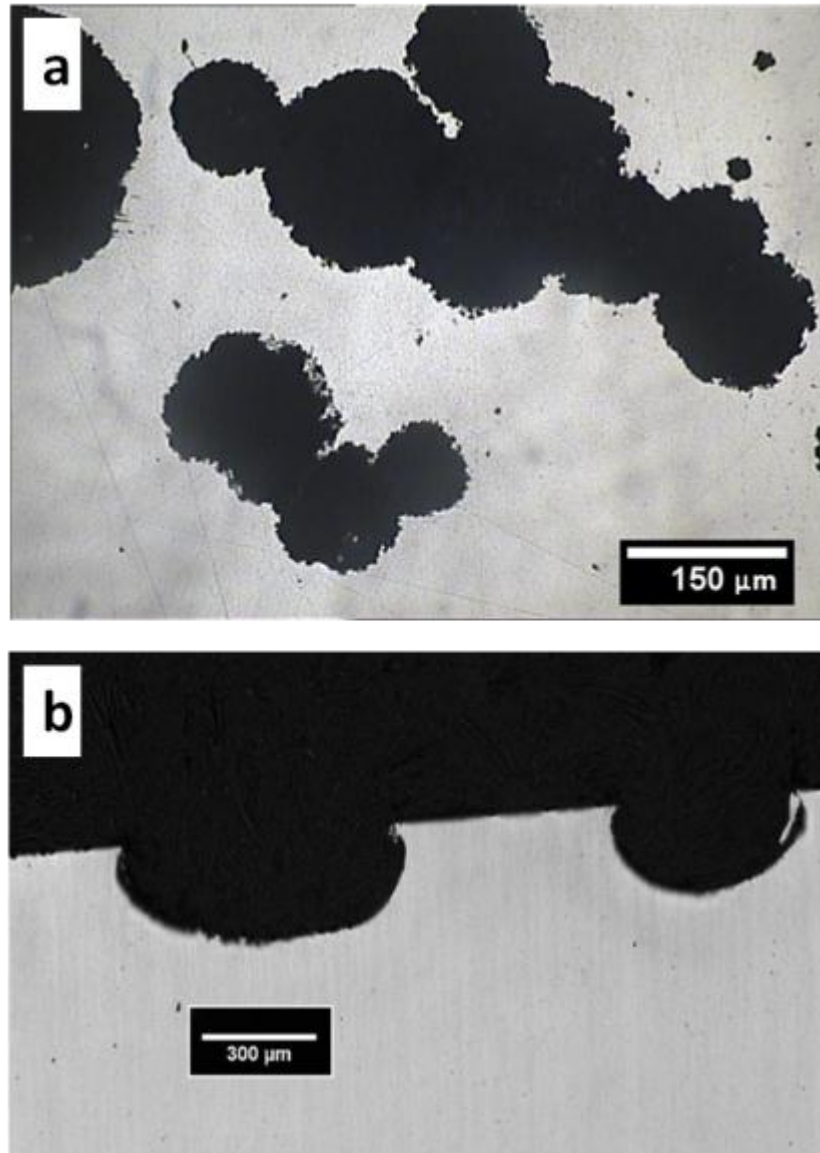


Figure 4-4: Change in the solution colour after testing samples in 30%NaCl at 80°C, pH=5.8, half cycle polarisation test shown in Figure 4-3.

### 4.3 Observations of Pitting after Electrochemical Testing

Pitting was observed in the polarisation tests in 5M NaCl solution at temperatures of 70°C (Figure 4-5) and 80° C (Figure4-6). The density of the pits is higher at 80°C compared to 70°C, while there was no pitting at all in the material tested at 55° C.



**Figure 4-5: Optical micrographs for a) the pits with lacy appearance and b) for cross section of sample all created in the sample after polarisation testing in 5M NaCl at 70°C.**

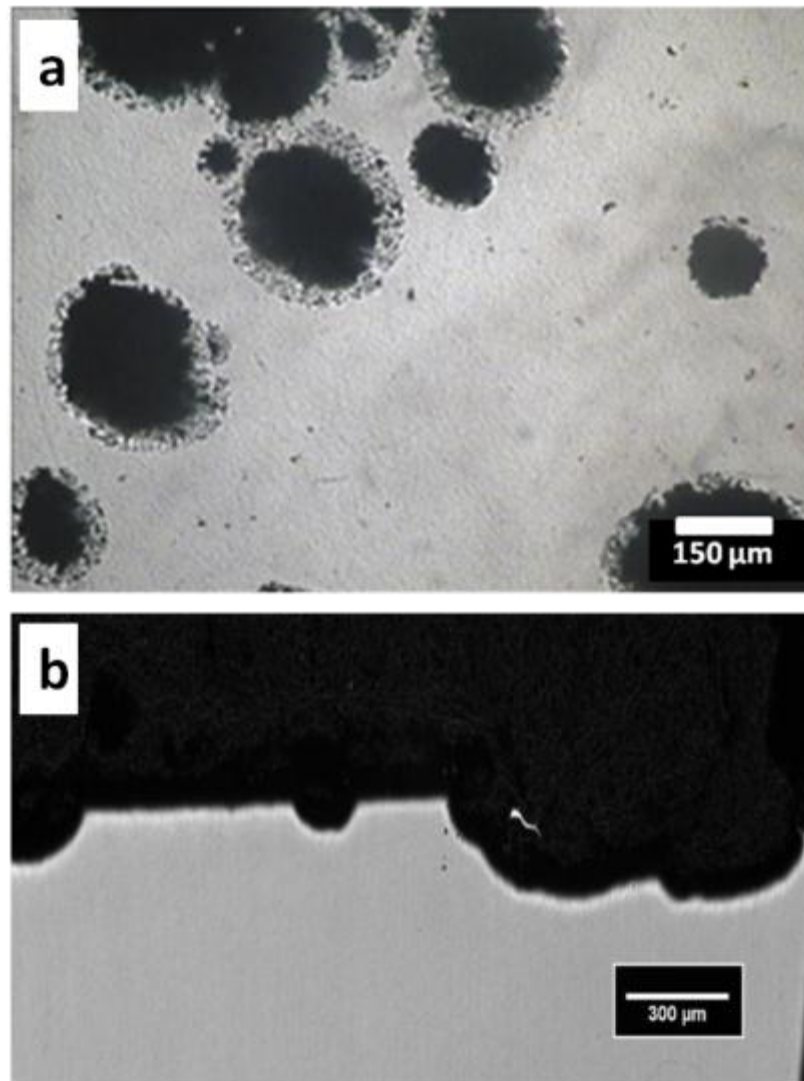


**Figure 4-6: Optical micrographs for a) the pits on the surface and b) for cross section of sample all created in the sample after polarisation testing in 5M NaCl at 80°C.**

Scanning Electron Microscope observations of the pits created after the polarisation tests of the sample in 5M NaCl at 80°C are shown in Figure 4-7.

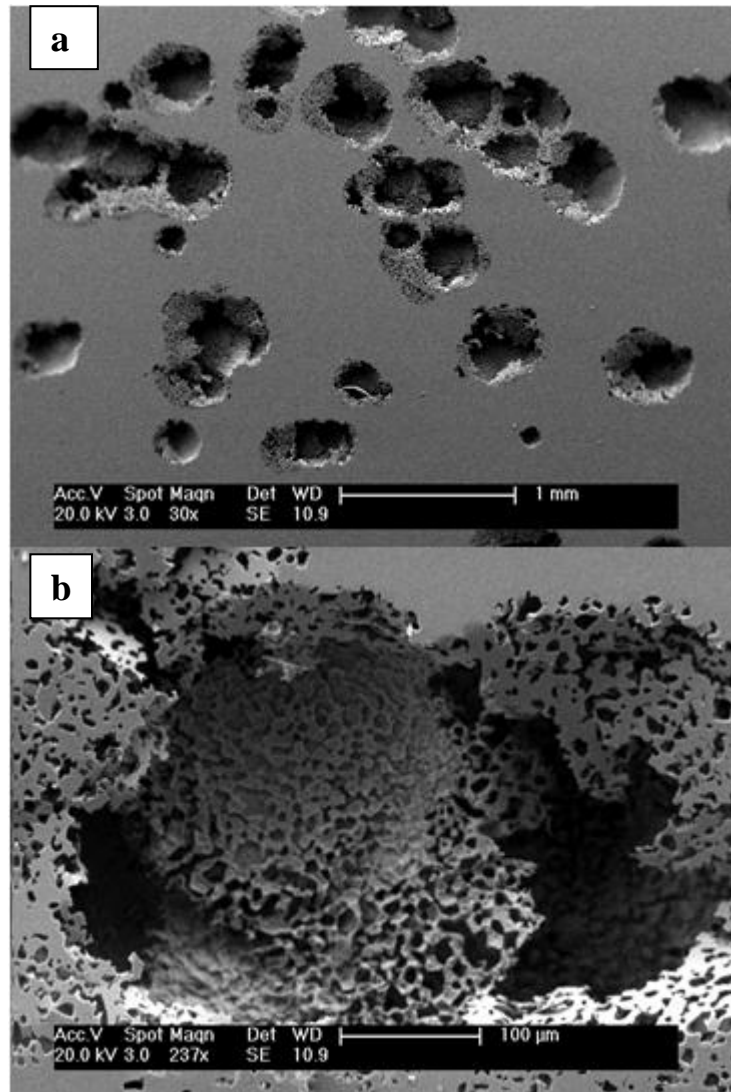


**Figure 4-7: SEM micrographs for sample after polarisation testing in 5M NaCl at 80°C, a) At 30x and b) higher magnification shows the formations of metallic caps cover the pits.**

#### **4.4 Characterisation of U-Bend Test with Salt Deposits**

The optical micrographs for the U-bend sample, taken from the 3-mm plate, after testing by depositing salt droplets of 0.52M MgCl<sub>2</sub> at 80°C and 42% RH for 1800 hours (Figure4-8 and Figure4-9) show the appearance of the stress corrosion cracks, oriented perpendicular to the tensile stress direction and appear to be associated with machining marks.

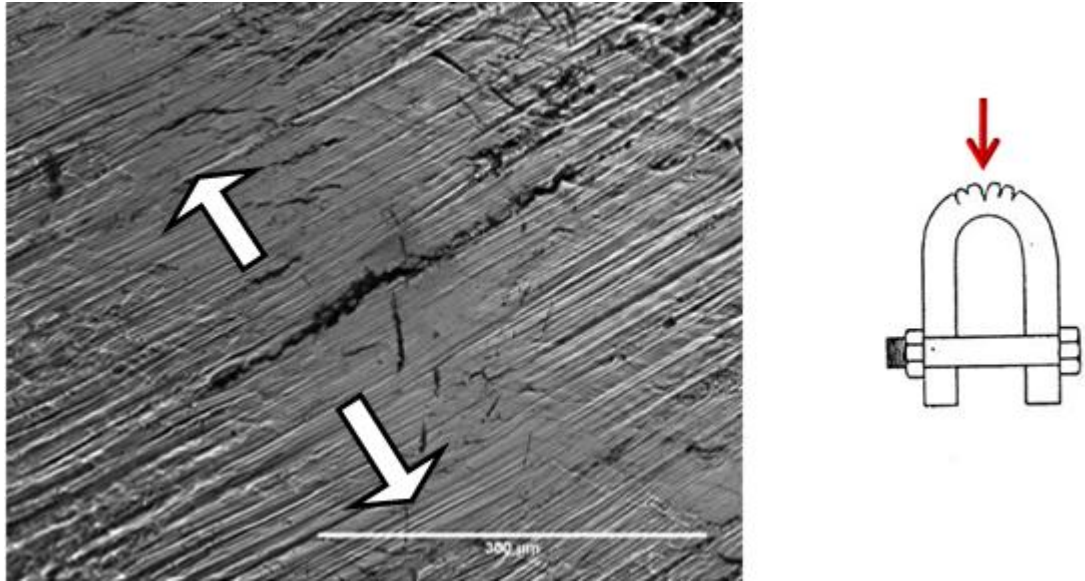


Figure 4-8: Optical micrograph for the top surface of the U-bend sample after testing under droplets of 0.52M  $MgCl_2$  at 80°C and 42% RH. The white arrows on Figure indicate to the tensile direction.

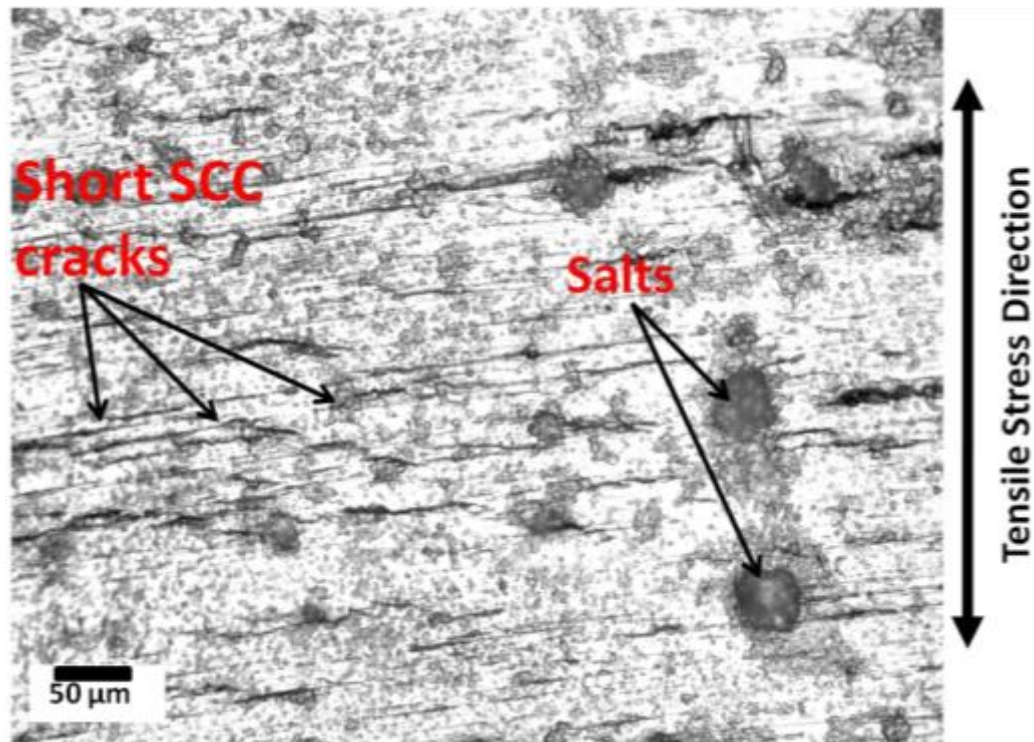


Figure 4-9: Optical micrograph for the top surface of the U-bend sample after the test shows the initiation of the stress corrosion cracking normal to the loading direction

#### 4.5 Mechanical Testing

The maximum hardness in the U-bend sample of 334 Hv (30kg) was observed at the 0° position (Figure4-10). Table 4-1 shows the strain and hardness values of three levels of reduction. A 10% reduction in thickness was expected to give approximately the same hardness as the top surface of the U-Bend sample.

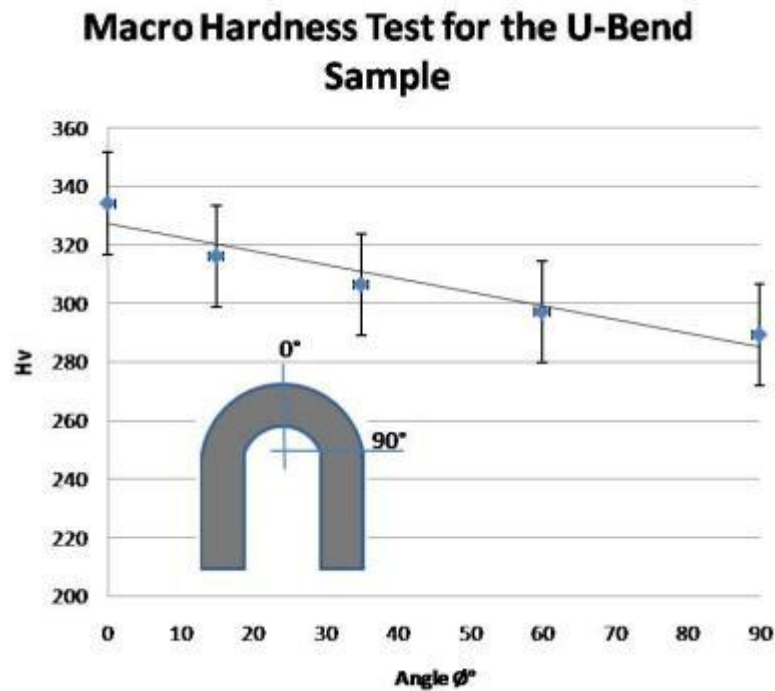


Figure 4-10: Macrohardness test of the U-Bend sample.

Reduction in thickness %	Strain	Hardness Hv
8	0.1	322 ±4.3
10	0.125	346 ±6.96
20	0.23	375.8 ±7.94

Table 4-1: Strain and hardness values achieved from three levels of reduction.

The tensile data at 80°C are shown in Figure4-11 and table 4-2 for the as received material and that with 10% reduction in thickness. The SCC tests of the 10% cold-rolled material were performed at an applied strain value of 3% ( $1.05\sigma_y$ ).

The strain gauge output was tested for more than 10 hours at 80°C to confirm that there is no relaxation in the sample (Figure 4-12) by loading the sample in the tensile cell manually and place it in the oven at 80°C. The effect of heating the sample from room temperature to 80°C caused the applied strain to increase by 3.2% to 0.03102 mm/mm from 0.03 mm/mm because of the thermal expansion in the whole tensile cell relative to the sample.

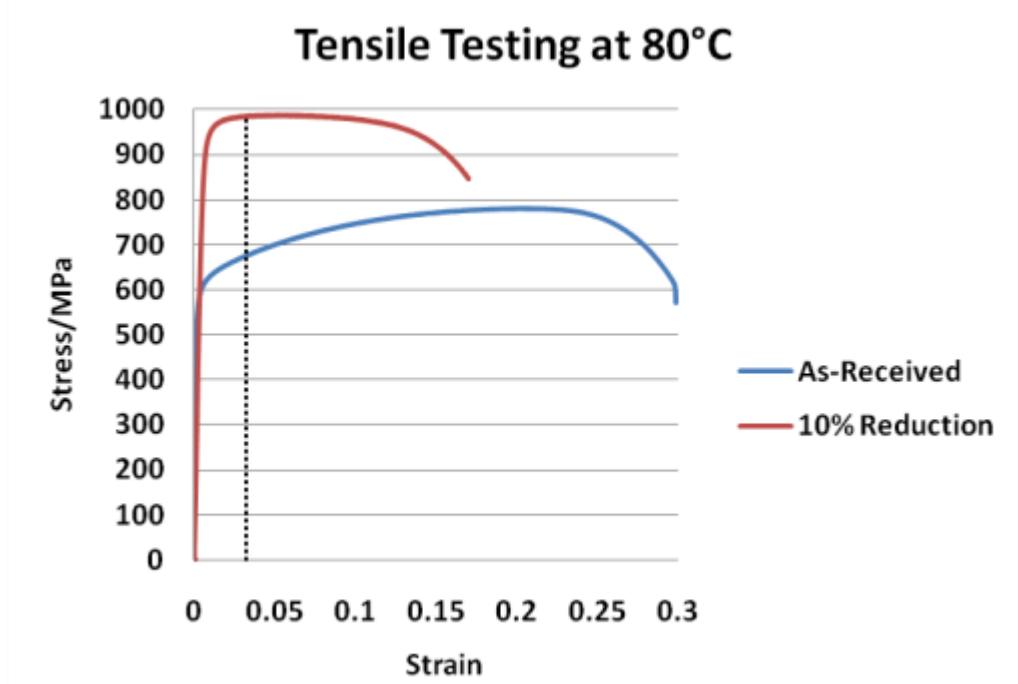


**Figure 4-11: Stress/Strain behaviours of the rolled and solution annealed sample tested at 80° C, dashed line indicated to the selected strain (3%) and the considered stresses ( $1.05\sigma_y$ ) for both samples.**

<b>Mechanical Properties at 80° C</b>	<b>Proof Stress 0.2% (MPa)</b>	<b>UTS (MPa)</b>
<b>As Received</b>	<b>482</b>	<b>780</b>
<b>Cold Rolled (10%)</b>	<b>821</b>	<b>983</b>

**Table 4-2: Mechanical properties of samples tested at 80°C.**

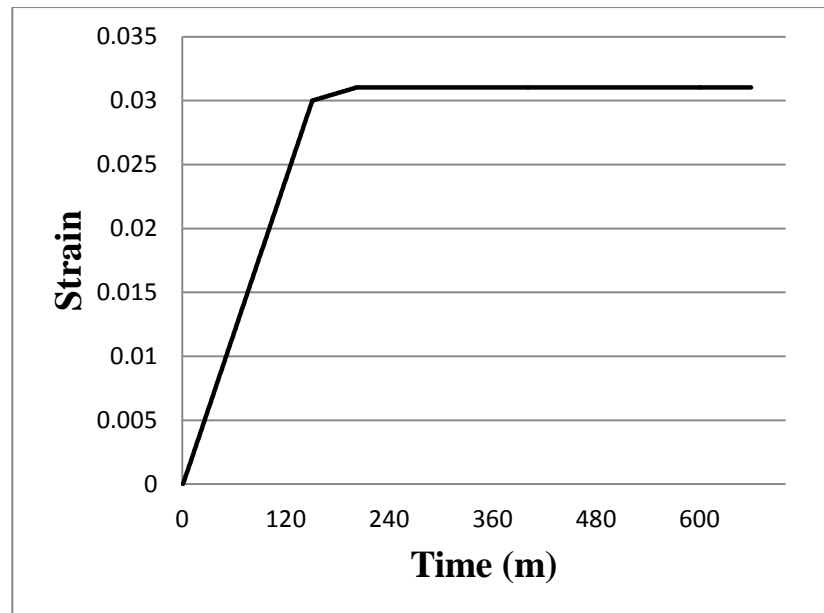


**Figure 4-12: Strain gauge data for the first 11 hours at 80°C.**

#### **4.6 Surface Preparation for the Digital Image Correlation Analysis**

The image correlation noise level for the electroetched surface (Figure 4-13) was tested under three levels of optical magnifications (5X, 10X and 20X). Table 4-3 shows a comparison of the best possible (optimum) error [116] with the experimental error established in this work. Experimental error was obtained by first capturing a set of images of the electroetched surface then moving the sample in x-direction for some pixels ( $\approx 20$  pixels) and re-focusing on the sample, and then capturing another set of images to be all proceeded through the DIC software to calculate the Root Mean Squared (RMS) value from the calculated x-displacement vectors (Figure4-14) with the maximum overlap used of 87%.

The electroetched surface shows distributed features in both phases (ferrite and austenite) and the noise test revealed the quality of that electroetching as shown in Figure 4-15. The most suitable lens was found to be 10x magnification, which gave an imaged area of around  $960 \times 960 \mu\text{m}$ . The noise level at window size of  $64 \times 64$  pixels ( $14.72 \mu\text{m}$ ) had  $\text{RMS} = 0.013 \mu\text{m}$  while larger window size of  $128 \times 128$  pixels ( $29.44 \mu\text{m}$ ) gave  $\text{RMS} = 0.01 \mu\text{m}$ .

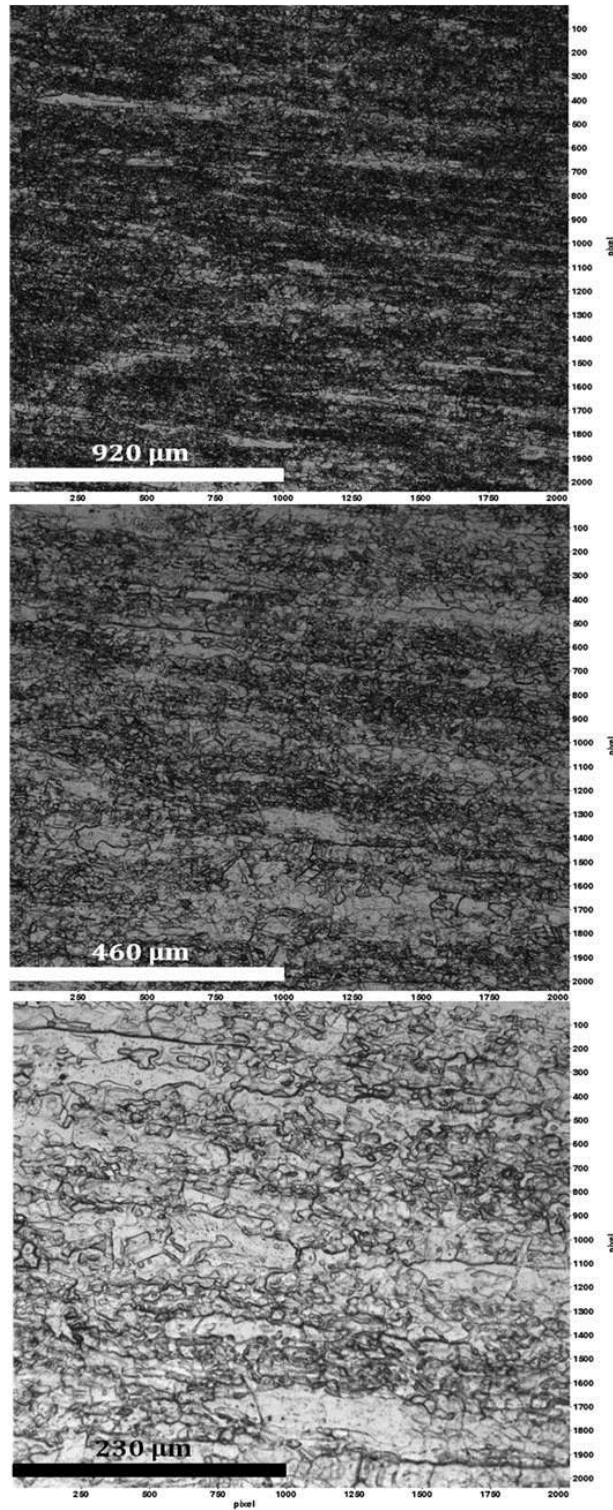


**Figure 4-13: Electroetched surface under three magnifications (5X, 10X and 20X) respectively.**

Window Size Size of Interrogation Window (pixels)	Optimum (pixels)	Experimental (pixels)
128x128	0.01 – 0.03	0.0217
64x64	0.02 – 0.05	0.028
32x32	0.05 – 0.2	0.071

Table 4-3: Optimum and experimental DIC accuracy (RMS) vs. window size.

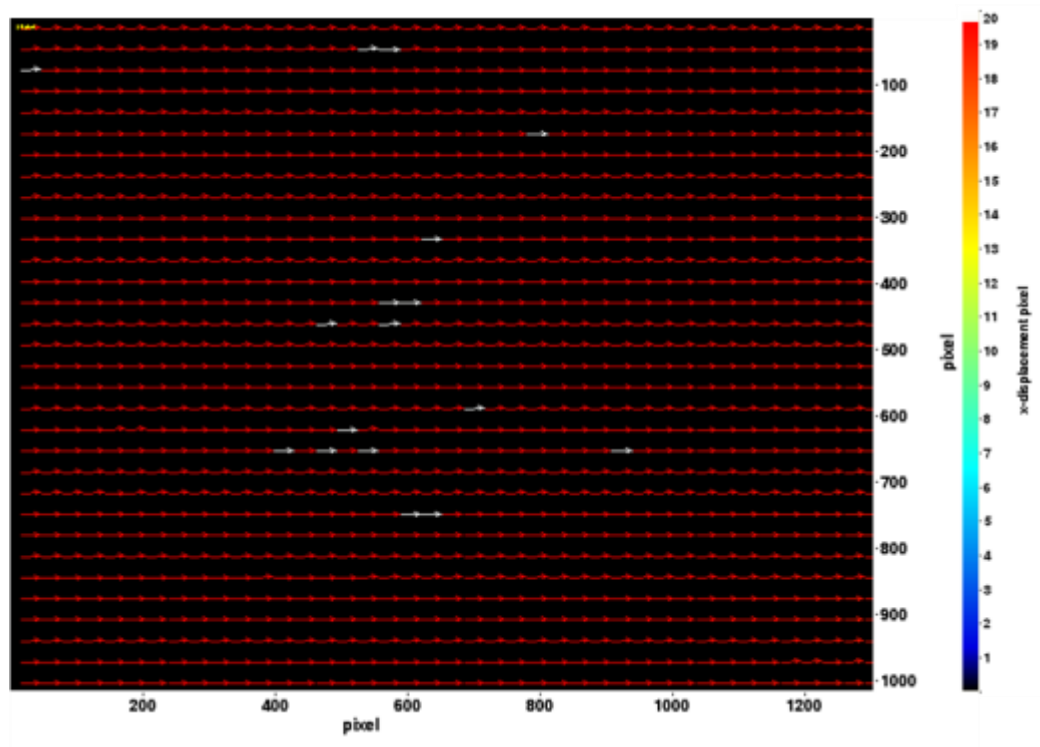
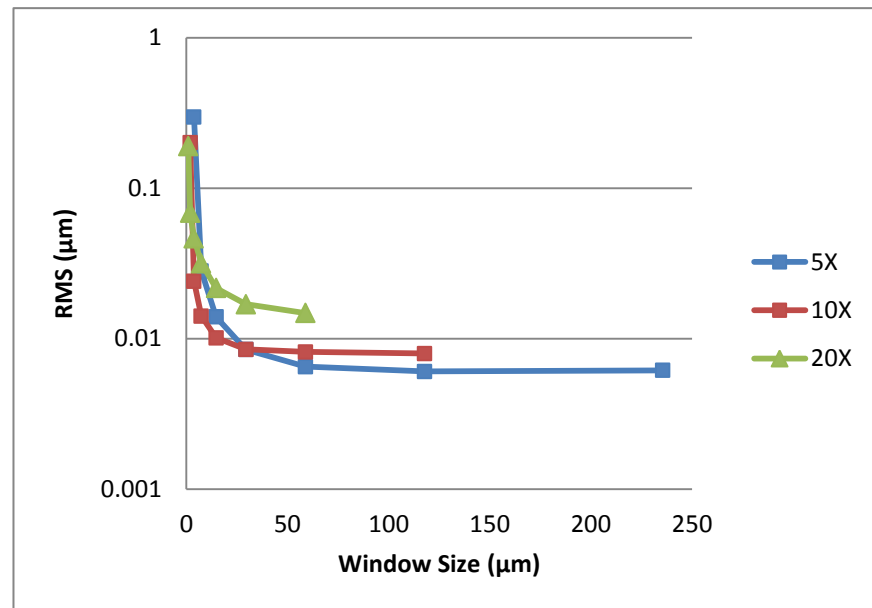


Figure 4-14: Displacement map of the electroetched surface moved in x-axis direction by around 20 pixels under the optical microscope (10X magnifications).



**Figure 4-15: RMS value vs. window sizes for the electroetched surface tested at three levels of magnifications 5X, 10X and 20X.**

#### **4.7 Digital Image Correlation Accuracy within the Salt Droplets**

The previous tests demonstrate an acceptable noise level of the dry surface of the sample. The DIC accuracy within the salt droplets was also tested. Figure 4-16 shows the earliest images of the wet and evaporated droplets, which reveal better observations inside the evaporated droplet compared to the wet one.

Figures 4-17 and 4-18 show the changes inside wet and evaporated droplets respectively during the tests. This is because of the development of corrosion products with time. Movement of the features in the droplets increases the uncertainty and noise level. Figures 4-19 and 4-20 illustrate the gray scale profile along the yellow line in the images taken after 600 hours, showing very low gray value (contrast) inside the droplets. This causes high noise in those regions.

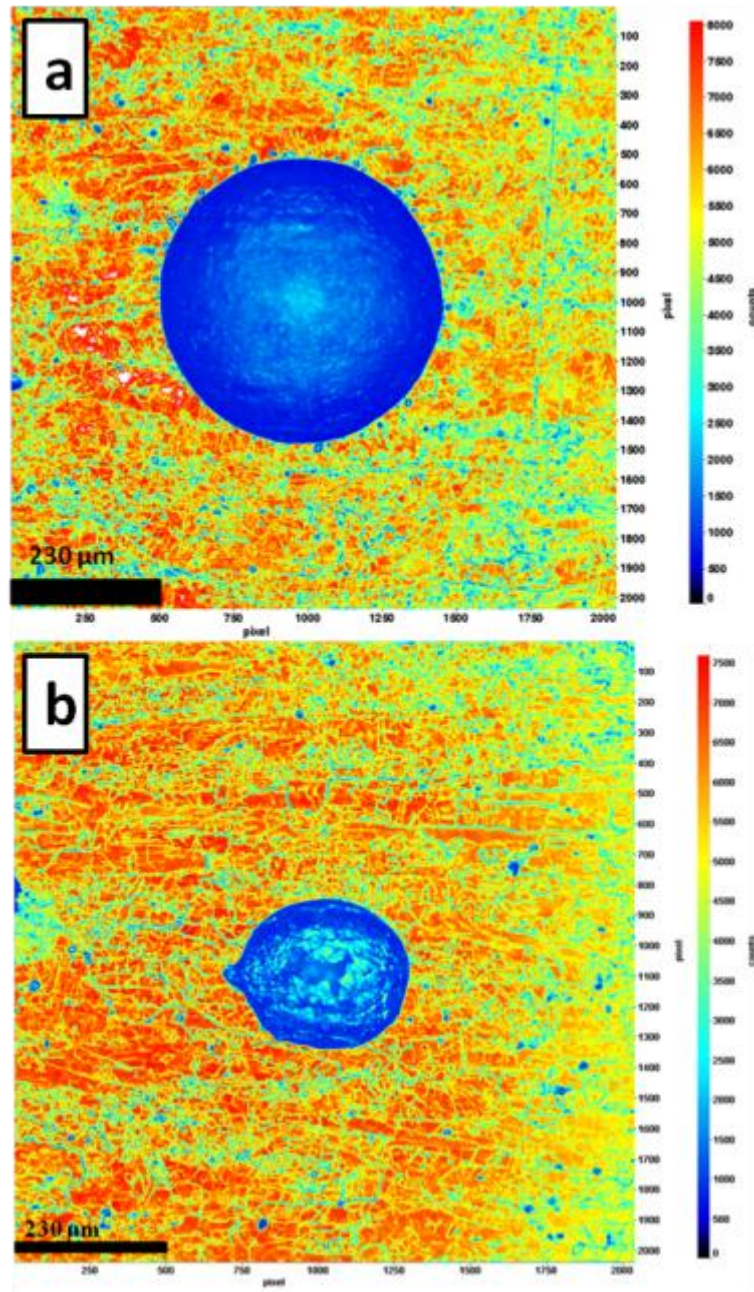


Figure 4-16: Optical images of a) a wet droplet and b) an evaporated droplet of  $\text{MgCl}_2$  at the beginning of the test.

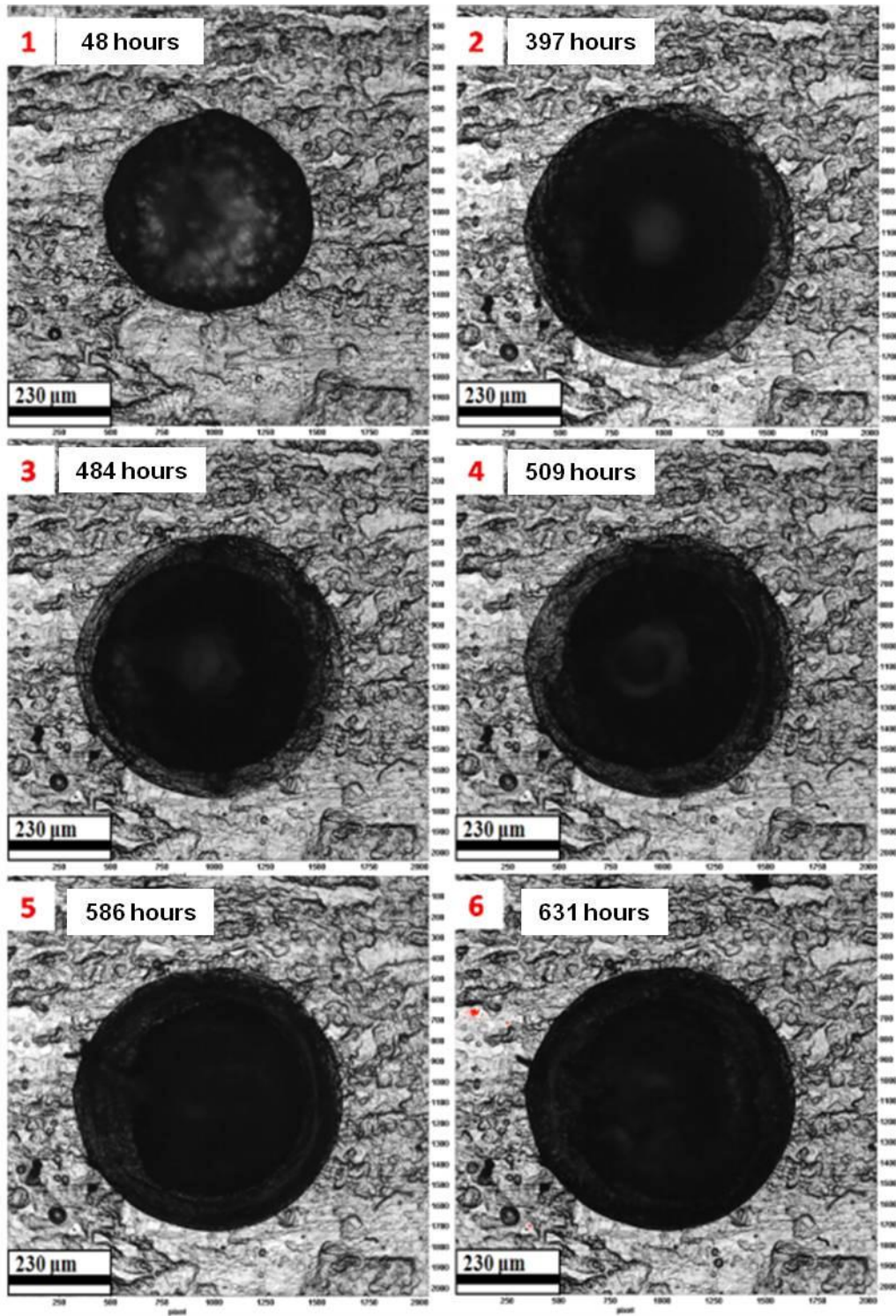


Figure 4-17: A series of DIC images show changes inside a wet droplet as a function of time during the first 600 hours.

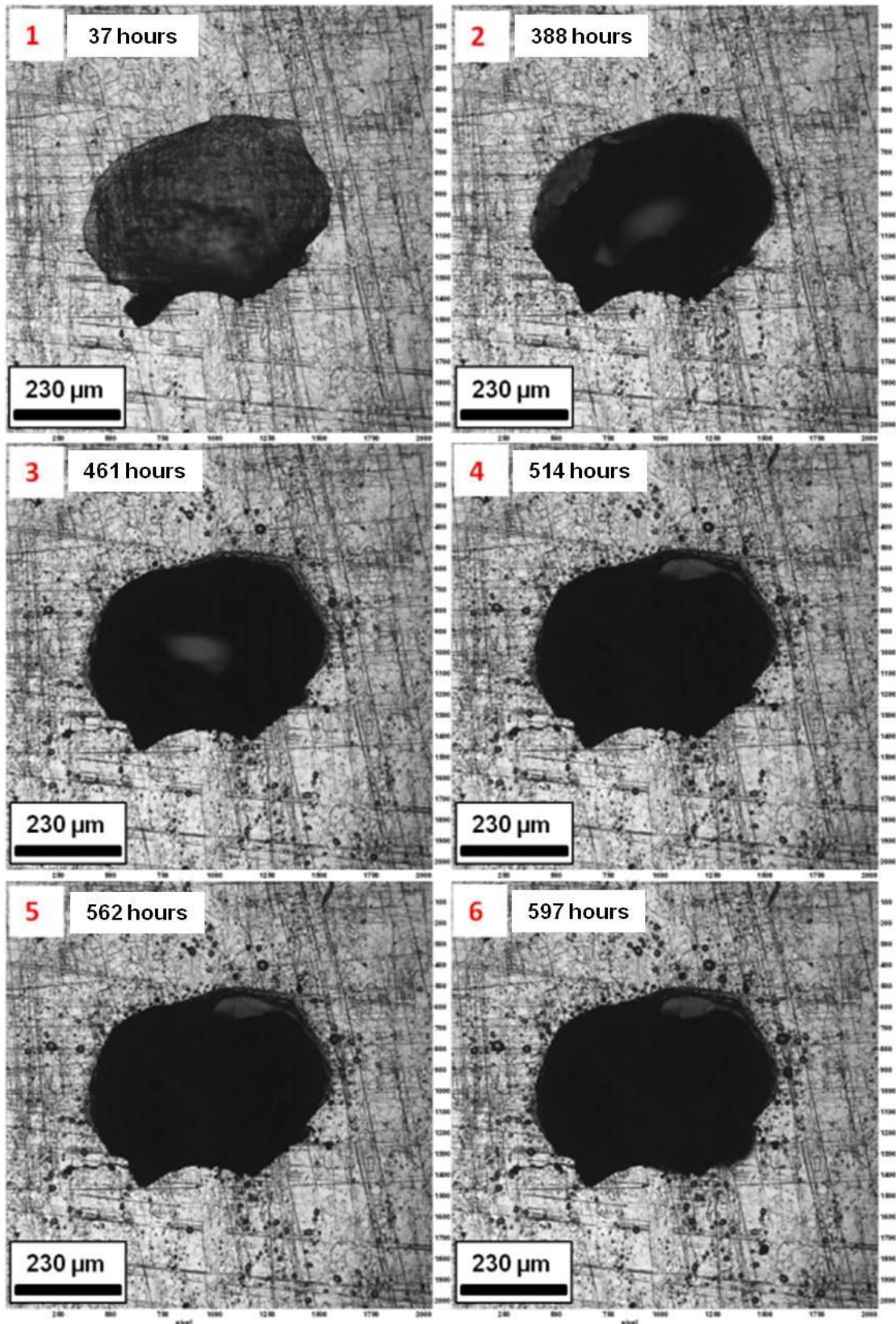
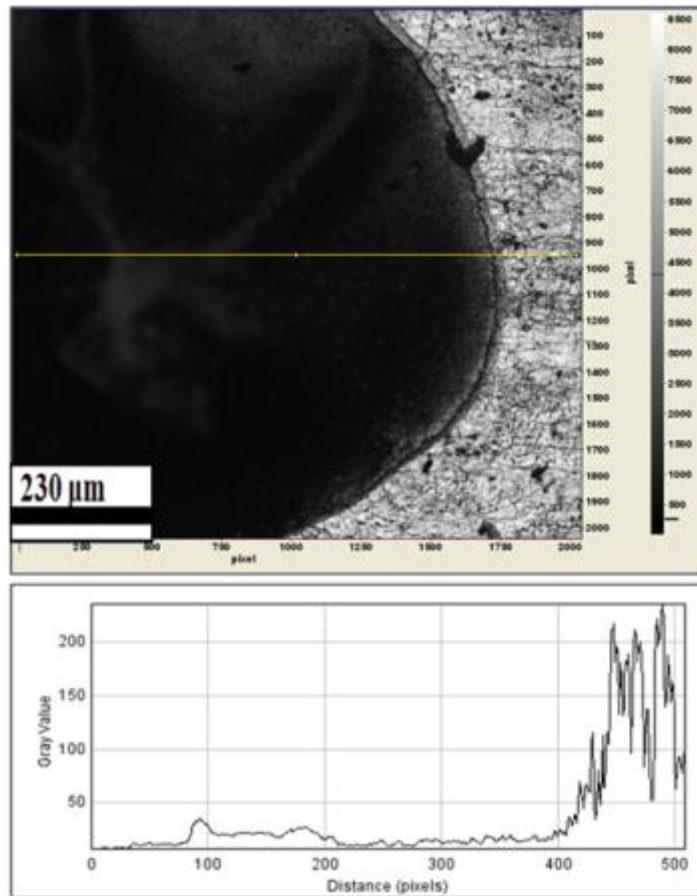
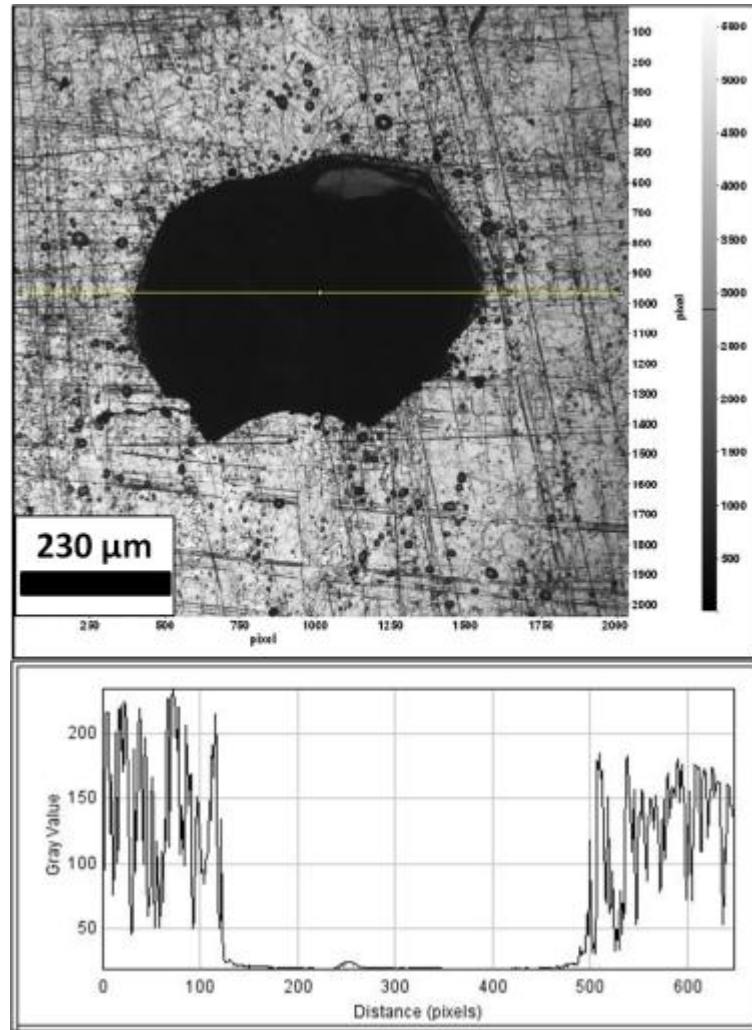


Figure 4-18: A series of DIC images show the changes inside an evaporated droplet in function of time during the first 600 hours.

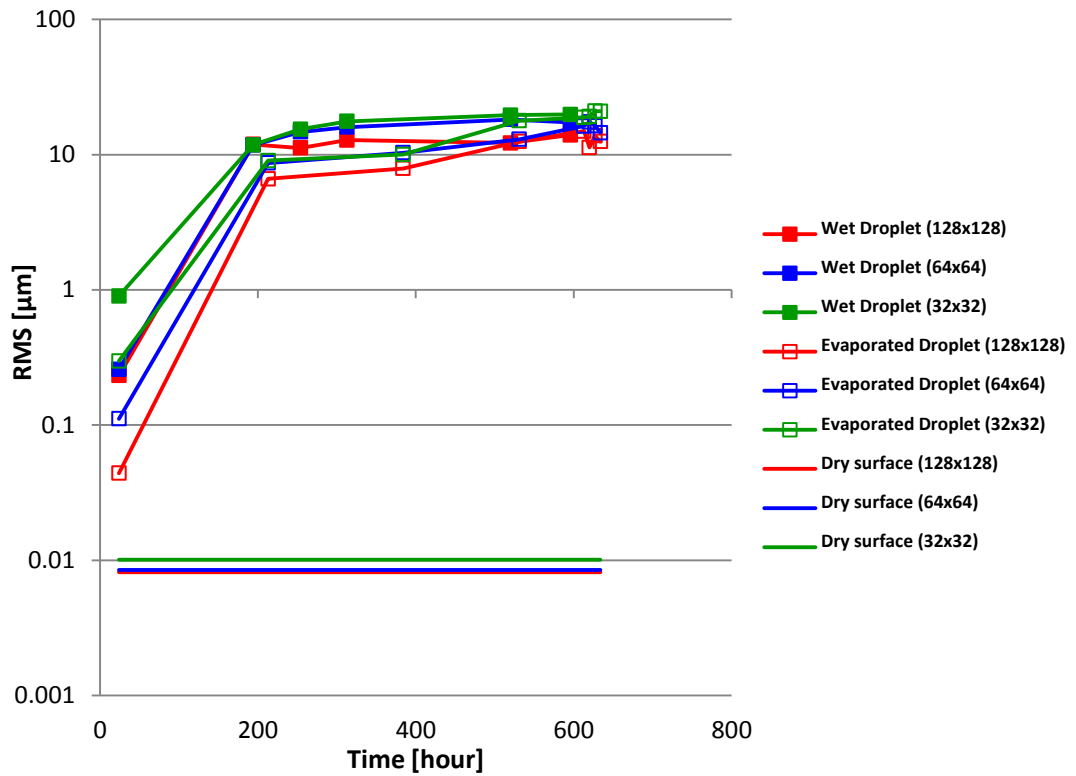


**Figure 4-19: DIC image shows the gray scale profile along the yellow line from right to left in the wet droplet after 500 hours.**



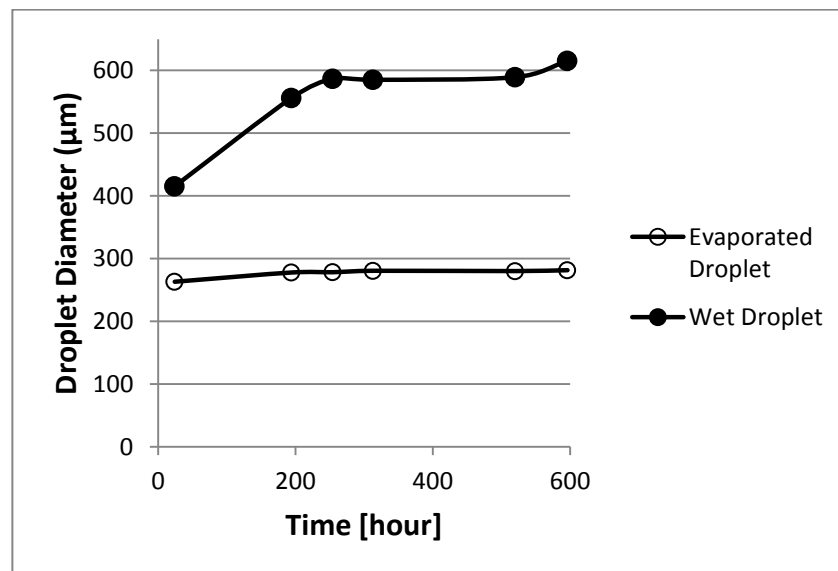
**Figure 4-20: DIC image shows the gray scale profile along the yellow line from right to left in the evaporated droplet after 500 hours.**

Figure 4-21 shows the noise development in the droplets (wet and evaporated salt droplets) at three sizes of interrogation windows during the test. The evaporated droplet shows less noise at the beginning but it increases once the corrosion starts inside the droplet, leading to noise levels similar to the wet droplets.



**Figure 4-21: Noise development with time inside the wet and evaporated droplets during the test (at 10X-Magnification).**

The change in the average diameter of the wet and evaporated droplets during the test is illustrated in Figure 4-22. This confirms better stability of the evaporated droplet size.



**Figure 4-22: The change in the droplets average diameter in function of time.**

## **4.8 Atmospheric Stress Corrosion Cracking Tests**

The tests were carried out using the tensile cell loaded in an environment of 80°C and relative humidity of 30-35%, as described in sections 3.9 and 3.10. Both solution annealed (as received) and 10% cold rolled samples were tested in two different orientations (rolling direction) with respect to the tensile load direction. Wet and evaporated droplets were used in the initial condition of the rolled sample with transverse orientation direction to the tensile load. The evaporated salt droplet was then used in all other tests performed after.

### **4.8.1 DIC Analysis**

#### **4.8.1.1 Rolled Sample: (Transverse to Tensile)/(wet salt droplet)**

The crack propagated in two branches with total length of 1.640 mm (including the diameter of the droplet) at 942 hours when it was first observed, and then it grew to be 3.174 mm within the next 10 hours (Figures 4-23 and 4-24). The crack growth rate was then estimated to be  $4.2 \times 10^{-8} \text{ ms}^{-1}$ .

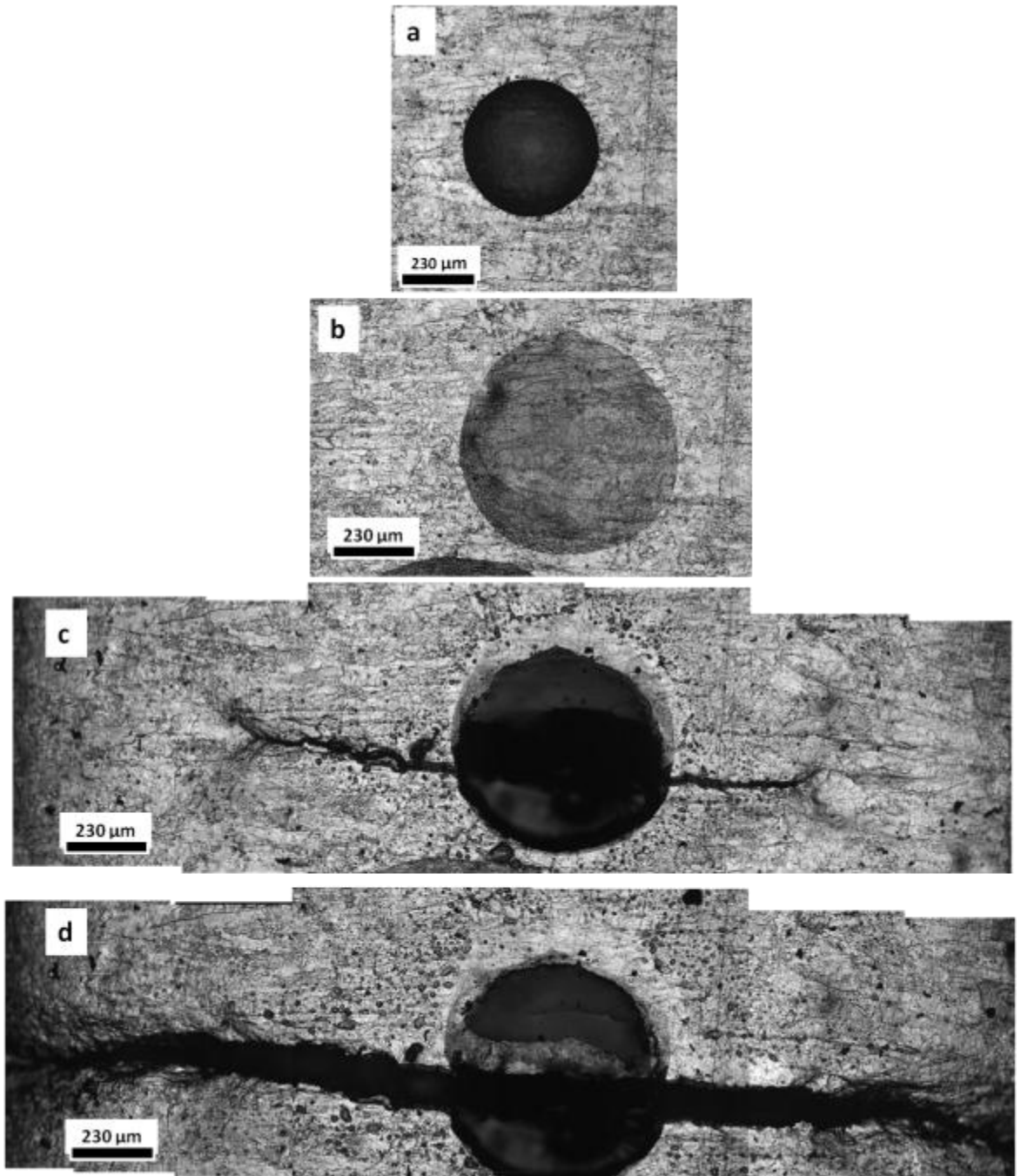


**Figure 4-23: Montage images showing a) the droplet at the beginning of the test, b) after 706 hours and c) after 942 hours d) after 952 hours.**

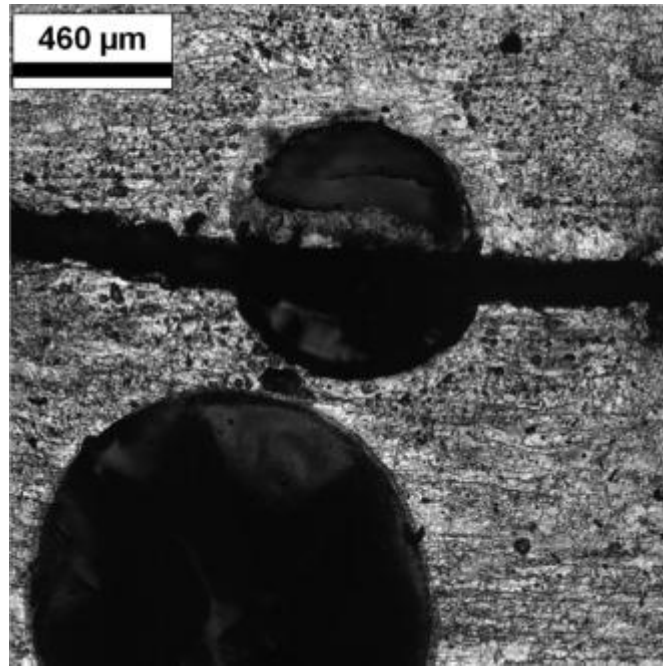


**Figure 4-24: Image of the crack in the wet droplet after 1050 hours.**

DIC's monitoring detected crack development only after the cracks emerged from the droplet. This is shown in the displacement and strain maps (Figures 4-25 and 4-26) obtained after 942 hours. The strain maps were calculated along Y-loading and X directions and the area inside the droplets were subtracted from the strain calculations by using the mask capability to take out the high noise level created by the low intensities and the movements of the corrosion products inside the corroded droplets..

In the next image recorded after 10 hours, propagation of the crack towards to the edges of the gauge length and normal to the loading direction as shown earlier in Figure 4-23 and leading to a fracture failure of the sample outside the field of view.

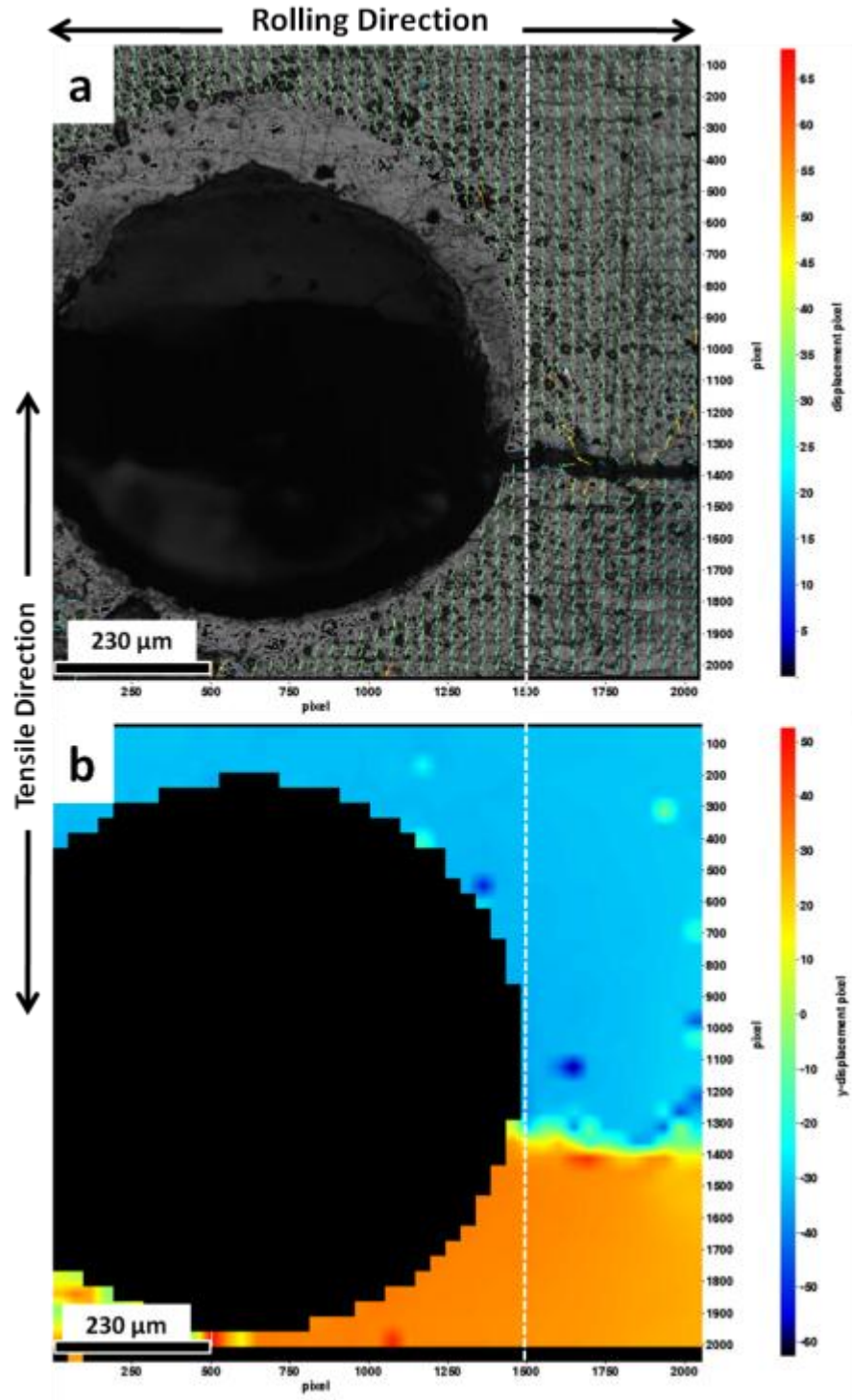
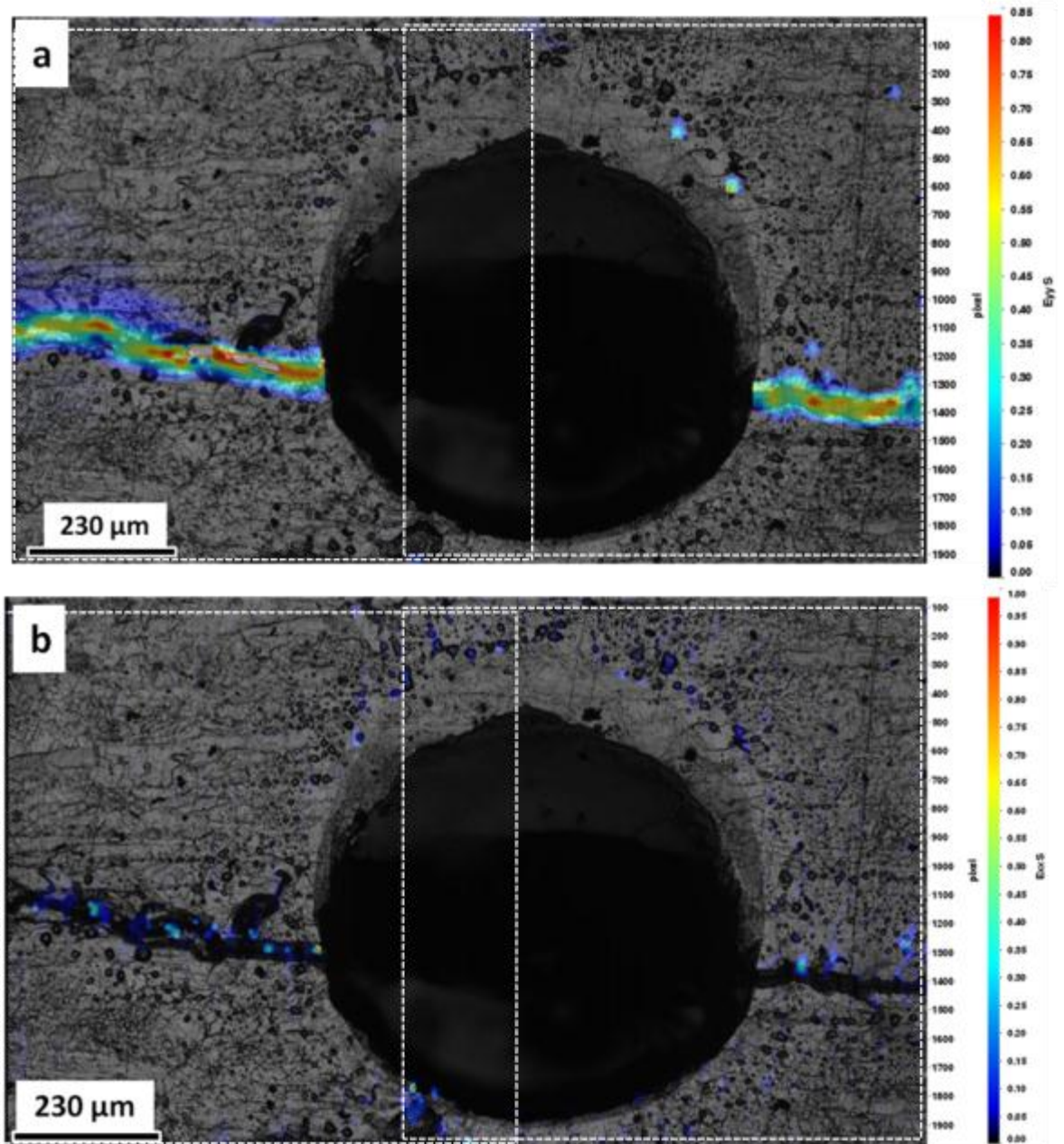


Figure 4-25: The first observed (a) vectors and (b) displacement maps after the crack initiated after (942 Hours-wet droplet)-right branch. Dashed line show the x-position for SCOD measurements.



**Figure 4-26: Strain maps of the propagated crack after 942 hours showing a) the  $E_{yy}$  strain (perpendicular to the crack) and b)  $E_{xx}$  strain (parallel to the crack). Dashed rectangles show the actual locations of two sets of images used to obtain the overlapped strain maps.**

The crack opening displacements (Y-displacements) were measured along the crack (Figure 4-27) for the right and left branches at 942 hours, as a function of the distance from the edge of the droplet as shown in Figure 4-28. The DIC measurements in this experiment did not capture the whole crack's profile because it was propagated outside the field of

view. The droplet edge was stable and did not move between these observations. The strain gauge reading data and average background strain calculated by the DIC were illustrated in Figure 4-29 after 942 hours. The DIC software calculated the average background strain by using the differentiations in the vertical vectors displacements on both sides of the crack and then divide it on the window size to show the average background strain including the crack itself. Figure 4-29 shows the strain gauge reading data and average background strain calculated by the DIC vector displacement analysis vs. time.

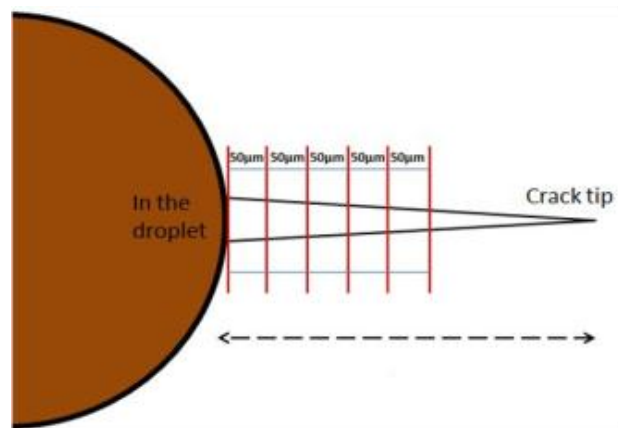


**Figure 4-27: Sketch of the right crack after 942 hours shows how the SCOD measured by using the DIC vertical line profiles analysis from y-displacements images ( $V_y$ ).**

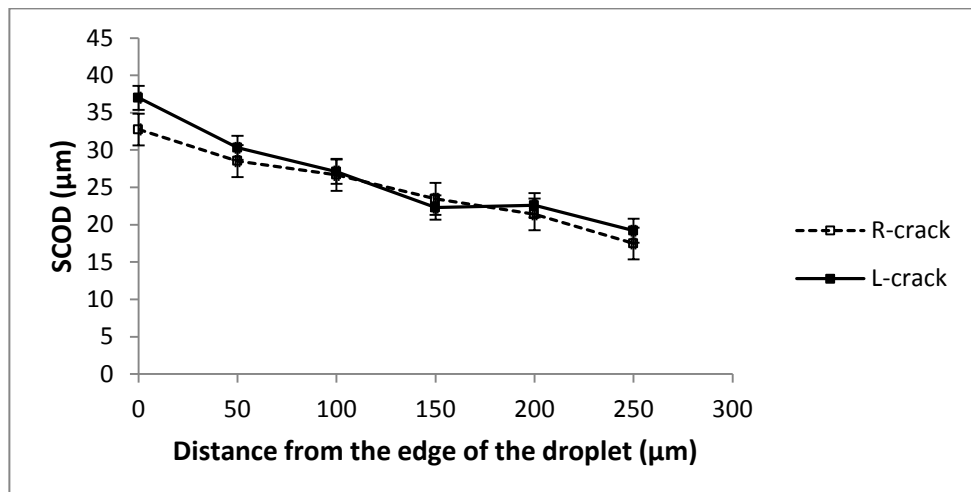


**Figure 4-28: SCOD in (µm) vs. distance from the edge of the droplet for the right and left cracks after 942 hours.**

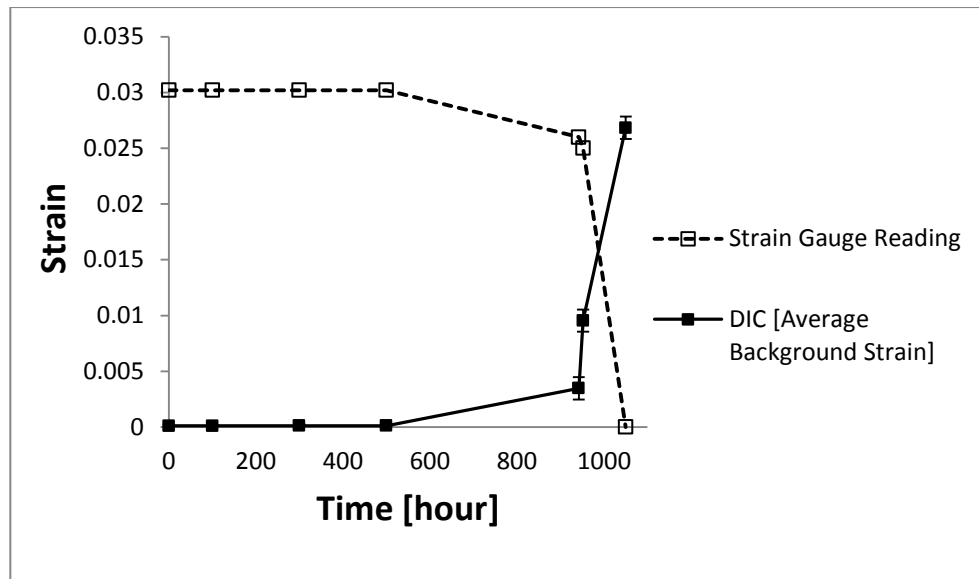


**Figure 4-29: Strain gauge reading data and average background strain calculated by the DIC displacement analysis vs. time.**

#### 4.8.1.2 Rolled Sample: (Transverse to Tensile)/(evaporated salt droplet)

Crack propagation was first noticed after 611 hours from the beginning of the experiment. The previous observation at 542 hours did not show any visible cracking. The experiment was stopped after 665 hours as significant crack propagation occurred. Figure 4-30 shows a series of selected DIC optical images captured at different stages of the experiment in function of the time to illustrate the progress of cracking.

Figures 4-31 and 4-32 show the DIC analysis of the same set of images for the right and left cracks propagated out of the salt droplet. The interrogation window size used was 128 x128 pixels with the maximum overlap used of 87%. The line profiles (showed by a dotted line) in Figures 4-31 and 4-32 were used to measure the vertical strain ( $E_{yy}$ ) along that lines (close to the edges of the droplet) and illustrated in Figure 4-33 for both sides of the crack. Crack length and crack opening displacement with time for both sides were also measured with time as shown in Figures 4-34 and 4-35.

The strain gauge reading data and average background strain calculated by the DIC analysis were illustrated in Figure 4-36 which approved better strain reading for the actual cracked surface by using the DIC analysis which was more sensitive to the strain development on the observed surface. Also, measurements of the crack length determined

by using the optical microscopy and DIC analysis (from the strain maps) are shown in Figure 4-37 for the right and left cracks. Both Figures (4-36 and 4-37) illustrate that application of DIC analysis allows to detection of the occurrence of cracks at an earlier time and those optical observations could lead to underestimate the surface crack measurements.

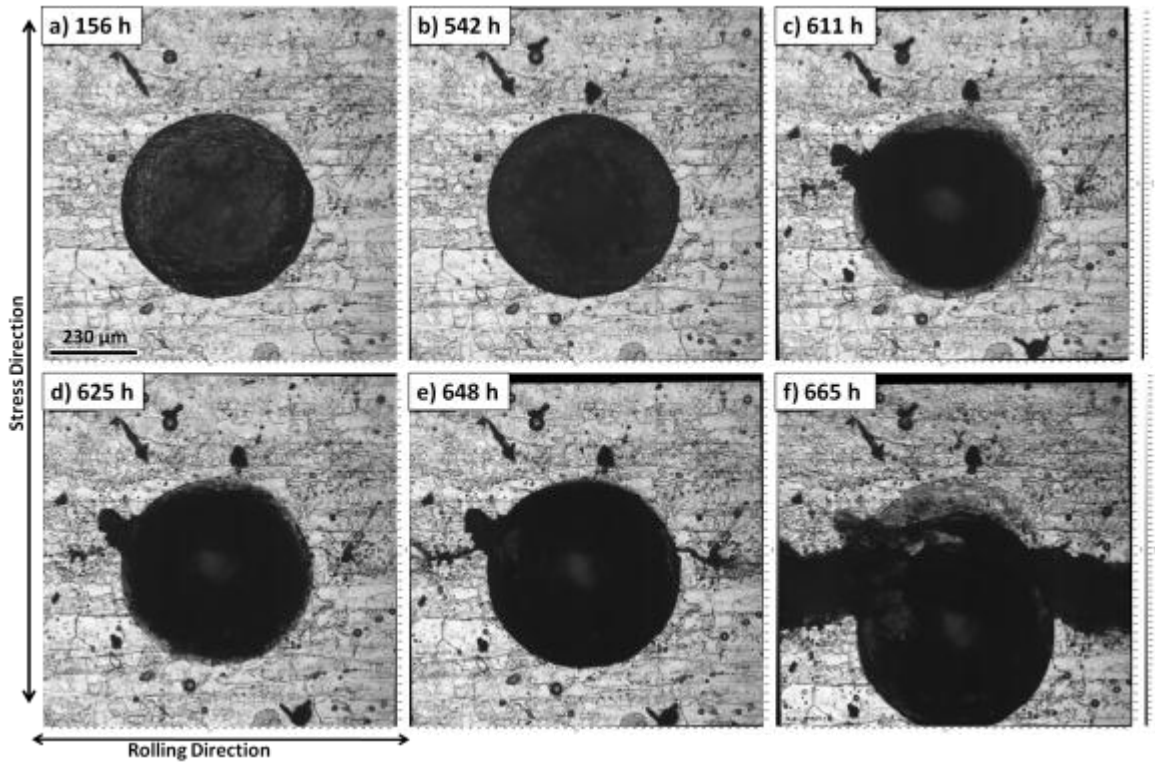


**Figure 4-30: A series of DIC images show different stages of the experiment: a) and b) before the crack initiation, c), d) and e) show the crack propagation out of the salt droplet, f) show the crack view after 665 hours after stopping the test.**

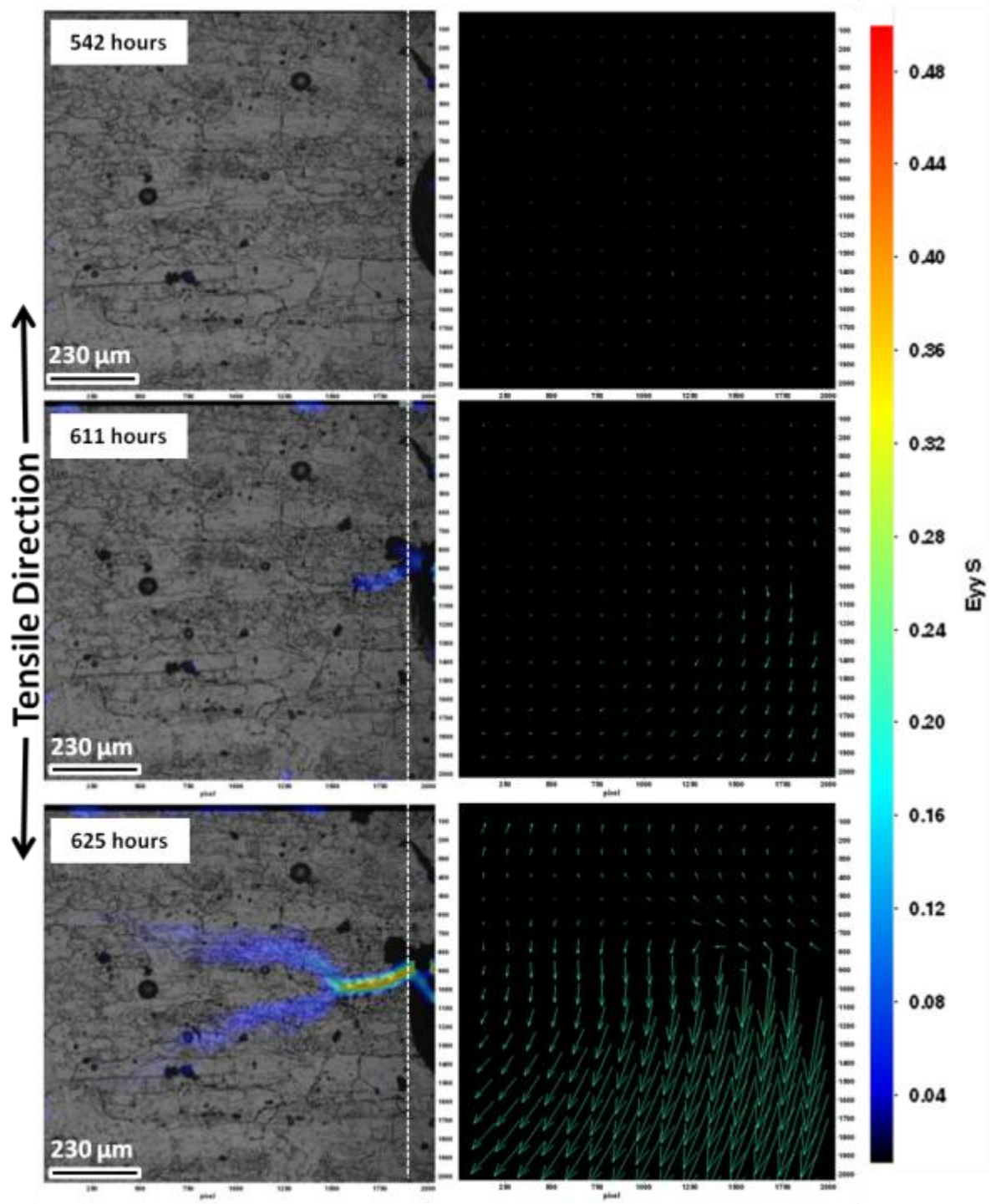


Figure 4-31: A series micrographs with strain maps superimposed and vertical displacements maps to show crack opening displacements relative to the first image (T-T sample, crack propagation perpendicular to the loading direction).

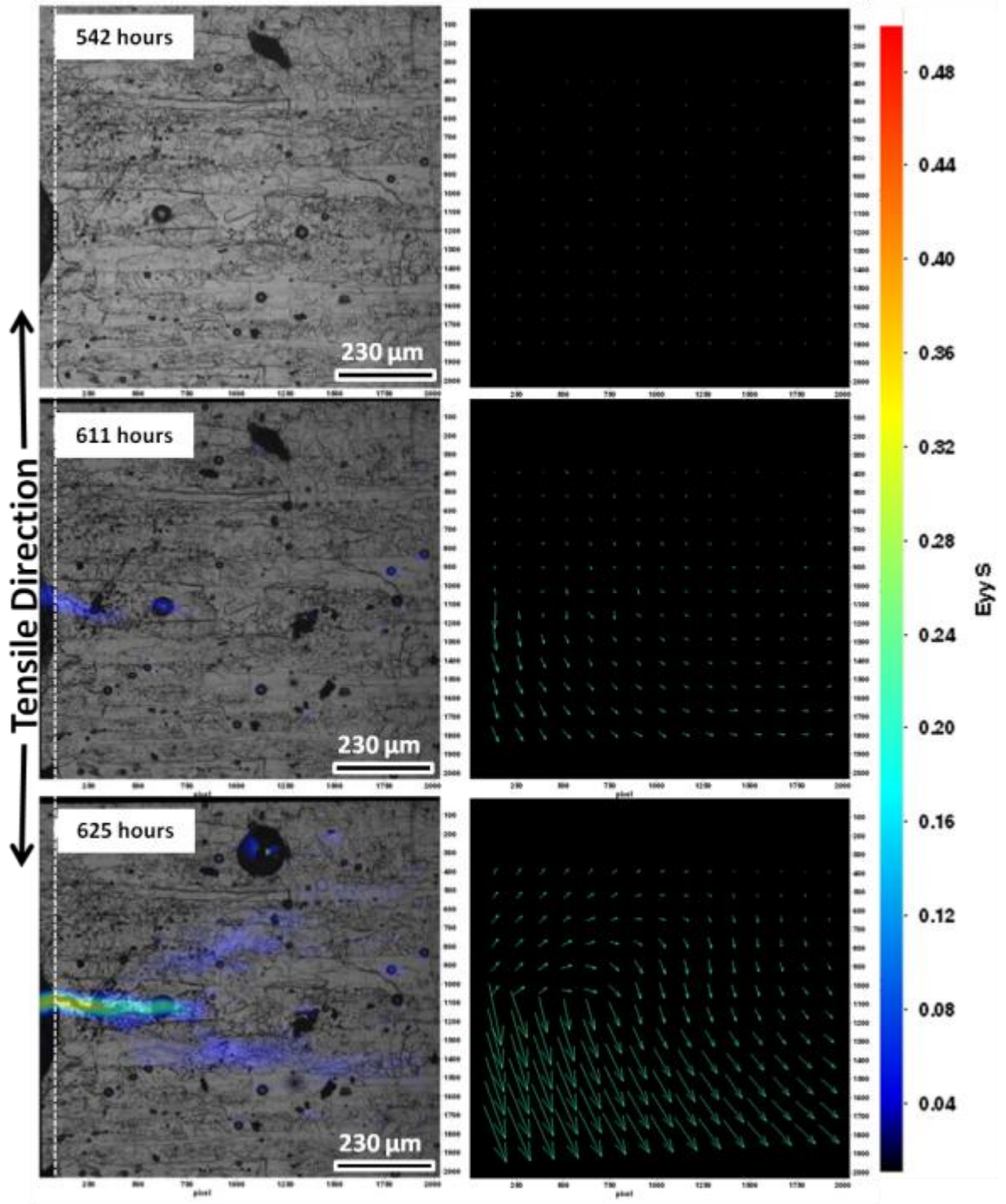


Figure 4-32: A series micrographs with strain maps superimposed and vertical displacements maps to show crack opening displacements relative to the first image (T-T sample, crack propagation perpendicular to the loading direction).

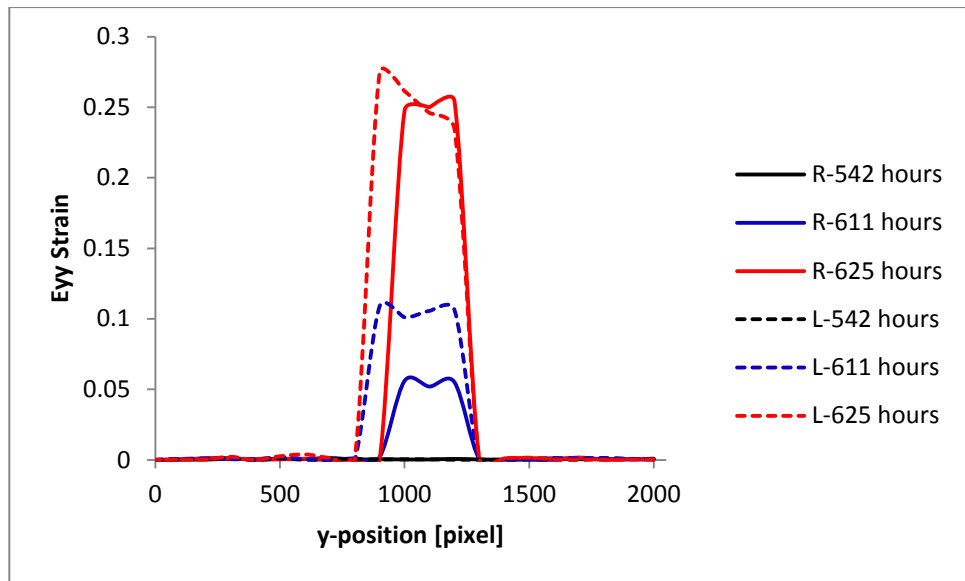


Figure 4-33: Eyy strain profile vs. y-position measured along a line close to the edges of the droplet (indicated by dotted lines in Figures 4-31 and 4-32) with uncertainty  $\approx 0.01 \mu\text{m}$ .

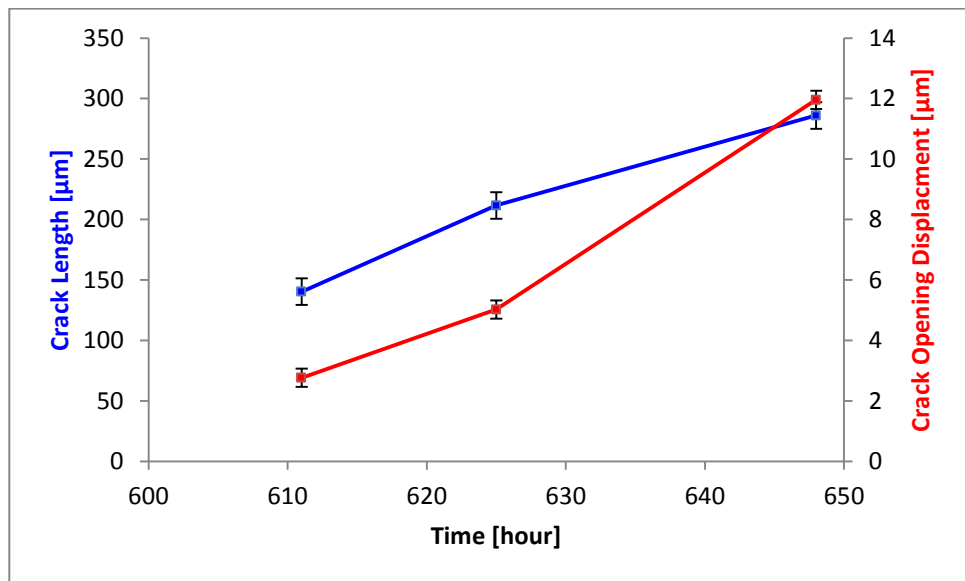


Figure 4-34: Crack length and crack opening displacement with time for the left crack shown in Figure 4-31.

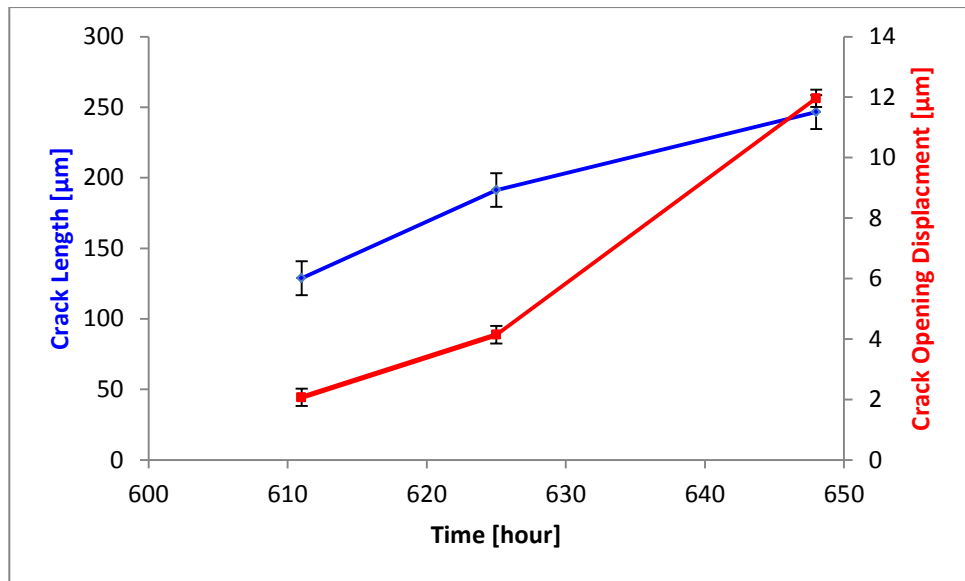


Figure 4-35: Crack length and crack opening displacement with time for the right crack shown in Figure 4-32.

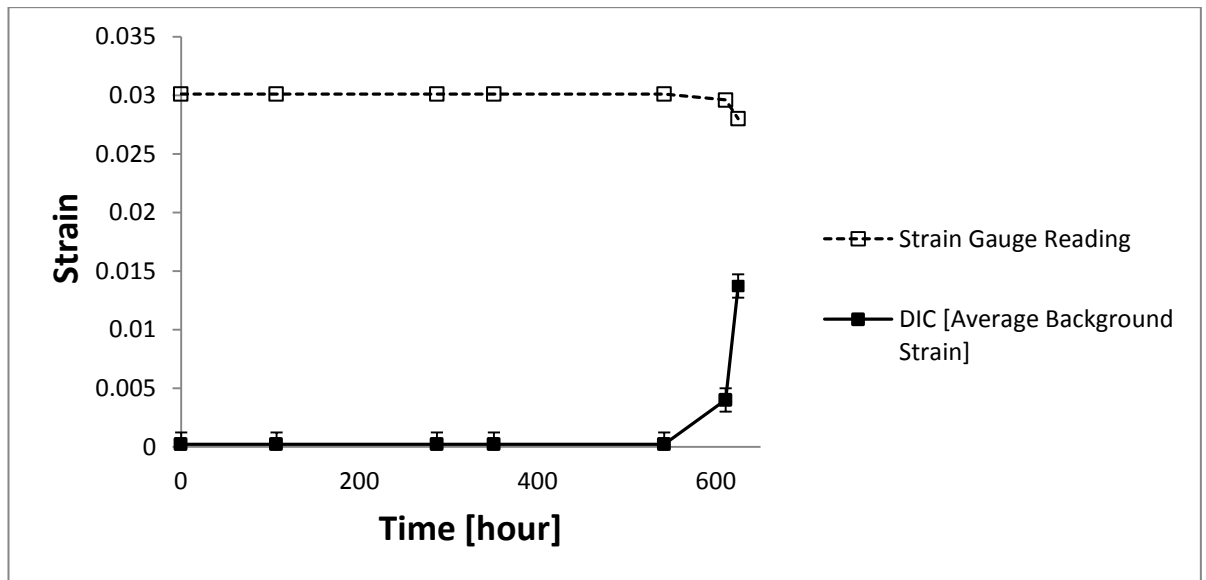
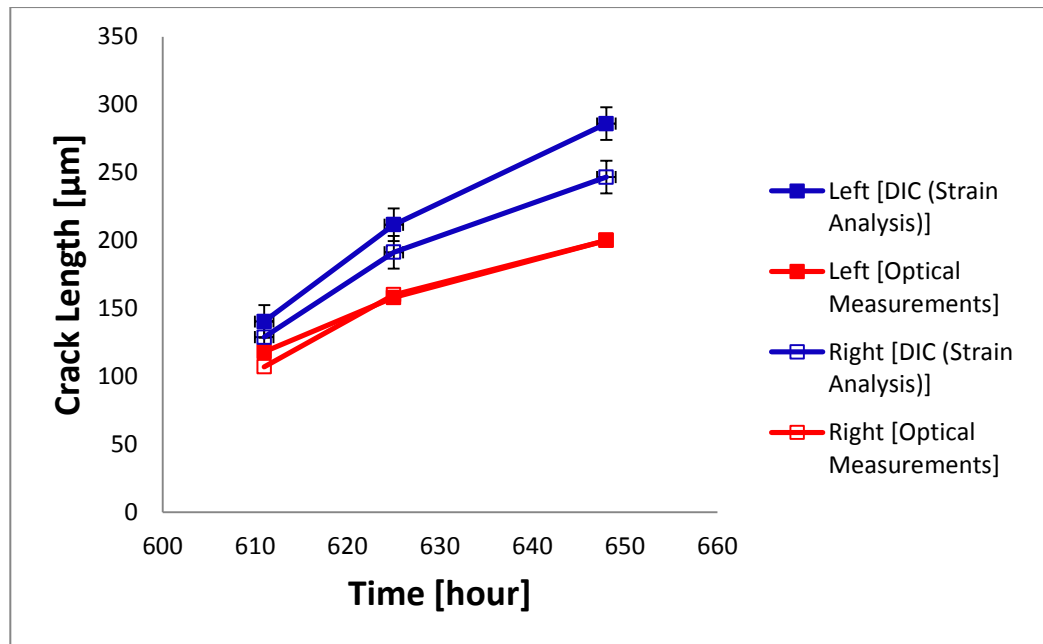


Figure 4-36: Strain gauge reading data and average background strain calculated by the DIC vs. time.



**Figure 4-37: Evaluation of crack length as measured by optical measurements and DIC (strain analysis) for left and right cracks shown in Figures 4-31 and 4-32.**

#### 4.8.1.3 Rolled Sample: (Longitudinal to Tensile)

Figures 4-38 shows a series of selected DIC images captured at different stages of the experiment in function of the time to illustrate the progress of the SCC process as explained earlier. The first crack was noticed and developed out of the droplet after 628 hours and then stopped for more than 100 hours. The test was ended after 734 hours to avoid the crevice corrosion in the crack. The crack opening displacement and the length of the crack were illustrated against the time in Figure 4-39.

The strain gauge reading data did not show any obvious change in the strain value until the test was stopped while the average background strain calculated by the DIC vector analysis confirmed a clear development (at 628 hours) which detect an occurrence of a crack in the observed surface earlier than the strain gauge as illustrated in Figure 4-40.

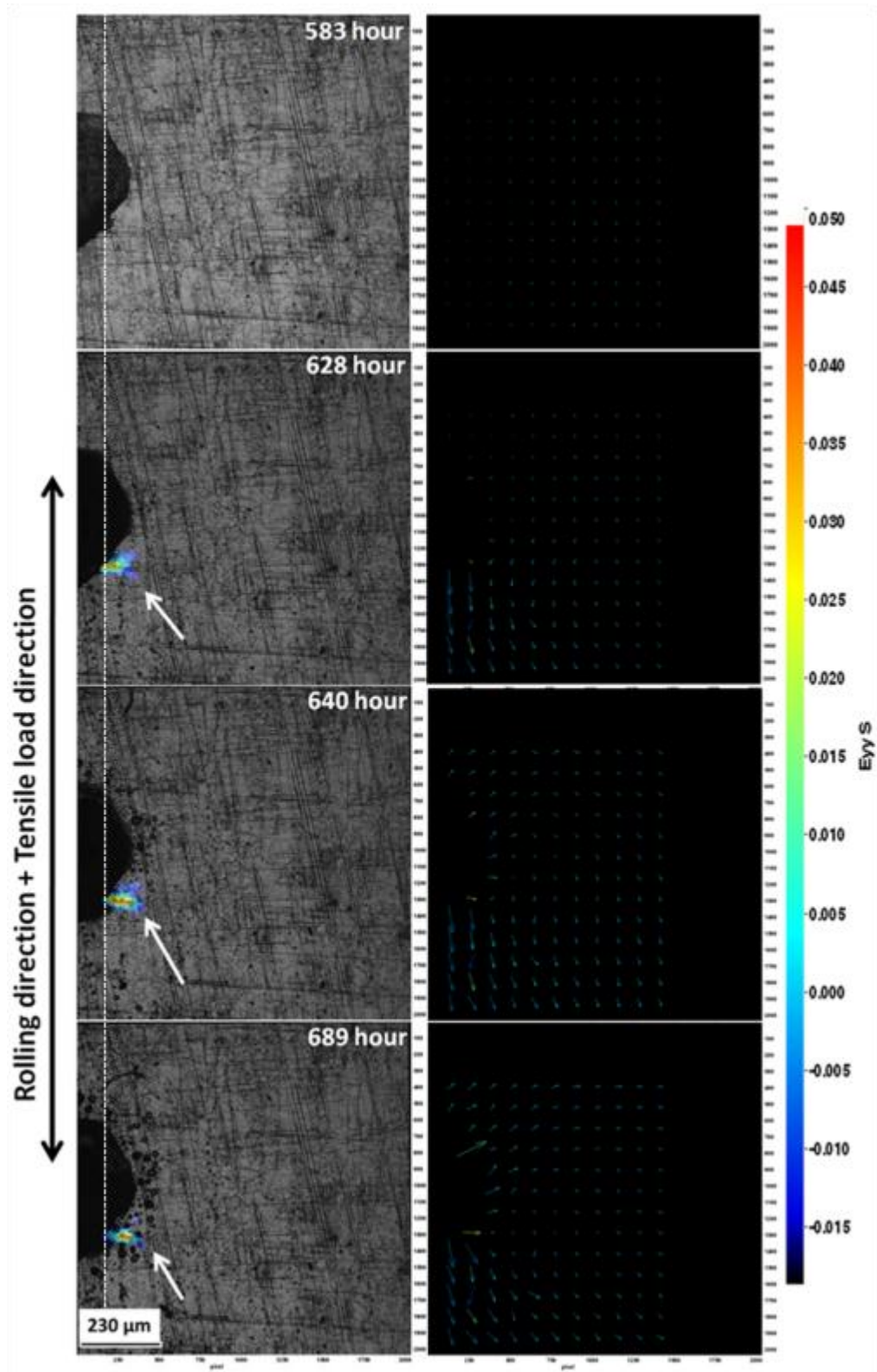
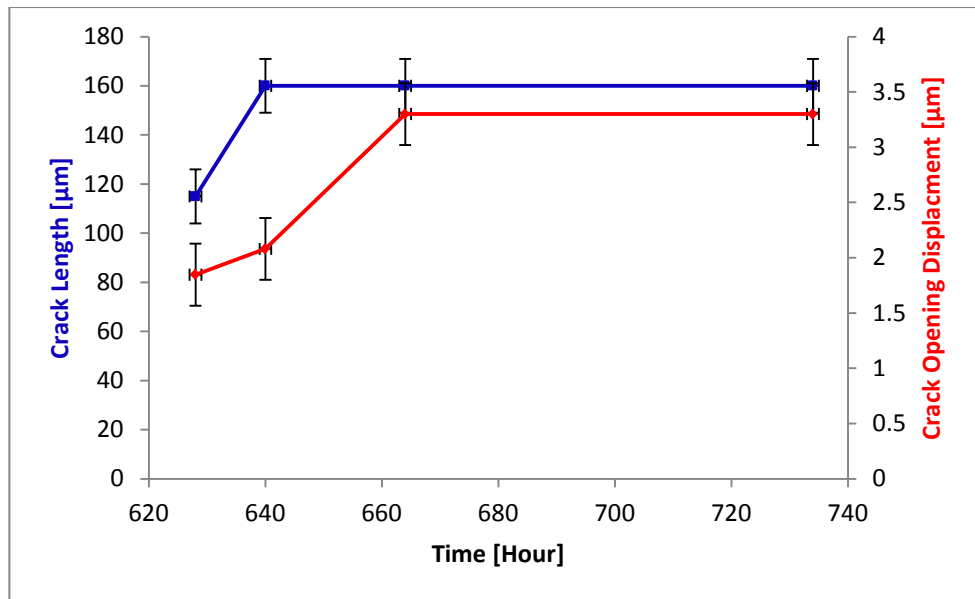
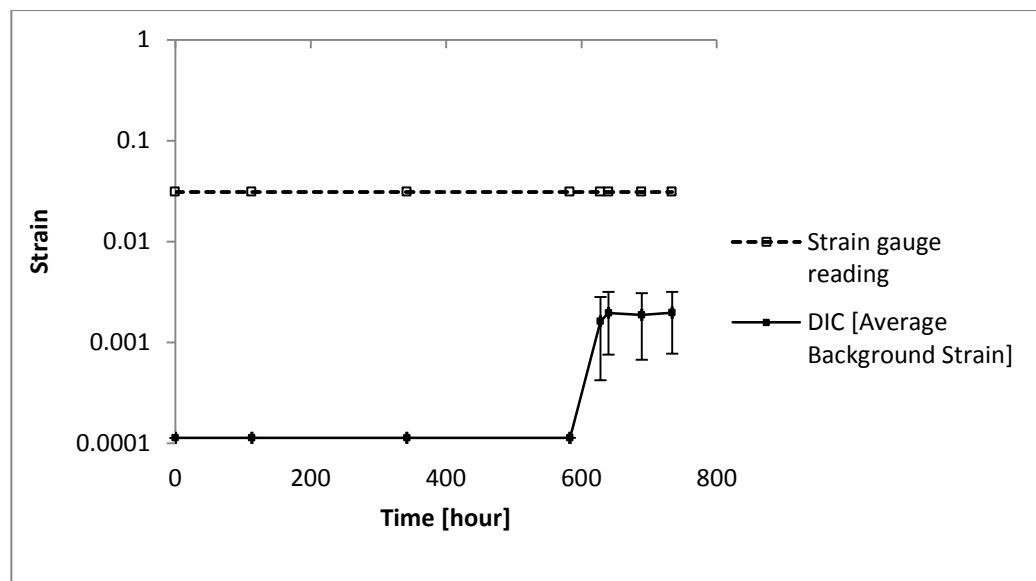


Figure 4-38: A series micrographs with strain maps superimposed and vertical displacements maps to show crack opening displacements relative to the first image (L-T sample, crack propagation perpendicular to the loading direction).



**Figure 4-39: Crack length and crack opening displacement with time for the crack shown in Figure 4-38.**



**Figure 4-40: Strain gauge reading data and average background strain (contains the crack) calculated by the DIC vector displacement analysis vs. time.**

**4.8.1.4 As Received: (Transverse to Tensile)**

DIC monitoring did not detect crack propagation until the crack emerged from the droplet after 1100 hours in both salt droplets. In the first droplet (Figure 4-41), the crack observed after 1263 hours and it was propagated normal to the tensile load in both sides of the

droplet as measured by using the DIC analysis and illustrated in Figures 4-43 and 4-44 for both side cracks at two time intervals. The DIC measurements did not include the whole crack profile because the crack propagated outside the field of view and the tip was beyond the end of the image.

The strain gauge reading data did not show any clear change in the strain value at the back of the sample until the test was stopped while the average background strain calculated by the DIC analysis confirmed a clear development which detect the occurrence of the crack in the observed surface as illustrated in Figure 4-45.

Another droplet on the same sample (Figure 4-42) shows almost the same behaviour and the propagation of the crack was stopped for more than 200 hours at the same place which resulted to stopping the test to study the interaction of the crack with the microstructure and to avoid the crevice corrosion in the crack. Corrosion products clustering from this salt droplet did not allow having accurate results from the DIC analysis comparing to the earlier DIC results.

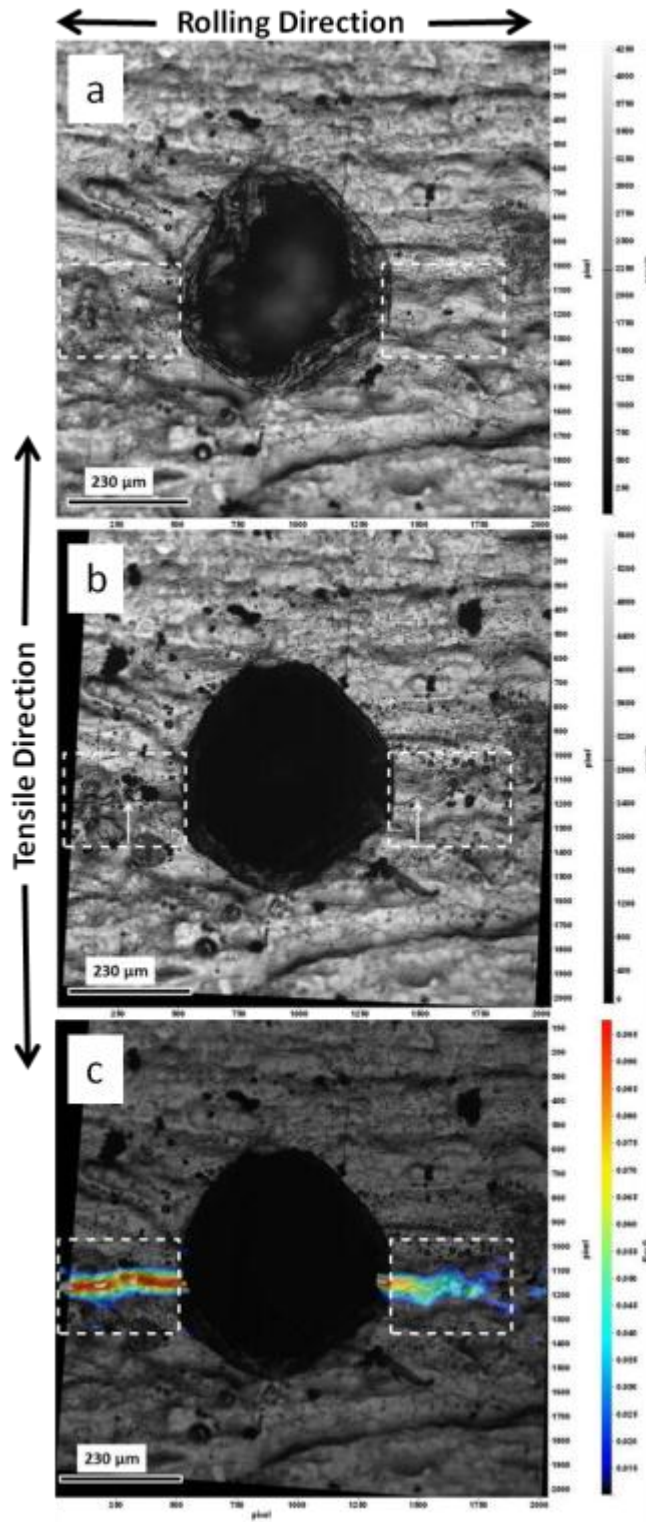
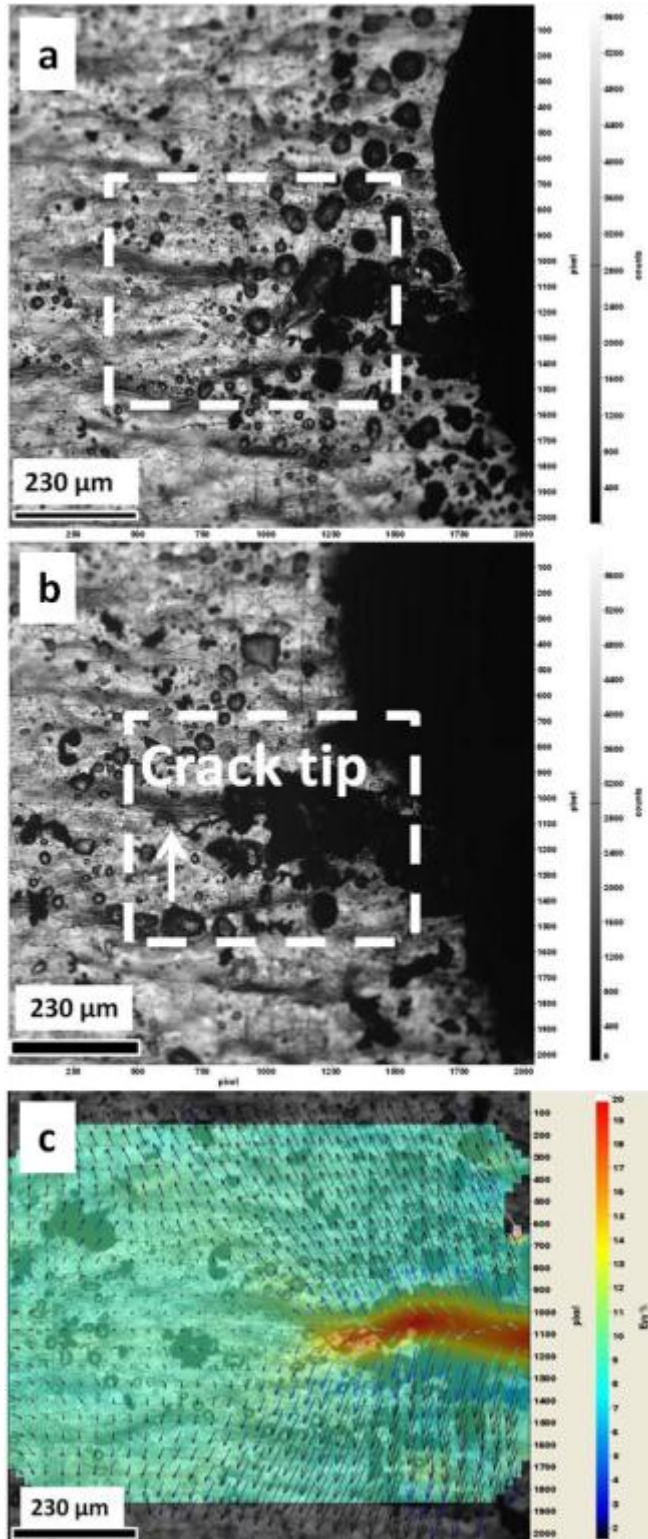


Figure 4-41: Series micrographs with strain maps superimposed relative to the first image, a) after 1116 hours-no cracks out of the droplet , b) after 1263 hours-crack propagated out of the droplet and normal to the loading direction, c) strain map at 1263 hours- shows the strain profile along the crack.



**Figure 4-42: Series micrographs with strain and vectors displacement maps superimposed relative to the first image a) after 1116 hours, b) after 1263 hours and c) vectors displacement map after 1263 hours (crack propagation perpendicular to the loading direction).**

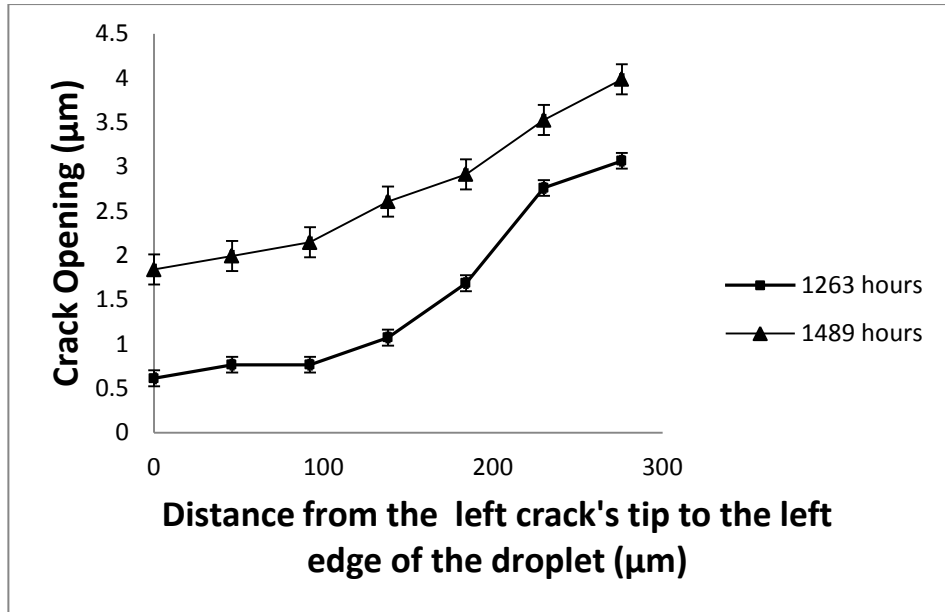


Figure 4-43: SCOD along the left crack (µm) vs. distance from the crack tip.

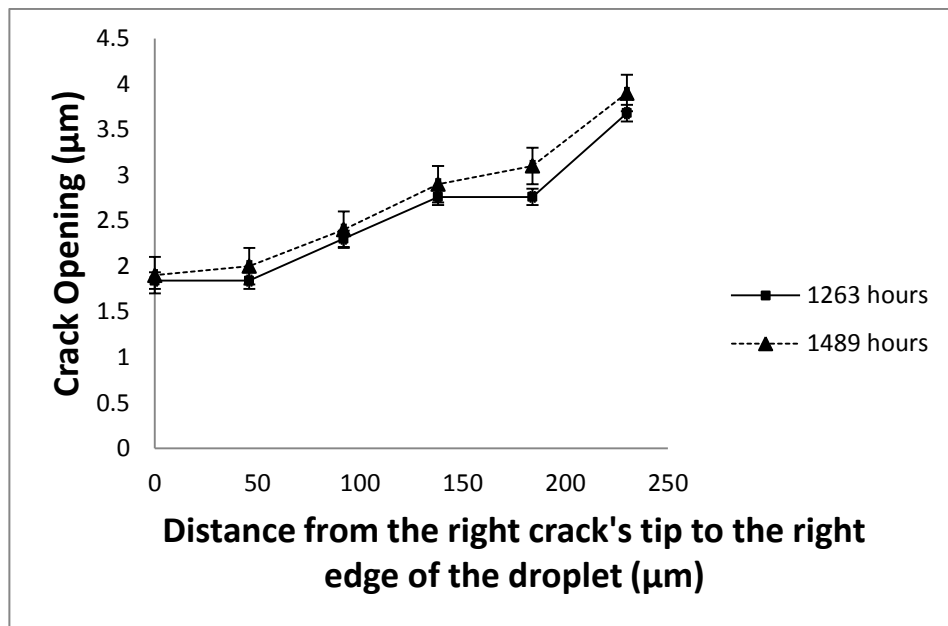
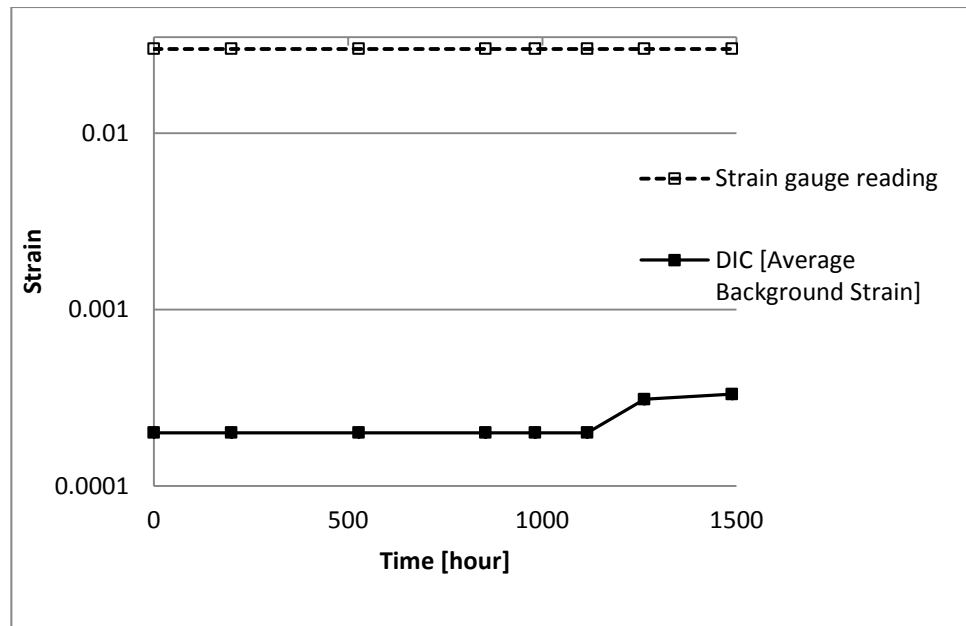


Figure 4-44: SCOD along the right crack (µm) vs. distance from the crack tip.



**Figure 4-45: Strain gauge reading data and average background strain (contains the crack) calculated by the DIC vector displacement analysis vs. time (uncertainty  $\approx 0.00027$ ).**

#### 4.8.1.5 As Received: (Longitudinal to Tensile)

The DIC analysis for this sample did not detect any crack propagation after 1500 hours of testing. The test was then stopped to examine the corrosion occurrence under the salt droplet as shown in the following section.

### 4.8.2 Surface Characterization and Fractography

#### 4.8.2.1 Rolled Sample: (Transverse to Tensile)

In Figure 4-46, the SEM micrograph shows the salt droplets positions and the cracks that propagated perpendicularly to the tensile load. Figures 4-47 and 4-48 show the selective dissolution and pitting, and initiation of short cracks perpendicular to the loading direction under the salt droplet. Moreover, the EBSD analyses show the cracking in  $\alpha$  phase,  $\alpha/\gamma$  and  $\gamma/\gamma$  as shown in Figure 4-49.

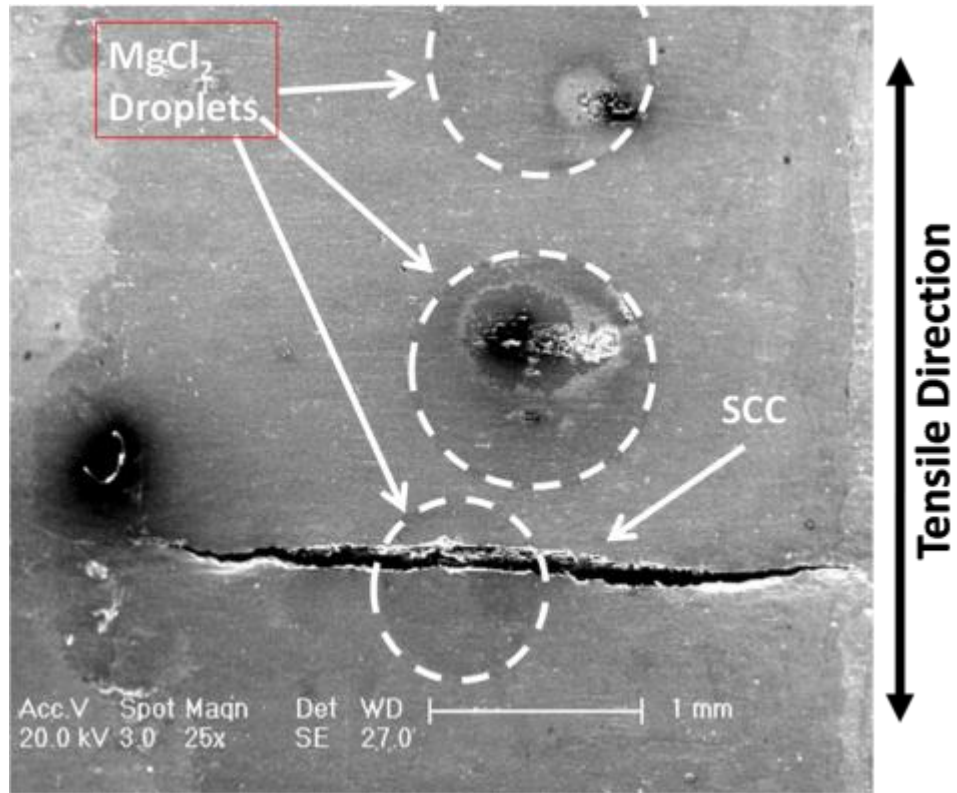


Figure 4-46: SEM micrograph shows the salt droplets and the crack locations.

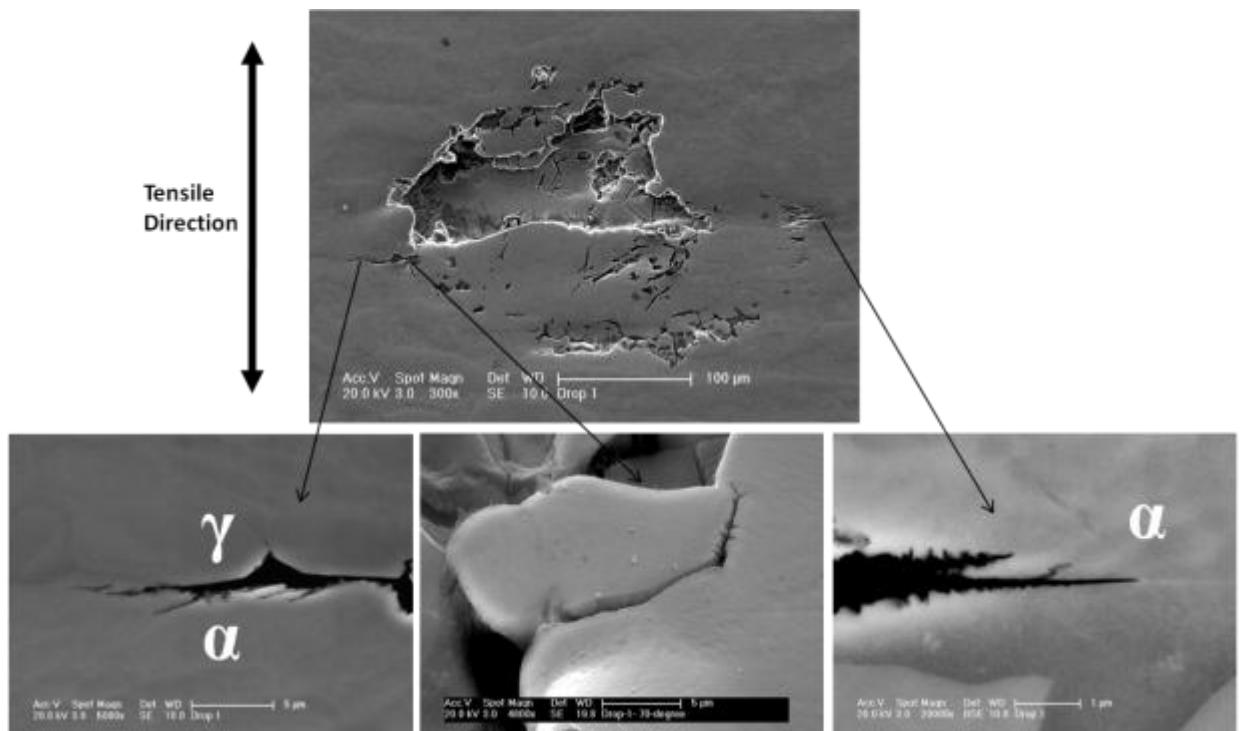
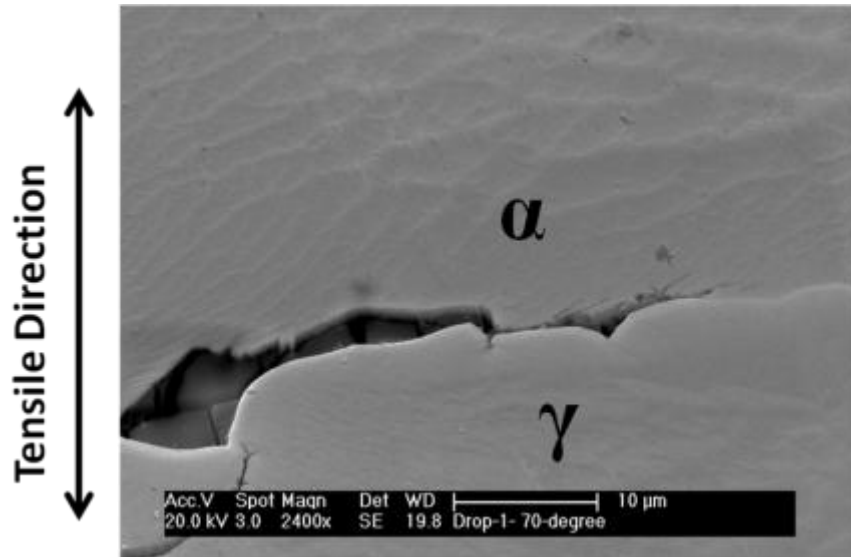
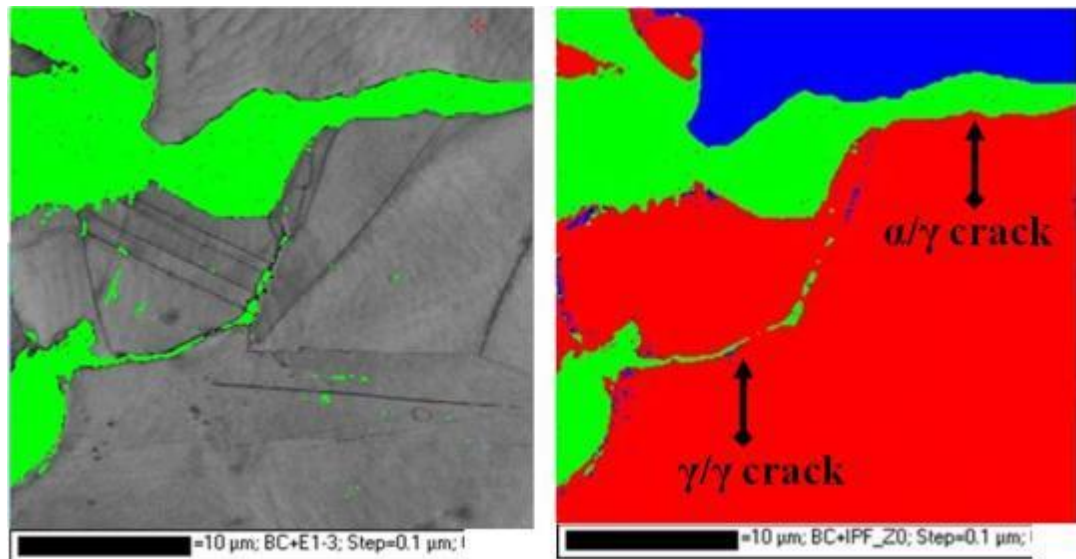


Figure 4-47: Selective dissolution and pitting resulted in initiation of short cracks perpendicular to the load direction under the salt droplets.



**Figure 4-48: SEM micrograph shows interphase corrosion intergranularly ( $\alpha/\gamma$ ).**



**Figure 4-49: EBSD analysis for the crack shown in Figure 4-48 ( $\alpha$ -Blue/ $\gamma$ -Red).**

SEM analysis (Figure 4-50) of the localized corrosion demonstrate the pitting initiated in ferrite phase, short cracks initiated from the pit and along the deformation bands in ferrite phase. The EBSD analysis (Figure 4-51) shows the locations of those short cracks in  $\alpha$ ,  $\alpha/\alpha$  and  $\alpha/\gamma$  (the interphase interface). The crack trace was then compared with the possible traces of  $\{110\}$  and  $\{112\}$  in ferrite and  $\{111\}$  in austenite. The pole Figure shown in Figure4-52 illustrates the crack trace in Figure4-50 which was consistent with the  $\{110\}$  plane.

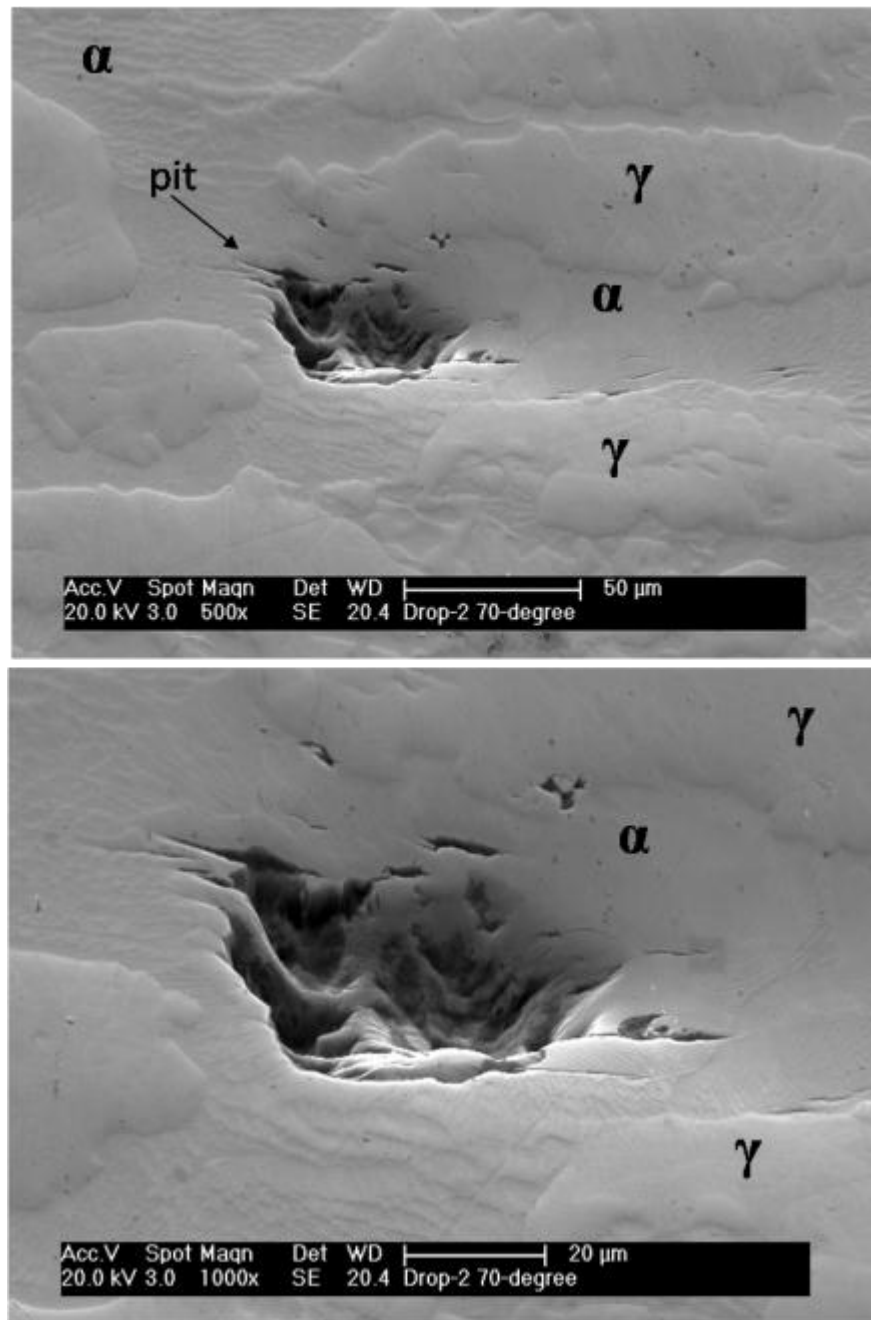


**Figure 4-50: SEM micrographs show pitting in ferrite phase and short cracks initiated from the pit in ferrite phase under the salt droplets shown in Figure 4-44, the austenite and ferrite were identified by using the EBSD technique.**

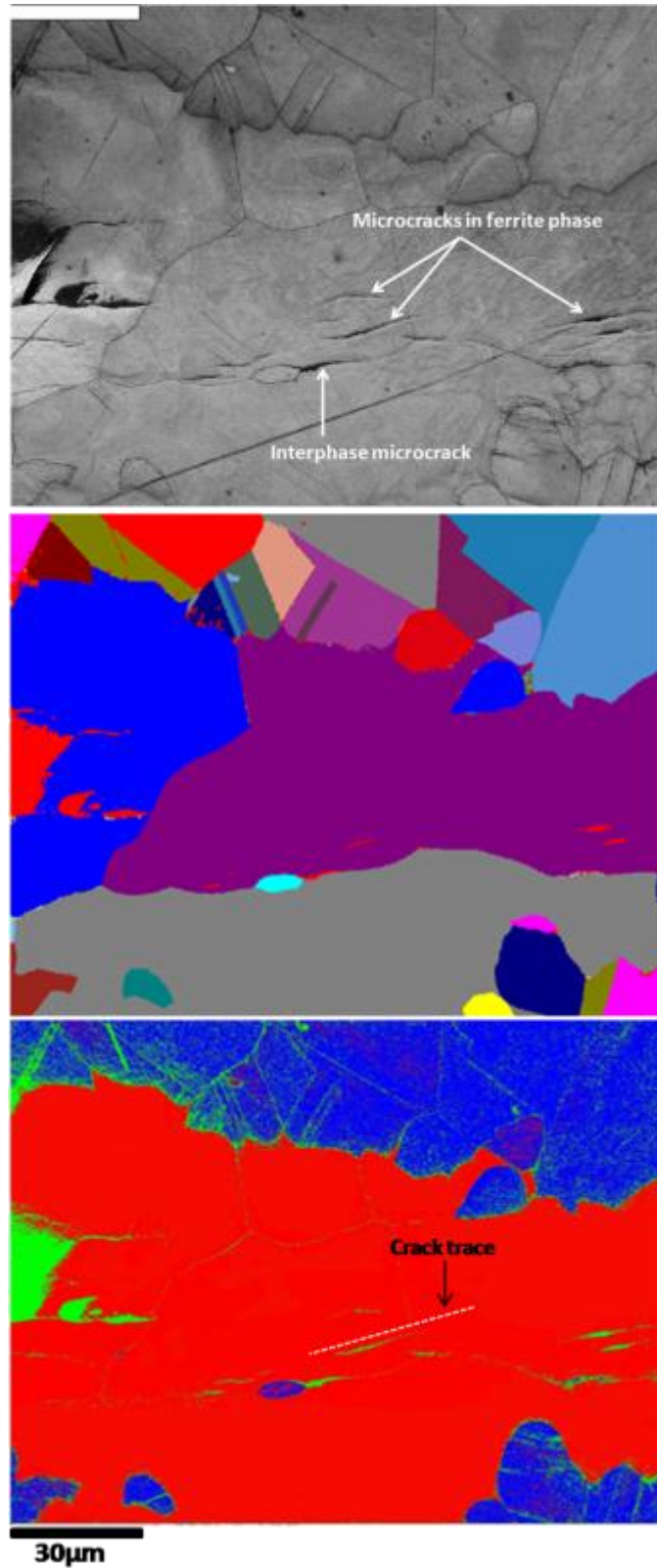
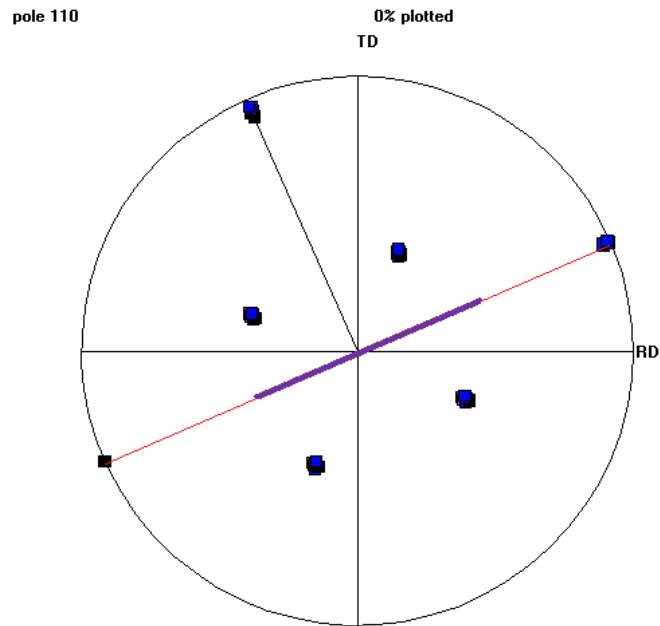
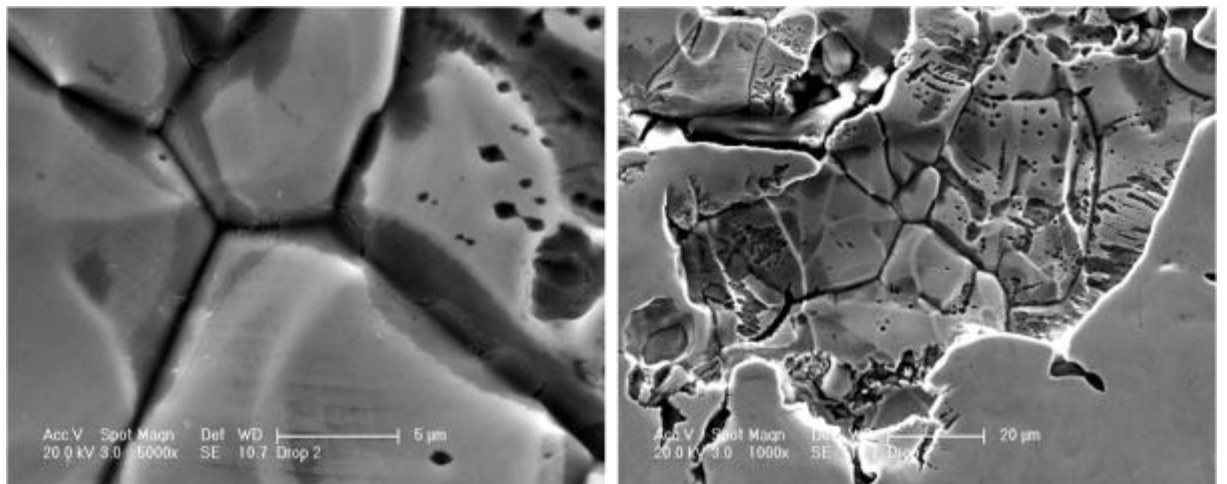


Figure 4-51: EBSD analysis for the microcracks initiated under the salt droplets shown in Figure 4-50 ( $\alpha$ -Red/ $\gamma$ -Blue).



**Figure 4-52: Trace of the short crack shown in the phase map (Figure 4-51) on {110} planes in  $\alpha$ -Phase, Euler1=19°, Euler2=4.8°, Euler3=51°, RD[1-30], TD[62-1] and normal [001].**

Figure 4-53 shows examples of the localized corrosion under the salt droplet which is suffering from intergranular corrosion, selective dissolution and pitting corrosion.



**Figure 4-53: Intergranular corrosion, selective dissolution and pitting observed under the salt droplets.**

Figures 4-54 and 4-55 show the SCC propagation at the back side of the gauge length. They showed clearly that the crack propagates both transgranularly and intergranularly in

both phases. The crack trace in the ferrite was compared with the possible traces of {110} and {112} in ferrite. The pole Figure shown in Figure 4-56 illustrates the crack trace in Figure4-55 which was consistent with the {110} plane.

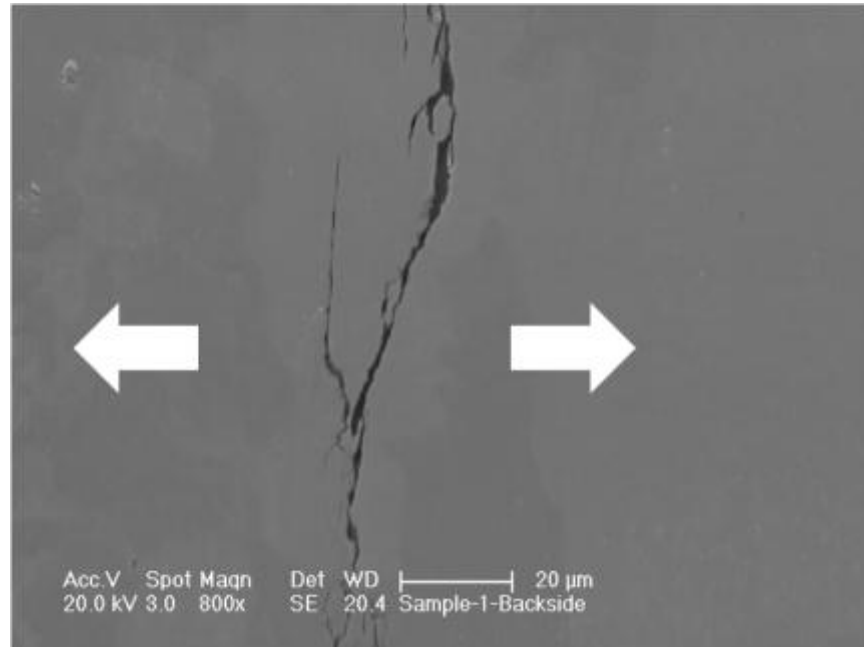


**Figure 4-54: Cracks at the backside of the gauge length, arrows are representing to the tensile direction.**

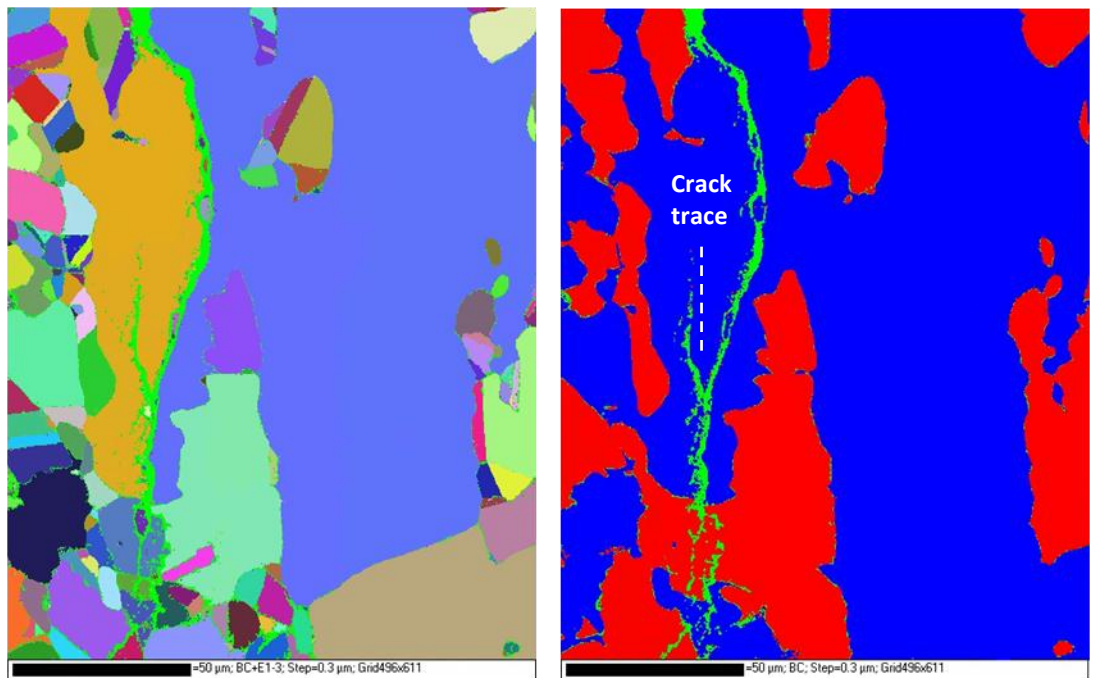


**Figure 4-55: EBSD analysis for the backside cracks shown in Figure 4-52 ( $\alpha$ -Blue/ $\gamma$ -Red).**

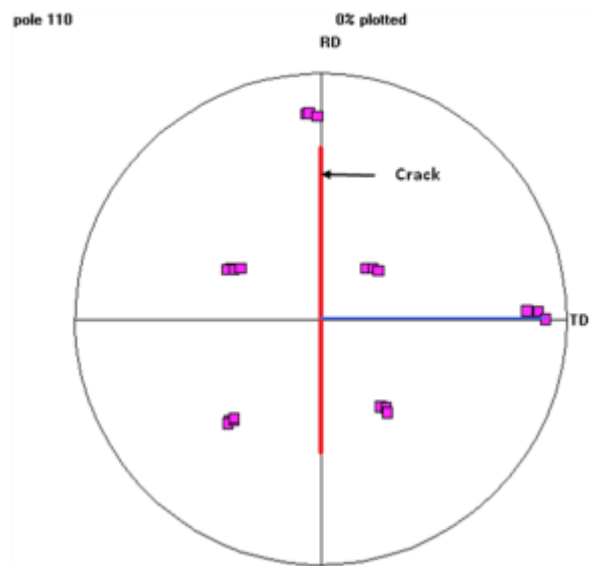


**Figure 4-56: Trace of the crack shown in Figure 4-55 on {110} planes in  $\alpha$ -Phase, Euler1=22.6°, Euler2=9.7°, Euler3=23.5°, RD[6-61], TD[55-1] and normal [016].**

#### 4.8.2.1.1 Fracture surface

Figure 4-57 shows the fracture surface of the rolled sample broken by the normal mechanical tensile testing in the air to be compared with Figures 4-58 and 4-59 that show typical SCC fracture surface of the sample. Since it is well known that Cr is enriched in ferrite whereas Ni is enriched in austenite in DSS, EDX analysis of the spectrums selected in the observed grains was used to distinguish between the phases in the fracture surface as shown in Figures 4-60 and 4-61 depending on the Cr/Ni percentage [168] which confirm the secondary cracking in  $\alpha/\gamma$  interface as shown in Figure 4-62. Also, the EBSD analysis of the cross section of the fracture surface illustrates the secondary cracking in  $\alpha/\gamma$  interface as shown in Figure 4-63.

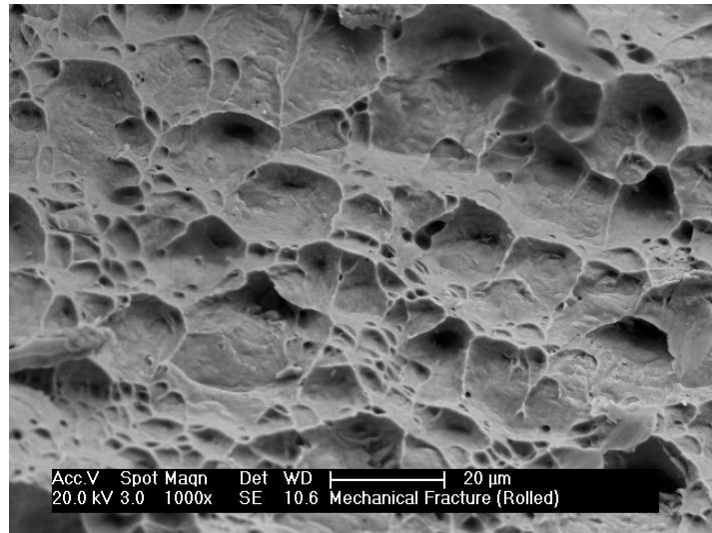


**Figure 4-57: Mechanical fracture of the rolled Sample to compare it with the SCC fracture surface.**

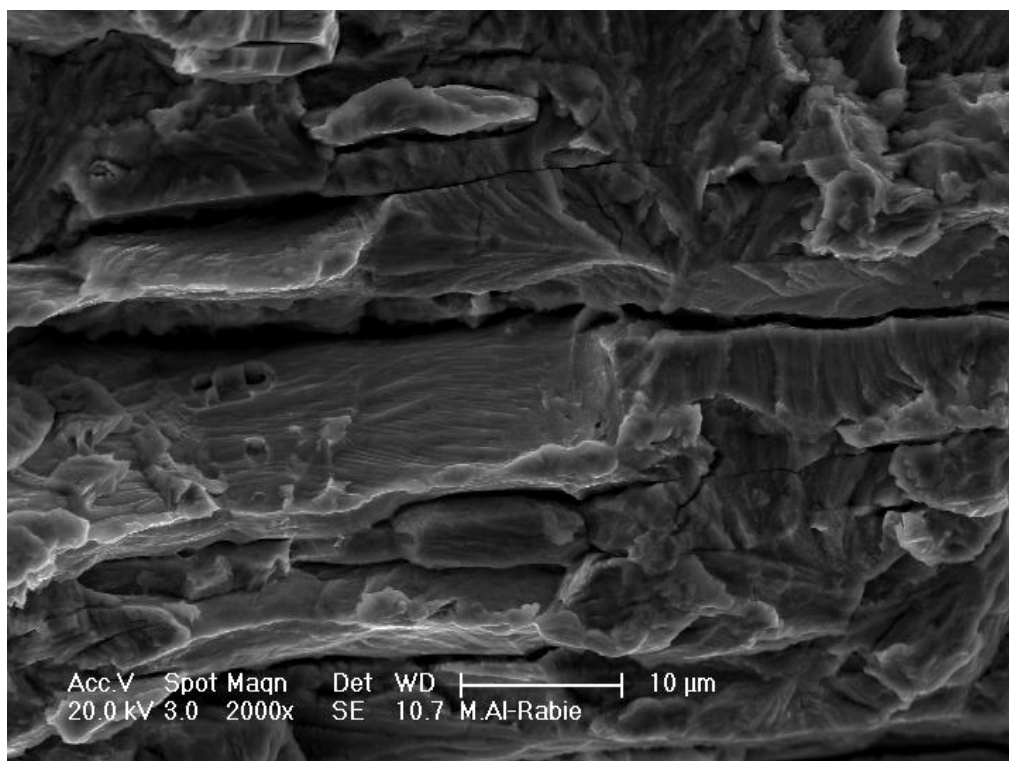


**Figure 4-58: The fracture surface shows a typical stress corrosion cracking fracture.**

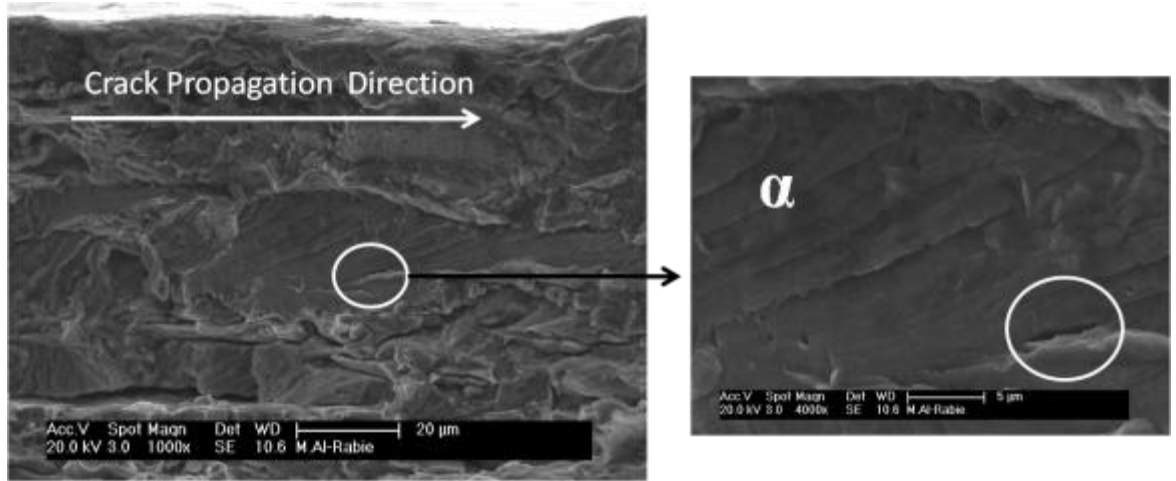


Figure 4-59: SEM micrograph of the fracture surface shows a microcrack along the facets in ferrite ( $\alpha$ -Phase indicated by EDX analysis).

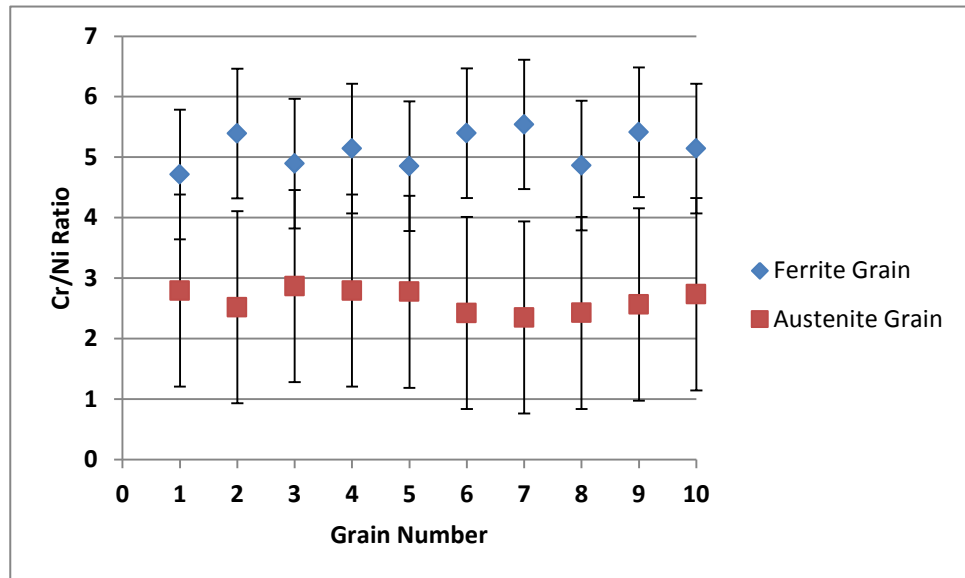


Figure 4-60: Austenite and ferrite grains Cr/Ni ratio measured by EDX analysis in as polished sample.

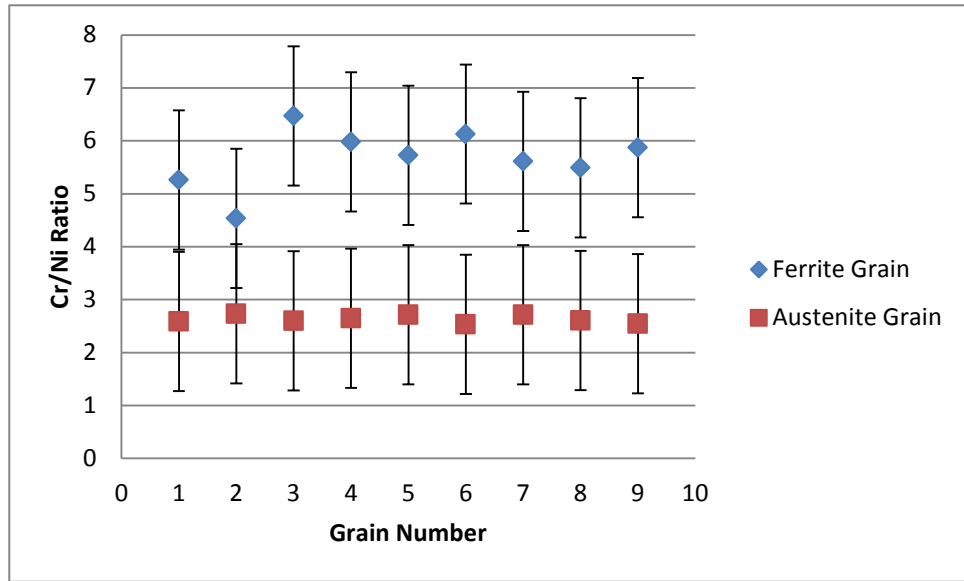


Figure 4-61: Austenite and ferrite grains Cr/Ni ratio measured by EDX analysis in the fracture surface.

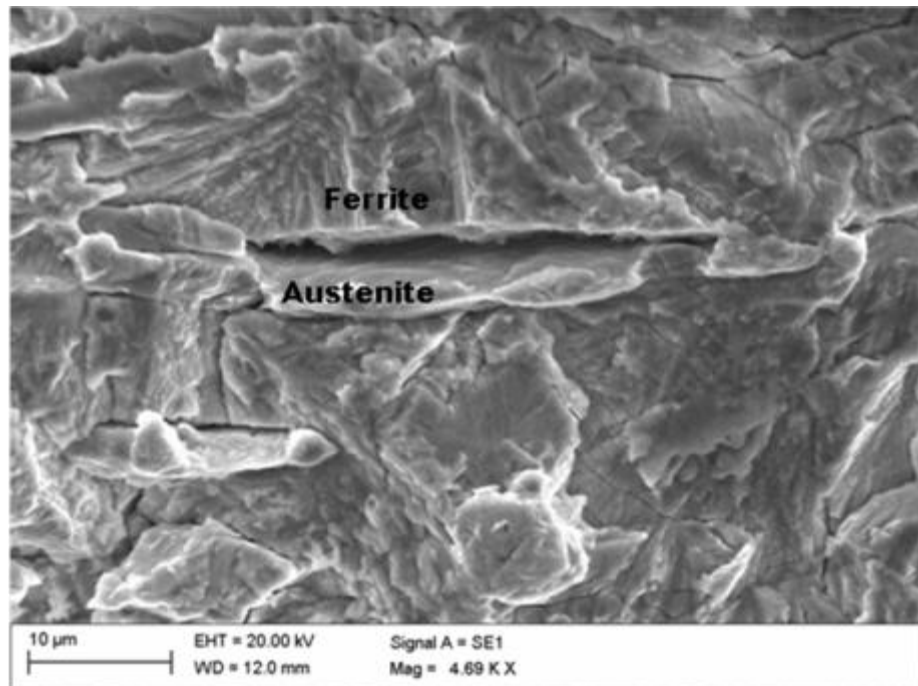
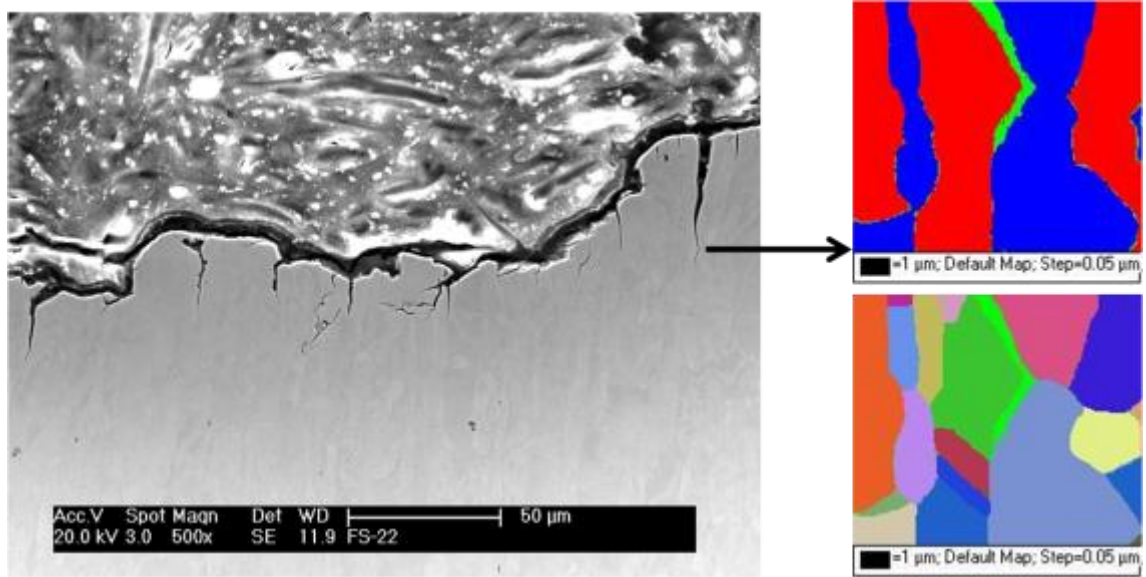


Figure 4-62: Fracture surface observed for specimen shows secondary cracking in  $\alpha/\gamma$ .



**Figure 4-63: SEM image shows the secondary cracks in the cross section of the fracture surface propagated vertical to the main cracking direction along  $\alpha/\gamma$  interphase.**

#### **4.8.2.1.2 Tomography**

X-Ray Tomography was used to look at the crack profile and the shape of the crack in 3D to identify features of the crack, and most importantly, to observe secondary cracks emanating from the primary crack (the one which cracked through) as shown in Figure 4-64. Furthermore, the 2D slices of the same crack showed the behaviour of the crack propagation through the sample and the secondary cracks propagated through (Figure 4-65).

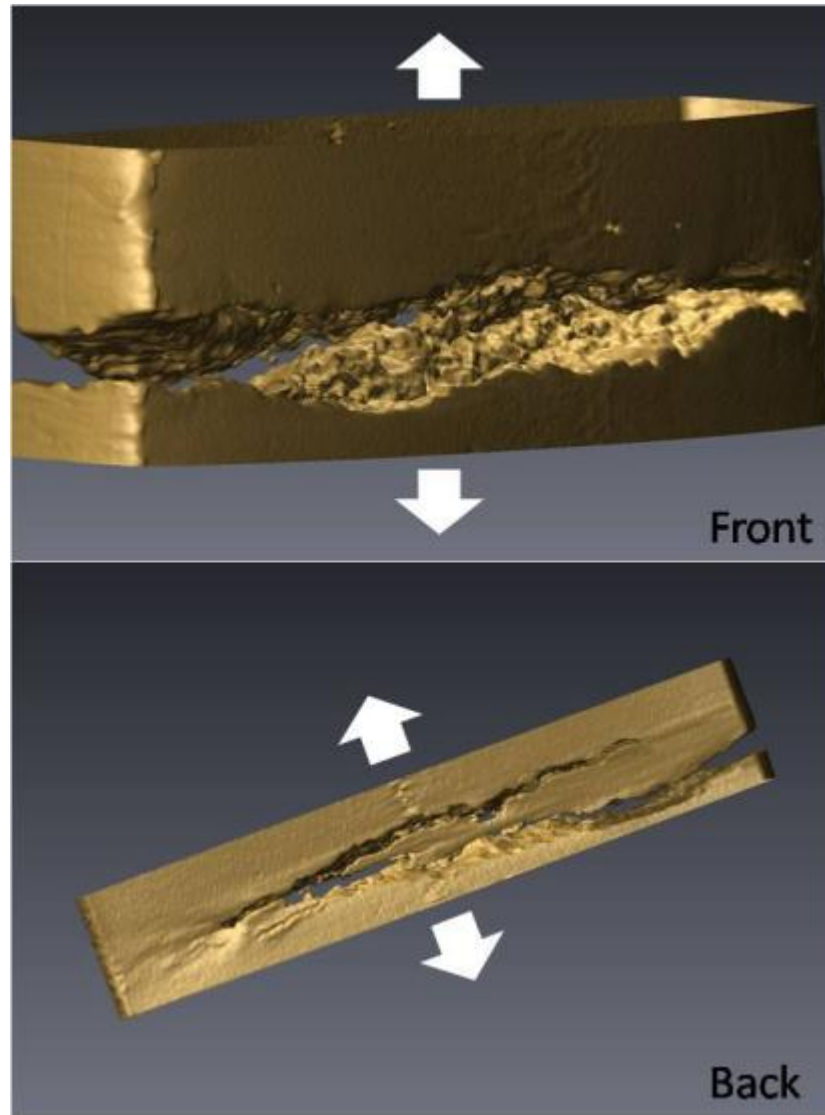


**Figure 4-64: Reconstructed 3-D tomography images for the crack created in the rolled sample, the arrows show the loading direction.**

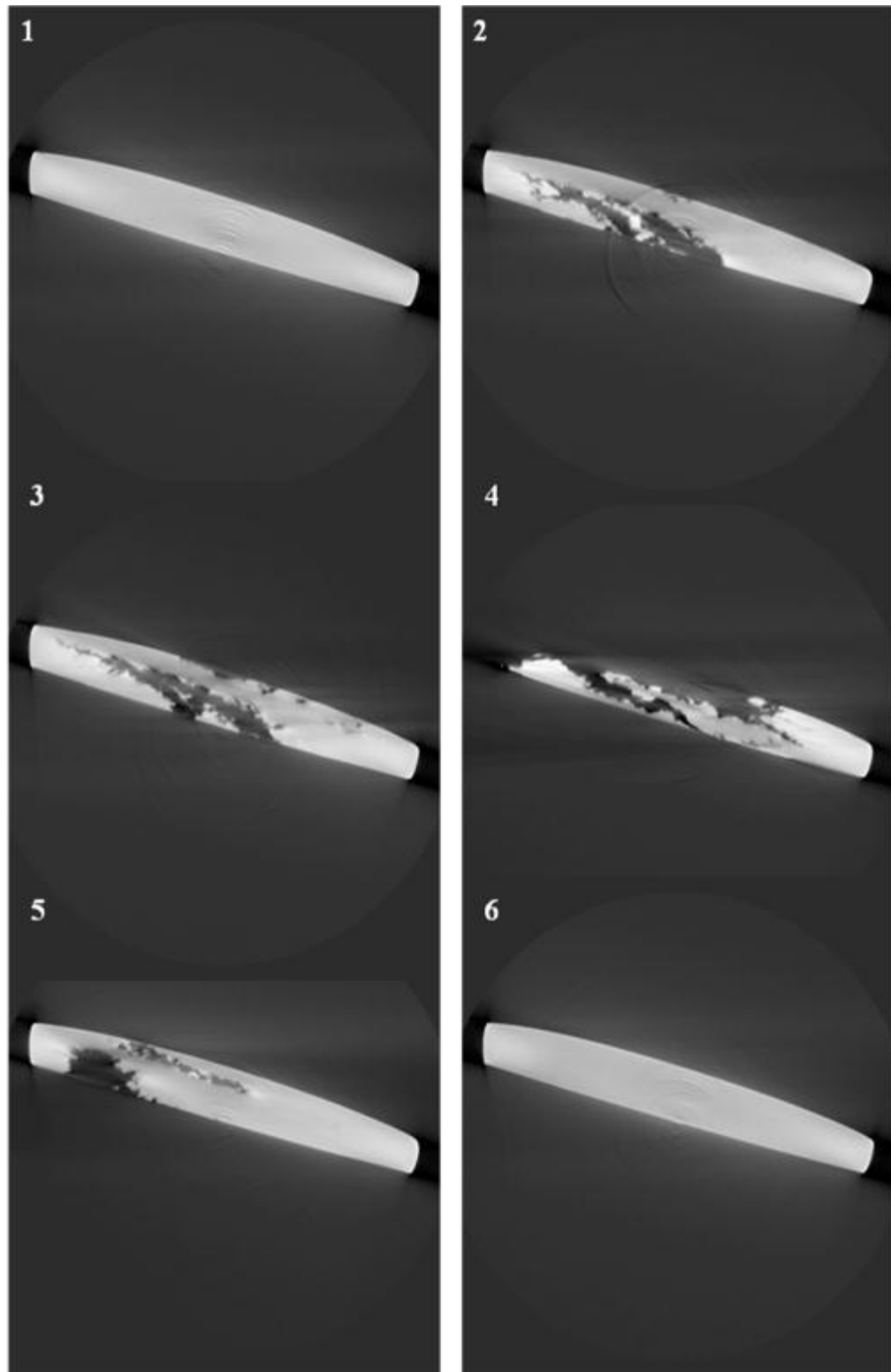


**Figure 4-65: 2D Tomography sections through the data collected from the crack in the rolled sample.**

#### 4.8.2.2 Rolled Sample: (Longitudinal to Tensile)

After the test was stopped and the sample was cleaned in boiling deionised water for two hours, the corroded patches located under the salt droplets were investigated by the SEM. Figure 4-66 shows the localized corrosion created under the salt droplet and the crack propagated out of the droplet normal to the tensile load. Figure 4-67 displays an example of the corrosion occurred along the slip bands in the austenite grains under the salt droplet, the austenite and ferrite grains were identified by using the EDX technique (Cr/Ni %). The EBSD analysis (Figure 4-68) shows the phase map of the area around the crack tip which shows the propagation of the crack through the interphase interface ( $\alpha/\gamma$ ) and stopped for more than 100 hours at high angle boundary  $\gamma/\gamma$  (Figure 4-69).

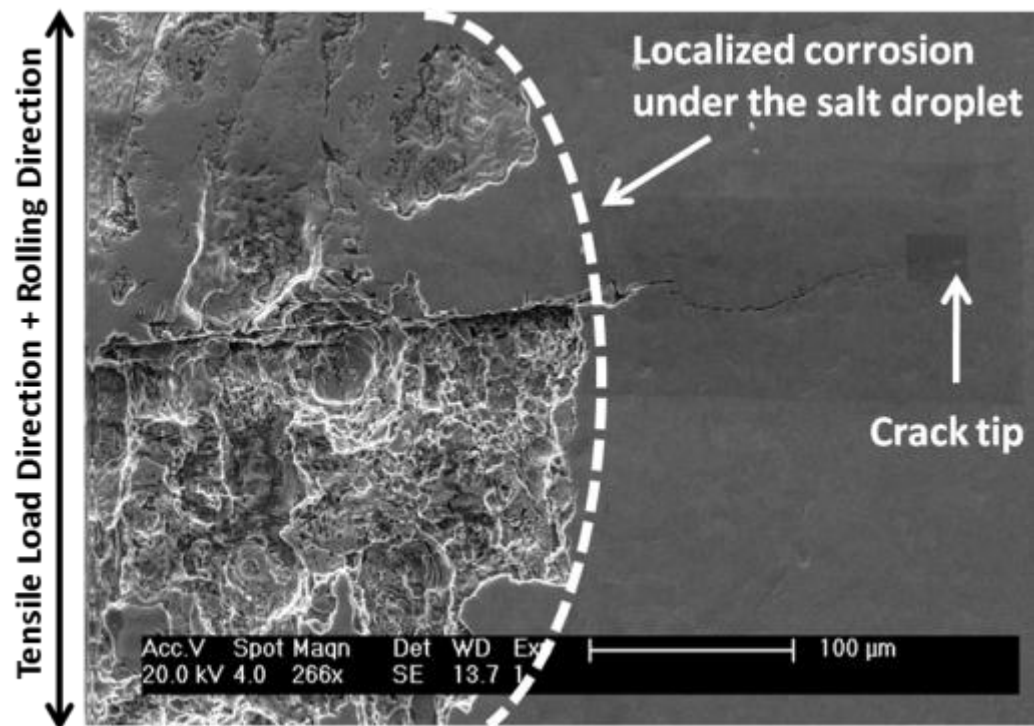


**Figure 4-66: SEM micrograph shows the localized corrosion under the salt droplet and the crack propagated out of the droplet and normal to the loading direction.**

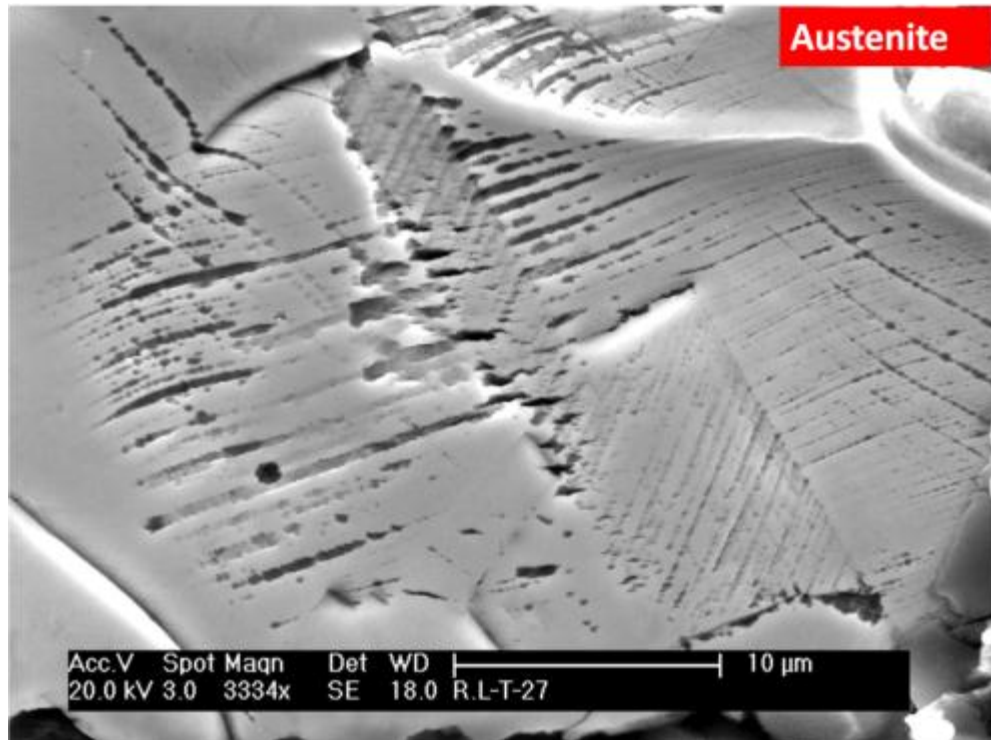


Figure 4-67: SEM micrograph shows the slip bands corrosion in the austenite phase under the salt droplets shown in Figure 4-66, the austenite and ferrite grains were identified by using the EDX technique.

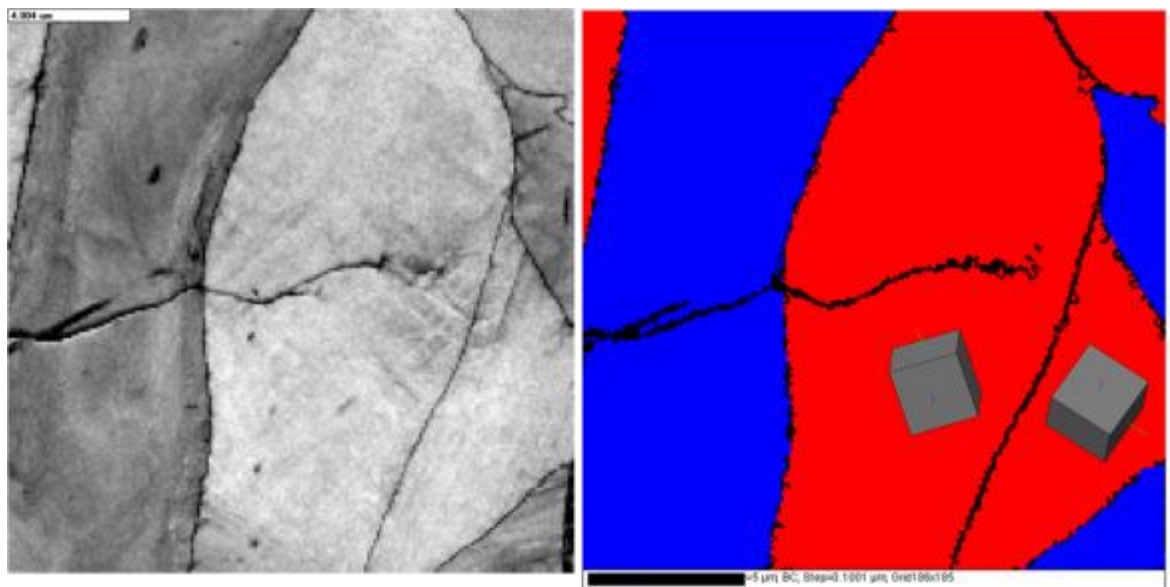
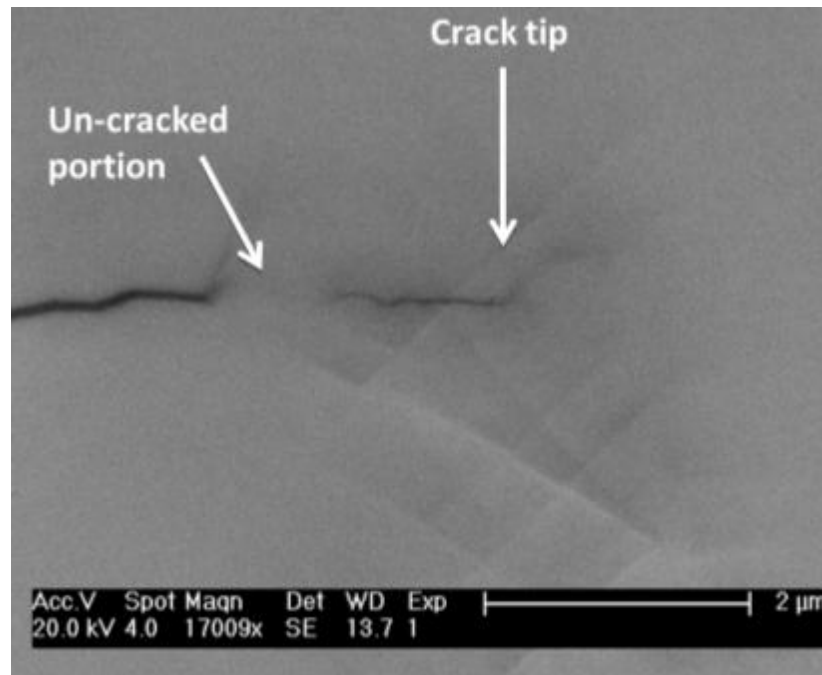


Figure 4-68: EBSD analysis of the crack tip shown in Figure 4-66 ( $\alpha$ -Blue/ $\gamma$ -Red).



**Figure 4-69: SEM Micrograph shows the crack tip position and the un-cracked portion in the same crack shown in Figure 4-68.**

#### **4.8.2.3 As Received: (Transverse to Tensile)**

After the test was stopped and the sample was cleaned in the boiling deionised water for two hours, the corroded patches located under the salt droplets were investigated by the SEM. The arrested crack shown in Figure 4-70 was propagated out of the salt droplet and kinked by the interphase and then stopped at the austenite again and caused a deformation for the grains at the crack tip (Figure 4-71). Moreover, the SEM micrographs in Figure 4-72 show some examples of the localized corrosion created under the salt droplet.

The EBSD maps shown in Figure 4-73 display the phase map of the area around the crack. It shows the propagation of the crack in the ferrite phase and then deflected by the interphase boundary ( $\alpha/\gamma$ ). Furthermore, the cracks traces shown by the dotted white lines in Figure 4-73 in the ferrite were compared with the possible traces of  $\{110\}$ ,  $\{112\}$  and  $\{123\}$  in ferrite as shown in the pole Figures (Figure 4-74).

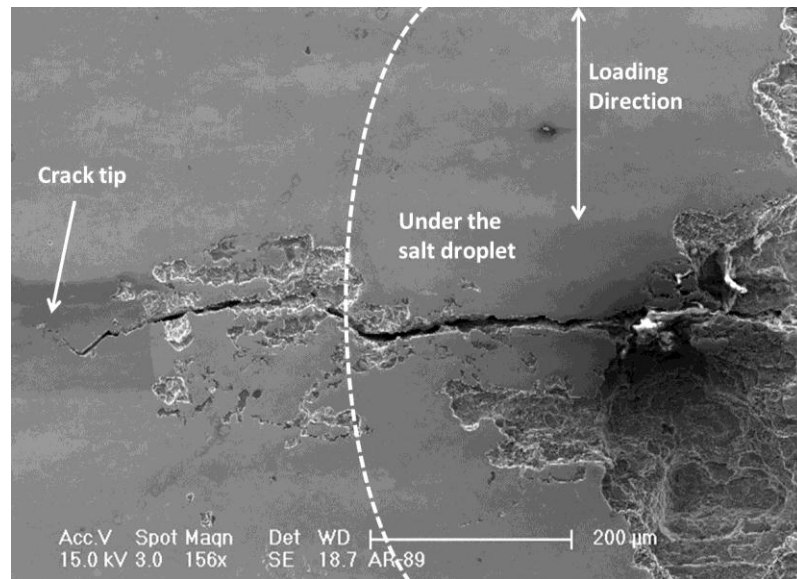


**Figure 4-70:** SEM micrograph shows the localized corrosion under the salt droplet and the crack propagated out of the droplet and normal to the loading direction.

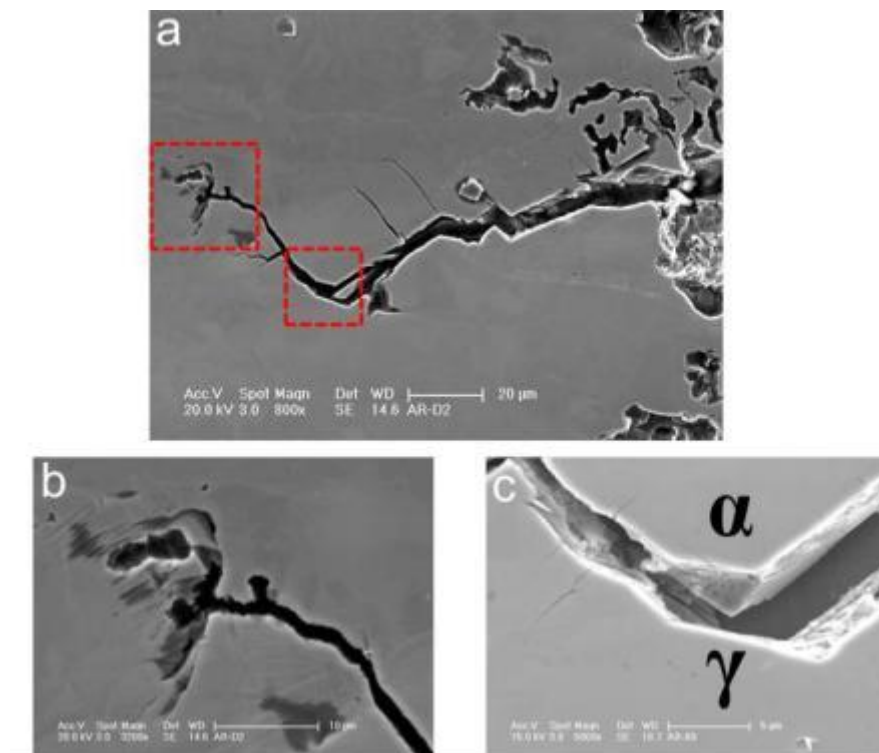


**Figure 4-71:** SEM micrographs show a) the localized corrosion under the salt droplet and the crack propagated out of the droplet, b) the grain deformation at the crack tip and c) the deflection of the crack at the austenite grain, the grains were identified by using the EBSD analysis.

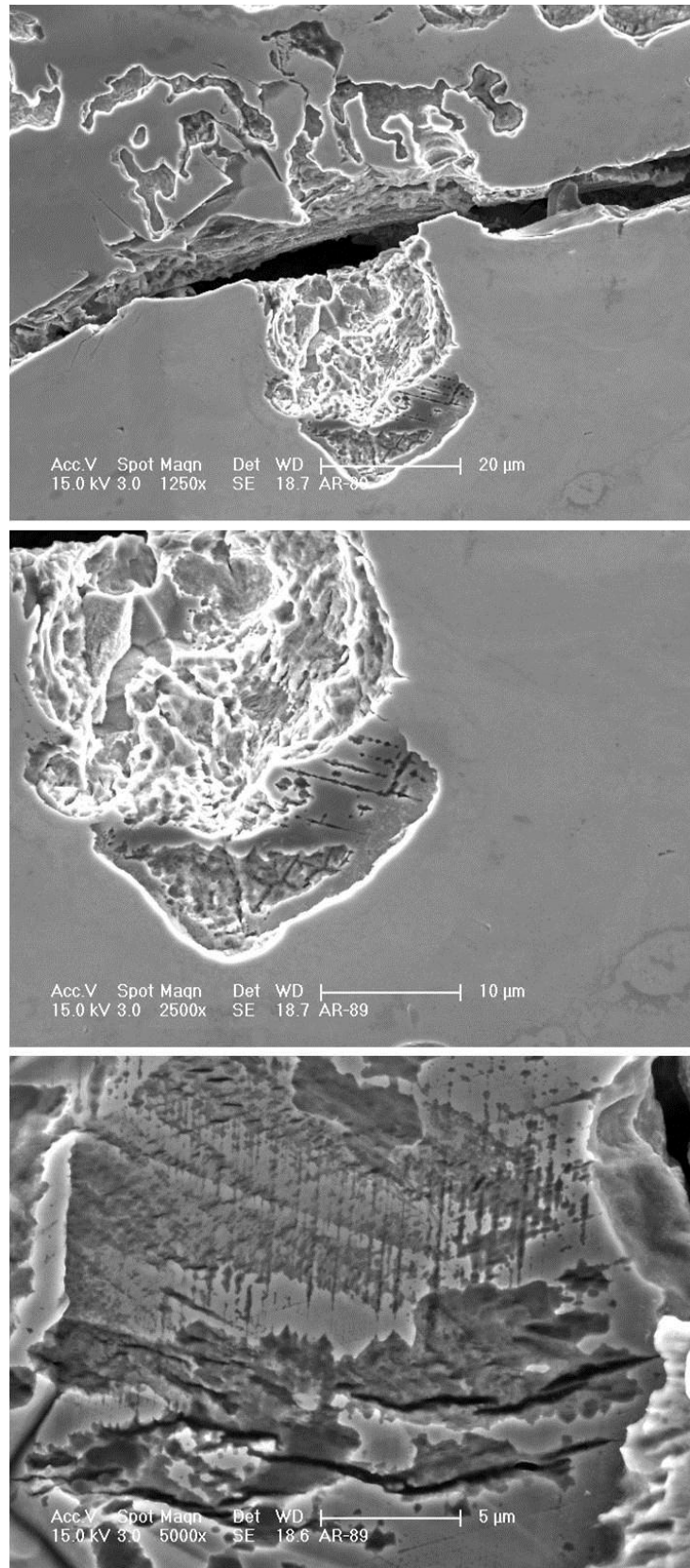


**Figure 4-72: Forms of the localized corrosion and cracks created under the salt droplet.**

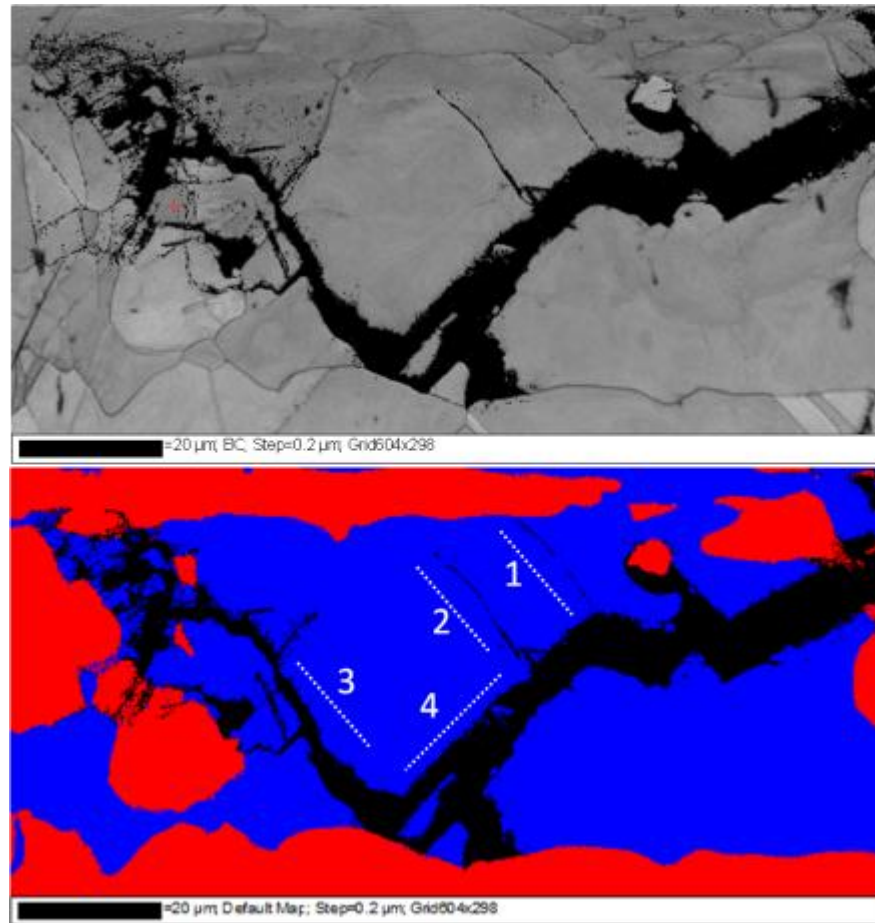


Figure 4-73: EBSD analysis for the crack in Figure 4-71 shows the band contrast and phase maps ( $\alpha$ -Blue/ $\gamma$ -Red).

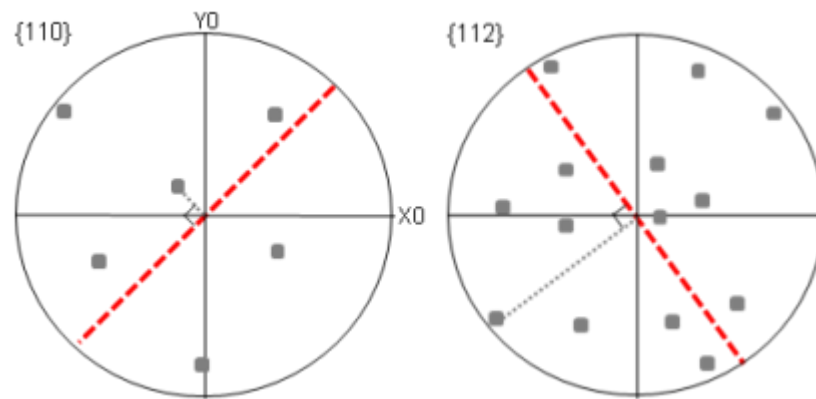
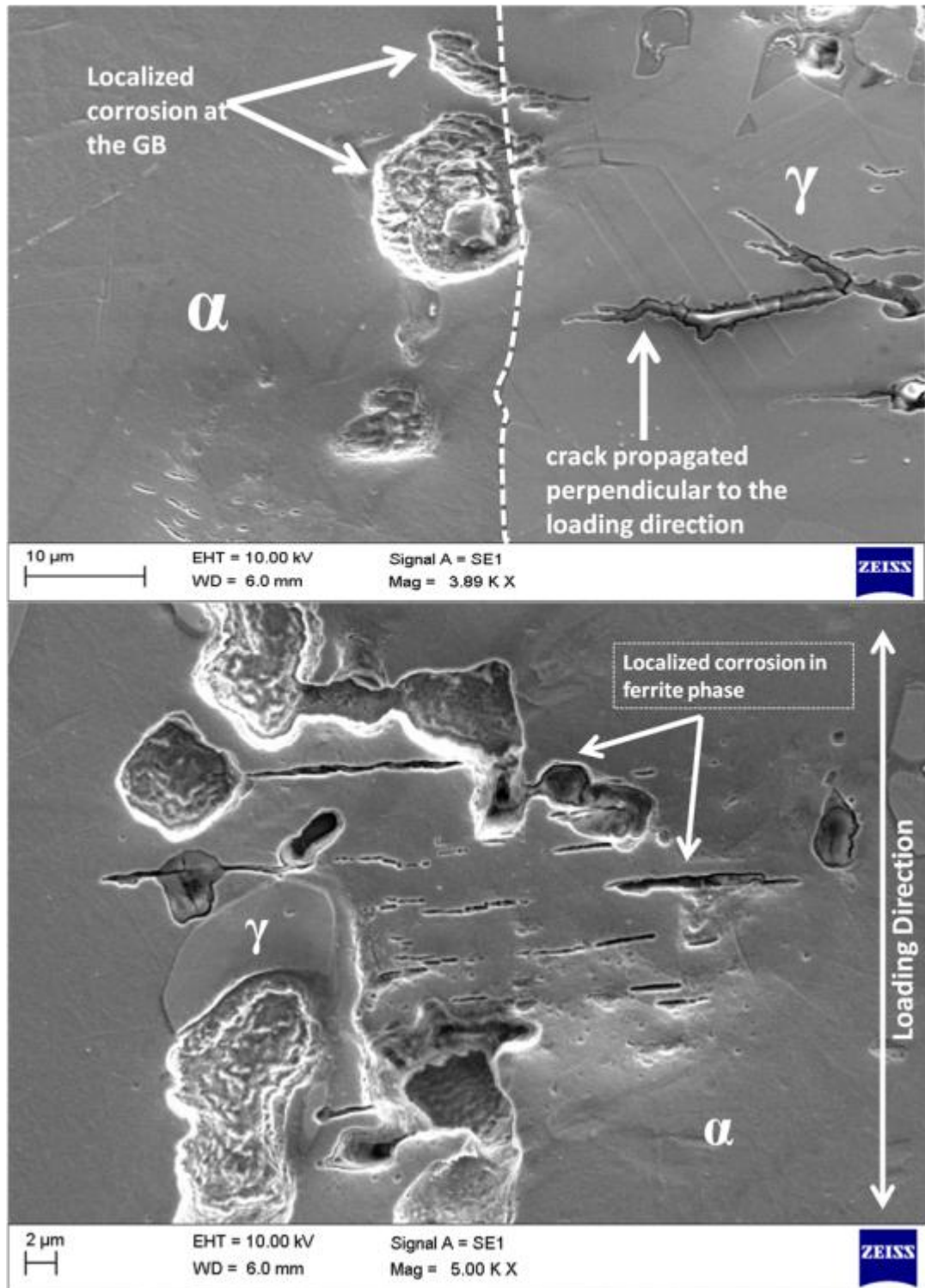


Figure 4-74: Traces of the cracks shown in Figure 4-73 on {110} and {112} planes in  $\alpha$ -Phase, Euler1=344°, Euler2=35.4°, Euler3=22.2°, X[6-1-1], Y[03-2] and normal [123].

#### **4.8.2.4 As Received: (Longitudinal to Tensile)**

After the test was stopped and the sample was cleaned in the boiling deionised water for two hours, the corroded patches located under the salt droplets were investigated by the SEM. Figure 4-75 confirmed the initiation of the localized corrosion in the ferrite phase and at the interphase boundaries ( $\alpha/\gamma$ ) as preferable sites of the pitting corrosion initiation. Also, some micro cracks were found to be propagated in the normal direction to the tensile load direction as shown in the same Figure. Additionally, Figure 4-76 displays an example of the corrosion occurred along the wavy slip bands in the ferrite grains under the salt droplet, the austenite and ferrite grains were identified by using the EDX technique (Cr/Ni %).



**Figure 4-75: Localized corrosion morphology found under the salt droplet after 1500 hours in the solution annealed sample with rolling direction longitudinal to the tensile.**

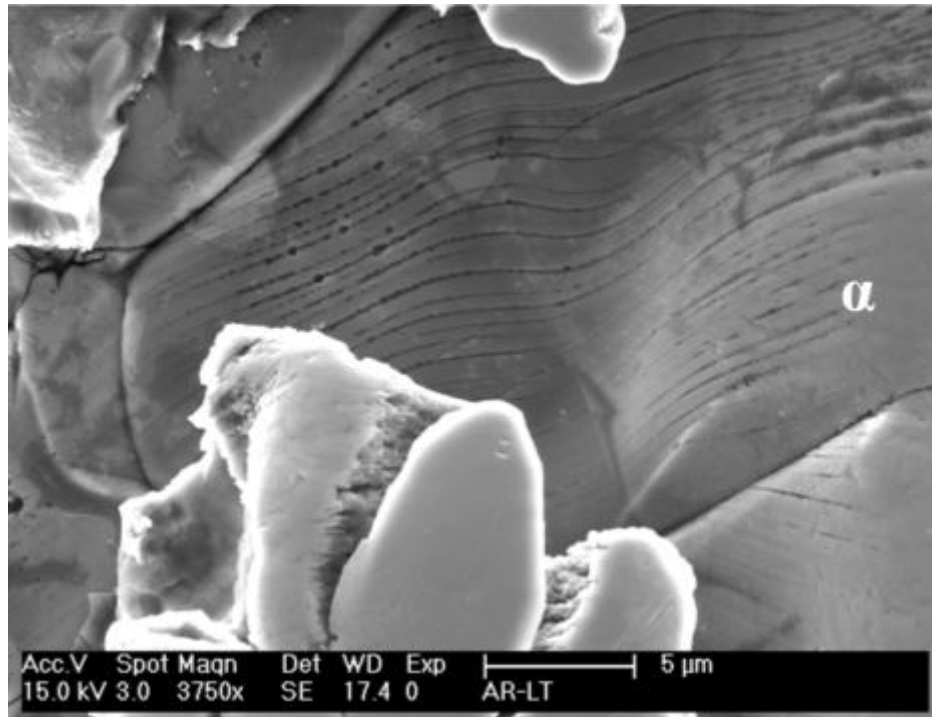


**Figure 4-76: SEM micrograph shows the wavy slip bands corrosion in the ferrite phase under the salt droplet after 1500 hours, the austenite and ferrite grains were identified by using the EDX technique.**

#### **4.8.2.5 Rolled sample tested without load**

Rolled sample of the same material SDSS was tested at the same corrosion environment but without any loading. The evaporated salt droplet was deposited on the sample and then tested for 1500 hours. After the test was stopped and the sample was cleaned, the corroded patches placed beneath the salt droplets were cleaned and then investigated by the SEM. Figure 4-77 confirmed the initiation of the localized corrosion in the ferrite phase and at the interphase boundaries ( $\alpha/\gamma$ ) as desirable sites of the localized corrosion initiation. Additionally, Figure 4-78 shows a close-up view of the localized corrosion behaviour in the ferrite phase and revealed the crystallographic pitting corrosion progress occurred in the ferrite phase.

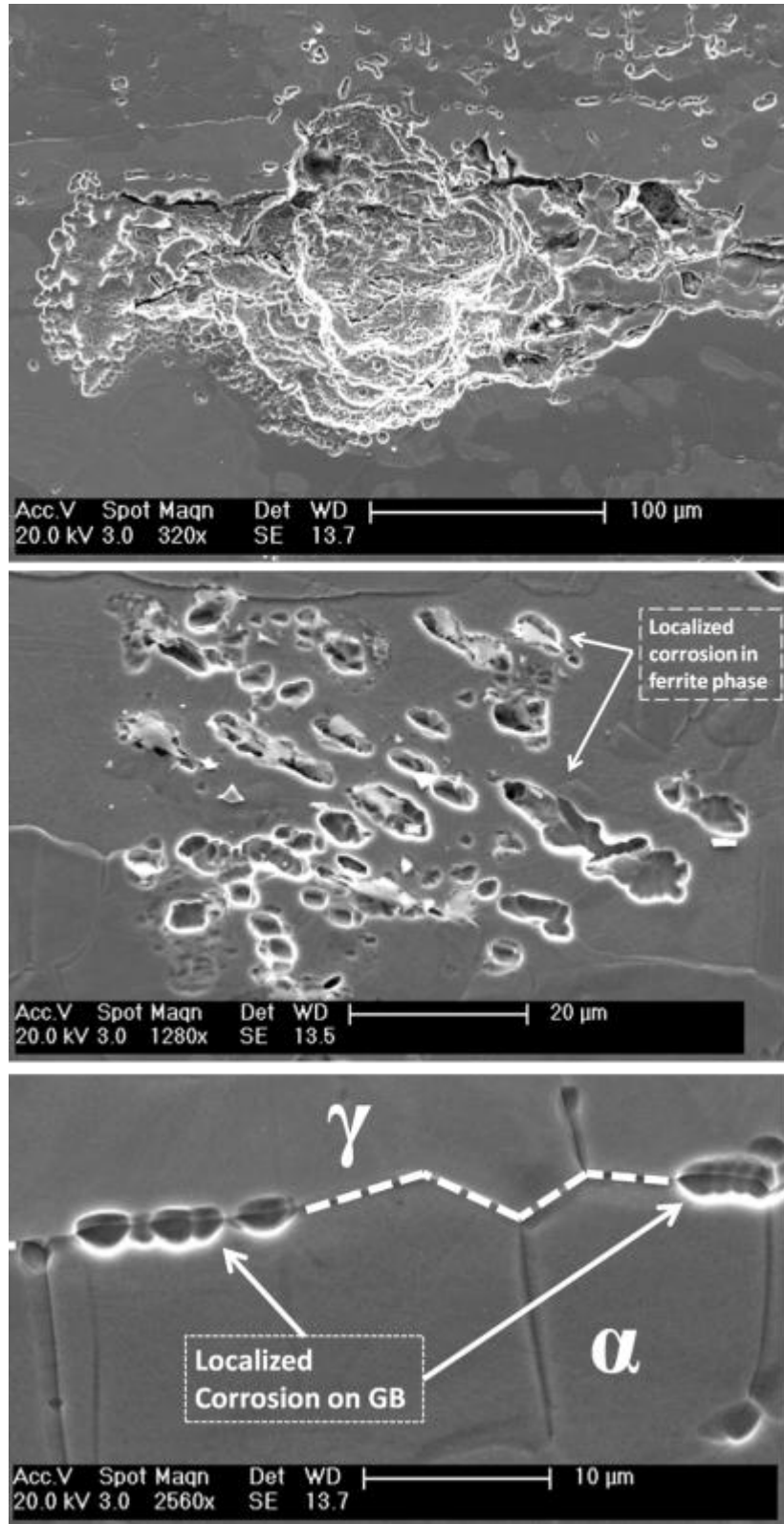


**Figure 4-77: Localized corrosion morphology found under the salt droplet after 1500 hours. Localized corrosion occurred at the interphase boundaries  $\alpha/\gamma$  and in the ferrite phase.**

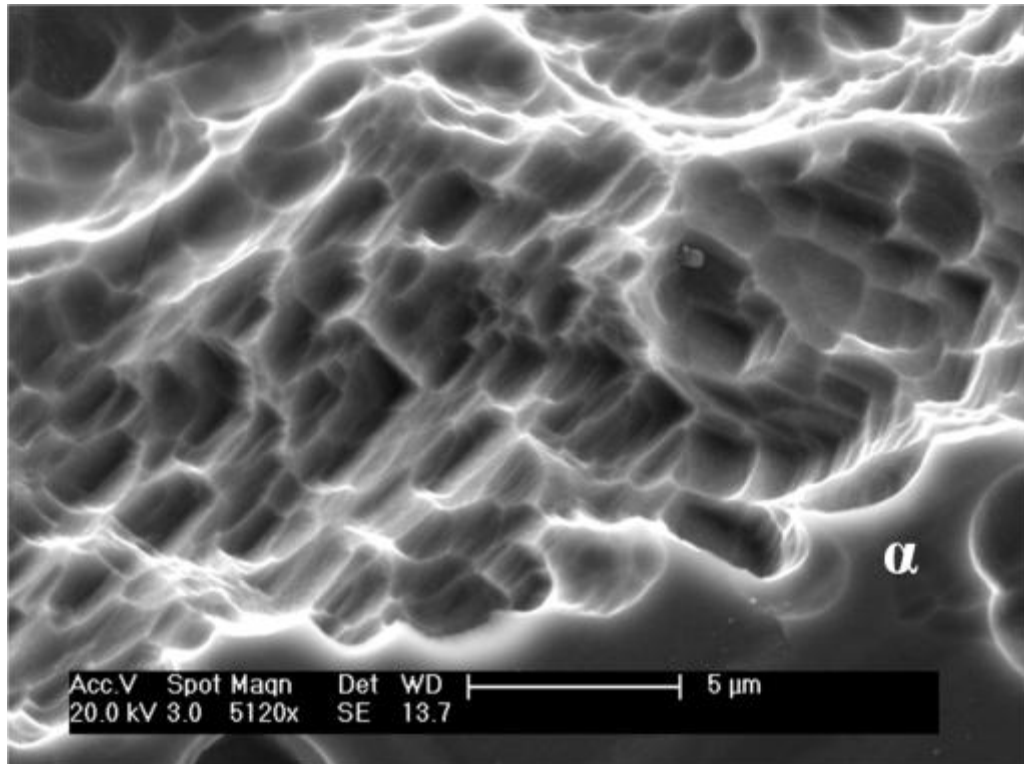


**Figure 4-78: A close-up view of the localized corrosion behaviour in the ferrite phase reflected the fine-scale crystallographic (faceted) corrosion.**

#### **4.8.2.6 Solution annealed sample tested without load**

Solution annealed sample was tested also at the same corrosion environment but without any stress. The evaporated salt droplet was deposited on the sample and then tested for 1500 hours. After the test was stopped and the sample was cleaned, the corroded patches were investigated by the SEM. Figure 4-79 confirmed the initiation of the localized corrosion mainly at the interphase boundaries ( $\alpha/\gamma$ ).

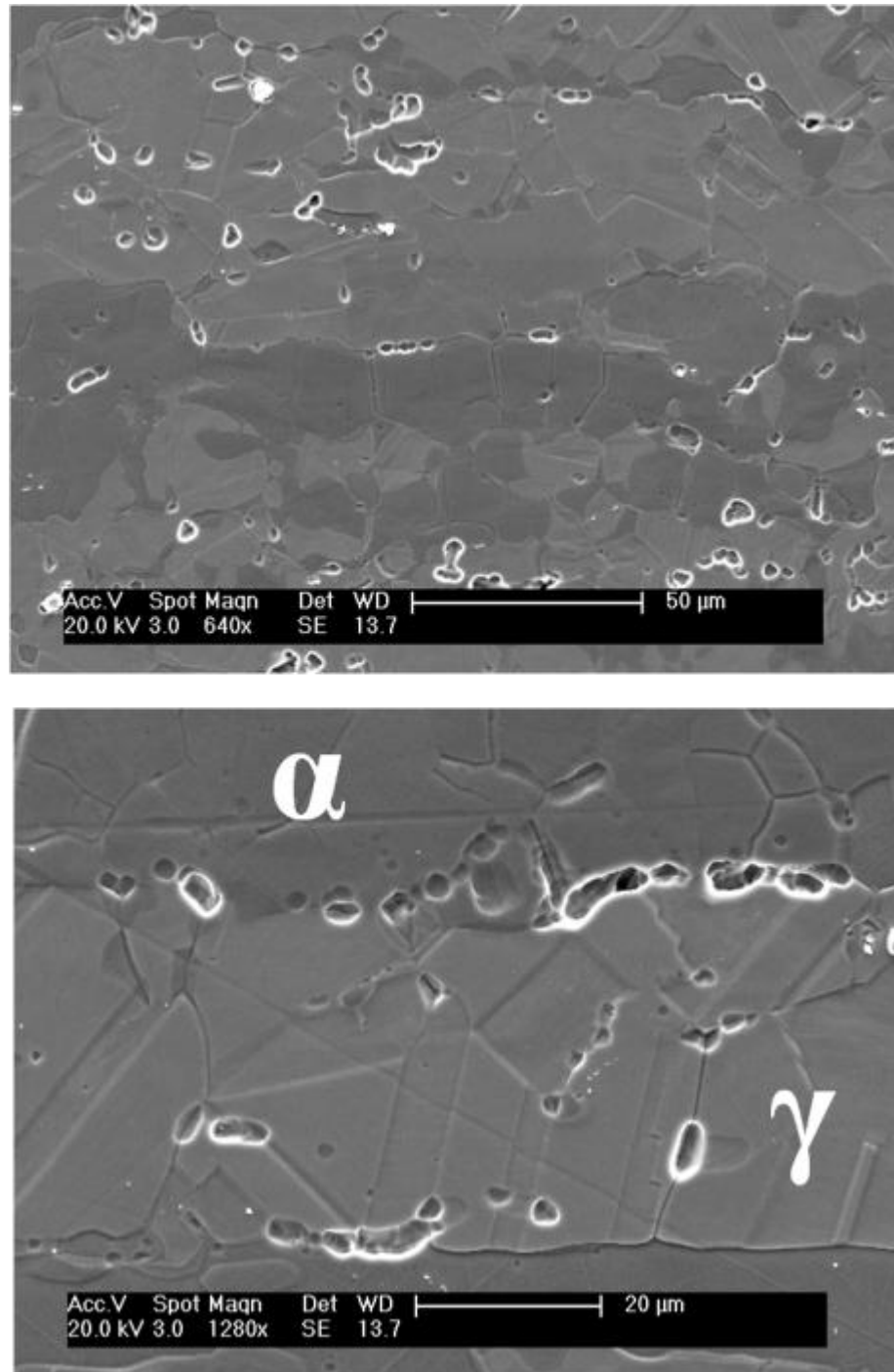


**Figure 4-79: Localized corrosion morphology found under the salt droplet after 1500 hours. Localized corrosion occurred mostly at the interphase boundaries  $\alpha/\gamma$ . Ferrite is dark gray and austenite is light gray.**

#### 4.9 In-Situ Tensile Testing

In this study, the development of the strain was observed on the microstructure scale as a function of the applied tensile load in three intervals of straining (1%, 2% and 3%) as shown in Figure 4-80. The in-situ images were captured at the beginning of the test and by the end of each strain interval as shown in Figure 4-81 which showed high density of deformation bands occurred in the austenite earlier than ferrite's deformation. The ferrite phase shows some deformation features are clearly seen after the 2% strain level.

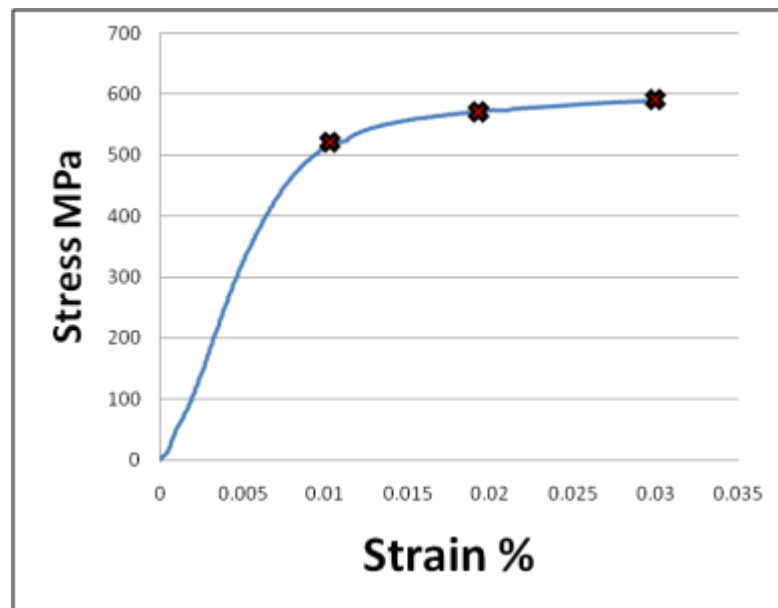


**Figure 4-80: Nominal stress vs. strain curve of the Mini-Flat tensile test in the Microtester. The markers indicate to the points at which images were acquired.**

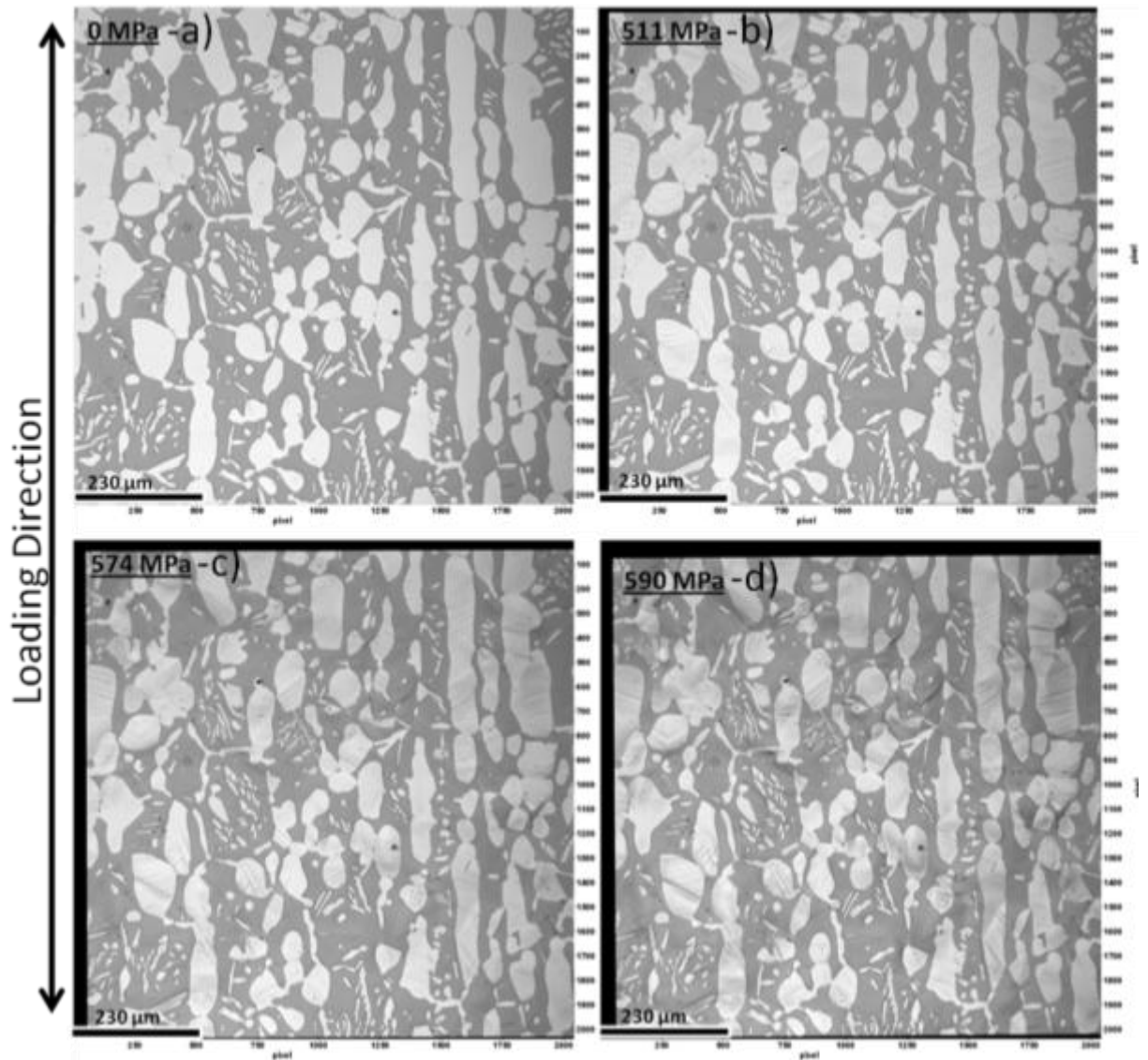


**Figure 4-81: Optical micrographs captured at four different strain levels of a) No Stress, b) at 511 MPa -1% Strain, c) at 574 MPa – 2% Strain and d) at 590 MPa -3% Strain (ferrite is dark and austenite is light).**

#### 4.9.1 DIC Analysis

Figure 4-82 is a maximum normal strain map taken from the DIC analysis at the end of the test (3% bulk strain), it can be seen that there is a significant variation in strain all over the microstructure. The maximum strains are to be found in some of the austenite grains and at their boundaries with ferrite. Figure 4-83 shows the maximum normal strain maps at the three strain levels of 1%, 2% and 3% respectively.

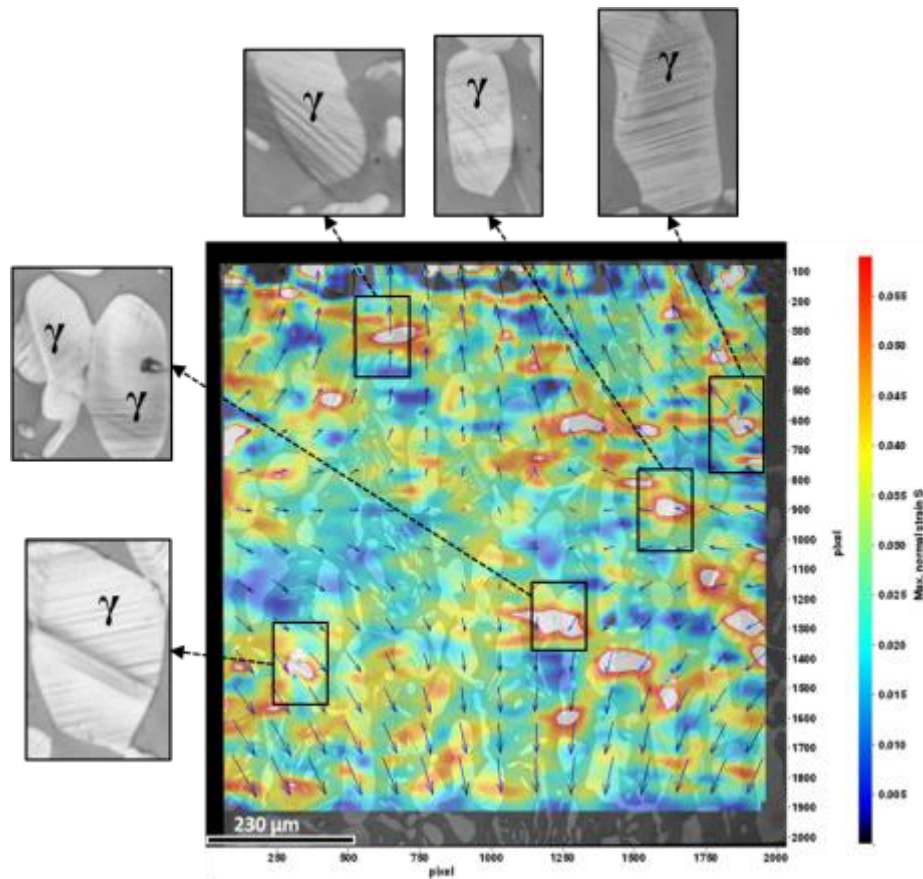


Figure 4-82: Strain map from last image taken at 3% bulk strain (window size is 64x64 and smoothing = 2) and external squares show examples of strain localization regions.

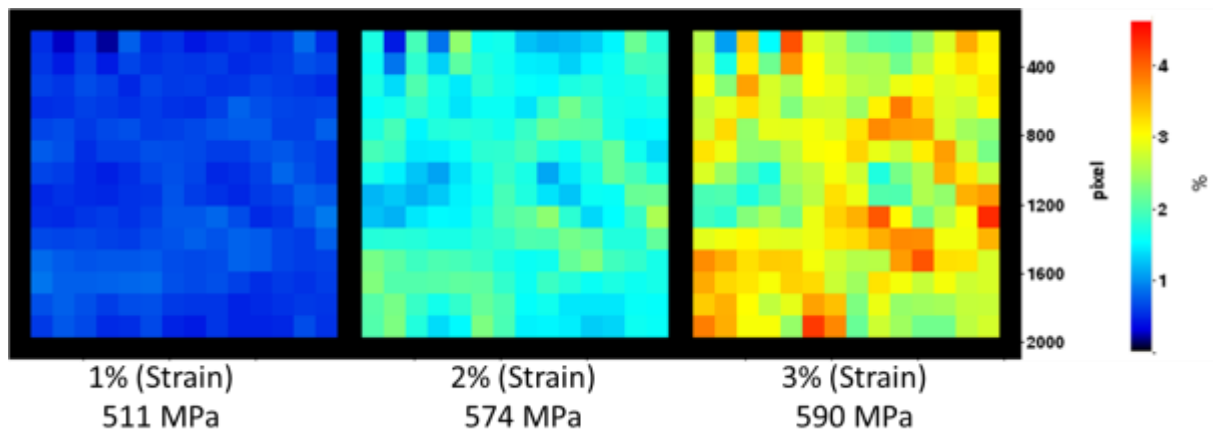
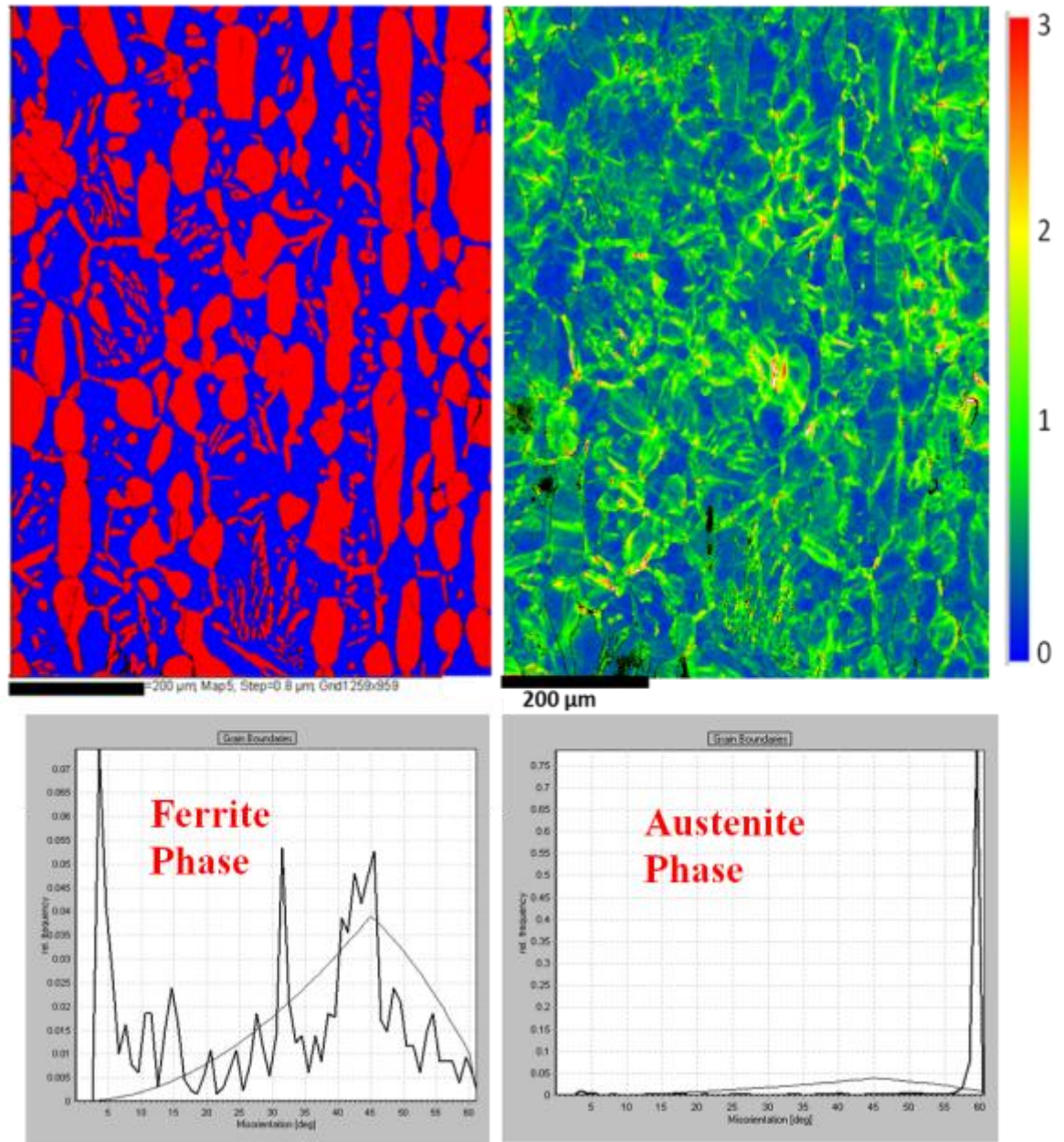


Figure 4-83: Maximum strain maps from images taken at 1%, 2% and 3% (bulk strain) respectively without smoothing. The scale bar ranges from 0.0% to 5.0 % maximum strain (window size is 64x64, 1 pixel is = 0.46 μm).

#### 4.9.2 EBSD Analysis

The same observed area under the DIC analysis was also analysed by the EBSD technique in order to give an idea of the scale, phase balance and local misorientations as shown in Figure 4-84. The local misorientation map showed more localization of misorientation at the grain boundaries.



**Figure 4-84: EBSD phase map ( $\alpha$ -Blue/ $\gamma$ -Red), local misorientation map and misorientation's frequency of both phases of the same deformed area (3% strain), black pixels are unindexed points.**

### 4.9.3 Pitting initiation test

The deformed sample was polarised in 5M NaCl at 70° C at a rate of 10mV/min. The polarisation curve was recorded from 200 mV below the free corrosion potential and stopped when there is a clear pitting initiated by watching the increasing in the current density value as shown in Figure 4-85.

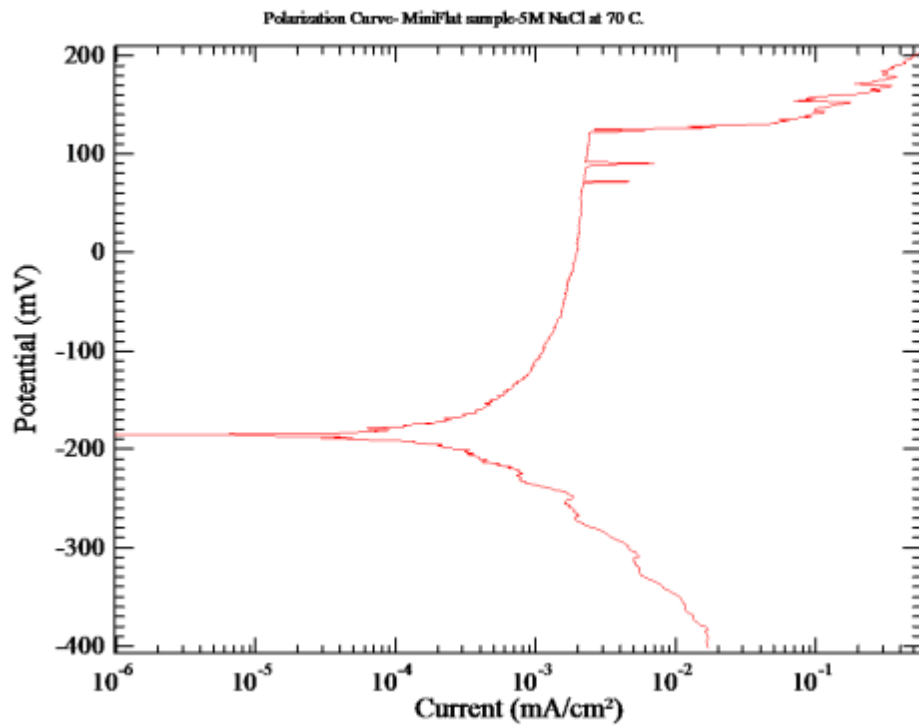


**Figure 4-85: Potentiodynamic polarisation curve of the strained mini flat sample in 5M NaCl at 70°C, potential was measured versus a saturated calomel electrode (SCE)with a scan rate of 10 mV/min.**

### 4.9.4 Strain distribution in both phases

Observations of the deformed surface by the SEM technique revealed slip-line formation in both phases, with a higher density in the austenite phase as shown in Figure 4-86.

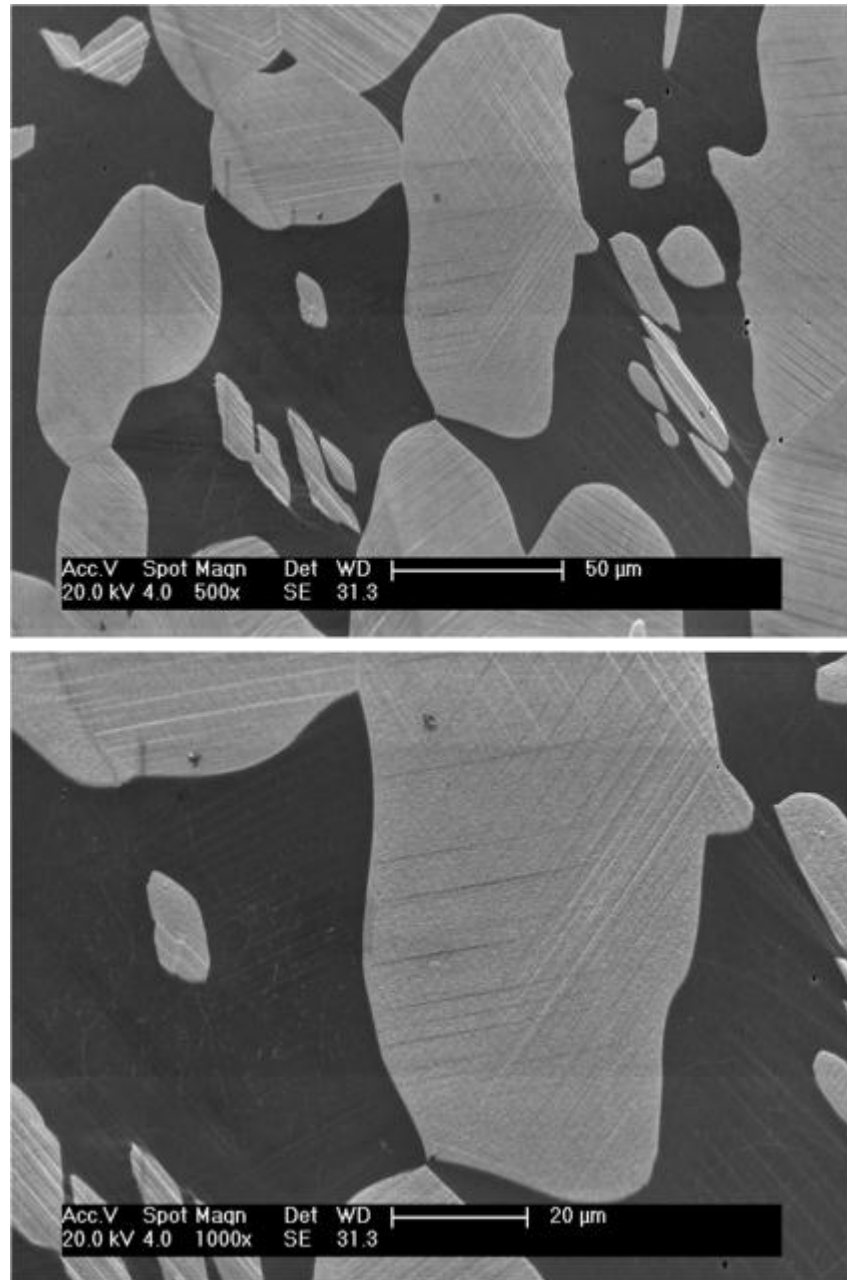


**Figure 4-86: SEM micrographs of deformed area showing the slip bands formation, ferrite is dark and austenite is light.**

To inspect the strain distribution in both phases by using the DIC maximum strain map at bulk strain of 3%, 15 austenite grains (Figure 4-87 (a)) and 15 ferrite grains (Figure 4-87 (b)) were selected from the image of the observed area to show the average strain value on both phases as shown in Figure 4-87. The average strain in each grain was then calculated as the average strain of the all interrogated windows sited in the desired grain at window size of 64x64 with maximum overlap percentage 87% as shown in Figure 4-88.

Considering the normal strain, the austenite was found to undergo more plastic strain in average of 3.9% for an applied bulk strain of 3%. Also, a highly heterogeneous strain distribution mainly was controlled by the density of the slip bands that were found in this phase (Austenite). The ferrite showed less normal strain in average (2.6% plastic strain in average) than the austenite.

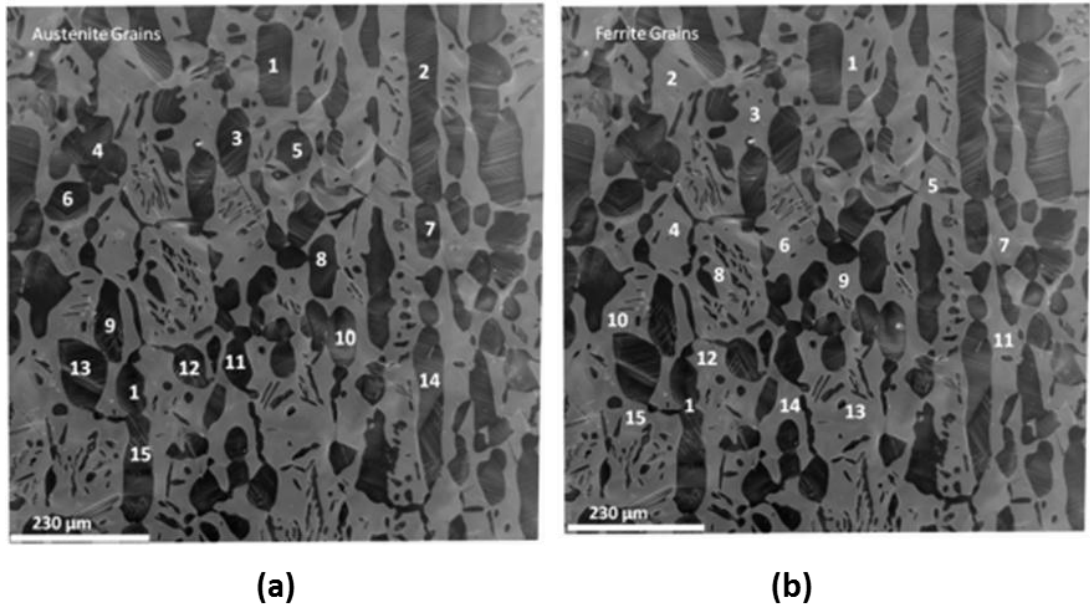


Figure 4-87: Optical images of the strained area showing the selected (a) austenite grains and (b) ferrite grains, ( $\alpha$ -light/ $\gamma$ -dark).

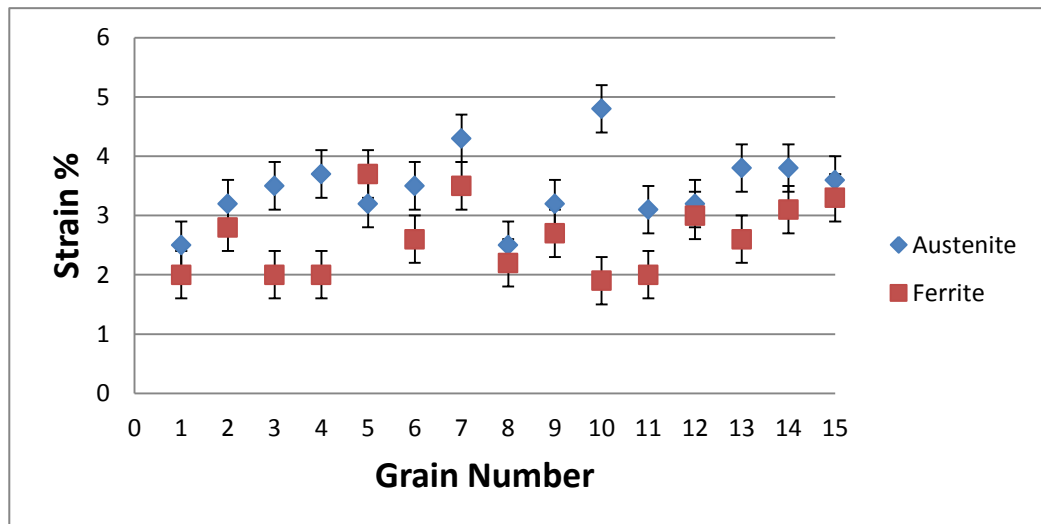
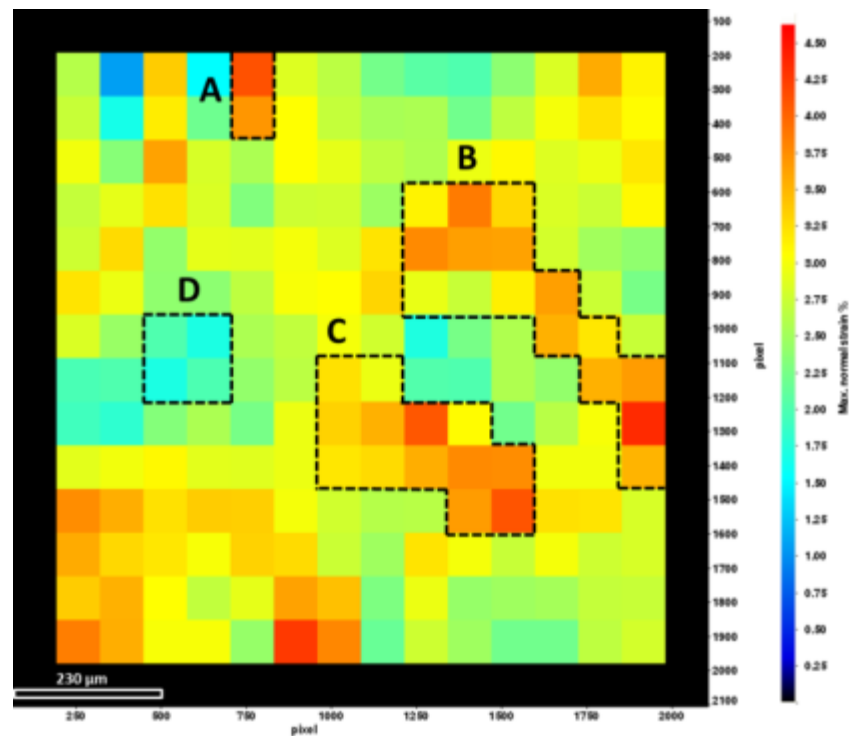


Figure 4-88: Grain number vs. the average maximum strain (from DIC analysis) for the grains shown in Figure 4-87.

#### 4.9.5 Pitting Density vs. Strain

The DIC strain map was divided for 14 x 14 grid (Figure 4-89) to be examined (each square individually) by the SEM to check the relation of the pitting density to the strain's level around the observed area. More observation was done on the bounded areas shown on the same Figure because A, B and C have higher level of strain more than the bulk strain (3%) while D has less strain than the bulk, Figures 4-90 and 4-91. There was no clear correlation observed between the strain localization and the pitting density.



**Figure 4-89:** Strain map of the observed area shows the maximum strain level, 1 pixel is = 0.46  $\mu\text{m}$ .

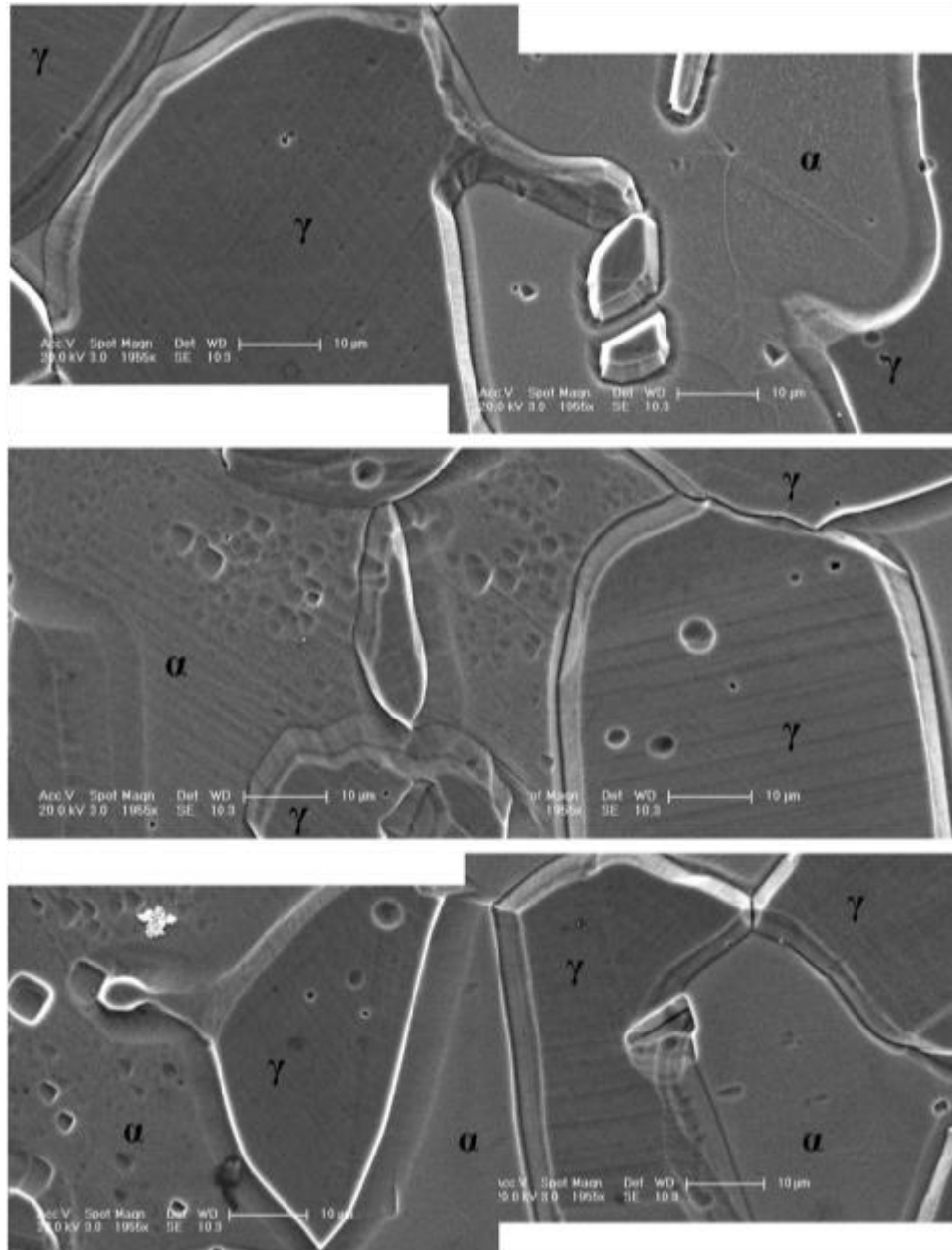


**Figure 4-90: SEM Micrographs of area (B) shown in Figure 4-89 as examples of areas with strain > 3% after potentiodynamic polarisation showing attack of phase boundaries within corroded area and micropitting corrosion.**

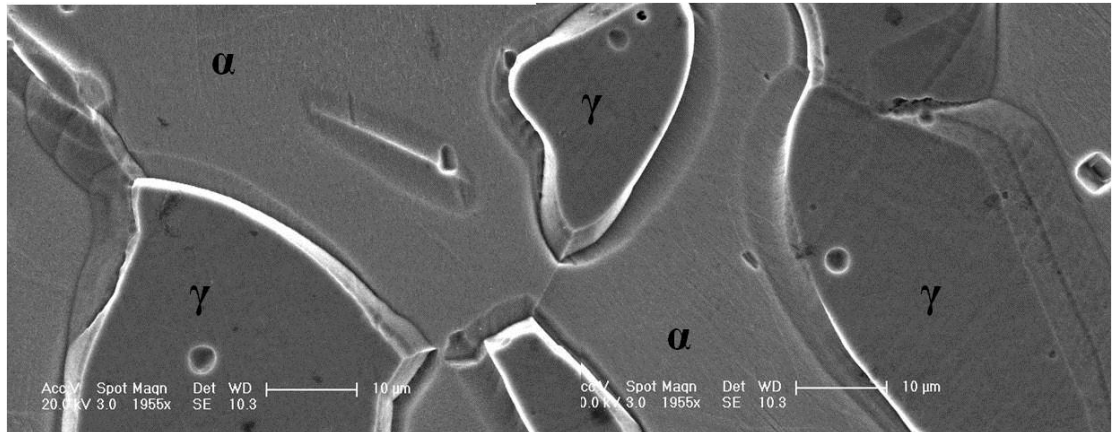


**Figure 4-91: SEM Micrograph of area (D) shown in Figure 4-89 as an example of areas with strain < 3% after potentiodynamic polarisation showing attack of phase boundaries within corroded area and micropitting corrosion.**

Extremely localized corrosion attack was noticed along interphase boundaries  $\alpha/\gamma$  as shown in Figure 4-92. Pitting density were almost have the same distribution and shapes (hemispherical) within austenitic phase and they were observed mainly nucleated within the austenitic's slip bands created by the plastic deformation as shown in Figures 4-92 and 4-93. Furthermore, pitting nucleation within the ferrite phase seems to be depending mainly on the crystallographic orientation of the ferrite (bcc) grains because they all show faceted crystallographic pits (square shape) as shown in Figures 4-94.

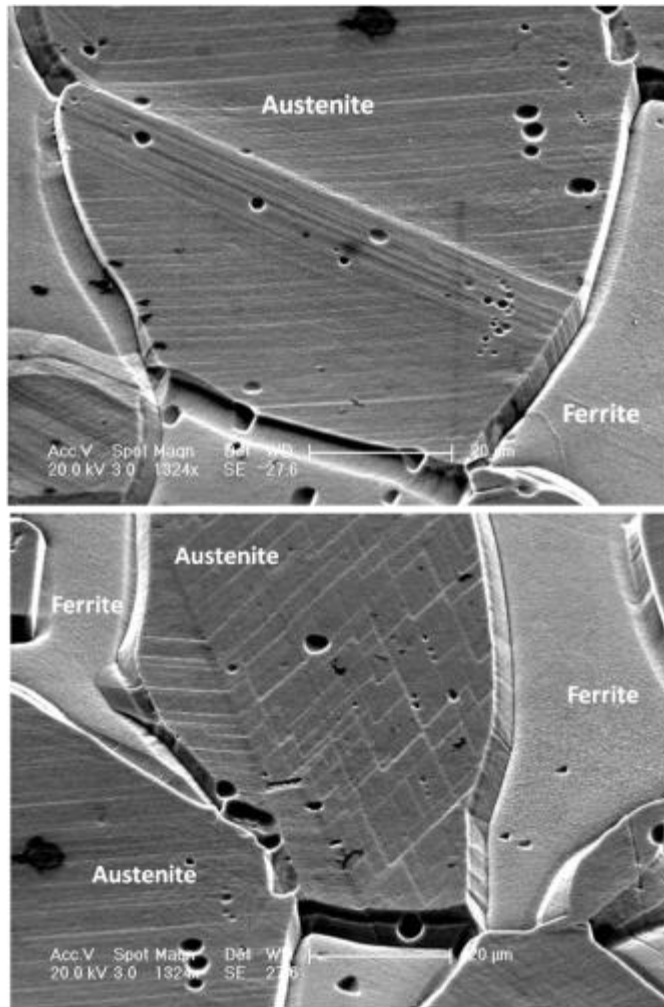


**Figure 4-92: SEM micrographs show the localized corrosion attack on the interphase boundaries  $\alpha/\gamma$  and the pitting occurred in the austenite grains.**

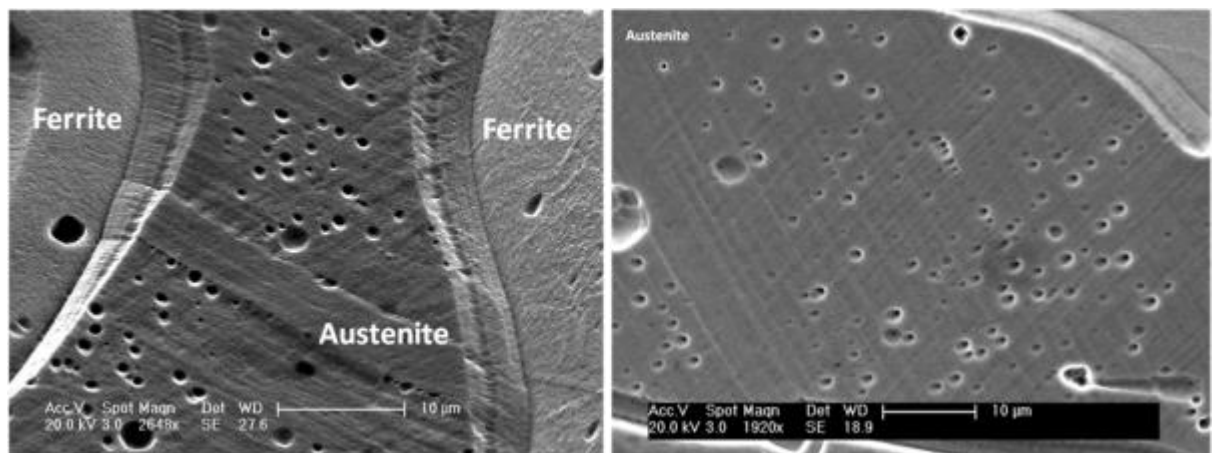


**Figure 4-93: SEM micrographs show the pitting corrosion attack occurred preferentially on the slip bands within the austenite grains ( $\gamma$ ).**

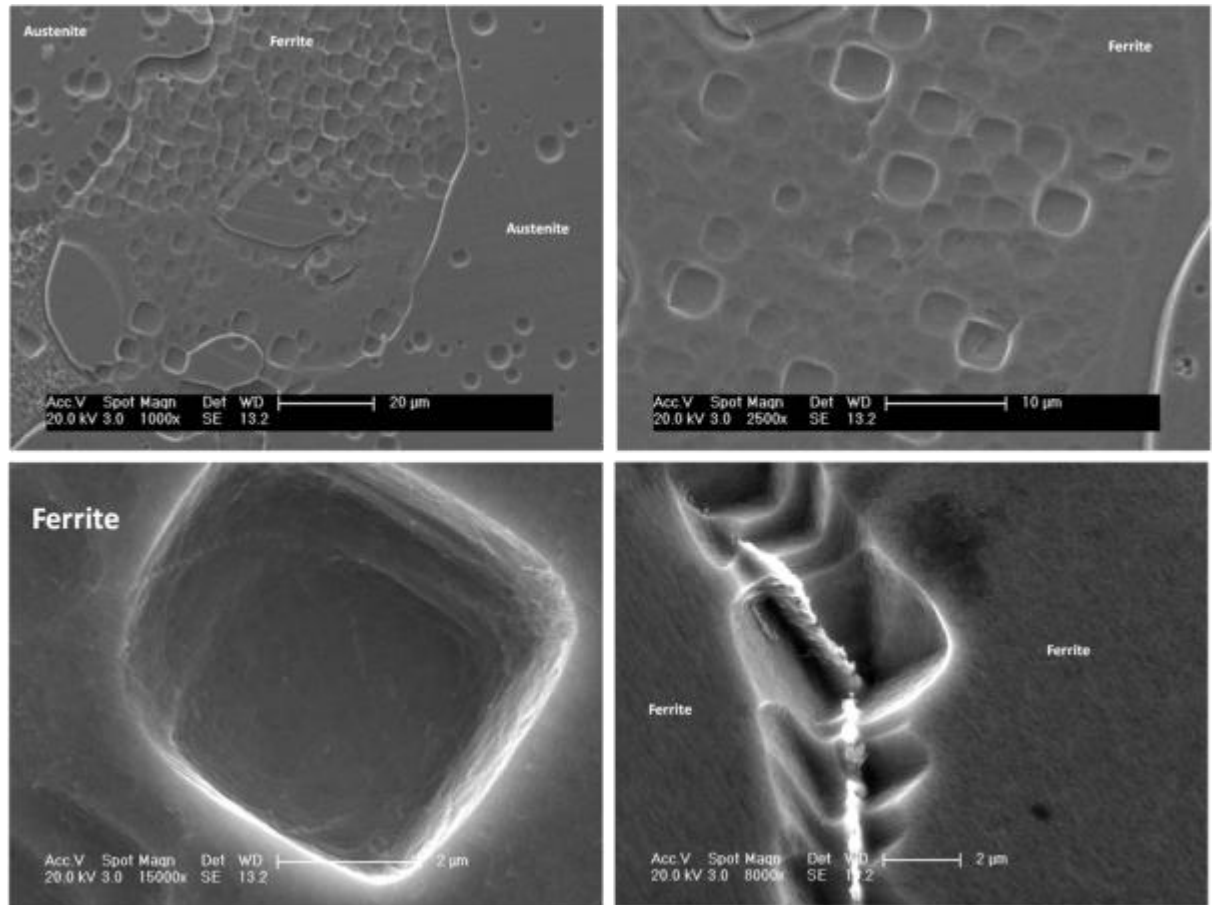


**Figure 4-94: SEM micrographs show close-up views of pits reflected the fine-scale crystallographic (faceted) pit in ferrite phase.**

#### 4.9.6 Summary

The results section shows the key findings out of the experimental works and methodology explained earlier in chapter 3. Stress corrosion cracking were initiated and grown in the vicinity of deposits of  $\text{MgCl}_2$  under controlled environmental conditions of temperature  $80^\circ\text{C}$  and (30-33%) RH, which is the relative humidity associated with a saturated  $\text{MgCl}_2$  solution at  $80^\circ\text{C}$  and loading to  $1.05\sigma_y$ . DIC differentiation analysis was applied on all samples and shows the strain gradients through the crack propagation successfully out of the droplets. The technique was not possible to give right results inside the salt droplets due to the corrosion products that banned the vision inside the droplets. Also, optical microscopy, scanning electron microscopy and electron backscatter diffraction were tools used to characterise cracks and pits morphologies in all samples. The in situ tensile testing was also performed and shows no correlation between the locations of strain gradients and

the pitting density. The crystallographic morphology of the pitting in the ferrite phase could explain the effects of grain crystallographic orientations on the pitting initiation.

The implications of those experiments and results will be related to the previously published literatures and discussed in the following discussion chapter (Chapter 5).

## 5 DISCUSSION

### 5.1 Material and Electrochemical Characterization

The chemical composition of the as-received materials shown in Table 3-1, (super duplex stainless steel type Zeron 100 in sheet plates, supplied by the manufacturer) is within the range specified by the ASTM standard [1]. The microstructures consist mainly of austenitic islands ( $\gamma$ -phase) elongated in the rolling direction, embedded in a ferritic matrix ( $\alpha$ -phase).

The electrochemical immersion tests were done as preliminary experiments to identify the effects of chloride content  $\text{Cl}^-$  and solution temperature on the corrosion initiation behaviour, and to add to the knowledge available about the lowest temperature that caused stress corrosion cracking in the tested materials. Most of the studies mentioned in the literature [81, 82, 169] were done at temperatures above  $100^\circ\text{C}$  and in this study it was intended to initiate stress corrosion cracking at a lower temperature ( $<100^\circ\text{C}$ ) to allow closer monitoring by using the DIC technique.

The polarisation curves (Figure. 4-3) show the importance of the chloride content and the solution temperature for the creation of pits in the tested surfaces of Zeron 100, which is known to possess high resistance to localized corrosion as well as stress corrosion cracking [1, 2, 10, 82]. It was found that increasing the chloride concentration increased the critical pitting current density and decreased the pitting potential. This corresponds well with previous observations on duplex stainless steels [48]. The pitting potential of duplex stainless steel is strongly influenced by the solution temperature and decreases with increase in temperature of the solution.

Pits are initiated by a rupture of the protective oxide film on the metal surface, which may occur because of either mechanical or chemical action. They act as stress concentration sites that allow the initiation of corrosion cracking, starting at the root or the walls of the pit. Pits can allow stress intensities to reach levels where a crack may be initiated by a geometric feature, which is able to concentrate the stress. The tested samples suffered from pitting corrosion with a random distribution of pits at solution temperatures of  $70^\circ$  and  $80^\circ\text{C}$  and pH of 5.8. However, there was no sign of any general or localized attack on the samples at temperature less than  $55^\circ\text{C}$  even in 30% NaCl, (Figures 4-5, 4-6 and 4-7) which give an indication of the lowest temperature that could be used in this study to

initiate the SCC in the test samples. As a general finding from this section, the materials showed high resistance to pitting but it could be initiated at sufficiently concentrated chloride and intermediate temperature 70°-80°C

## **5.2 Crack Nucleation from Concentrated Salt Deposits**

Super duplex stainless steels have high resistance against stress corrosion cracking in immersion tests. Other researchers [84, 85, 170, 171] found that salt deposit testing to be a more aggressive environment in which to initiate localized corrosion. In controlled environmental conditions of relative humidity can keep the salt at the deliquescence point. Figure 5-1 displays a plot of temperature versus relative humidity in  $MgCl_2$  and  $NaCl$  [171-174]. When the relative humidity is located above the corresponding deliquescence point of the deposited salt, then the solution becomes more diluted (less chloride concentration). In contrast, the deposited salt remains in a dry state (no solution creation) when the relative humidity is lower than the deliquescence point of the salt. It was shown [157, 171, 172] that stainless steels covered with chloride salt deposits have the highest susceptibility to stress corrosion cracking when exposed in atmospheric to relative humidity equivalent to the deliquescence point of that salt. This is because the concentration of the chloride in the solution formed on the surface reached the maximum value at its related deliquescence point (see Figure 5-2). A. Cook et al. [157] show that stress corrosion cracks occurs and grown in type 304 austenitic stainless steel, loaded to  $1.2\sigma_{ys}$ , under deposits of  $MgCl_2$  and controlled environmental conditions of temperature (40°C) and RH (30 %). Therefore, the relative humidity and temperature conditions of the salt are of important aspects to be considered in the initiation and propagation of stress corrosion cracking.

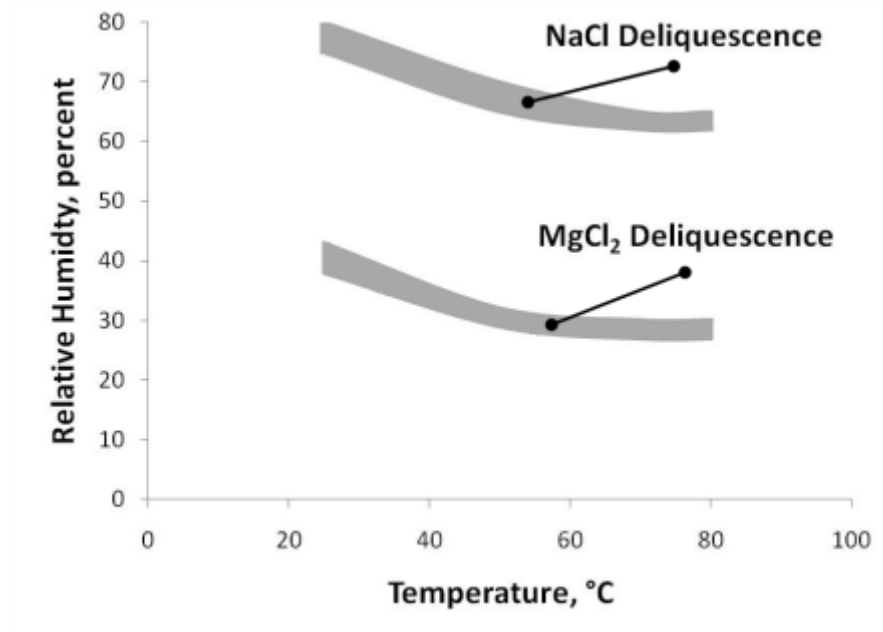


**Figure 5-1: Temperature versus Relative Humidity of  $\text{MgCl}_2$  and  $\text{NaCl}$  to show the deliquescence regions for those salts [171, 172].**

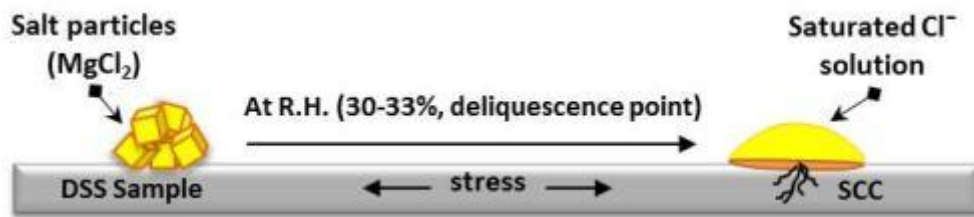


**Figure 5-2: A schematic Figure shows the deposited  $\text{MgCl}_2$  salt which transferred to saturated  $\text{Cl}^-$  solution at R.H. (30-35%) resulted in atmospherically induced SCC.**

The U-bend test was used to check if stress corrosion could be induced by this method in the super duplex stainless steel and explore non-immersed environments that may be more suitable for image correlation experiments. The optical micrographs for the U-bend sample after 1800 hours in conditions where  $\text{MgCl}_2$  salt droplets deposited on the surface show the appearance of cracks perpendicular to the tensile stress direction applied to the sample by bending (Figures 4-8 and 4-9). Since the saturated  $\text{MgCl}_2$  film has high viscosity, the film sticks and crystallizes on the surface of the specimen. This evaporation can lead to a build-up of chloride concentration on that surface. From this experiment, the

key finding was that cracking did occur in that environment and it is possible to consider a monitoring approach based on periodical DIC monitoring.

As a result of the U-bend tests a dog bone tensile sample was prepared from the same plate in the as-received condition and by using cold rolling (work hardening  $\approx 10\%$  reduction) to provide a second material condition to be tested in the same environmental conditions. Taking into account the high resistance of Zeron 100 to stress corrosion cracking, the samples were plastically deformed in the tensile cell by a tensile stress of  $1.05\sigma_{ys}$  and a strain of 3% in rolling directions (transverse and longitudinal to the tensile load) as initial conditions and then followed by as-received conditions.

Stress corrosion cracks were initiated and grown in the vicinity of deposits of  $MgCl_2$  under controlled environmental conditions of temperature  $80^\circ C$  and (30-33%) RH, which is the relative humidity associated with a saturated  $MgCl_2$  solution at  $80^\circ C$  (e.g. Figures 4-23 and 4-30). Deformation bands were observed on surfaces that were subjected to tensile strain. These deformations developed on the surface and took various forms which changed according to the phases in which they developed. This was discussed earlier in the literature review [23, 25, 26]. These deformation bands containing a high density of dislocations being high energy regions can act as potential pitting sites in both phases (see e.g. Figures 4-67 and 4-72). The SEM and EBSD analysis revealed pit initiation and selective dissolution preferentially in the ferrite phase as shown in Figures 4-50 to 4-53. This has also been reported in the literature [81, 91], where selective phase attack has been described as being due to galvanic attack because of the ferrite being anodic to the austenite [104] due to the difference in chemical composition of the two component phases.

In this project, it was also observed that microcracks initiated from pits and along slip bands (e.g. Figures 4-46, 4-72 and 4-75), resulting in microcrack propagation following the slip bands. This suggests a combination of microplastic strain and attack of oxide film-rupture sites because of plastic deformation is responsible for SCC initiation. A possible explanation for the selective attack that leads to cracking of ferrite phase (Figure 4-73) could be hydrogen embrittlement. This phenomenon needs three factors to occur, which are a source of sufficient hydrogen, tensile stress and a susceptible material. The highly aggressive environment (saturated  $MgCl_2$ ) under the salt droplets could generate a quite

acidic pH values through hydrolysis of ferric ions [84]. The ferrite is highly susceptible to the hydrogen embrittlement because it has high hydrogen diffusivity. This is also known to be increased with the plastic deformation due to the creation of slip bands and dislocations as sites encourage hydrogen adsorption on the metal surface [93, 110, 175, 176]. As a result, the behaviour of the tested material may be consistent with susceptibility to hydrogen embrittlement. Nevertheless, it is also evident from Figure 4-55 that the cracks propagate through both phases with examples of branching, especially along austenite-ferrite phase boundaries.

When comparing the cold-rolled sample and the as-received samples, tested with the same grain orientations, this study found SCC initiated earlier (around 500 hours) and propagated faster in the cold-rolled sample than the as-received condition (Figures 4-36 and 4-45). The earliest cracks that initiated in the T-T (Transverse Orientation) cold rolled samples were noticed after 600 hours with total length of 1.64 mm (including the diameter of the droplet) and had developed extensive cracking resulting in specimen fracture. The first crack was noticed in the as-received T-T samples after 1200 hours and the sample reached 1500 hours without failure. In the L-T (Longitudinal Orientation) samples, the cold-rolled sample showed crack propagation out of the droplet after about 628 hours but had more difficulty in propagating because the grain orientation plays a key role in propagation. The as-received samples passed the test period of 1500 hours without any noticeable cracking. This suggests that SCC is highly influenced by cold deformation, which may be created during the manufacturing process. The reduced stress corrosion cracking resistance of the samples is a result of the decrease of plastic properties in the cold worked microstructure because the surface layer of the tested sample becomes more brittle and easy breaks under tensile stresses creating more crack initiation sites [177]. Such behaviour was also reported in the literature review [65-67].

This study also found that orientation was significant in the sample's susceptibility to stress corrosion cracking, a feature which was noted in the literature review [78, 79]. It was found that crack propagation was easier in the T-T samples than the L-T samples and this suggested that stress corrosion cracking in DSS was more severe in transverse specimens than in longitudinal specimens. It was considered that the lower SCC resistance of the transverse direction is caused by the configuration of austenite grains, which have a

key role as crack propagation barriers, as shown in Figure 4-68. Thus, manufacturing and detail design can reduce the risk of SCC failures by reducing tensile stresses acting in the transverse direction in the material by modifying the manufacturing process to change the grain orientation with respect to the direction of expected tensile stress.

Metallographic examinations were carried out to compare surface corrosion damage of cold rolled un-loaded specimens with as-received conditions. The un-loaded specimens were exposed to the same environment (in the same chamber) to provide a basis for comparison. Some regions of localized corrosion were observed under the salt deposits. The cold rolled sample shows more severe localized corrosion initiated mainly in the ferrite phase and at the ferrite-austenite boundaries (Figure 4-77). The as-received sample shows the initiation of the corrosion mainly at the boundaries (Figure 4-79), but the bulk of ferrite and austenite grains were almost free of localized corrosion. This suggests the importance of the cold deformation in the corrosion initiation process in the DSS microstructure because it enhances the initiation of corrosion in the ferrite phase which is the weak phase in corrosion initiation in this dual phase microstructure. The implication is that microplastic strain plays a key role in the corrosion process as well as leading to SCC, as been reported also by other researchers [84, 90].

### **5.3 Analysis of crack path and arrested crack**

Duplex stainless steels are known to have greater SCC resistance than austenitic stainless steels. The critical question here is why? Much of the answer lies in the way in which a crack can propagate in a complex two-phase microstructure. Cracks are more likely to be deflected or arrested at interfaces in such a microstructure [88, 178]. In this study, stress corrosion cracks were seen to initiate from micro-scale corrosion damage and at active sites such as slip bands and interphase locations. Cold work caused a marked increase in the number of these sites of deformation (Figures 4-49, 4-50 and 4-51).

The ferrite phase was found both to be more susceptible to SCC initiation and to provide an easier path for crack propagation. Figure 4-55 shows a stress corrosion crack in a duplex stainless steel initiated in the cold-rolled sample with T-T orientation. Also, as received sample with T-T orientation suffered from SCC with the crack exhibits transgranular and sometimes branched propagation in ferrite (Figure 4-71-and 4-73), which

is the more continuous phase. In places, the crack seems to avoid the austenite passing instead along the phase boundary. In places there is transgranular cracking in the austenite too. One of the simplest explanations is that the two component phases of duplex stainless steel exhibit different slip behaviour as a result of their differing crystal structures. The crack paths in the ferrite phase were found to be consistent with possible slip systems in the BCC system: mostly on {110} and occasionally on {112} slip planes (Figure 4-52, 4-56 and 4-73). This indicates the crystallographic failure of ferrite [24, 178]. The cracked ferrite grains were mapped using EBSD and the orientation data was plotted in pole Figures in order for the identification of the active cracking planes. The present data are in agreement with other studies [179-181], which also showed that crack propagation occurred almost consistently on the {110} planes and the {112} planes, which are also the habit planes for twinning in ferrite. This twinning is thought to cause local depassivation and enhancement of crack propagation along deformation bands as reported by Magnin et al. [88, 90].

One of the interesting results of this study is that cracking was detected to initiate from the localised corrosion under the salt deposit by DIC (Figure 4-68). The crack was detected using DIC analysis while it could not be detected optically. It was seen to initiate within 611 hours and then propagate perpendicular to the tensile load direction in the rolled L-T sample until it was arrested for more than 100 hours by a  $\gamma/\gamma$  grain boundary (G1/G2). The crack can be seen in Figure 5-3 where the main crack propagated in a zig-zag manner and deformation bands were clearly accumulated and visible ahead of the crack. This crack was then characterized using an electron backscatter diffraction technique to study the possible reasons for crack arrest.

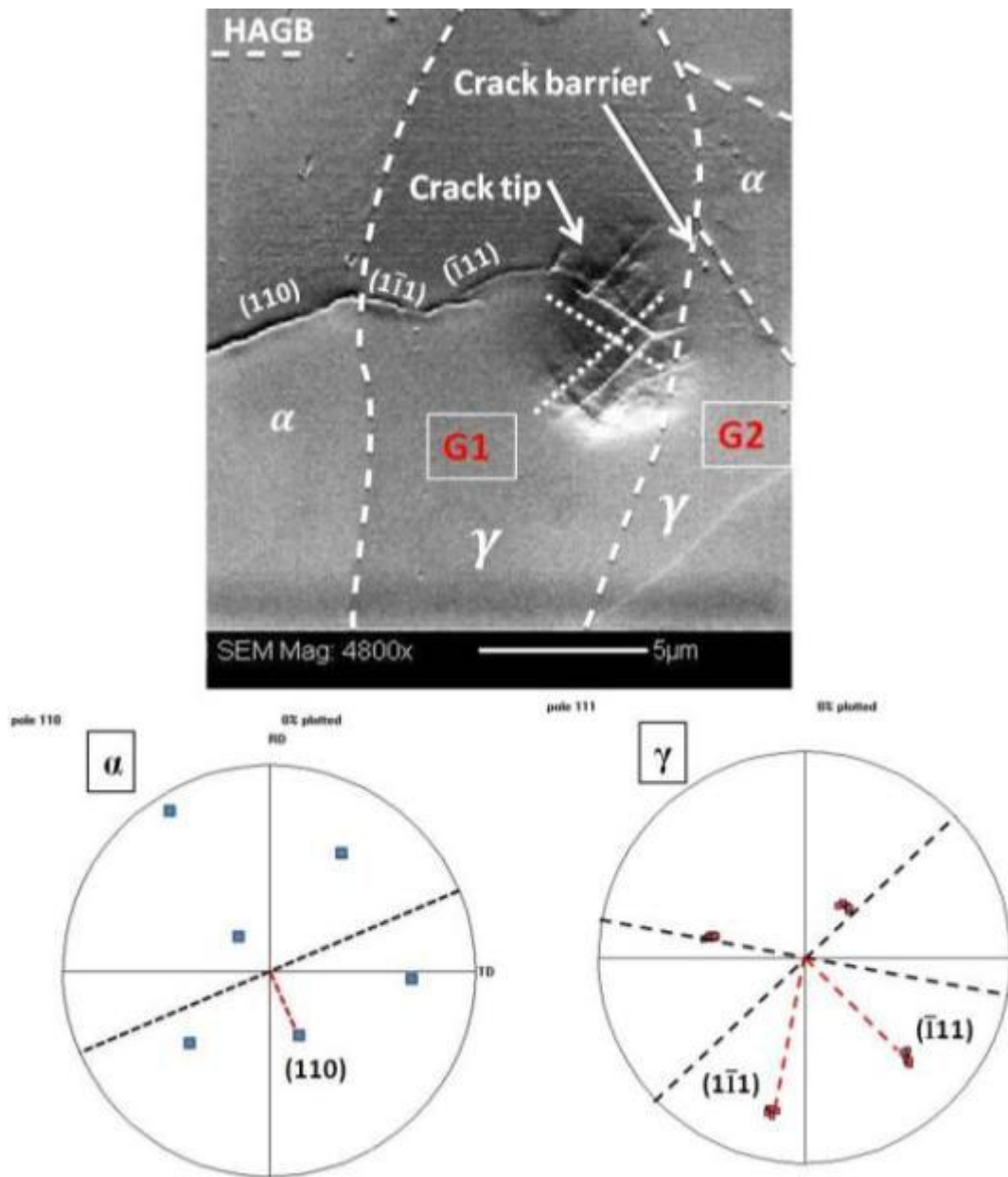


**Figure 5-3: SEM micrograph for the arrested crack with the deformation bands at the crack tip and the traces of the crack on  $\{110\}$  for  $\alpha$ -Phase and on  $\{\bar{1}\bar{1}\bar{1}\}$  for  $\gamma$ -Phase.**

The Schmid factors of the grains of interest were calculated using the orientation ( $g$ ) matrices. These were derived from the experimentally determined orientation matrices which were obtained from the Euler angles ( $\varphi_1$ ,  $\Phi$ ,  $\varphi_2$ ) measured and calculated by the EBSD system. An orientation matrix is a 3x3 matrix that relates the crystal coordinate system (e.g. the  $[100]/[010]/[001]$  system in a cubic structure) and the sample coordinate

system (e.g. the Cartesian coordinate system, X-Y-Z (see Figure 5-4). With X aligned with the loading axis) [182].

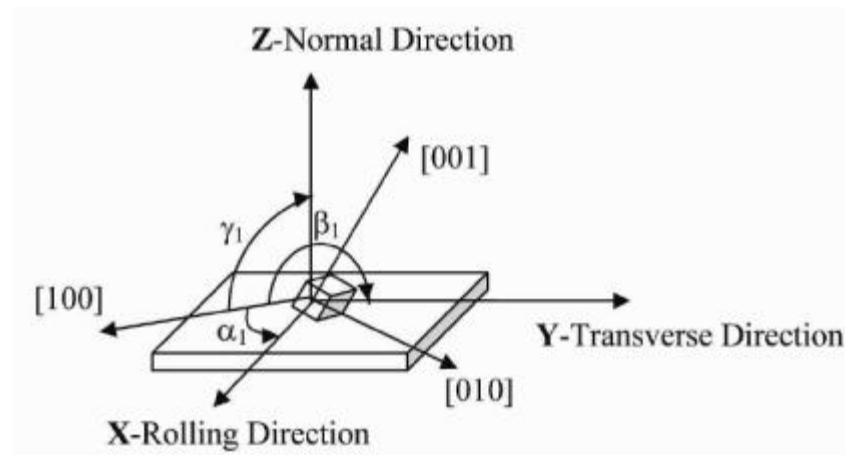


**Figure 5-4: Relationship between the specimen coordinate system RD, TD, ND and the crystal coordinate systems [100], [010], [001] [182].**

Once the specimen and crystal coordinate systems are stated, the relation between crystal and sample coordinate systems is given by equation below:

$$C_c = g C_s \quad (\text{eq. 5-1})$$

Where  $C_c$  and  $C_s$  are the crystal and specimen coordinate systems respectively and  $g$  is the 3x3 orientation matrix,

$$\begin{pmatrix} \cos\alpha_1 & \cos\beta_1 & \cos\gamma_1 \\ \cos\alpha_2 & \cos\beta_2 & \cos\gamma_2 \\ \cos\alpha_3 & \cos\beta_3 & \cos\gamma_3 \end{pmatrix} = \begin{pmatrix} g_{11} & g_{12} & g_{13} \\ g_{21} & g_{22} & g_{23} \\ g_{31} & g_{32} & g_{33} \end{pmatrix} \quad (\text{eq. 5-2})$$

The first row of the matrix is given by the cosines of the angles between the first crystal axis, [100] and three specimen axes X, Y, Z and the other two rows are related to the other two crystal axis and can be calculated in the same way. These three angles  $\alpha_1, \beta_1, \gamma_1$  are shown on Figure 5-4. The elements of the orientation matrix in terms of the Euler angles are given by equation 5-2 and it could be achieved directly from the crystallographic raw data obtained from the electron backscattered diffraction (EBSD).

$$\begin{aligned}
g_{11} &= \cos \varphi_1 \cos \varphi_2 - \sin \varphi_1 \sin \varphi_2 \cos \Phi \\
g_{12} &= \sin \varphi_1 \cos \varphi_2 + \cos \varphi_1 \sin \varphi_2 \cos \Phi \\
g_{13} &= \sin \varphi_2 \sin \Phi \\
g_{21} &= -\cos \varphi_1 \sin \varphi_2 - \sin \varphi_1 \cos \varphi_2 \cos \Phi \\
g_{22} &= -\sin \varphi_1 \sin \varphi_2 + \cos \varphi_1 \cos \varphi_2 \cos \Phi \\
g_{23} &= \cos \varphi_2 \sin \Phi \\
g_{31} &= \sin \varphi_1 \sin \Phi \\
g_{32} &= -\cos \varphi_1 \sin \Phi \\
g_{33} &= \cos \Phi
\end{aligned} \tag{eq. 5-3}$$

EBSD was employed in the area around the crack tip and then the raw data obtained was analysed using V-map software [165]. The orientation data obtained for the grains G1 and G2 were given in table 5-1 with respect to the coordinate systems shown in Figure 5-4.

Grain	$g_{11}$	$g_{12}$	$g_{13}$	$g_{21}$	$g_{22}$	$g_{23}$	$g_{31}$	$g_{32}$	$g_{33}$
G1	0.137	0.369	0.919	0.951	-0.308	-0.019	0.276	0.877	-0.394
G2	0.376	0.161	0.913	-0.517	0.853	0.063	-0.769	-0.496	0.404
	x			y			z		
	Loading axis						Surface Normal		

**Table 5-1: Orientation data for the grains G1 and G2 from the EBSD analysis.**

Assuming purely tensile stress in the same rolling direction of the test sample, the highest Schmid factor may be determined by using the orientation matrix and the following equation [183, 184]:

$$S^\alpha = (gl \cdot n^\alpha)(gl \cdot S^\alpha) \tag{eq. 5-4}$$

Where  $n^\alpha$  and  $S^\alpha$  are the fcc unit normal to the slip planes, four {111} slip planes in FCC crystals, and three possible <110> slip directions respectively, in which  $\alpha = 1, \dots, 12$  [180]. The absolute Schmid factor calculated for all 12 systems in both grains G1 and G2 are shown in table 5-2.

System	$(hkl)$	$[uvw]$	G1			G2		
			$\emptyset$	$\lambda$	Schmid	$\emptyset$	$\lambda$	Schmid
1	(111)	$[\bar{1}10]$	68.89	152.88	<b>0.321</b>	76.69	14.49	<b>0.223</b>
2	$(\bar{1}11)$	[101]	137.54	48.78	<b>0.486</b>	34.22	108.71	<b>0.265</b>
3	$(\bar{1}\bar{1}1)$	$[10\bar{1}]$	99.13	41.71	<b>0.491</b>	138.95	114.20	<b>0.309</b>
4	$(\bar{1}\bar{1}\bar{1})$	[101]	112.47	48.78	<b>0.252</b>	99.06	108.71	<b>0.051</b>
5	(111)	$[\bar{1}01]$	68.89	133.30	<b>0.247</b>	76.69	65.80	<b>0.094</b>
6	$(\bar{1}11)$	$[0\bar{1}1]$	137.54	78.21	<b>0.151</b>	34.22	123.94	<b>0.462</b>
7	$(\bar{1}\bar{1}1)$	[110]	44.29	62.96	<b>0.325</b>	138.95	76.26	<b>0.179</b>
8	$(\bar{1}\bar{1}\bar{1})$	[011]	112.47	103.37	<b>0.088</b>	99.06	49.66	<b>0.102</b>
9	(111)	$[0\bar{1}\bar{1}]$	68.89	78.21	<b>0.074</b>	76.69	123.94	<b>0.129</b>
10	$(\bar{1}11)$	[110]	137.54	62.96	<b>0.335</b>	34.22	76.26	<b>0.196</b>
11	$(\bar{1}\bar{1}1)$	[011]	44.29	103.37	<b>0.165</b>	138.95	49.66	<b>0.488</b>
12	$(\bar{1}\bar{1}\bar{1})$	$[\bar{1}\bar{1}0]$	112.47	27.12	<b>0.340</b>	99.06	165.51	<b>0.153</b>

**Table 5-2: The Schmid factors (absolute values) of slip systems in G1 and G2 (highlighted rows show highest Schmid factor). The angles  $\emptyset$  and  $\lambda$  are relative to the load direction.**

According to the calculated results in table 5-2, slip systems of  $(\bar{1}11)/[\bar{1}01]$  and  $(\bar{1}\bar{1}1)/[101]$  are the systems working alternatively in G1 while the slip systems of  $(\bar{1}\bar{1}\bar{1})/[011]$  and  $(\bar{1}11)/[0\bar{1}\bar{1}]$  should operate most readily in G2.

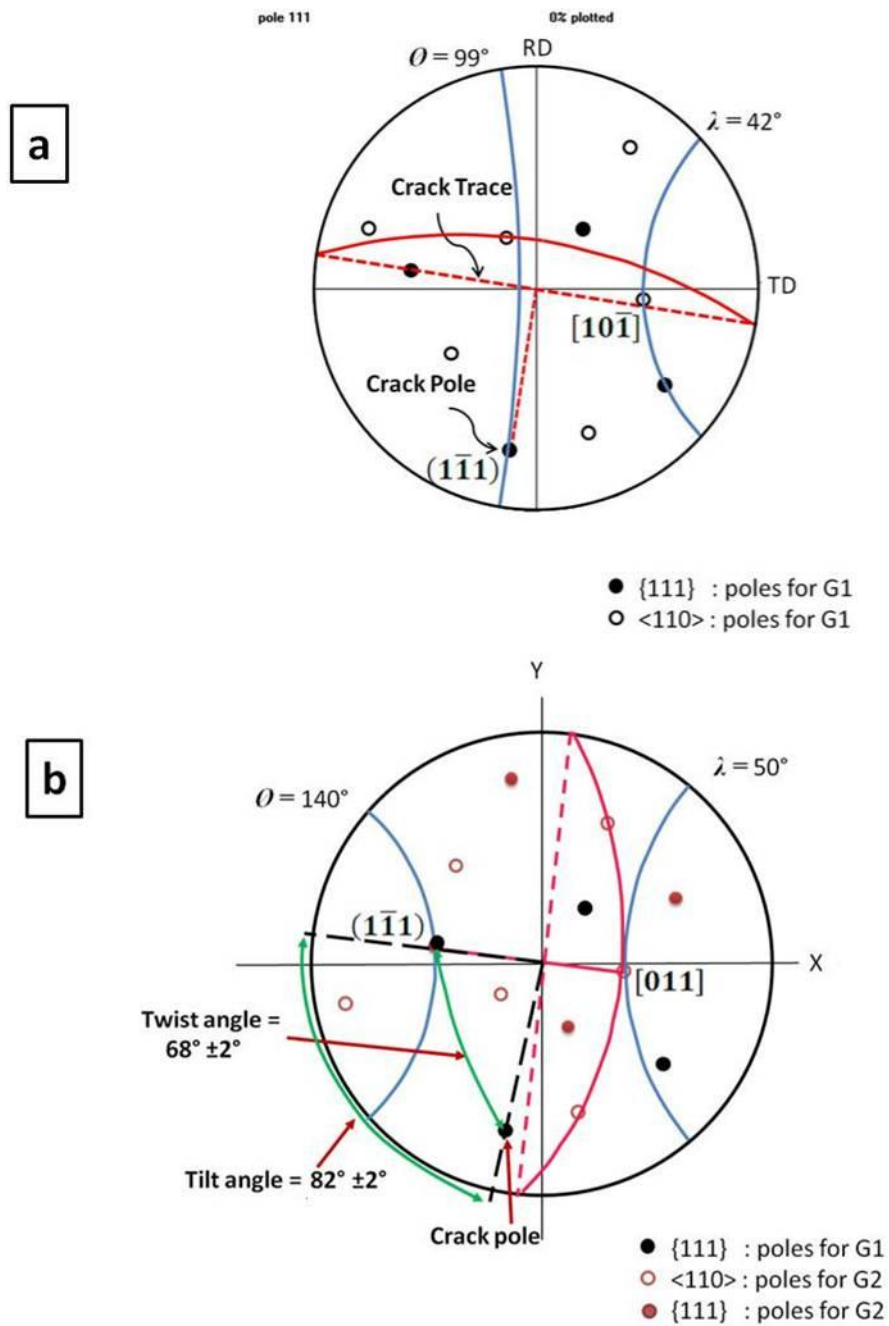


**Figure 5-5: a) stereographic projection  $\{111\}$  pole Figure for grain G1 with the plane system of the highest Schmid factor trace, b) determination of cracked plane, twist and tilt angles components;  $\{111\}$  pole Figure for grains G1 and G2.**

As shown in Figure 5-5, the highest Schmid factor planes from Table 5-2 are presented on pole Figures. The calculated  $\theta$ ,  $\lambda$  (blue lines) were drawn by using the Wulff net and relative to the loading direction (parallel to Y). The poles of slip plane  $\{111\}$  and slip

direction  $\{110\}$  set on those circles. The Wulff net was then used to measure an angle of  $90^\circ$  to get the great circle (red circle in the Figures) of the slip plane to match the highest Schmid factor. As seen in Figure 5-5(a), that the continued crack trace almost matches with the calculated ones of  $(\bar{1}\bar{1}1)/[10\bar{1}]$  plane system in G1, demonstrating that this slip plane was to be expected to be the crack plane nominated to transfer to G2 while there was no matching between the calculated slip plane systems of G2 and the continued crack trace from G1 as shown in Figure 5-5(b). This suggests that the crack does not meet a matching slip plane when it reaches G2. This could be a reason for the arresting of the crack.

Previous studies have proposed that the twist and tilt angles (Figure 5-6) between the adjacent grains is an important parameter controlling the crack interaction with grain boundaries [185]. The tilt and twist components of boundaries may determine whether the crack can cross the boundary. A grain boundary can have both components. These two factors are exhibited in Figure 5-6. In the case of 5-6(a) (a tilt boundary) a crack may propagate across the boundary more easily than in the case of 5-6(b) (a twist boundary). In the latter case the crack may be forced to continue into the next grain by two possible methods: i) initiation of a new crack on part of the boundary or ii) by going via a neighbouring grain with a low twist component.

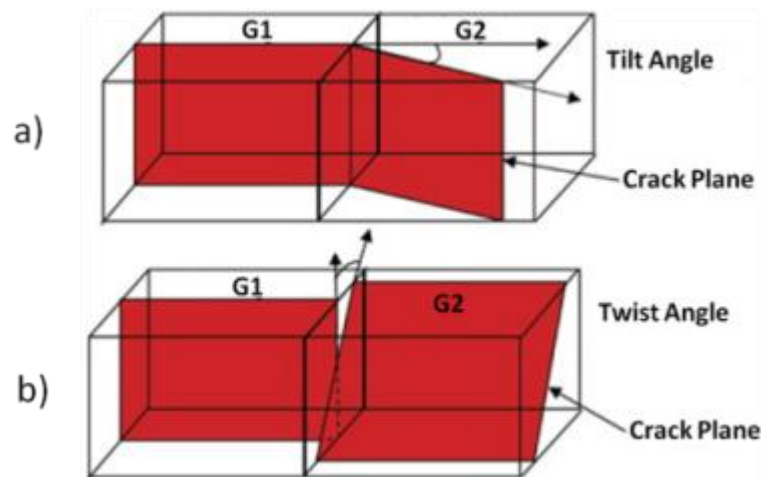


**Figure 5-6: Schematic describing the crack plane misorientation across a grain boundary in terms of the tilt angle (a), and the twist angle (b).**

Figure 5-5-b shows the pole Figure of  $\{111\}$  for G1 and the grain boundary in G2. The Wulff net was used to measure the twist angle which is located between the pole of the crack and the pole of the active slip plane in G2. Also, the tilt angle which is located between the normal to the crack trace and the normal to the predicted active slip planes in G2 was measured. The first predicted slip plane in G2 was  $(\bar{1}11)/[011]$  with a Schmid factor of 0.488. It shows a tilt angle of about  $82^\circ \pm 2^\circ$  and a twist angle of about  $68^\circ \pm 2^\circ$  relative to the plane of the crack in G1. In addition, the second predicted slip plane of  $(\bar{1}11)/[\bar{0}11]$  has a similarly high Schmid factor (0.462) with a tilt angle of  $148^\circ \pm 2^\circ$  and a twist angle of  $108^\circ \pm 2^\circ$  to the continued active slip plane in G1. These angles are all large and so may explain the difficulty in propagation and transfer of deformation across the grain boundary from G1 to G2. This supports the suggestion of the large misorientation between the planes of the highest Schmid factors of the two grains.

Figure 4-69 shows a close up view of the arrested crack tip that propagated through the FCC grain G1 until it arrested. The crack appears to be discontinuous, but why is it so? This might be interpreted in terms of a specific SCC model: the corrosion tunnel model [12, 76]. This model suggests that cracking is initiated at slip steps by the formation of arrays of fine corrosion tunnels (Figure 5-7), which grow in length and diameter until the remaining metal ligament fails. The crack is then thought to propagate in a discontinuous manner by repeated cycles of tunnel growth and ductile fracture. This model is applicable for transgranular stress corrosion cracking only. Thus, this argument led us to consider that the austenite grain size and distribution may have some control on retardation of short crack propagation in DSS.

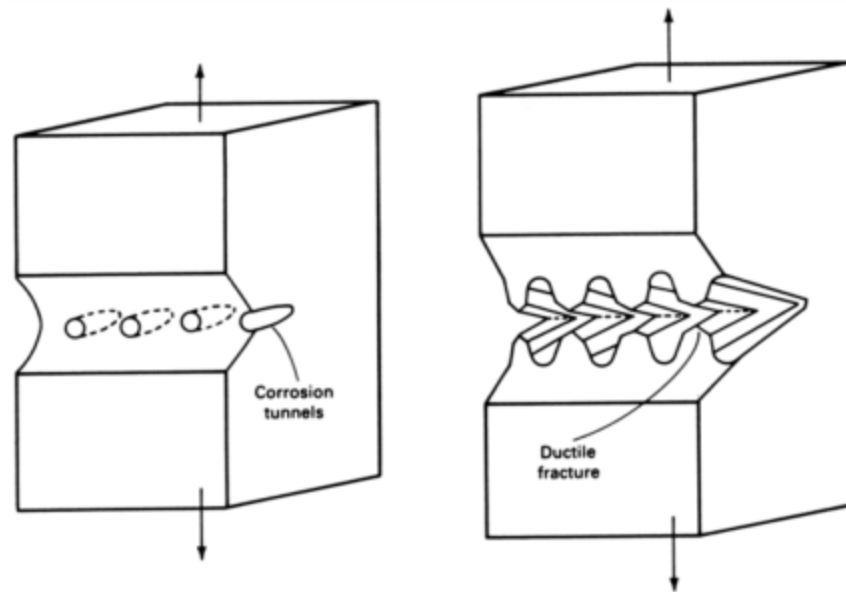


**Figure 5-7: Schematic of tunnel model showing the formation of corrosion tunnels at slip steps and ductile deformation and fracture of the remaining ligaments [44].**

#### **5.4 Suitability of Digital Image Correlation**

In the current study, digital image correlation was used, for the first time, to observe the short stress corrosion cracking behaviour in the super duplex stainless steel Zeron 100. When using DIC it is important that the sample surface has sufficient number and distribution of suitably-sized features on it to enable accurate strain mapping to be performed. When this is the case the noise levels in the strain map will be low enough to allow determination of significant strains.

As shown in Figure 4-13, encouraging results are achieved when the surfaces of the samples were prepared by grinding (4000 grit) then electroetched in 50% nitric acid at 3V for 4min. To determine the strain noise, it was necessary to carry out the process of image correlation in circumstances where no strain had occurred, but displacement had. Then the ambient strain level could be determined by determining the strain map. Ideally the strain map would be blank as this would indicate that no strain was present in the microstructure, but some strain does show up on such a map and this is noise. An RMS measure of this noise can be obtained from the DIC. By using (X5, X10 and X20) lens objectives of the optical microscope, two images of the same area were selected with a very small displacement between the images (20 pixels) to achieve an image correlation where no

strain should be present. The analysis chosen involved a multi-pass scheme in which the size of the image sub regions (windows) decrease in size from 512x512 to 32x32 pixels with the maximum overlap of 87%. Depending on the trends of that analysis (Figure 4-15), it could be confirmed that the increase in the window size will improve (decrease) the noise level because of the increasing in the number of features per window that give better comparisons of the windows before and after the deformation. Simply increasing the magnification leads to more noise because of the lower number of features in the field of view and the larger spacing between those features, increasing the uncertainty. It could also result in greater difficulty in focusing the entire image when at higher magnification, possibly due to variations in sample height which has greater effect when at high magnification.

The best magnification considered was 10x, and this was combined with the smallest possible sub-window sizes to provide spatial resolutions closest to the optimum desired. A magnification of 20x was too high to give a valuable insight into the behaviour as fewer grains were displayed in each image. 20x also yielded higher noise values and the acceptable window size was too large to be able to measure strains inside many grains. On the other hand a magnification of 5x has too many grains but they are too small to draw reasonable conclusions from. The most suitable lens was found to be 10x magnification because it demonstrates a noise level of  $RMS = 0.013 \mu m$  at window size of (64x64 Pixels =  $14.72 \mu m$ ), while a larger window of (128x128 pixels =  $29.44 \mu m$ ) could give  $RMS = 0.01 \mu m$ .

The DIC accuracy within the salt droplets (both wet and evaporated) was tested to illustrate the noise development within the droplets at three sizes of interrogation window during the test as shown in Figure 4-21. The evaporated droplet shows better vision and less noise at the beginning, but the noise grew once corrosion started inside the droplet which gave a higher noise level similar to the wet droplets. An explanation for the general increase in RMS within the salt droplets is an insufficient range of light intensities when the images were captured, which result in regions of identical intensity that is impossible for the DIC software to recognise because the algorithm uses contrast to calculate displacements. Figures 4-17 and 4-18 show the changes inside the wet and evaporated droplets respectively because increasing corrosion products with time leads to a change in the

surface finish and the movement of features in the droplets which increase the uncertainty and the internal noise level. Figures 4-19 and 4-20 for the wet and evaporated droplets show the gray scale profile along the yellow line in the images taken after 600 hours and confirm very low gray value (contrast) inside the droplets which causes high noise, and high gray values outside the salt droplets. Further trials were carried out of the same tests to improve the vision inside the salt droplets by using different illumination intensities from 3000 to 10000 counts, but all of them showed the same noise development behaviour in the DIC image quality.

In contrast, DIC monitoring of SCC development out of the droplets was calculated successfully between images where the only changes are the crack opening displacements. Comparing the results achieved in this study with those studies mentioned earlier [154, 157, 186] and performed on austenitic stainless steels, the other studies gave better observation inside the droplets which enabled them to notice crack initiation - but that may be because the environmental temperature which was less severe than in this study. Also, serious consideration should be given to the microstructure tested in this study as dual phase (ferrite/austenite), and the ferrite phase may be responsible for the bulky corrosion products which accumulated inside the salt droplets and make it a dark almost preventing observation of the area under the droplet.

Displacement vectors data were used to determine the crack opening displacement by calculating the differences between displacement vectors on either side of the crack along its length, and that gave precise data, better than could be achieved by optical measurements as shown in Figures (4-28, 4-34, 4-35 and 4-37). Furthermore, the comparison of background strains measured by DIC analysis and the strain gauge data (Figures 4-36, 4-40 and 4-45), has confirmed that the DIC measurements could detect the appearance of the cracks before they could be shown in the strain gauge data as a significant change in the strain reading or detected by the optical microscope as a visible crack. The strain maps were overlaid on the optical images and also used to identify regions of localized strain and hence crack locations and propagations. Such overlays are displayed in Figures 4-31, 4-32, 4-38 and 4-41. Also, the good resolution and low noise threshold of this experiment (T-T rolled sample) has led to the observation that a plastic zone exists at the tip of the cracks. The detailed study of plastic zones was not a part of

this project but it is mentioned here to show the potential capability of the DIC to show the spread of plasticity ahead of the crack (Figure 5-8). This analysis could offers the opportunity to investigate relationship between the mechanical force driving cracking, the stress intensity at the crack tip and the resulting crack growth rates [157, 172].

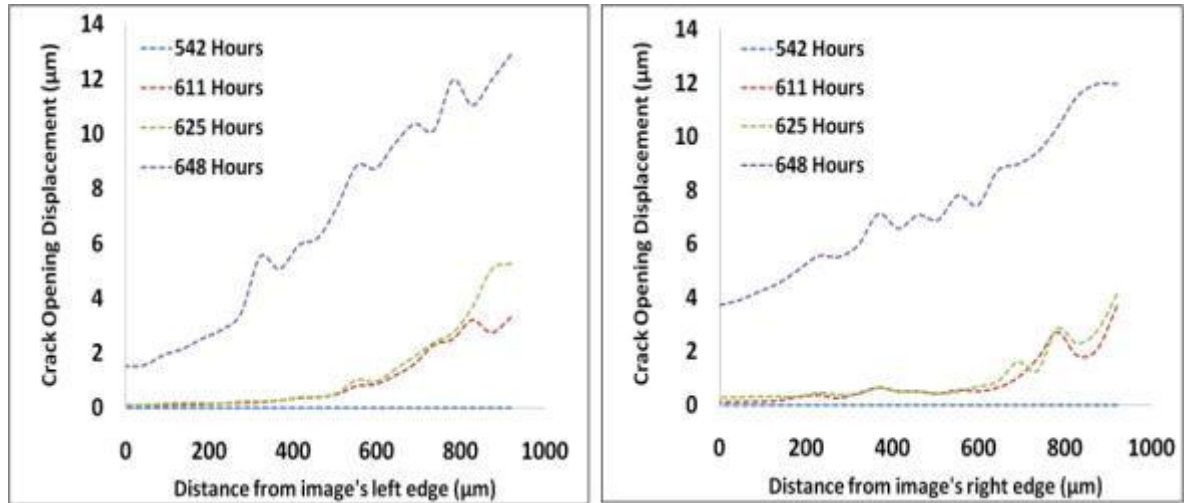


**Figure 5-8: Displacement across the crack derived from the DIC analysis presented in Figures 4-31 (left) and 4-32 (right), the crack tip plastic zone is also shown (RMS =  $\pm 0.3 \mu\text{m}$ ).**

In the rolled sample with rolling direction longitudinal to the loading direction, the crack was clearly detected and measured by the DIC analysis (Figures 4-38, 4-39 and 4-40) before it was noticed by visual inspection or even by strain gauge data. Also, in the as-received samples, with rolling direction transverse to the loading stress, the crack was detected and measured by the DIC analysis before it could be noticed by the strain gauge measurements (Figures 4-43, 4-44 and 4-45). The data shown in Figure 4-37 show that optical observations tend to underestimate the surface crack length.

In this study, the cracks (out of the droplet) with surface crack opening displacements from  $2 \mu\text{m}$  could be distinguished by the DIC technique (see Figures 4-34, 4-35 and 4-39) considering the RMS values to be the minimum detectable crack opening size, while optical inspections (Figure 4-37) show less accurate reading for the crack dimensions and a minimum detectable crack opening size of  $10 \pm 5 \mu\text{m}$  calculated visually from the optical images as the width of the dark area inside the visible crack as illustrated in Figure 5-9 as an example. This shows the crack opening displacement (COD) measured along the cracks

as a function of distance from the crack tips. The measurement results show that the crack tip was lost optically when the surface crack opening is less than around 10  $\mu\text{m}$ , which is consistent with the estimate. In the L-T rolled sample (Figure 4-38), the crack with COD of 2 to 4  $\mu\text{m}$  was detected by the strain maps allowed the DIC technique to show its subsequent elongation and opening (see Figure 4-39) while it was not visible optically because of its narrowness.

Bearing in mind, that many short cracks nucleated under the salty droplets (see Figures 4-47, 4-48 and 4-72) have crack opening of 1 to 5  $\mu\text{m}$ . It could be established that if the experiment is done with higher quality transparency through the salty droplets and less strain threshold noise (compatible with smaller windows), the DIC technique may be helpful to study the early stages of crack growth where changes in dimensions cannot be visualised optically because of the crack narrowness. Such improvement in the image noise will help to investigate the role of the mechanical crack driving force described by the estimated equivalent stress intensity factor [157, 186]. That will show whether crack growth rates may be related to mechanical driving force as the driving force for crack growth along the surface is expected to depend on the surface crack length, load applied to the crack and the crack depth [186].

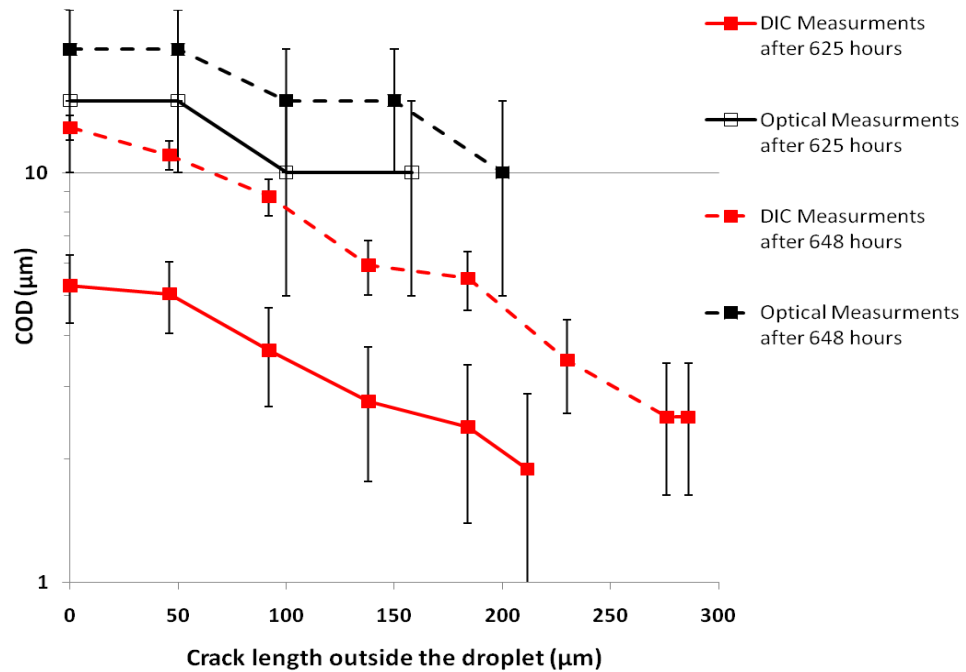


**Figure 5-9: Comparison of cracks measurements done by DIC and optical means showing the potential of the DIC to give better inspection.**

DIC is a new type of technique which has the potential to allow the in-situ observation of SCC. However, in this study, the DIC show a limitation on its usefulness in the study of SCC initiation in DSS because imaging was almost impossible through the salty corroded layers. Thus more laboratory trials will be necessary to develop and implement more practical monitoring inside the droplets, possibly by using a solution for in-situ application which may give a chance for the SCC initiation to be detected earlier and before the corrosion production products block observations. Also, a larger imaging view would allow scanning of the whole specimen at the same time would be useful to detect any changes in the strain around the observed area that could occur in relation to SCC initiation.

### **5.5 Strain partitioning and pitting**

Considering that pitting and localized corrosion are the initiation sites for SCC under an applied stress or strain and the role of plastic deformation on the corrosion behaviour of a super-duplex stainless steel (SDSS) has been reported in previous works [29, 65-67], it was suggested that the strain concentration at these corrosion sites initiates microcracks and

helps continue their propagation normal to the main tensile load. The two phases in the duplex microstructure differ in some of their properties (yield stress, for example) which in turn lead to variations in microstructural behaviour and results in heterogeneity in the strain on the microstructural level (strain partitioning). Thus it was planned to investigate if there is a correlation between strain localization and pitting behaviour in super duplex stainless steels.

In-situ tensile testing and DIC have been used to produce full field strain maps of the strain heterogeneities in the microstructure of forged Zeron 100 duplex stainless steel. Figures 4-81 and 4-83 show the development in the strain field of the observed surface. Some of the areas of high strain appear to be the result of localised straining within austenite grains (Figure 4-82) and some high strain regions coincide with austenite/austenite boundaries, although the strain appears to vary inside the grains, which could mean both that the strain varies within the grains and that the noise level is higher than expected and is causing the apparent variation. Both phases experience plastic deformation and Figure 4-88 shows that some austenite grains revealed higher strain levels than the bulk strain (3%) and ferrite grains. An important outcome of this result is that when the sample was tested at the same bulk strain level, the amount of plastic strain induced in the specimens is significantly different between both phases and will therefore have an impact on the SCC mechanism. Figure 4-89 contains areas of strain a few percent below bulk and that could be due to remaining compressive phase stresses in certain grains.

Heterogeneous strain within austenite grains could be a result of a build-up of dislocations at a boundary that is hard to cross [26-28] and shown in the EBSD local misorientation map (Figure 4-84) which gives a better understanding of the relationship between local misorientation and susceptibility to corrosion. However, this study could not draw a firm conclusion of the relationship between the measurement of local plastic strain distribution and the pitting density because this EBSD analysis has some basic limitations related to the step size, as has been demonstrated by Kamaya [187, 188]. The combination of this EBSD result and pitting density measurements could provide better knowledge about any link between the local misorientation level and the susceptibility to corrosion initiation, and then to stress corrosion cracking.

As austenite grains could be in simultaneous contact with various differently orientated ferrite boundaries it is possible that some areas could see a greater build-up of strain than others [189, 190]. Also, during straining, significant changes could happen to the surface such as the emergence of slip steps and changes to the surface flatness (Figures 4-81, 4-82 and 4-86), both of which would make focussing harder and also make it harder for the DIC software to read the surface given the disappearance and emergence of features. Moreover, it should be noticed that the ferrite phase has fewer features than the austenite phase which may lead to undervaluation of the maximum strain measured by the DIC technique.

At the scales used, all of the austenite grains showed initiation of slip bands containing a high density of dislocations and these slip bands were favourable sites for pitting in addition to the high dislocation densities areas at grain boundaries. But there was no clear evidence of any relation between the strain level and the density of pits in either phase. Generally, the data was scattered to be able to draw clear conclusions from this test. However, surface preparation using the focused ion beam technique [134-137] or using conventional electron beam lithography to deposit grid points on the specimen surface could show a micro-scale strain distribution as observed by Vignal [67] with the possibility to extend the strain to more than 3% [66].

## 5.6 Summary

Several observations taken from the experimental results are highlighted below:

- Despite the high resistance of the tested material to corrosion in chloride environment, the pitting corrosion could be initiated at sufficiently concentrated chloride and intermediate temperature 70°-80°C.
- Atmospheric-induced chloride stress corrosion cracks have been initiated and grown beneath magnesium chloride droplets at a temperature of 80°C and relative humidity 30-33% and SCC was initiated with the assistance of localized corrosion as pitting and selective dissolution preferentially in the ferrite phase.
- Early stages microcracks were initiated in  $\alpha$  phase and along  $\alpha/\gamma$  boundaries with easier propagation through the crystallographic slip systems in ferrite phase.

- Rolled sample shows faster SCC initiation and propagation comparing to the as received samples. Changes in the topography of the surface during strain deformation developed slip bands acting as preferential sites for localized corrosion and leading to the SCC.
- SCC propagation was easier in the T-T samples than the L-T samples which were affected mainly by the  $\alpha/\gamma$  and  $\gamma/\gamma$  boundaries as major barriers could cause a deflection or retardation in the crack path.
- The surface of the tested sample was prepared successfully and the DIC technique was capable of detecting changes in the surface strain, the crack propagation and the measurement of crack opening displacements in the area outside of the droplets that are difficult to be detected via conventional optical microscopy. Evaporated droplets allowed more precise visions inside the droplet but before the corrosion start inside. Once the corrosion starts inside the droplet, the evaporated droplet show almost the same uncertainty level like the wet droplets.
- No relation between the strain level and the density of pits in either phase has been established; further experimental work would be required for this.

## 6 CONCLUSION AND FUTURE WORKS

From these experimental results a number of conclusions can be reached and some areas for further work identified:

- Atmospheric-induced chloride stress corrosion cracks have been initiated and grown in type Zeron 100 super duplex stainless steel (loaded to  $1.05\sigma_y$ ) beneath magnesium chloride droplets at a temperature of 80°C and relative humidity 30-33%.
- It is clear that SCC was initiated with the assistance of localized corrosion as crystallographic pitting and selective dissolution along the deformation bands observed in the ferrite phase.
- Early stage microcracks were initiated in ferrite phase and ferrite/austenite interfaces and propagated preferentially in the ferrite phase.
- The crack initiation and propagation were faster in the cold-rolled samples comparing to the as received samples.
- The sample orientation to the loading direction has a significant effect on the stress corrosion cracking propagation susceptibility. The transverse orientation to the tensile loading (T-T) provided an easier path for cracking than the longitudinal orientation.
- Arrested short crack nuclei were observed in the rolled L-T sample. They were arrested at  $\gamma/\gamma$  twin boundaries. The arrest could be explained by the large misorientation between the planes of highest Schmid factor in the cracked grain and the  $\gamma/\gamma$  twin.
- DIC was effectively used to observe the strain developments and the displacements in observed surfaces and outside of the droplets where changes in dimensions cannot be measured visually, due to crack narrowness.
- Up to this level, digital image correlation could not identify or quantify the initiation of the cracks inside the droplets because of the mobility of the salt film and the high amount of the corrosion products formed which obscure the vision under the droplet.

- There was no relation established between the strain level and the density of pitting in either phase.

A number of areas for future examination and work exist to provide a better characterisation of the surfaces and analysis of stress corrosion cracking and pitting performance as detailed below:

- The stress corrosion cracking of super duplex stainless steel was examined in this study at 80°C and a stress level of  $1.05\sigma_y$  (3% bulk strain). Further tests parameters could be investigated, for example, different exposure temperatures and stress magnitudes, to get more information about the stress corrosion cracking behaviour of the material. Lower exposure temperature and stress levels are expected to show a reduced tendency of cracking nucleation. A similar relationship may also exist with the degree of cold deformation. These tests will allow a better understanding of the effects of different microstructure and environmental parameters on SCC initiation and propagation [191-193]. The main aim of these experiments would be to investigate the envelope of material susceptibility parameters as a function of temperature and stress level.
- The surface preparation and the imaging setup are the main causes of error as these results in strains that may not be present. Important improvements that should be made in future include optimize the surface preparation so that a smaller sub-window size and therefore a higher spatial resolution can be used. This could be done by trying ion milling using focused ion beam technique of a smooth surface to introduce the patterns (micro-markers) [134-137]. Also, it is suggested to carry out further DIC tests with a stereo microscope in order to achieve a greater depth of field, to maintain focus even when the surface loses its flatness. Another important point is the possibility to observe a larger surface area, which is beneficial for the observation of (probabilistic) pitting events. Another option would be to translate the camera across the specimen surface for extended area capture.
- The relationship between strain localization and pit density was studied using DIC. Improved spatial resolution may be achieved using a microgrid overlay produced

by electron beam lithography [67, 138]. The use of microgrid points fabricated through electron lithography processes will allow a higher resolution mapping of strain development at the sample's surface and a bulk strain >3% could easily be also tested. Electron back scattered diffraction (EBSD) could be used to improve the experimental setup. Combined DIC and EBSD studies allow for the examination of ferrite, austenite, grain boundaries and interfaces boundaries, producing a more accurate identification of strain gradients and correlation to crystallographic orientations and pitting criteria in a duplex stainless steel. EBSD analysis may also provide information between the relationship of pitting corrosion and crystallographic orientation of the metal.

## 7 REFERENCES

1. Gunn, R.N., *Duplex stainless steels : microstructure, properties and applications*. 1997, Cambridge, England: Abington Pub.
2. Alvarez-Armas, I., *Duplex Stainless Steels: Brief History and Some Recent Alloys*. Recent Patents on Mechanical Engineering, 2008. 1: p. 51-57.
3. Jan Olsson, M.S., *Duplex – A new generation of stainless steels for desalination plants*. Desalination 205 (2007), 2007: p. 104–113.
4. Lee, J.-B., *Effects of alloying elements, Cr, Mo and N on repassivation characteristics of stainless steels using the abrading electrode technique*. Materials Chemistry and Physics, 2006. 99(2-3): p. 224-234.
5. Lula, R.A., *Stainless Steels*, ed. A.S.f. Metals. 1986.
6. Honeycombe, R.W.K. and H.K.D.H. Bhadeshia, *Steels : microstructure and properties*. Metallurgy and materials science. 2003, London: Edward Arnold.
7. Leffler, B. (2005) *Stainless steels and their properties*.
8. Davis, J.R. and A.S.M.I.H. Committee, *Stainless steels*. ASM specialty handbook. 1994, Materials Park, Ohio: ASM International.
9. Database, K.t.M. [cited 2008; 208-232]. Available from: <http://steel.keytometals.com/default.aspx?ID=CheckArticle&LN=AR&NM=208>.
10. J.Charles, *Past, Present and Future of the duplex stainless steels*.
11. <http://www.bssa.org.uk>. [cited 2009; British Stainless Steel Association].
12. Sedriks, A.J., *Corrosion of Stainless Steels*. Corrosion monograph series. Electrochemical Society 1996, New York: Wiley.
13. Chai, G., U. Kivisäkk, J. Tokaruk†, and J. Eidhagen, *Hyper duplex stainless steel for deep subsea applications*. Stainless Steels World, March 2009. R&D Center, PA Tube, Sandvik Materials Technology, 811 81 Sandviken, Sweden.
14. Campbell, F.C., *Elements of metallurgy and engineering alloys*. 2008, Materials Park, Ohio: ASM International.
15. Redmond, R.M.D.a.J.D., *A guide to using duplex stainless steels*. MATERIALS & DESIGN Vol. 12 No. 4 AUGUST (1991) p. 187-192.
16. Perren, R.A., T. Suter, C. Solenthaler, G. Gullo, P.J. Uggowitzer, H. Bohni, and M.O. Speidel, *Corrosion resistance of super duplex stainless steels in chloride ion containing environments: investigations by means of a new microelectrochemical method II. Influence of precipitates*. Corrosion Science, 2001. 43(4): p. 727-745.
17. Sourmail, T. and H. Bhadeshia. [cited 2009; Available from: [http://www.msm.cam.ac.uk/phase-trans/2005/Stainless\\_steels/stainless.html](http://www.msm.cam.ac.uk/phase-trans/2005/Stainless_steels/stainless.html)].
18. Weber, L. and P.J. Uggowitzer, *Partitioning of chromium and molybdenum in super duplex stainless steels with respect to nitrogen and nickel content*. Materials Science and Engineering A, 1998. 242(1-2): p. 222-229.
19. Marshall, P., *Austenitic stainless steels : microstructure and mechanical properties*. 1984, London: Elsevier Applied Science.
20. Tseng, C.-M., H.-Y. Liou, and W.-T. Tsai, *Mechanical Behavior - Effect of Nitrogen Content on the Environmentally-Assisted Cracking Susceptibility of Duplex Stainless Steels*. Metallurgical and materials transactions. A, Physical metallurgy and materials science., 2003. 34(1): p. 95.
21. Dakhlaoui, R., C. Braham, and A. Baczanski, *Mechanical properties of phases in austeno-ferritic duplex stainless steel- Surface stresses studied by X-ray diffraction*. Materials Science and Engineering a-Structural Materials Properties Microstructure and Processing, 2007. 444(1-2): p. 6-17.

22. Van der Walt, C.M., *Slip in the B.C.C. metals*. Acta Metallurgica, 1969. 17(4): p. 393-395.
23. Dieter, G.E. and D. Bacon, *Mechanical metallurgy*. McGraw-Hill series in materials science and engineering. 2001, London [u.a.]: McGraw-Hill.
24. El Bartali, A., V. Aubin, L. Sabatier, P. Villechaise, and S. Degallaix-Moreuil, *Identification and analysis of slip systems activated during low-cycle fatigue in a duplex stainless steel*. Scripta Materialia, 2008. 59(12): p. 1231-1234.
25. Wasen J. , E.E., U. Karlsson B. , *Near-threshold Fatigue Growth in a Microduplex Stainless Steel*. Yourk Ins.Metals (1987) p. 357-362.
26. Serre, I., D. Salazar, and J.B. Vogt, *Atomic force microscopy investigation of surface relief in individual phases of deformed duplex stainless steel*. Materials Science and Engineering a-Structural Materials Properties Microstructure and Processing, 2008. 492(1-2): p. 428-433.
27. Jia, N., R. Lin Peng, G.C. Chai, S. Johansson, and Y.D. Wang, *Direct experimental mapping of microscale deformation heterogeneity in duplex stainless steel*. Materials Science and Engineering: A, 2008. 491(1-2): p. 425-433.
28. Frechard, S., F. Martin, C. Clement, and J. Cousty, *AFM and EBSD combined studies of plastic deformation in a duplex stainless steel*. Materials Science and Engineering a-Structural Materials Properties Microstructure and Processing, 2006. 418(1-2): p. 312-319.
29. Kempf, D., V. Vignal, G. Cailletaud, R. Oltra, J.C. Weeber, and E. Finot, *High spatial resolution strain measurements at the surface of duplex stainless steels*. PHILOSOPHICAL MAGAZINE, 2007. 87(8-9): p. 1379-1399.
30. Francis, R. and G. Byrne, *Experiences With Super Duplex Stainless Steel in Seawater*, in *CORROSION 2003*. 2003, NACE International: San Diego Ca.
31. Byrne, G., R. Francis, and G. Warburton, *The Selection Of Superduplex Stainless Steel For Oilfield Applications*. NACE International. Publications Division, Houston USA, 2004. 04123(CORROSION 2004).
32. Snis, M. and J. Olsson, *Reduce costs for storage and distribution of desalted water -- use duplex stainless steel*. Desalination, 2008. 223(1-3): p. 476-486.
33. SABIC., S.A.B.I.C., *Applications of Duplex Stainless Steels in SABIC's Affiliates.:* Jubail Industrial City.
34. Wilhelmsson, G.B.a.P., *Fabrication and Practical Experience of Duplex Stainless Steels*. MATERIALS & DESIGN Vol. 10 No. 1 JANUARY/FEBRUARY (1989) p. 23-28.
35. Kaesche, H., *Metallic corrosion : principles of physical chemistry and current problems*. 1985, Houston, Tex.: National Association of Corrosion Engineers.
36. Cottis, R.A. and L.L. Shreir, *Shreir's corrosion*. 2010, Amsterdam; London: Elsevier.
37. Ahmad, Z. and E. Institution of Chemical, *Principles of corrosion engineering and corrosion control*. 2006, Boston, MA: Elsevier/BH.
38. Shreir, L.L., G.T. Burstein, R.A. Jarman, and ScienceDirect, *Corrosion. Volume 1, Metal/environment reactions*. 1994, Oxford; Boston: Butterworth-Heinemann.
39. Jones, D.A., *Principles and prevention of corrosion*. 1996, Upper Saddle River, NJ: Prentice Hall.
40. VanDroffelaar, H., J.T.N. Atkinson, and E. National Association of Corrosion, *Corrosion and its control : an introduction to the subject*. 1995, Houston, TX (1440 S. Creek Dr., Houston 77084): NACE International.

41. Revie, R.W. and H.H. Uhlig, *Corrosion and corrosion control : an introduction to corrosion science and engineering*. 2008, Hoboken, N.J.: Wiley-Interscience.
42. <http://octane.nmt.edu/waterquality/corrosion/corrosion.htm>; New Mexico Water and Infrastructure Data System:[Corrosion pages].
43. Scully, J.C., *The fundamentals of corrosion*. 2nd ed. 1975, Oxford [etc.]: Pergamon Press.
44. Cramer, S.D., B.S. Covino, and c. Asm international. Handbook, *ASM Handbook. Volume 13A, Corrosion*. 2003, Materials Park (Ohio): ASM International.
45. Frankel, G.S., *Pitting Corrosion, Corrosion: Fundamentals, Testing, and Protection*. ASM International, 2003. Vol 13A, ASM Handbook: p. 236–241.
46. Kopeliovich, D. [http://www.substech.com/dokuwiki/doku.php?id=pitting\\_corrosion](http://www.substech.com/dokuwiki/doku.php?id=pitting_corrosion).
47. Manning, P.E. and J. Duquette, *The effect of temperature (25°-289°C) on pit initiation in single phase and duplex 304L stainless steels in 100 ppm Cl- solution*. Corrosion Science, 1980. 20(4): p. 597-609.
48. Saithala, J.R. and J. Atkinson, *Effect of Temperature and Chloride Concentration on The Pitting Behavior of Zeron 100, 2205 and Ferralium alloy 225 duplex stainless steels*. Sheffield Hallam University.
49. Ernst, P. and R.C. Newman, *Explanation of the effect of high chloride concentration on the critical pitting temperature of stainless steel*. Corrosion Science, 2007. 49(9): p. 3705-3715.
50. Prawoto, Y., K. Ibrahim, and W.B.W. Nik, *Effect of ph and chloride concentration on the corrosion of duplex stainless steel*. Arab. J. Sci. Eng. Arabian Journal for Science and Engineering, 2009. 34(2 C): p. 115-127.
51. Australia, A.S., <http://www.azom.com/Details.asp?ArticleID=470>. 2001
52. Nana, S. and M.B. Cortie, *microstructure and corrosion resistance of experimental low-nickel duplex stainless steel*. Journal of The South African Institute of Mining and Metallurgy, 1993. 93(11/12): p. 307-315.
53. Malik, A.U., P.C. Mayan Kutty, N.A. Siddiqi, I.N. Andijani, and S. Ahmed, *The influence of pH and chloride concentration on the corrosion behaviour of AISI 316L steel in aqueous solutions*. Corrosion Science, 1992. 33(11): p. 1809-1827.
54. Rieder, E.S., M. Ashworth, and J.P.G. Farra, *The Effect of Nitrogen on the Stability of the Passive Film on a Zeron 100 Super Duplex Stainless Steel*. Electrochemical and Solid-State Letters, 1999. 2(1): p. 19-21.
55. Jeffrey A. Platt, A.G., Arnaldo Zuccari, David W. Thornburg, Barbara F. Rhodes, Yoshiki Oshida, and B. Keith Moore, *Corrosion behaviour of 2205 duplex stainless steel*. American Journal of Orthodontics and Dentofacial Orthopaedics, 1997. 112: p. 69-79.
56. Deng, B., Y. Jiang, J. Gong, C. Zhong, J. Gao, and J. Li, *Critical pitting and repassivation temperatures for duplex stainless steel in chloride solutions*. Electrochim Acta Electrochimica Acta, 2008. 53(16): p. 5220-5225.
57. Garfias-Mesias, L.F., J.M. Sykes, and C.D.S. Tuck, *The effect of phase compositions on the pitting corrosion of 25 Cr duplex stainless steel in chloride solutions*. Corrosion science., 1996. 38(8): p. 1319-1330.
58. Femenia, M., J. Pan, and C. Leygraf, *Characterization of Ferrite-Austenite Boundary Region of Duplex Stainless Steels by SAES*. Journal of The Electrochemical Society, 2004. 151(11): p. B581-B585.
59. Shih, S.T., T.P. Perng, and C.Y. Tai, *Corrosion Behavior of Two-Phase Fe-Mn-Al Alloys in 3.5% NaCl Solution*. Corrosion, 1993. 49(02).

60. Batista, S.R.F. and S.E. Kuri, *Aspects of selective and pitting corrosion in cast duplex stainless steels*. Anti-Corrosion Methods and Materials, 2004. 51(3): p. 205-208.
61. Gadgil, V., J. Swens, and B. Kolster, *Chromium concentration in and around ferrite-austenite phase boundaries in duplex stainless steels*. Journal de Physique Colloques 1989. 50: p. C8-361-C8-364.
62. Friedel, J., *Dislocations*. Pergamon Press (1964), 1964.
63. Vignal, V., R. Oltra, and C. Josse, *Local analysis of the mechanical behaviour of inclusions-containing stainless steels under straining conditions*. Scripta Materialia, 2003. 49(8): p. 779-784.
64. Kamachi Mudali, U., P. Shankar, S. Ningshen, R.K. Dayal, H.S. Khatak, and B. Raj, *On the pitting corrosion resistance of nitrogen alloyed cold worked austenitic stainless steels*. Corrosion Science, 2002. 44(10): p. 2183-2198.
65. Elhoud, A., N. Renton, and W. Deans, *The effect of manufacturing variables on the corrosion resistance of a super duplex stainless steel*. The International Journal of Advanced Manufacturing Technology, 2010: p. 1-11.
66. Elhoud, A., H. Ezuber, and W. Deans, *Influence of cold work and sigma phase on the pitting corrosion behavior of 25 chromium super duplex stainless steel in 3.5% sodium chloride solution*. Materials and Corrosion, 2010. 61(3): p. 199-204.
67. Vignal, V. and D. Kempf, *Influence of heterogeneous plastic strain fields on the corrosion susceptibility of duplex stainless steels at the microscale*. ADVANCES IN MATERIALS SCIENCE, 2007. 7(No. 1 (11)): p. 77-82.
68. Peguet, L., B. Malki, and B. Baroux, *Influence of cold working on the pitting corrosion resistance of stainless steels*. Corrosion Science, 2007. 49(4): p. 1933-1948.
69. Yamamoto, T., K. Fushimi, S. Miura, and H. Konno, *Influence of Substrate Dislocation on Passivation of Pure Iron in pH 8.4 Borate Buffer Solution*. Journal of The Electrochemical Society, 2010. 157(7): p. C231-C237.
70. Jones, R.H., *Stress-corrosion cracking*. 1992, Materials Park, Ohio: ASM International. viii, 448 p.
71. Turnbull, A., *Stress Corrosion Cracking: Mechanisms*, in *Encyclopedia of Materials: Science and Technology*. 2001. p. 8886-8892.
72. Turnbull, A., D. Horner, and B. Connolly, *Challenges in modelling the evolution of stress corrosion cracks from pits*. Engineering Fracture Mechanics, 2009. 76(5): p. 633-640.
73. Horner, D., B. Connolly, S. Zhou, and A. Turnbull. *Novel Images of the Evolution of Stress Corrosion Cracks from Corrosion Pits*. 2007.
74. Parkins, R.N., *Mechanistic Aspect of Stress Corrosion Cracking*. In: Cincinnati (Eds.).Parkins Symposium on Fundamental Aspects of Stress Corrosion Cracking., 1991: p. 3-39.
75. Rahimi, S., *Behaviour of Short Intergranular Stress Corrosion Crack in Type 304 Austenitic Stainless Steel*, in *School of Materials*. 2009, Manchester: Manchester,UK.
76. Marcus, P., *Corrosion mechanisms in theory and practice*. 2nd ed. 2002, New York: Marcel Dekker.
77. Sedriks, A.J., *Stress corrosion cracking test methods*. Corrosion testing made easy. 1990, Houston, TX: National Association of Corrosion Engineers. 87 p.
78. Jiang, X.-G., W.-Y. Chu, and J.-M. Xiao, *Fractal analysis of orientation effect on  $K_{Ic}$  and  $K_{Isc}$* . Engineering Fracture Mechanics, 1995. 51(5): p. 805-808.

79. Van Gelder, K., J.G. Erlings, J.W.M. Damen, and A. Visser, *The stress corrosion cracking of duplex stainless steel in H<sub>2</sub>S/CO<sub>2</sub>/Cl<sup>-</sup> environments*. Corrosion Science, 1987. 27(10-11): p. 1271-1279.
80. Saithala, J.R. and J. D. Atkinson, *Stress corrosion behaviour of super duplex stainless steel in dilute chloride solution at 130°C*. Material Engineering Research Institute Sheffield Hallam University.
81. J.R. Saithala, S. McCoy, A. Houghton, J.D. Atkinson, and H.S. Ubhi, *Stress corrosion cracking of super duplex stainless steels above and below the pitting potential*, in *CORROSION 2009*, NACE International: Atlanta, GA.
82. Cottis, R.A. and R.C. Newman, *Stress corrosion cracking resistance of duplex stainless steels*. 1995: HSE Books.
83. Talbot, D. and J. Talbot, *Corrosion science and technology*. 1998, Boca Raton: CRC Press.
84. Hinds, G. and A. Turnbull, *Threshold temperature for stress corrosion cracking of duplex stainless steel under evaporative seawater conditions*. Corrosion, 2008. 64(2): p. 101-106.
85. Johansson, E. and T. Prosek, *stress corrosion cracking properties of UNS S32101*. NACE International 2007. Houston TX USA, 2007. paper 07475.
86. Andersen, H., P.E. Arnvig, W. Wasielewska, L. Wegrelius, and C. Wolfe, *SCC of Stainless Steel Under Evaporative Conditions*. CORROSION - NATIONAL ASSOCIATION OF CORROSION ENGINEERS ANNUAL CONFERENCE, 1998(251).
87. Arnvig, P.-E. and W. Wasielewska, *stress corrosion behaviour of highly alloyed stainless steels under severe evaporative conditions*: Sweden.
88. Kangas, P. and J.M. Nicholls, *Chloride-induced stress corrosion cracking of Duplex stainless steels. Models, test methods and experience*. Materials and Corrosion, 1995. 46(6): p. 354-365.
89. R.F.A. Jargelius, R.B., S. Hertzman, J. Linder, Duplex stainless steels 91, 1991: p. 211-220.
90. Magnin, T., J. Le Coze, A. Desestret, M. American Society for, and A.S.M.M. Congress, *Twinning and stress corrosion cracking of ferrite phases of duplex stainless steels*. Metals/materials technology series. 1982, Metals Park, Ohio: American Society for Metals.
91. Tsai, W.-T. and M.-S. Chen, *Stress corrosion cracking behavior of 2205 duplex stainless steel in concentrated NaCl solution*. Corrosion Science, 2000. 42(3): p. 545-559.
92. Tsai, W.-T. and S.-L. Chou, *Environmentally assisted cracking behavior of duplex stainless steel in concentrated sodium chloride solution*. Corrosion Science, 2000. 42(10): p. 1741-1762.
93. Francis, R., G.R. Warburton, and G. Byrne, *Effects of Cathodic Protection on Duplex Stainless Steels in Seawater*. Corrosion, 1997. 53(03).
94. Silcock, J.M. and P.R. Swann, *Nucleation and Growth of Transgranular Stress Corrosion Cracks in Austenitic Stainless Steels*. Z.A. Foroulis (Eds.). Environment Sensitive Fracture of Engineering Materials. TMS, Warrendale, PA, 1979: p. 133-152.
95. Krupp, U., O. Düber, H.J. Christ, B. Künkler, A. Schick, and C.P. Fritzen, *Application of the EBSD technique to describe the initiation and growth behaviour of microstructurally short fatigue cracks in a duplex steel*. Journal of Microscopy, 2004. 213(3): p. 313-320.

96. Düber, O., B. Künkler, U. Krupp, H.J. Christ, and C.P. Fritzen, *Experimental characterization and two-dimensional simulation of short-crack propagation in an austenitic-ferritic duplex steel*. International Journal of Fatigue, 2006. 28(9): p. 983-992.
97. Parkins, R.N., *The application of stress-corrosion crack-growth kinetics to predicting lifetimes of structures*. Corrosion Science, 1989. 29(8): p. 1019-1038.
98. Turnbull, A., *Environment-assisted Fatigue in Liquid Environments*, in *Comprehensive Structural Integrity*, I. Milne, R.O. Ritchie, and B. Karihaloo, Editors. 2003, Pergamon: Oxford. p. 163-210.
99. O. Düber, B.K., U.Krupp, H.-J. Christ, C.-P. Fritzen, *short crack propagation in duplex steel-experimental characterization and modelling*.
100. Künkler, B., O. Düber, P. Köster, U. Krupp, C.P. Fritzen, and H.J. Christ, *Modelling of short crack propagation - Transition from stage I to stage II*. Engineering Fracture Mechanics. 75(3-4): p. 715-725.
101. C. M. Holtam, D.P.B., *Environment assisted cracking assessment methods: the behaviour of shallow cracks*, in *ESIA9 - 9th International Conference on Engineering Structural Integrity Assessment*. 15-19 October 2007: Beijing, China.
102. Hänninen, H.E., *Stress Corrosion Cracking*, in *Comprehensive Structural Integrity*, I. Milne, R.O. Ritchie, and B. Karihaloo, Editors. 2003, Pergamon: Oxford. p. 1-29.
103. Kwon, H.-S. and H.-S. Kim, *Investigation of stress corrosion susceptibility of duplex ([alpha] + [gamma]) stainless steel in a hot chloride solution*. Materials Science and Engineering: A, 1993. 172(1-2): p. 159-165.
104. S. Shimodaira, M.T., Y. Takizawa and H. Kamide, in R. W. Staehle, J. Hochmann, R. D. McCright and J. E. Slater, *Stress Corrosion Cracking and Hydrogen Embrittlement of Iron Base Alloys*. NACE, Houston, TX, 1977: p. 1003.
105. Korb, L.J. and A.S.M.I.H. Committee, *ASM Handbook. Volume 13. Corrosion*. 1998, Materials Park, Ohio: ASM International.
106. Sieradzki, K. and R.C. Newman, *Brittle behavior of ductile metals during stress-corrosion cracking*. Philosophical Magazine A, 1985. 51(1): p. 95 - 132.
107. T. James Marrow, S.K., Jin-Taek Oh., *The Effect of Microstructure on Brittle Fracture and Stress Corrosion Cracking in Duplex Stainless Steel*, in *Stainless Steels World 1999*.
108. Raymond, L., A.S.F.o.H. Embrittlement, P. National Symposium on Test Methods for Hydrogen Embrittlement, and Control. *Hydrogen embrittlement : prevention and control*. Philadelphia, PA: ASTM.
109. Marrow, T.J., A. Steuwer, F. Mohammed, D. Engelberg, and M. Sarwar, *Measurement of crack bridging stresses in environment-assisted cracking of duplex stainless by synchrotron diffraction*. Fatigue and Fracture of Engineering Materials and Structures, 2006. 29(6): p. 464-471.
110. Elhoud, A.M., N.C. Renton, and W.F. Deans, *Hydrogen embrittlement of super duplex stainless steel in acid solution*. International Journal of Hydrogen Energy, 2010. 35(12): p. 6455-6464.
111. Dietzel, W. and A. Turnbull, *Stress Corrosion Cracking*, in *Comprehensive Structural Integrity*, I. Milne, R.O. Ritchie, and B. Karihaloo, Editors. 2007, Pergamon: Oxford. p. 43-74.
112. Sutton, M.A., W.J. Wolters, W.H. Peters, W.F. Ranson, and S.R. McNeill, *Determination of displacements using an improved digital correlation method*. Image and Vision Computing, 1983. 1(3): p. 133-139.

113. Sutton, M., S. McNeill, J. Helm, and Y. Chao, *Advances in Two-Dimensional and Three-Dimensional Computer Vision*, in *Photomechanics*, P. Rastogi, Editor. 2000, Springer Berlin / Heidelberg. p. 323-372.
114. Hung, P.-C. and A.S. Voloshin, *In-plane strain measurement by digital image correlation*. Journal of the Brazilian Society of Mechanical Sciences and Engineering, 2003. 25: p. 215-221.
115. Yoneyama, S. and Y. Morimoto, *Accurate Displacement Measurement by Correlation of Colored Random Patterns*. JSME International Journal Series A Solid Mechanics and Material Engineering, 2003. 46(2): p. 178-184.
116. LaVision, *DaVis Strain Master Master Software Manual 7.1.*, in *LaVision GmbH*,. 2006, Gottingen.
117. Hild, F. and S. Roux, *REVIEW ARTICLE: Digital Image Correlation: from Displacement Measurement to Identification of Elastic Properties - a Review*. Strain, 2006. 42(2): p. 69-80.
118. Ronneberger, O., M. Raffel, and J. Kompenhans, *Advanced Evaluation Algorithms for Standard and Dual Plane Particle Image Velocimetry*. 1998.
119. Hua, T., H. Xie, S. Wang, Z. Hu, P. Chen, and Q. Zhang, *Evaluation of the quality of a speckle pattern in the digital image correlation method by mean subset fluctuation*. Optics & Laser Technology, 2011. 43(1): p. 9-13.
120. Da Fonseca, J.Q., P.M. Mummery, and P.J. Withers, *Full-field strain mapping by optical correlation of micrographs acquired during deformation*. Journal of Microscopy-Oxford, 2005. 218: p. 9-21.
121. Pertl, A., *Digital image correlation with an analytical plotter*. Photogrammetria, 1985. 40(1): p. 9-19.
122. Tang, Z.-Z., J. Liang, Z.-Z. Xiao, C. Guo, and H. Hu, *Three-dimensional digital image correlation system for deformation measurement in experimental mechanics*. Optical Engineering, 2010. 49(10): p. 103601-9.
123. Hunt, B.R., *Bayesian Methods in Nonlinear Digital Image Restoration*. IEEE Transactions on Computers, 1977. 26: p. 219-229.
124. W. F. Clocksin, K.F.C., P. H. S. Torr, J. Quinta Da Fonseca, P. J. Withers, *Inspection of surface strain in materials using dense displacement fields*. Proceedings of the 4th International Conference on New Challenges in Mesomechanics, Aalborg University, 2002. 2: p. 467-474.
125. William F. Clocksin, J.Q.d.F., P. J. Withers, Philip H. S. Torr, *Image Processing Issues in Digital Strain Mapping* Proceedings of the SPIE 4790, 21 Nov. 2002. 4790: p. 384-395.
126. Fincham, A.M. and G.R. Spedding, *Low cost, high resolution DPIV for measurement of turbulent fluid flow*. Experiments in Fluids, 1997. 23(6): p. 449-462.
127. Duff, A.J. and J.T. Marrow, *In-situ observations of intergranular stress corrosion cracking*, in *ASME Pressure Vessels and Piping Conference PVP2008*. 2008: Chicago.
128. Chu, T., W. Ranson, and M. Sutton, *Applications of digital-image-correlation techniques to experimental mechanics*. Experimental Mechanics, 1985. 25(3): p. 232-244.
129. Dickinson, A.S., A.C. Taylor, H. Ozturk, and M. Browne, *Experimental Validation of a Finite Element Model of the Proximal Femur Using Digital Image Correlation and a Composite Bone Model*. Journal of Biomechanical Engineering, 2011. 133(1): p. 014504-6.

130. Durif, E., M. Fregonese, J. Rethore, and A. Combescure, *Development of a Digital Image Correlation controlled fatigue crack propagation experiment*. EPJ Web of Conferences, 2010. 6: p. 31012.
131. Luo, Y., J. Ruff, R. Ray, Y. Gu, H.J. Ploehn, and W.A. Scrivens, *Vapor-Assisted Remodeling of Thin Gold Films*. Chemistry of Materials, 2005. 17(20): p. 5014-5023.
132. Sutton, M., N. Li, D. Joy, A. Reynolds, and X. Li, *Scanning Electron Microscopy for Quantitative Small and Large Deformation Measurements Part I: SEM Imaging at Magnifications from 200 to 10,000*. Experimental Mechanics, 2007. 47(6): p. 775-787.
133. Sutton, M.A., J.-J. Orteu, and H.W. Schreier, *Image correlation for shape, motion and deformation measurements : basic concepts, theory and applications*. 2009, New York, N.Y.: Springer.
134. Michel, B., D. Vogel, N. Sabate, and D. Lieske, *A New Method for Local Strain Field Analysis Near Cracks in Micro- and Nanotechnology Applications*, in *Fracture of Nano and Engineering Materials and Structures*, E.E. Gdoutos, Editor. 2006, Springer Netherlands. p. 729-730.
135. Sabaté, N. and et al., *Digital image correlation of nanoscale deformation fields for local stress measurement in thin films*. Nanotechnology, 2006. 17(20): p. 5264.
136. Liu, Z., H. Xie, D. Fang, C. Gu, Y. Meng, W. Wang, Y. Fang, and J. Miao, *Deformation analysis in microstructures and micro-devices*. Microelectronics Reliability, 2007. 47(12): p. 2226-2230.
137. Sabaté, N., D. Vogel, J. Keller, A. Gollhardt, J. Marcos, I. Gràcia, C. Cané, and B. Michel, *FIB-based technique for stress characterization on thin films for reliability purposes*. Microelectronic Engineering. 84(5-8): p. 1783-1787.
138. Hernandez-Castillo, L.E., J.H. Beynon, C. Pinna, and S. Van Der Zwaag, *Micro-scale strain distribution in hot-worked duplex stainless steel*. 2005, Stahleisen GMBH.
139. El Bartali, A., V. Aubin, and S. Degallaix, *Fatigue damage analysis in a duplex stainless steel by digital image correlation technique*. Fatigue & Fracture of Engineering Materials & Structures, 2008. 31(2): p. 137-151.
140. Forquin, P., L. Rota, Y. Charles, and F. Hild, *A method to determine the macroscopic toughness scatter of brittle materials*. International Journal of Fracture, 2004. 125(1-2): p. 171-187.
141. Schwalbe, K.-H., J.C. Newman, and J.L. Shannon, *Fracture mechanics testing on specimens with low constraint--standardisation activities within ISO and ASTM*. Engineering Fracture Mechanics, 2005. 72(4): p. 557-576.
142. Heerens, J. and M. Schödel, *Characterization of stable crack extension in aluminium sheet material using the crack tip opening angle determined optically and by the  $[\delta]_5$  clip gauge technique*. Engineering Fracture Mechanics, 2009. 76(1): p. 101-113.
143. Newman, J.C., M.A. James, and U. Zerbst, *A review of the CTOA/CTOD fracture criterion*. Engineering Fracture Mechanics. 70(3-4): p. 371-385.
144. Dawicke, D. and M. Sutton, *CTOA and crack-tunneling measurements in thin sheet 2024-T3 aluminum alloy*. Experimental Mechanics, 1994. 34(4): p. 357-368.
145. Mostafavi, M. and T.J. Marrow, *In situ observation of crack nuclei in poly-granular graphite under ring-on-ring equi-biaxial and flexural loading*. Engineering Fracture Mechanics. In Press, Corrected Proof.

146. Khan, A. and T.J. Marrow, *In-situ Observation of Damage Mechanisms by Digital Image Correlation during Tension and Low Cycle Fatigue of Magnesium alloys*, in *12th International Conference of Fracture, ICF12*. 2009: Ottawa, CANADA.
147. Krasovskii, A.Y. and I.S. Pinyak, *A Method for Measuring Current Values of the Crack-Tip Opening Displacement under Cyclic Loading*. *Strength of Materials*, 2002. 34(4): p. 322-333.
148. Darcis, P.P., C.N. McCowan, H. Windhoff, J.D. McColskey, and T.A. Siewert, *Crack tip opening angle optical measurement methods in five pipeline steels*. *Engineering Fracture Mechanics*, 2008. 75(8): p. 2453-2468.
149. Jr., W.N.S., *Crack-Tip Opening Displacement Measurement Techniques*. *Experimental Techniques in Fracture*, 1983. 1993(VCH Weinheim): p. 348.
150. Roux, S. and F. Hild, *Stress intensity factor measurements from digital image correlation: post-processing and integrated approaches*. *International Journal of Fracture*, 2006. 140(1): p. 141-157.
151. Réthoré, J., A. Gravouil, F. Morestin, and A. Combescure, *Estimation of mixed-mode stress intensity factors using digital image correlation and an interaction integral*. *International Journal of Fracture*, 2005. 132(1): p. 65-79.
152. Roux, S., J. Réthoré, and F. Hild, *Digital image correlation and fracture: an advanced technique for estimating stress intensity factors of 2D and 3D cracks*. *Journal of Physics D: Applied Physics*, 2009. 42(21): p. 214004.
153. McNeill, S.R., W.H. Peters, and M.A. Sutton, *Estimation of stress intensity factor by digital image correlation*. *Engineering Fracture Mechanics*, 1987. 28(1): p. 101-112.
154. Rahimi, S., D.L. Engelberg, J.A. Duff, and T.J. Marrow, *In situ observation of intergranular crack nucleation in a grain boundary controlled austenitic stainless steel*. *Journal of Microscopy-Oxford*, 2009. 233(3): p. 423-431.
155. Marrow, T.J., *New Techniques for In-Situ Observations of Crack Growth Behaviour*. In: *17th European Conference on Fracture (ECF17)*, 2008. 2-5 September, 2008(Brno, Czech Republic).
156. Kovac, J., C. Alaux, T.J. Marrow, E. Govekar, and A. Legat, *Correlations of electrochemical noise, acoustic emission and complementary monitoring techniques during intergranular stress-corrosion cracking of austenitic stainless steel*. *Corrosion Science*, 2010. 52(6): p. 2015-2025.
157. A. Cook, J.D., N. Stevens, S. Lyon, A. Sherry and T. J. Marrow, *Preliminary Evaluation of Digital Image Correlation for In-situ Observation of Low Temperature Atmospheric-Induced Chloride Stress Corrosion Cracking in Austenitic Stainless Steels*, in *216th ECS (Electrochemical Society) Meeting*. 4-9 Oct 2009: Vienna.
158. Jandejsek, I., O. Jirousek, and D. Vavřík, *Precise strain measurement in complex materials using Digital Volumetric Correlation and time lapse micro-CT data*. *Procedia Engineering*, 2011. 10: p. 1734-1739.
159. *Crack propagation mechanisms studied with DVC*. 2011 [cited 2011; Available from: <http://www.lavision.de/en/news/2011/1409/>].
160. ESRF. *Basics of Tomography*. 17-10-2008 Available from: <http://www.esrf.eu/UsersAndScience/Experiments/Imaging/ID22/Applications/Imaging/TomoBasics>.
161. *ASTM G 5 – 94(2004) Standard Reference Test Method for Making Potentiostatic and Potentiodynamic Anodic Polarization Measurements*. 2004, West Conshohocken: ASTM.

162. ASTM G30-97(2003) *standard practice for making and using u-bend stress-corrosion test specimens*. 2003, West Conshohocken: ASTM International.
163. Jiang, Z., Z. Sun, and P. Wang, *Internal relative humidity distribution in high-performance cement paste due to moisture diffusion and self-desiccation*. Cement and Concrete Research, 2006. 36(2): p. 320-325.
164. Humphreys, F.J., *Review Grain and subgrain characterisation by electron backscatter diffraction*. Journal of Materials Science, 2001. 36(16): p. 3833-3854.
165. Humphreys, F.J., *Vmap Manual - Orientation Mapping and Quantitative Metallography by EBSD*. Manchester Materials Science Centre, 2001.
166. Humphreys, F.J. and I. Brough, *High resolution electron backscatter diffraction with a field emission gun scanning electron microscope*. Journal of Microscopy, 1999. 195(1).
167. Bradley, R. *Xradia microXCT* 07 February 2011 Available from: [http://xray-imaging.org.uk/index.php?option=com\\_content&view=article&id=9&Itemid=54](http://xray-imaging.org.uk/index.php?option=com_content&view=article&id=9&Itemid=54).
168. Faraj, M., *Stress Corrosion Cracking In Duplex Stainless Steels*, in *School of Materials*. 2003, University of Manchester Institute of Science and Technology: Manchester.
169. J.R.Saithala, S.McCoy, J.D.Atkinson, and H.S.Ubhi, *Critical stress corrosion cracking potentials of stainless steels in dilute chloride solutions*, in *CORROSION 2010*. 2010, NACE International: San Antonio, TX.
170. Frankel, G.S., *Electrochemical Techniques in Corrosion: Status, Limitations, and Needs*. Journal of ASTM International, 2008. 5(2).
171. Shoji, S. and N. Ohnaka, *Effects of RH and chloride type on stainless steel room temperature atmospheric stress corrosion cracking*. Corrosion Engineering, 1993. 42(877): p. Corrosion Engineering, 42, 877 (1993).
172. Stevens, N.P.C., T. Cook, S.B. Lyon, and J. Duff, *Atmospheric corrosion of nuclear waste containers*, in *DIAMOND'10 Conference*. 2010: Manchester, UK.
173. Lindström, R., J.E. Svensson, and L.G. Johansson, *The Influence of Salt Deposits on the Atmospheric Corrosion of Zinc. The Important Role of the Sodium Ion*. Journal of the Electrochemical Society, 2002. 149: p. B57.
174. Mintz, T.S., L.S. Caseres, D.S. Dunn, and M.S. Bayssie, *Atmospheric Salt Fog Testing to Evaluate Chloride Induced Stress Corrosion Cracking of Type 304, 304L, And 316L Stainless Steel*. CORROSION 2010.
175. Chou, S.L. and W.T. Tsai, *Hydrogen embrittlement of duplex stainless steel in concentrated sodium chloride solution*. Materials chemistry and physics, 1999. 60(2): p. 137-142.
176. Elhoud, A., N. Renton, and W. Deans, *Hydrogen Embrittlement Enhanced by Plastic Deformation of Super Duplex Stainless Steel*. Damage and Fracture Mechanics, 2009: p. 59-67.
177. abanowski, J. and A. Ossowska, *Influence of burnishing on stress corrosion cracking susceptibility of duplex steel*. Juurnal of Achievements in Materials and Manufacturing Engineering, 2006. 19(1): p. 7.
178. Delafosse, D., J. Chateau, and T. Magnin, *Microfracture by pile-up formation at a stress corrosion crack tip: Numerical simulations of hydrogen/dislocation interactions*. Le Journal de Physique IV, 1999. 9(PR9).
179. Marrow, T. and J. King, *Microstructural and environmental effects on fatigue crack propagation in duplex stainless steels*. Fatigue & Fracture of Engineering Materials & Structures, 1994. 17(7): p. 761-771.

180. Gironès, A., P. Villechaise, A. Mateo, M. Anglada, and J. Méndez, *EBSD studies on the influence of texture on the surface damage mechanisms developed in cyclically loaded aged duplex stainless steels*. Materials Science and Engineering A, 2004. 387-389: p. 516-521.
181. Sarwar, M., E. Ahmad, and T. Manzoor, *Crack Bridging in Stress Corrosion Cracking of Duplex Stainless Steels*. Key Engineering Materials, 2010. 442: p. 445-452.
182. Randle, V. and O. Engler, *Introduction to texture analysis*. 2000, Boca Raton: CRC Press.
183. Al-Shahrani, S. and T.J. Marrow, *Influence of Twins on Short Fatigue Cracks in Type 316L Stainless Steel*. Key Engineering Materials, Trans Tech Publications, Switzerland, 2011. 465(2011): p. 507-510.
184. Dunne, F.P.E., A.J. Wilkinson, and R. Allen, *Experimental and computational studies of low cycle fatigue crack nucleation in a polycrystal* International Journal of Plasticity, 2007. 23 (2007).
185. Kumar, S. and W.A. Curtin, *Crack interaction with microstructure*. Materials Today, 2007. 10(9): p. 34-44.
186. Duff, J.A. and T.J. Marrow, *In-Situ Observations of Intergranular Stress Corrosion Cracking*. Proceedings of the Asme Pressure Vessels and Piping Conference - 2008, Vol 6, Pt a and B, 2009: p. 847-854.
187. Kamaya, M., *Measurement of local plastic strain distribution of stainless steel by electron backscatter diffraction*. Materials Characterization, 2009. 60(2): p. 125-132.
188. Wilkinson, A.J., *New method for determining small misorientations from electron back scatter diffraction patterns*. Scripta Materialia(USA), 2001. 44(10): p. 2379-2385.
189. Wilson, D., *Relationships between microstructure and behaviour in the uniaxial tensile test*. Journal of Physics D: Applied Physics, 1974. 7: p. 954.
190. Ry , J. and M. Witkowska, *Microstructure and Deformation Behavior of Cold-Rolled Super-Duplex Stainless Steel*. Solid State Phenomena, 2010. 163: p. 151-156.
191. Guerre, C., O. Raquet, E. Herms, M. Le Calvar, and G. Turluer. *SCC growth behavior of austenitic stainless steels in PWR primary water conditions*. 2005.
192. Kitikhun, S., J. Nathapon, S. Weerawat, C. Jirawat, and W. Pornwasa, *Stress Corrosion Cracking Behavior of Austenitic Stainless Steel AISI 304 with Cold Work Severities of 60 and 90 Percent Reduction in Thickness*. Journal of Metals, Materials and Minerals, 2010. 20(3): p. 25-29.
193. Raquet, O., E. Herms, F. Vaillant, T. Couvant, and J.M. Boursier, *SCC of cold-worked austenitic stainless steels in PWR conditions*. Advances in Materials Science, 2007. 7(1): p. 11.

## *Appendix*

### **The Author:**

#### **Education:**

-The University of Manchester-UK (started 2008), current study as a PhD candidate in the School of Materials.

-The University of Sheffield-UK, 2003-2004, (Master of Metallurgy).

-King Fahd University of Petroleum and Minerals-Saudi Arabia, 1994- 1999 (B.A. -Applied Mechanical Engineering).

#### **Employer:**

1999–current, Lab. Engineer at Research and Technology Centre, Saudi Basic Industries Corporation (SABIC), Jubail Industrial City, Saudi Arabia.

#### **Publications and Posters:**

-During this PhD study, the following papers have been selected:

**M. Al-Rabie and T.J. Marrow:** Observation of Stress Corrosion Cracking in Super Duplex Stainless Steel (Zeron 100) Using Digital Image Correlation, The European Corrosion Congress 2011, 4 to 8 September 2011 in Stockholm, Sweden.

**M. Al-Rabie and T.J. Marrow:** Influence of High Misorientation Angle on Retardation of Short Stress Corrosion Cracking in Super Duplex Stainless Steel, The 5<sup>th</sup> Saudi International Conference, Coventry, UK, 2011.

-The following poster has been presented:

**M. Al-Rabie and T.J. Marrow:** In-situ observations of stress corrosion cracking behaviour in Super Duplex Stainless Steel, School of Materials-PG Conference, University of Manchester- UK, May 2010.